

High-energy processes in low-mass protostars – an X-ray to radio multi-wavelength perspective

Dissertation

zur Erlangung des Doktorgrades (Dr. rer. nat.)
der Mathematisch-Naturwissenschaftlichen Fakultät
der Rheinischen Friedrich-Wilhelms-Universität Bonn

vorgelegt von
Jan Forbrich
aus Niebüll

Bonn 2006

Angefertigt mit Genehmigung der Mathematisch-Naturwissenschaftlichen Fakultät
der Rheinischen Friedrich-Wilhelms-Universität Bonn

- 1. Referent:** Prof. Dr. rer. nat. Karl M. Menten
- 2. Referent:** Prof. Dr. rer. nat. Pavel Kroupa

Tag der Promotion: 6. Februar 2007

Diese Dissertation ist auf dem Hochschulschriftenserver der ULB Bonn
http://hss.ulb.uni-bonn.de/diss_online
elektronisch publiziert. Das Erscheinungsjahr ist 2007.

Meinen Eltern

High-energy processes in low-mass protostars – an X-ray to radio multi-wavelength perspective

Abstract

High-energy processes in protostars remain poorly understood. Only after the recently finished Chandra Orion Ultra-deep Project (COUP), statistically significant information on X-ray emission from Young Stellar Objects (YSOs) has been obtained. For an understanding of the mechanisms responsible for the X-ray emission, multi-wavelength correlations of flares, especially in the radio regime, are necessary and have become an active field of research. Magnetic fields cause several high-energy phenomena in the coronae of YSOs mainly due to magnetic reconnection which are observable in a wide wavelength range from nonthermal centimetric radio emission to X-rays. In this work, these processes were probed using a variety of very different methods which can be grouped into three major topics:

X-ray to radio multi-wavelength variability of Young Stellar Objects The *Coronet* cluster in the nearby R CrA dark cloud offers the rare opportunity to study a compact cluster of several very young protostars which are detected at radio- and X-ray wavelengths. Initially, a study focusing separately on X-ray and radio variability of these sources was conducted. Subsequently, in August 2005, the same region was studied in the first simultaneous X-ray, radio, near-infrared, and optical monitoring campaign of YSOs. Several observatories were observing simultaneously, namely the *Chandra* X-ray Observatory, the VLA, as well as telescopes with optical and near-infrared detectors in Chile and South Africa. Remarkable intra-band variability but no clearly correlated variability was found. This most importantly suggests that there is no direct link between the X-ray and optical/infrared emission and supports the notion that accretion is *not* an important source for the X-ray emission of these YSOs. Combining the *Chandra* X-ray data collected in the course of the multi-wavelength campaign with previous archival data, one of the deepest X-ray datasets ever obtained of a star-forming region is obtained and discussed.

Radio emission from protostars Looking for compact nonthermal centimetric radio emission, high-sensitivity Very-Long-Baseline Interferometry (VLBI) observations of four nearby protostars were carried out, yielding the currently most sensitive data of such sources. Weak compact emission was found in the VLBI data of the class 0/I binary YLW 15 VLA 2, constraining the size of its corona to $< 0.4 \times 0.1$ AU. Since this source is part of a binary system with observed orbital motion, further VLBI observations will allow to quickly determine the orbit very accurately. The observed sources apparently were showing quiescent radio emission on the larger scales probed by the Very Large Array (VLA). Until now, only very few radio flares of YSOs have been observed in detail. In further work, two such examples are presented and analyzed: a flaring, deeply embedded protostar in Orion and a flaring binary T Tauri system whose activity is due to inter-binary coronal interaction.

The earliest stages: Magnetic fields in molecular clouds While mapping molecular clouds in polarized dust continuum emission has become a standard technique, the potentially more powerful technique using the “Goldreich-Kylafis” effect has been only rarely used until now. This effect predicts weakly linearly polarized molecular line emission under certain circumstances. By choosing different transitions, it is possible to probe the magnetic field direction in different regions in a molecular cloud core, and additionally one gets information along the line of sight for optically thin emission lines. The XPOL correlation polarimeter at the IRAM 30m telescope was used in a search for such linearly polarized emission in several bright molecular transition lines towards prominent star-forming regions. The combined effects of instrumental polarization and extended emission were simulated for a thorough interpretation of the results. In one case, the observed polarization exceeds the simulated instrumental value.

Contents

List of Figures	v
List of Tables	vii
1 Introduction	1
1.1 An overview of low-mass star formation	2
1.1.1 Evolutionary stages	2
1.1.2 Initial conditions	4
1.1.3 Slow vs. fast star formation	6
1.2 Observations of magnetic fields in star formation	6
1.2.1 The earliest stages: Magnetic fields in molecular clouds	6
1.2.2 X-ray emission from YSOs	7
1.2.3 Radio emission from YSOs	9
1.2.4 Magnetic field structure in the vicinities of YSOs	10
1.2.5 Simultaneous multi-wavelength variability	12
1.3 YSOs in the <i>Coronet</i> cluster	13
1.4 Observatories	14
1.5 Objectives of this work	16
2 Radio and X-ray variability of Young Stellar Objects in the Coronet cluster	19
2.1 Introduction	19
2.2 Observations and data analysis	19
2.2.1 Radio observations	19
2.2.2 Archival X-ray data	21
2.3 Results	22
2.3.1 Radio monitoring	22
2.3.2 Archival X-ray data	24
2.3.3 Synthesis	25
2.3.3.1 The class I protostars IRS 2, IRS 5, IRS 1, and IRS 9	25
2.3.3.2 Radio Source 5 and IRS 6: A candidate brown dwarf and a T Tauri star	29
2.3.3.3 The IRS 7 complex with its two deeply embedded protostars	30
2.3.3.4 The Herbig Ae star R CrA	31
2.4 Conclusions	34
3 Simultaneous multi-wavelength monitoring of YSOs in the Coronet cluster	37
3.1 Introduction	37
3.2 Observations and data reduction	37
3.2.1 X-ray observations	39
3.2.2 Radio observations	40
3.2.3 Near-infrared and optical observations, photometry	41

3.2.3.1	S CrA	41
3.3	Single-wavelength variability	42
3.3.1	Radio data	42
3.3.2	X-ray data	44
3.3.3	Near-infrared and optical data	44
3.4	Multi-wavelength variability	45
3.4.1	The class I protostars IRS 2, 5, 1, and 9	45
3.4.2	The Herbig Ae/Be stars R CrA, T CrA, and TY CrA	47
3.4.3	The classical T Tauri stars S CrA and IRS 6	49
3.4.4	Additional sources	50
3.5	Conclusions	51
4	Coronae in the Coronet: A very deep X-ray look into a stellar nursery	53
4.1	Introduction	53
4.2	Chandra observations and data analysis	53
4.3	X-ray sources and cluster members	55
4.3.1	Source identification	55
4.3.2	X-ray emission and membership in the star-forming region	58
4.3.2.1	Optically visible member candidates	58
4.3.2.2	Mid-Infrared excess sources as seen with the Infrared Space Observatory (ISO)	59
4.3.2.3	Very low-mass stars	59
4.3.2.4	IRS 3: a background giant rather than a YSO	59
4.3.2.5	YSO candidates from <i>Spitzer</i> -IRAC photometry	60
4.4	X-ray properties of the YSOs	61
4.4.1	X-ray variability and spectroscopic analysis	61
4.4.2	X-ray properties of different object classes	61
4.4.2.1	B- to F-type stars	61
4.4.2.2	T Tauri Stars	66
4.4.2.3	The class 0 protostar candidate IRS 7E	67
4.4.2.4	Class I protostars	68
4.4.2.5	Brown Dwarfs	69
4.4.2.6	Comparison of the X-ray properties of different object classes	71
4.5	Diffuse X-ray emission	72
4.6	An X-ray census of young stars in the <i>Coronet</i> region	72
4.7	Conclusions	74
5	Searching for coronal radio emission from protostars by VLBI	79
5.1	Introduction	79
5.2	Target selection	80
5.2.1	The binary protostar YLW 15	80
5.2.2	The binary protostar LDN 1551 IRS 5	81
5.2.3	The class I/II transition protostar HL Tau	81
5.2.4	The Proto-Herbig Ae/Be star EC 95	82
5.3	Observations and data analysis	82
5.4	Results	85
5.4.1	VLA data	85
5.4.2	VLBI data	86
5.5	Summary	88
6	A 1.3 cm radio flare from a deeply embedded source in the Orion Nebula	89

6.1	Introduction	89
6.2	Observations and results	89
6.2.1	Radio data: VLA observations	89
6.2.1.1	Basic calibration and imaging	89
6.2.1.2	Further Processing	91
6.2.1.3	Results: Time variability	93
6.2.2	Radio data: VLA 8.4 GHz archival data	93
6.2.3	X-ray data: Archival Chandra observations	96
6.2.4	Infrared data: Archival HST, VLT, and <i>Spitzer</i> data	97
6.3	Summary	98
7	Synchrotron millimeter radio emission from a T Tauri binary system	101
7.1	Introduction	101
7.2	The V773 Tau A binary system	102
7.3	Observations and data reduction	104
7.4	Rapid flare decay: leakage of the emitting particles	104
7.5	The flaring phase: a propagating shock	106
7.6	Magnetic configuration	107
7.7	Conclusions	109
7.8	Appendix: Energetic considerations	110
8	Search for weak linear polarization in molecular line emission towards proto-stars	113
8.1	Introduction	113
8.2	Observations and data analysis	114
8.3	Results and discussion	116
8.3.1	Simulating the instrumental response	117
8.3.2	G34.3+0.2: Intrinsically polarized?	118
8.4	Summary	119
9	Summary	129
A	Some constants and units	133
A.1	Astronomical constants	133
A.2	Units	133
	Bibliography	135
	Acknowledgments	151

List of Figures

1.1	Total extinction cross section from infrared to X-rays	2
1.2	The stages of low-mass protostellar evolution	3
1.3	Four magnetic-field configurations that may be responsible for the magnetic activity of class I protostars.	11
1.4	Optical (DSS2, left) and near-infrared (K' , right) views of the <i>Coronet</i> cluster . .	13
2.1	VLA and <i>Chandra</i> views of the <i>Coronet</i> cluster	20
2.2	Radio flux density curves of sources identified in the 1998 VLA data.	26
2.3	IRS 5 epoch-averaged polarization degrees in percent.	26
2.4	X-ray spectra of IRS 2, 5 and 1 derived from the five X-ray datasets.	27
2.5	Results of fitting XSWABS×XSAPEC, fit parameters N_{H} and kT.	27
2.6	X-ray luminosity curves for the three class I protostars IRS 2,5, and 1.	28
2.7	X-ray vs. radio luminosity of identified YSOs for which X-ray luminosities can be derived from spectra.	30
2.8	IRS 7E X-ray luminosity	32
2.9	R CrA X-ray spectra	32
2.10	R CrA X-ray luminosity curves	33
3.1	Plot of the <i>Coronet</i> region covered in this multi-wavelength dataset	38
3.2	Graphical depiction of the observing times at the different observatories indicated on the lefthand side.	39
3.3	Combined <i>Chandra</i> data (Obs ID 5402-5406, smoothed for better depiction). The circle denotes the approximate VLA half-power primary beam.	40
3.4	Exemplary VLA radio flux density curves for the three class I protostars IRS 1, 2, and 5, as well as for R CrA	43
3.5	The double source IRS 5 (marginally resolved here) and its neighbouring source IRS 5N seen in K_S (SofI/NTT) on August 9, 2005.	44
3.6	<i>Chandra</i> X-ray light curves of IRS 5 for the five observations S1-S5 and K_S -band differential photometry taken with SIRIUS and SofI	45
3.7	<i>Chandra</i> X-ray light curves for YSOs with near-simultaneous IRSF J -band data	46
3.8	<i>Chandra</i> X-ray light curves for YSOs with simultaneous CTIO I -band data	48
3.9	The total I -band magnitude of S CrA and the magnitude difference between the two components of S CrA	51
3.10	Detail of the X-ray and I -band light curves of S CrA	51
3.11	CTIO- I light curves for T CrA and HBC 680	52
4.1	<i>Spitzer</i> IRAC $3.6\ \mu\text{m}$ image of the <i>Coronet</i> region	57
4.2	Long-term evolution of the X-ray emission of selected sources in the <i>Coronet</i> region	62
4.3	<i>Chandra</i> X-ray spectra of some YSOs in the <i>Coronet</i> region	63
4.4	IRAC mid-infrared colors of the Perseus class I protostars and the likely class 0 protostar IRS 7E	67

4.5	<i>Chandra</i> image of the IRS 5 a/b region, original data and maximum-likelihood-reconstructed super-resolution image	68
4.6	Detail of the X-ray spectrum of IRS 5 around the 6.7 keV iron line	68
4.7	Plasma temperatures versus X-ray luminosities for the CrA members with sufficient counts for X-ray spectral fitting	71
4.8	<i>Chandra</i> X-ray image of the central region, showing the diffuse emission between IRS 7 W and R CrA	71
4.9	Extinction map of the CrA star-forming region from Dobashi et al. (2005)	72
5.1	VLA-only maps of YLW 15-VLA2, EC95, HL Tau, and L1551 IRS5	83
5.2	VLA-only map of YLW 15, restored with a circular 0''4 beam	84
5.3	VLBI maps of the phase calibrators used in the experiments	85
5.4	Weak source found in the VLBI data of YLW 15 YLW 2	87
5.5	Archival VLT-ISAAC <i>J</i> -band data of YLW 15	88
6.1	The Orion 1.3 cm sources overlaid onto a <i>JHK</i> color composite of the region	90
6.2	HST-NICMOS and <i>Spitzer</i> views of the region	91
6.3	1.3 cm flux density curves for the six brightest sources	94
6.4	Light curves of the flaring source KBS and BN for comparison	95
6.5	Source elevation during the discussed 1.3 cm observation.	96
6.6	Maps of the flare source	97
6.7	COUP X-ray image of KBS/COUP 647	98
6.8	COUP X-ray light curve of KBS/COUP 647	99
7.1	Radio spectra of the Sun and UX Arietis	102
7.2	V773 Tau A flare observed August 6, 2003	105
7.3	Variations of the height H_1 , where magnetic reconnection occurs, as a function of magnetic field intensity and plasma density and Alfvén radius as a function of magnetic field intensity and mass loss rate	108
7.4	Sketch of the magnetic structure of a helmet streamer	109
7.5	Sketch of the binary system with the orbit parameters of Welty (1995)	109
8.1	Stokes spectra (I, Q, U, V) and resulting linear (p_L, χ) as well as circular (p_C) polarizations	120
8.2	Beam maps of the 30m telescope (in Stokes- I, Q, U , and V)	124
8.3	On-the-fly maps of DR21(OH), G34.3+0.2, and W3(OH)	125
8.4	Simulated linear polarization after convolving the measured maps of the line-integrated source environments with the Stokes beam maps	126
8.5	Line ratio $^{13}\text{CO}(1-0)/\text{C}^{18}\text{O}(1-0)$ for G34.3+0.2 (where both lines have $T_a > 0.1$ K) with inferred optical depth τ of the $^{13}\text{CO}(1-0)$ transition indicated	127

List of Tables

2.1	VLA <i>Coronet</i> observation dates	21
2.2	Archival X-ray data used in this study	21
2.3	Positions and identification of <i>Coronet</i> radio and X-ray sources	22
2.4	<i>Coronet</i> sources, radio data	23
2.5	<i>Coronet</i> sources, X-ray data	23
2.6	X-ray spectral fitting results for IRS 2, 1, 5, and R CrA: Absorbing column density and plasma temperature	24
2.7	Comparison of column densities towards IRS 2, 5, and 1 derived from NIR and X-ray emission	25
2.8	Bolometric and X-ray luminosities (derived from X-ray spectra)	25
3.1	Simultaneous observations of the <i>Coronet</i> with <i>Chandra</i> and the VLA	39
3.2	Radio flux densities of the <i>Coronet</i> sources	42
3.3	X-ray count rates for the five <i>Chandra</i> observations, 0.5-10 keV, corrected for effective exposure	43
3.4	X-ray count rates for discussed sources outside the VLA primary beam	50
4.1	<i>Chandra</i> observations of the CrA star-forming region used in this study.	54
4.2	Identification of <i>Chandra</i> X-ray sources with optical or infrared counterparts	56
4.3	X-ray spectral fitting results for one- and two-temperature models	64
4.4	Results for the Brown Dwarf candidates	70
4.5	CrA acis_extract source list	76
5.1	Journal of VLBI observations	80
5.2	VLBI correlator parameters	84
5.3	VLA-only results	85
5.4	VLBI results	88
6.1	Sources detected in Orion 1.3 cm data after subtraction of the flare source	92
6.2	Results of fitting linear functions $f(x) = ax + b$ to the light curves	93
6.3	The double 8.4 GHz counterpart as observed on September 6, 1991 (M. Reid, priv.comm.). The synthesized beam size for this observation is 299×216 mas at position angle -39.2° . The corresponding rms map noise is ~ 0.04 mJy, and the positional Gaussian fitting error is $\sim 0.5 \times \text{HPBW}/\text{SNR} \approx 20$ mas (see Table 6.1).	96
7.1	Flux density of V773 Tau in November 2003	104
8.1	30m observations, April 2005: Source coordinates	114
8.2	30m observations, April 2005: Molecular transition lines, integration times, and hour angle ranges	115

Chapter 1

Introduction

For centuries, the question how stars form has been one of the major questions of astronomical research. Our current understanding of star formation has gradually developed from the “nebular hypothesis” put forward by Kant (1755) and a similar model proposed by Laplace (1796). Immanuel Kant suggested that our solar system was formed from a slowly rotating nebula, gradually contracting by gravitation and flattening into a disk. We now know that stars form by gravitational collapse of dense cores in molecular clouds containing dust and gas, predominantly in molecular form.

Rapid technological progress in astronomical detector development beginning in the 1970s combined with the nowadays routine availability of space-based observatories was followed by equally fundamental progress in our theoretical understanding of star formation in recent decades. In order to observe the deeply embedded earliest stages of star formation, it was especially important to extend the observable part of the electromagnetic spectrum from visible light to longer wavelengths up to the far infrared, and from centimetric radio waves to shorter wavelengths, the millimeter and submillimeter wavelength regime. In fact, these two initially fundamentally different technical developments are about to meet to close this gap in wavelength coverage. Of comparable importance was the development of X-ray astronomy leading to observations of deeply embedded protostars since the 1990s. The extinction cross section of the interstellar medium is roughly comparable for soft X-rays and near-infrared light (see Fig. 1.1, Ryter 1996), on the slopes towards short and longer wavelengths starting at the Lyman discontinuity in the UV range. Star formation research thus has become an inherently multi-wavelength business, each wavelength range providing pieces of a large jigsaw puzzle. Of course, observational aspects are closely interacting with theoretical modeling of protostellar evolution trying to understand what is observed and making predictions what should be observed in order to discriminate between different models.

Consequently, star formation research saw the development of a ‘standard’ model of low-mass star formation¹ (for an early, very influential, review, see Shu et al. 1987). According to this ‘standard’ model, magnetic fields dominate the early star formation process by initially stabilizing self-gravitating molecular cloud cores against collapse, thus determining the timescale of star formation. However, with the competing paradigm of turbulence-controlled star formation (e.g. Ballesteros-Paredes et al. 2006) predicting no significant role for magnetic fields in the star formation process, their role remains at the same time unclear and crucial to our understanding of star formation.

After a brief introduction to low-mass star formation, observable manifestations of magnetic fields and ensuing high-energy processes from the earliest stages of star formation to protostars are presented. Subsequently, the *Coronet* cluster, a protostar cluster extensively studied in

¹High-mass star formation of stars with masses $\gtrsim 10 M_{\odot}$ is more difficult to classify because their rapid evolution leads to their arrival on the main sequence with accretion still ongoing. In the following, only low-mass star formation will be discussed.

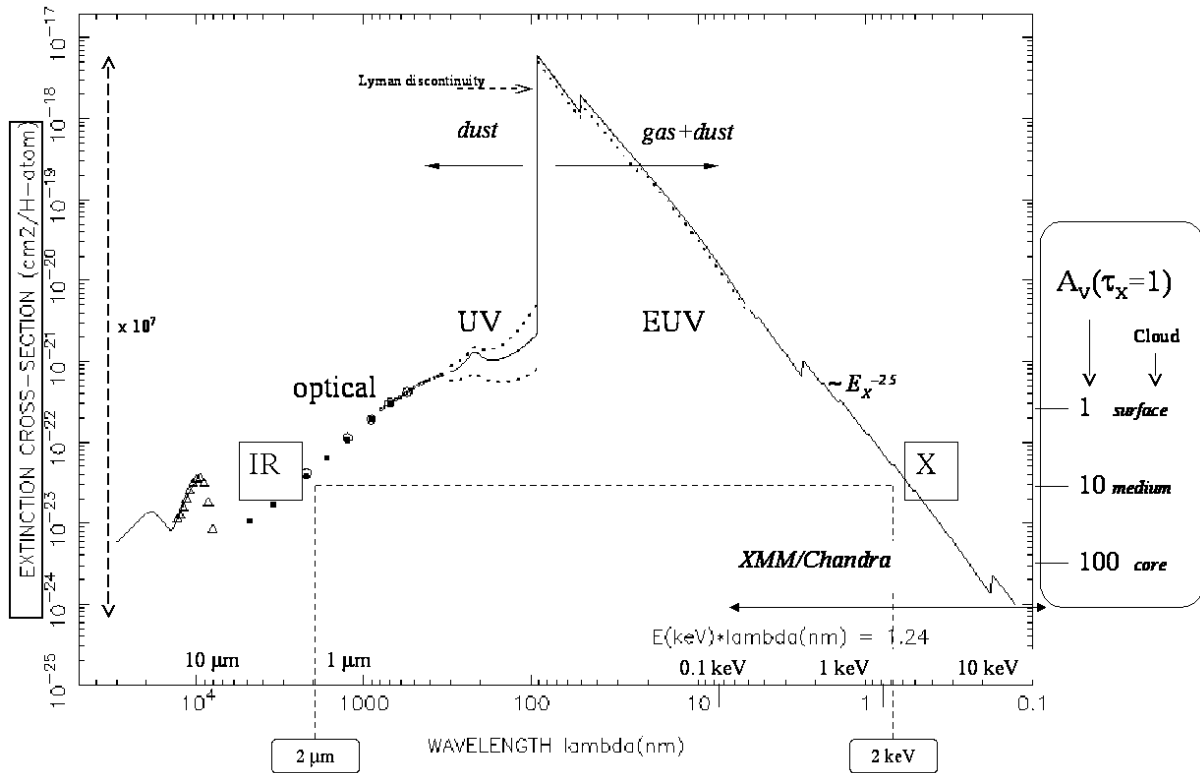


Figure 1.1: Total extinction cross section from infrared to X-rays (from Montmerle 2001, based on Ryter 1996). As indicated, the extinction cross section is equivalent for near-infrared and soft X-ray emission. How deeply X-rays can penetrate molecular clouds is shown at right by the equivalent visual extinctions A_V . See Ryter (1996) for a detailed discussion and the sources of the data at different wavelengths.

Chapters 2 to 4, is introduced. Finally, the scientific objectives of this work are summarized.

1.1 An overview of low-mass star formation

1.1.1 Evolutionary stages

While the ‘standard’ model evolved, a first classification scheme for different evolutionary stages of low-mass protostars was conceived, based on observable properties in the infrared and sub-millimeter regime (Lada 1987; André et al. 1993; André & Montmerle 1994). According to this scheme, low-mass Young Stellar Objects (YSOs) evolve through a series of stages termed class 0 to class III with preceding collapse and accretion (see Fig. 1.2). Basically, the spectral energy distribution (SED) of these objects develops from cold blackbody radiation with a peak at submillimeter wavelengths to subsequently higher temperatures seen correspondingly also at shorter wavelengths. For the stages I–III which are well observable in the infrared wavelength range, the spectral slope is a direct classification criterion when assuming a simple power-law spectrum, $\lambda F_\lambda \propto \lambda^n$: A steep spectrum with $n > 0$ identifies a class I object, $-2 < n < 0$ a class II object, and $n < -2$ a class III object.

- When the gravitational collapse of a molecular cloud core has just started, it enters the stage of a class 0 protostar. Material is rapidly accreted onto a central object, and soon after the onset of accretion, disks as well as powerful bipolar outflows and jets develop. Shocked material along and leading a collimated jet is observed as “Herbig-Haro” (HH) objects. Most of the material is still in the circumstellar envelope. Since the protostar is

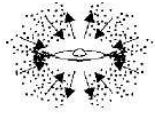
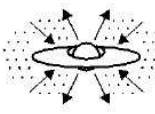
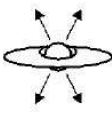
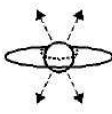

PROPERTIES	<i>Infalling Protostar</i>	<i>Evolved Protostar</i>	<i>Classical T Tauri Star</i>	<i>Weak-lined T Tauri Star</i>	<i>Main Sequence Star</i>
SKETCH					
AGE (YEARS)	10^4	10^5	$10^6 - 10^7$	$10^6 - 10^7$	$> 10^7$
mm/INFRARED CLASS	Class 0	Class I	Class II	Class III	(Class III)
DISK	Yes	Thick	Thick	Thin or Non-existent	Possible Planetary System
X-RAY	?	Yes	Strong	Strong	Weak
THERMAL RADIO	Yes	Yes	Yes	No	No
NON-THERMAL RADIO	No	Yes	No ?	Yes	Yes

Figure 1.2: The stages of low-mass protostellar evolution (from Feigelson & Montmerle 1999).

still deeply embedded in the cloud core, this stage can only be observed by the submillimeter to millimeter continuum emission of the cold envelope and in molecular line emission which may show signs of outflowing material in the line wings. Sometimes, the central source can be detected in centimetric radio emission due to thermal emission from ionized material, e.g. at the base of outflows. The question at which point protostars start to emit X-ray radiation remains unclear. After this onset, X-ray activity persists throughout the subsequent evolutionary stages. This evolutionary phase lasts for only about $\sim 10^4$ years.

- In the class I stage, the protostellar luminosity is still mainly due to accretion, although a considerable fraction of the final matter has already been accreted. The accretion rate is already lower than in the class 0 stage. With diminishing extinction, class I protostars can already be detected in the near-infrared. An infrared excess when compared to mere blackbody radiation is caused by the emitting circumstellar disk. The outflow mass loss rate is already decreasing. The class I phase lasts for about $\sim 10^5$ years. Only a single clearly identified class I object, CrA-IRS 5, shows nonthermal radio emission, probably due to extinction in other cases (see Section 1.2.3). This source is discussed in detail in this work (Chapters 2 to 4).
- In the subsequent class II phase, the object is also called a “classical T Tauri star” (CTTS). At this stage, the star is already close to its final mass but is still undergoing disk accretion. Outflow activity, while still present initially, comes to a halt while disk winds are still important. Typical ages of these sources are on the order of several 10^6 years. From this stage onwards, there is no more envelope material, and only the disk remains so that the nascent star becomes optically visible. No nonthermal radio emission has been found

towards these sources which is likely again due to extinction.

- The class III YSOs, also called “weak-line T Tauri stars” (WTTS) only have remnant debris disks although they are still pre-main sequence stars. Typical ages are on the order of $10^6 - 10^7$ years. Subsequently, the main sequence is reached and star formation is finished. Several WTTS with nonthermal radio emission have been detected.

With more and better data available especially in the infrared range, but also in X-rays, shortcomings of a classification scheme which mainly takes into account the circumstellar material rather than the central object have become more apparent. A promising way to characterize the continuous evolution of a YSO throughout the above stages is the use of mid-infrared spectra or at least colors, especially as determined from *Spitzer* mid-infrared photometry (e.g. Jørgensen et al. 2006 for the discrimination specifically of class 0 and class I sources). Still, information from all available wavelength ranges should be used to distinguish different evolutionary stages.

1.1.2 Initial conditions

In the simplified case of an isothermal and initially uniform gas without magnetic fields, a cloud core becomes gravitationally unstable once it becomes more massive than a certain critical mass, the Jeans mass. The criterion (Jeans 1928) is that a medium will be gravitationally unstable on length scales larger than a critical value, λ_J (the Jeans length). The corresponding critical mass for an initially uniform, isothermal gas with density ρ and sound speed c_s can be given as (Hartmann 1998)

$$M_J = \rho \lambda_J^3 = \left(\frac{\pi c_s^2}{G} \right)^{3/2} \rho^{-1/2} \approx 750 M_\odot T_{10}^{3/2} n_{H_2}^{1/2} \quad (1.1)$$

where T_{10} is the temperature in units of 10 K and n_{H_2} is the molecular hydrogen density in units of cm^{-3} (the latter approximation assumes pure molecular hydrogen gas).

Magnetic fields complicate the picture. Assuming that a small fraction of the interstellar medium in the cloud is ionized, e.g. by the surrounding radiation field especially in the outer regions of a cloud, these ions are coupled to a magnetic field by the Lorentz force.

Once a gas is sufficiently conducting, the magnetic flux per volume element remains constant. Since gravitational and magnetic pressure have the same – though opposite sign – dependency on radius, this means that if magnetic fields are able to prevent collapse once, they will always be able to do so. Still, the gravitational pressure dominates the magnetic pressure above a certain mass threshold. Inclusion of magnetic pressure in the equilibrium assessment of thermal and gravitational pressure leading to the critical Jeans mass yields a well-defined critical mass at which the stabilizing effect of magnetic fields is overcome and collapse occurs.

When calculating this critical mass M_B for different configurations, taking into account e.g. non-spherical clouds and non-uniform magnetic fields, Mouschovias & Spitzer (1976) found that the results differ only slightly. Approximately, the resulting M_B can be written as (Hartmann 1998)

$$M_B \approx 10^2 M_\odot \left(\frac{B_{cl}}{[100 \mu\text{G}]} \right)^3 \left(\frac{n_{H_2}}{[10^4 \text{cm}^{-3}]} \right)^{-2} \quad (1.2)$$

where B_{cl} is the mean magnetic field in the cloud and n_{H_2} is the mean density of molecular hydrogen. Assuming a typical cloud core density of 10^4cm^{-3} , a cloud of one solar mass, for example, could only collapse in case of $B_{cl} \leq 20 \mu\text{G}$.

In the ensuing collapse, among many open questions there are two main problems demanding explanation. On the one hand, magnetic fields in molecular clouds are often observed to be strong enough to support the clouds against gravitational collapse. On the other hand, the

conservation of angular momentum during the contraction of a molecular cloud over many orders of magnitude in linear scale leads to a rapid increase in rotational velocity even when starting out with only very low velocities. This also prevents further collapse. Some effective means of angular momentum transport is needed for star formation finally to occur.

The first problem, magnetic fluxes observed to be high enough to prevent collapse, can be overcome in the following way. Magnetic fields do not isotropically interact with the surrounding matter. Gas and dust with a certain degree of ionisation can move more easily along magnetic field lines than perpendicularly to them if there are no more obstacles to movement, e.g. turbulence. This leads to a dependency of the mean magnetic field B on the mean gas density ρ , $B \propto \rho^n$ with $1/3 \leq n \leq 1/2$ (Mouschovias 1991) which is, however, not yet sufficient to solve the problem.

In the dense inner parts of a molecular cloud extinction can be high enough to entirely absorb the interstellar ultraviolet radiation field leading to much lower ionisation degrees in the densest parts of a cloud compared to its less dense outer regions. This radiation field is important for the coupling of matter to the magnetic field by ionisation. While ions are coupled to the magnetic field by means of the Lorentz force, this is only indirectly the case for neutral species. Their coupling to the magnetic field is by collisions with ions. In a region with a considerably reduced degree of ionisation like the dense core of a cloud, these neutral particles can drift through the magnetic field lines and concentrate in the center quite undisturbed by a magnetic field. This relatively slow process of neutral species slipping through their ionized counterparts is called “ambipolar diffusion”, a concept developed early on in the history of star formation theory when it was unclear how a (then controversial) Galactic magnetic field would affect gravitational collapse (Mestel & Spitzer 1956).

Ambipolar diffusion is a very important part of the standard model of low-mass star formation. However, since it takes much more time than the free-fall timescale questions concerning the timescales of star formation are at the heart of the problem. Maybe even ambipolar diffusion is not a complete solution of the magnetic flux problem. Among indications to the contrary are, for example, the observation that the photoionisation rates of hot stars have apparently been underestimated (Myers & Khersonsky 1995), or the fact that in the Orion star-forming region, most star formation appears to take place on timescales of about a million years, too short for ambipolar diffusion to play a decisive role (e.g. Hillenbrand 1997).

Another unsolved problem becomes apparent when calculating the expected surface magnetic field of a T Tauri star when starting from the critical magnetic flux for the formation of a $0.5 M_{\odot}$ star. The resulting value of $\sim 10^7$ G is much higher than the stellar surface magnetic fields actually observed. These observations mostly make use of the Zeeman effect and yield values of $B \sim 1 - 3$ kG (e.g. Bouvier et al. 2006, and references therein), fulfilling a requirement of magnetospheric accretion models, namely a minimum field of a few kG in order to disrupt the circumstellar disk at a few stellar radii.

Magnetic fields also play an important role in solutions of the second problem mentioned above, the transport of angular momentum. The problem of increasing rotation velocities preventing further collapse is apparently circumvented by the formation of now frequently observed circumstellar disks (e.g. Dutrey et al. 2006) as well as outflows² (e.g. Bally et al. 2006) perpendicular to the plane of the disk.

The formation and collimation of outflows and jets can be explained by magnetic fields (for recent reviews, see Shang et al. 2006; Pudritz et al. 2006). However, the actual structure of the magnetic field in the vicinity of a protostar and its disk remains unknown. Since T Tauri stars without circumstellar disks (the weak-line T Tauri stars) do not show the same signs of outflows as do classical T Tauri stars and since for the archetypical FU Ori it was directly shown that its wind comes from the disk (Hartmann & Calvet 1995), it seems that these circumstellar disks

²It was initially surprising to see how energetic these outflows are (e.g. Lada 1985 for an early review), especially since naively one could have expected dominating *infall* motion.

play a central role in the explanation of outflows.

1.1.3 Slow vs. fast star formation

The paradigm of low-mass star-formation according to the 'standard' model with strong magnetic fields and ambipolar diffusion determining the star formation timescale is currently challenged by the paradigm of fast turbulence-controlled star formation in which magnetic fields play no significant role. In the latter picture, molecular clouds are dynamically controlled by turbulence and short-lived; star formation starts from transient density enhancements. It remains unclear, however, how turbulence on different spatial scales is constantly replenished. An important question in this context concerns the effect of these initial conditions on the initial mass function (IMF), i.e. the question what determines the final mass of a star. For a topical review of molecular cloud turbulence and star formation, see Ballesteros-Paredes et al. (2006). The 'standard' model is discussed by e.g. Mouschovias & Ciolek (1999). After initial claims that the observed ages of molecular clouds (sometimes only a few free-fall times, e.g. Lee & Myers 1999) are too low for the ambipolar-diffusion model to explain, it now seems that it can actually account also for these young ages (Ciolek & Basu 2001; Mouschovias et al. 2006).

A major difference between these two paradigms concerns the earliest stages of star formation, i.e. before a central protostar has formed. While part of the difficulty in discerning these two paradigms lies in the definition of the timescales involved, it is also not clear whether they possibly apply for different star-forming regions. Magnetic fields play a crucial role in the ambipolar-diffusion picture, however they are completely unimportant in the picture of turbulence-controlled star formation. Recent results from interferometric dust polarimetry towards the protostellar system NGC 1333 IRAS 4A show an hourglass-shaped magnetic field morphology (Girart et al. 2006), suggesting that magnetic fields are not negligible at least in this region.

1.2 Observations of magnetic fields in star formation

Observational techniques concerning the role of magnetic fields in star formation can be split into two main groups. On the one hand, there is the role of magnetic fields in the initial conditions of star formation which can be studied by observations of molecular clouds while on the other hand, magnetic fields cause several high-energy phenomena in the coronae of YSOs mainly due to magnetic reconnection. The very different techniques used in this work are briefly introduced in the following.

1.2.1 The earliest stages: Magnetic fields in molecular clouds

The earliest stages of star formation, i.e. the pre-collapse phase, can be observed by studying the emission of cold dust corresponding to blackbody temperatures of around 10 K or by studying correspondingly low rotational transitions of molecules. This radiation is best detected in the millimeter and submillimeter wavelength range.

There are three different possibilities for detecting magnetic fields in molecular clouds, namely observations of the Zeeman effect and linear polarization measurements of the thermal dust continuum as well as of molecular rotational emission lines³. These methods are sensitive to different projections of the magnetic field vector (parallel to the line of sight for Zeeman observations and perpendicular to it for polarization measurements).

The most established method allowing to map the magnetic field geometry of these early stages of star formation is the measurement of polarized dust continuum emission due to the

³For a full discussion of different methods for the observation of interstellar magnetic fields, see e.g. Crutcher et al. (2003).

alignment of non-spherical dust particles with the magnetic field. The strength of a magnetic field can only be indirectly inferred according to a method proposed by Chandrasekhar & Fermi (1953), but the dust polarization measurements allow to map the magnetic field direction projected onto the plane of the sky in different parts of a cloud. This is very important in the light of predictions concerning the presence of ordered large-scale magnetic fields on the one hand and mostly small-scale structure with globally insignificant magnetic fields on the other hand, as they are made in the paradigms of magnetically controlled and turbulence-controlled star formation, respectively.

A complementary method makes use of weak linear polarization in molecular line emission, due to the so-called Goldreich-Kylafis (GK) effect (Goldreich & Kylafis 1981, 1982). Like dust continuum polarimetry, this method yields the magnetic field direction projected onto the plane of the sky, not its total strength (which can be indirectly inferred). The principal advantages of this method when compared to dust continuum polarimetry is that the probed density range can be varied by choosing appropriate molecular line transitions, and the availability of velocity information, i.e. information on how the magnetic field direction varies along the line of sight. However, due to the low degrees of polarization involved, this method is instrumentally much more demanding.

The underlying physics of the GK effect can be best understood in the case of a molecule with only two levels of total angular momenta $F = 1$ and $F = 0$. A magnetic field removes the degeneracy of the three polarized sublevels in the $F = 1$ state, however the net polarization is zero as long as the population of the three sublevels is equal. If now there is an anisotropy in the radiation field, the radiative rates between $F = 0$ and the three sublevels of $F = 1$ become unequal, leading to a weak net polarization if the Zeeman splitting of the magnetic sublevels is larger than the natural line width. The expected degree of polarization depends on a number of parameters, and it turns out that the magnetic field direction is either parallel or perpendicular to the observed polarization direction.

1.2.2 X-ray emission from YSOs

X-ray radiation in this context is restricted to photon energies between ~ 0.1 keV and ~ 10 keV ('soft' to 'hard' emission) which is the interval which can be studied with current X-ray imaging satellites. The emission mechanism concerning us here is bremsstrahlung from hot thermalized plasmas ($T \gtrsim 10^6$ K). This is the typical emission process in the case of the sun and late-type stars where the emission comes from coronal plasmas. In these plasmas, depending on the temperature, also line emission from electron shell transitions in highly ionized elements like Fe is observed. OB stars produce strong winds with energetic shocks which are seen in X-rays. In case of sufficiently large electron energies and magnetic fields, also synchrotron emission can occur in X-rays (e.g. from neutron stars). Additionally, blackbody emission can extend into the X-ray range if temperatures are sufficiently high (e.g. in black hole accretion disks).

Young stars generally show high levels of X-ray activity, exceeding the emission level of the Sun and late-type field stars by several orders of magnitude. X-ray properties of YSOs were recently reviewed by see Feigelson et al. (2006). For a review of the associated high-energy processes, see Feigelson & Montmerle (1999), Preibisch (2004), or, in the framework of stellar radio and X-ray astronomy, Güdel (2002b, 2004). A good knowledge of the X-ray properties of YSOs is very important for the understanding of the underlying physical mechanisms and their relation to the magnetic activity. Also, the X-ray emission has far-reaching consequences for the physical processes in the circumstellar environment, the formation of planetary systems, and the evolution of protoplanetary atmospheres (e.g., Matsumura & Pudritz 2003; Glassgold et al. 2005; Feigelson 2005; Stäuber et al. 2005). In the investigation of the stellar populations of star-forming regions, X-ray studies are particularly effective in discriminating YSOs from unrelated fore- and background field stars. X-ray studies can give a census of the members of a

star-forming region that is independent of circumstellar material, allowing to overcome the bias in membership determinations based on infrared excess criteria. Furthermore, since radiation at energies above ~ 1 keV is much less affected by extinction than optical light, X-ray observations can penetrate up to $A_V \sim 500$ mag into the cloud and allow a deep look at embedded YSOs.

X-ray emission from classical and weak-line T Tauri stars has been known for some time and is thought to be produced in magnetically confined plasma in the coronae (Feigelson & Montmerle 1999; Favata & Micela 2003). During the 1990s, X-ray emission towards a few even younger class I protostars was discovered (reviewed by Neuhäuser 1997). With the launches of *Chandra* and *XMM-Newton*, X-ray observatories with higher spatial resolution and better sensitivity to harder photons (which are less affected by extinction) became available, allowing very sensitive studies of star-forming regions, such as the Orion Nebula Cluster (Garmire et al. 2000; Feigelson et al. 2002, 2003; Getman et al. 2005b), ρ Ophiuchi (Imanishi et al. 2001a; Ozawa et al. 2005) or IC 348 (Preibisch & Zinnecker 2001, 2002).

However, the processes giving rise to magnetic activity in young stars in general and class 0/I protostars in particular are still poorly understood. The deep *Chandra* data of the *Coronet* cluster discussed in Chapter 4 allow to address some of the most important topics in this context:

1) What is the dominant X-ray emission process in YSOs? In most young stars the X-ray emission is clearly related to coronal magnetic activity, in principle similar to what is seen from the Sun and late-type field stars, although at highly ($\sim 100 - 1000$ times) elevated emission levels and at considerably higher plasma temperatures ($\gtrsim 10$ MK). In YSOs that are still actively accreting, another source of X-ray emission may be the hot shocks where accreted material crashes onto the stellar surface (see, e.g., Kastner et al. 2002). X-ray emission from accretion shocks should be very soft and essentially restricted to energies below ~ 0.5 keV, due to the relatively low expected temperatures of at most a few MK in the shock zone. Although the *Chandra* Orion Ultradeep Project (COUP) data clearly showed that the bulk of the X-ray emission from most T Tauri stars is much too hard to be created in accretion shocks and must therefore be of coronal origin (Preibisch et al. 2005a), there is some evidence for a scenario of mixed X-ray emission in some accreting YSOs, where hot ($\gtrsim 10 - 30$ MK) coronal plasma coexists with cool ($\lesssim 1 - 2$ MK) plasma in accretion shocks (e.g. Schmitt et al. 2005). A reliable identification of the signatures of accretion-related X-ray emission (i.e. very low plasma temperatures in combination with rather high plasma densities) usually requires high-resolution X-ray spectra, but the presence of very cool ($\lesssim 2$ MK) plasma components in the fits to medium-resolution ACIS-I CCD spectra of accreting stars may also hint at accretion shocks (see, e.g., Flaccomio et al. 2006)

Nevertheless, there is a relation between X-ray activity and disk accretion in the sense that actively accreting T Tauri stars are *weaker* X-ray emitters than non-accreting T Tauri stars. This effect may be even more important for class I protostars. Possible explanations for this suppression of X-ray emission in accreting T Tauri stars are discussed in Preibisch et al. (2005a) and in Jardine et al. (2006).

Another case of non-solar-like X-ray emission processes may be related to the magnetospheric coupling between a YSO and its disk. In the model of Hayashi et al. (1996), closed magnetic loops connecting the central star and the disk are twisted by the rotation of the disk (see also e.g. Shu et al. 1997; Birk et al. 2000; Isobe et al. 2003). The loops expand with increasing twist until reconnection takes place, hot plasma giving rise to the X-ray and, conceivably, nonthermal radio emission. This mechanism predicts flare periodicity on the order of the rotation period of the innermost parts of the disk and is compatible with observed flare durations, i.e. several hours to days (e.g. Koyama et al. 1996). Montmerle et al. (2000), interpreting quasi-periodic flares on the binary class I object YLW 15, propose an evolutionary scenario explaining X-ray properties of protostars as depending on their rotation velocity. In this picture, young class I sources in which the rotation of star and disk is not yet synchronous, would constitute the strongest

X-ray emitting population of star formation. This phase quickly comes to an end (after a few 10^5 years) and coronal activity becomes the dominant source for X-ray emission. Thus, the following part of the class I stage is already comparable to the class II phase with synchronous rotation, however with much more extinction due to circumstellar material than in the later evolutionary stages. Until now, with no further periodicities found, observational evidence for star-disk magnetic coupling in these objects is inconclusive (Montmerle 2003). However, Favata et al. (2005) find evidence for such coupling from the analysis of intense X-ray flares necessitating large magnetic structures.

2) How early in the protostellar evolution does X-ray activity start? While class I protostars are well established X-ray emitters (e.g., Grosso et al. 1997; Neuhäuser & Preibisch 1997; Imanishi et al. 2001a), it is still unclear whether class 0 protostars, which represent an even earlier, extremely young evolutionary stage in which most of the mass resides still in the circumstellar environment, also show X-ray activity. The recent detection of an X-ray flare from the candidate class 0 protostar IRS 7E in the *Coronet* cluster by Hamaguchi et al. (2005a) provided the first piece of evidence for the presence of X-ray emission in extremely young objects, but the exact evolutionary stage of IRS 7E is not yet fully clear. IRS 7E is discussed further in Chapter 4. An earlier detection of X-rays towards two candidate class 0 sources in OMC-3 (Tsuboi et al. 2001) remains controversial because of the sources' identification as class 0 protostars, Tsujimoto et al. (2004) concluding that in one case the X-ray emission is shock-induced by jets from a nearby class I source.

3) What is the origin of the observed X-ray emission from young intermediate-mass (Herbig Ae/Be) stars? As these intermediate-mass stars have neither outer convection zones that may harbor a dynamo to produce magnetic activity, nor strong enough stellar winds to create X-rays in internal wind shocks, the detection of X-ray emission from a large fraction of the observed Herbig Ae/Be stars was surprising and still remains largely unexplained (e.g., Damiani et al. 1994; Zinnecker & Preibisch 1994; Hamaguchi et al. 2005b; Stelzer et al. 2005). *Chandra* observations with their superior spatial resolution revealed that in some of the X-ray-detected Herbig Ae/Be stars the true source of the X-ray emission is not the A or B star, but a nearby late-type companion. It cannot be excluded that in *all* detected cases the X-ray emission arises from (unresolved) late-type companions. This scenario would require a high multiplicity frequency of the Ae/Be stars and some specific binary mass-ratio distribution⁴. Swartz et al. (2005) recently suggested that X-ray emission from accretion shocks may explain the X-ray detections of Herbig Ae/Be stars at least in some cases.

1.2.3 Radio emission from YSOs

Centimetric radio emission from YSOs allows studying at the same time ionized winds e.g. at the base of outflows as well as magnetic fields in the surroundings of YSOs. Basically, these two different effects are probed by thermal (free-free) and nonthermal radio emission, respectively. The thermal emission is bremsstrahlung (or free-free emission) from a thermalized plasma. It is isotropic and unpolarized. In the context of YSOs, nonthermal radio emission is gyrosynchrotron emission from mildly relativistic electrons gyrating in magnetic fields. It is thus a direct tracer of circumstellar magnetic activity. Distinctive features of nonthermal radio emission include rapid variability, circular polarization, negative spectral indices and exceedingly high brightness

⁴Simulating companions by random sampling from a field IMF would predict most of the companions to be very-low mass (M-type) stars. An unpublished analysis of the COUP data suggests that under this assumption the simulated companions would be too weak X-ray emitters to reproduce the observed distribution of X-ray luminosities for the young A and B stars; companions of G and early K spectral type would be required (Preibisch, private communication).

temperatures ($> 10^7$ K at high spatial resolution). Relativistic electrons gyrating in magnetic fields emit synchrotron radiation which is linearly polarized. The radio properties of YSOs are reviewed by e.g. André (1996, see also André 1987); for a discussion of gyrosynchrotron radio emission from a young B star, see André et al. (1988). For a general discussion of the emission processes, see Dulk (1985).

A number of X-ray emitting classical and weak-line T Tauri stars are sources of nonthermal radio emission produced in large-scale magnetic structures in the coronae of these objects also giving rise to thermal X-ray emission from coronal plasmae. In particular, circularly polarized radio emission indicative of gyrosynchrotron emission has been observed towards several weak-line T Tauri stars (e.g. André et al. 1988, 1992; White et al. 1992; Skinner 1993; Phillips et al. 1993; Rodríguez et al. 1999). Surprisingly, nonthermal emission has not yet been observed towards classical T Tauri stars. This is probably due to optically thick thermal emission from ionized material e.g. at the base of outflows which can easily conceal compact nonthermal emission from underneath (e.g. André 1987).

Class I protostars have mostly been observed to be thermal radio sources. Shang et al. (2004) model the centimetric free-free emission of class I protostars based on the X-wind model (Shu et al. 1997) with X-ray emission as the main ionization source, and indeed some of the class I sources showing X-ray emission are known radio sources as well (e.g. Grosso et al. 1997; Feigelson et al. 1998; Smith et al. 1999). Only two protostars before the T Tauri stage show nonthermal radio emission, the class I object CrA-IRS5 and T Tau S, the infrared companion to T Tau. However, only in the former case, the source is clearly a class I object. Like for the classical T Tauri stars, this low detection rate probably is also due to optically thick thermal emission which makes it impossible to detect nonthermal radiation from underneath.

As at X-ray wavelengths, not all class I protostars are detected at radio wavelengths either: Lucas et al. (2000) detect four out of seven class I sources with outflow activity in Taurus, while Lehtinen et al. (2003) detect one out of four associated to Cederblad 110, interestingly the one with the largest far-infrared flux. These low numbers leave inconclusive the question on the fraction of radio-detected class I sources.

As mentioned above, among the class I sources discussed here in detail in Chapters 2 to 4, one (CrA-IRS 5) is observed to emit nonthermal radio emission (as reported earlier by Feigelson et al. 1998). Already its circular polarization is a clear sign; additionally, its short-term variability is difficult or impossible to reconcile with thermal emission.

An interesting aspect concerning the radio emission of YSOs is their short-term variability. While protostellar variability has recently been extensively studied at X-ray wavelengths, still little is known about short-term protostellar radio variability and even less about multi-wavelength correlations. Part of the difficulty of exploring transient radio phenomena in general is that the imaging algorithms used for interferometric image reconstruction assume constant source amplitudes so that strong variability of a source in the course of an observation may manifest itself in imaging artifacts unless data from suitably short time ranges are used to produce the images. Bower et al. (2003) presented the first observation of a strong millimeter radio flare of an embedded T Tauri star in Orion, using the VLA. We present a similar radio flare towards a much deeper embedded YSO in Orion in Chapter 6. Massi et al. (2006, see also Chapter 7) present a millimeter flare of the binary T Tauri system V773 Tau, interpreted as synchrotron radiation due to interacting coronae.

1.2.4 Magnetic field structure in the vicinities of YSOs

Powerful X-ray and gyrosynchrotron radio-continuum flares, orders of magnitudes stronger than solar flares, indicate that YSOs exhibit unusually high levels of magnetic activity. In their review “High-energy processes in young stellar objects”, Feigelson & Montmerle (1999) identify four possible magnetic geometries in which X-ray and nonthermal radio emission might arise (see

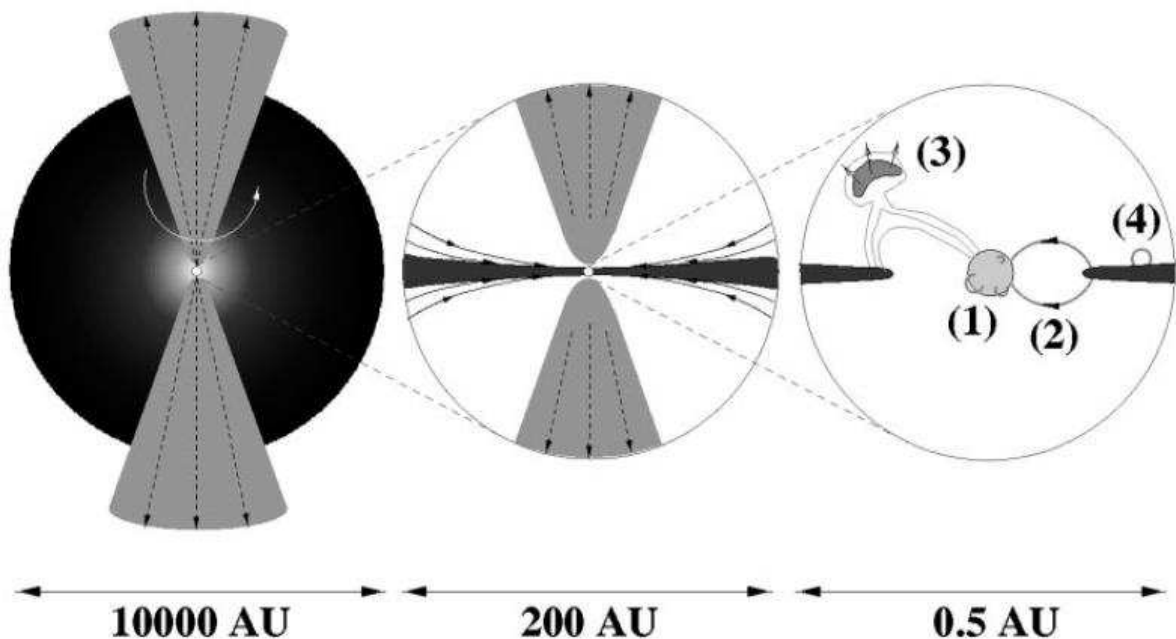


Figure 1.3: Four magnetic-field configurations that may be responsible for the magnetic activity of class I protostars. The X-rays come from the inner region of a complex structure comprising a collapsing extended envelope (left), an inner disk and outflow (center), and a star-disk magnetic-interaction region (right). From Feigelson & Montmerle (1999), see text.

also Fig. 1.3):

- (1) Solar-type multipolar fields with both footpoints rooted in the stellar photosphere.
- (2) Field lines connecting the star to the circumstellar disk at its co-rotation radius⁵.
- (3) Field lines beyond the co-rotation radius. Star–disk differential rotation and ensuing reconnection can cause X-ray emitting plasma to be ejected from the disk.
- (4) Magnetic loops with both footpoints in the disk.

The presence of a disk is fundamental for magnetic energy release in the three last cases, whereas the first case is disk-independent. Observing gyrosynchrotron radio emission with Very-Long-Baseline Interferometry (VLBI) in principle allows to probe the innermost vicinity of a YSO. The magnetic fields which lead to magnetic reconnection and generate flares at small scales ($\lesssim 0.1$ AU) play an important role in driving jets and bipolar outflows; the shock front produced by the collision of the outflows with the interstellar medium ionizes part of the gas and creates H II regions (i.e. regions with ionized hydrogen) appearing elongated at VLA resolutions (e.g. Tsujimoto et al. 2004). Any emission process taking place at smaller scales will suffer from significant free-free absorption and will be difficult to detect (e.g. André 1987). The magnetic field in the innermost regions around YSOs is very important as well for the research on how magnetospheric accretion works. Gregory et al. (2006) present the first model taking into account magnetic fields more complex than dipolar. For a review, see Bouvier et al. (2006).

In order to study the predicted role of the disk as described by Feigelson & Montmerle (1999), it is best to observe objects in an evolutionary stage earlier than class III. The difficulty of this task is that not only there are very few candidates (i.e. ideally class 0/I protostars showing signs

⁵This could be the explanation for the quasi-periodic X-ray flares observed towards the class I protostar YLW 15 (Tsuboi et al. 2000; Montmerle et al. 2000).

of both X-ray and nonthermal radio emission), but mainly that a putative weak radio source is likely embedded in a plasma from jet shocks showing optically thick thermal emission (see Section 1.2.3 above).

1.2.5 Simultaneous multi-wavelength variability

Flaring in YSOs is a ubiquitous phenomenon at diverse wavelengths, however it has not previously been studied simultaneously across the electromagnetic spectrum towards protostars and rarely towards more evolved YSOs, even though multi-wavelength correlations would contain additional information on underlying physics.

One would expect some correlation of thermal hot-plasma X-ray emission and nonthermal centimetric radio emission interpreted as gyrosynchrotron radiation due to magnetic fields because both types of radiation are partially produced in the same regions. For a discussion of radio and X-ray observations of (proto-)stellar coronae, see Güdel (2002b, 2004). Radio and X-ray emission both trace the innermost surroundings of protostars at less than a few stellar radii. A correlation of optical/near-infrared flares interpreted as accretion events and X-ray variability would allow to conclude on the connection of accretion and X-ray emission. Another cause for correlated variability are large cool star spots due to magnetic activity which may directly or indirectly influence X-ray emission. For variability in the near-infrared, processes in the circumstellar medium causing the infrared excess emission (e.g. the circumstellar disk) are more important than variability of the stellar photosphere itself (Eiroa et al. 2002). For the earliest evolutionary stages of stars, a direct comparison of optical and near-infrared variability is not possible since they can only be observed in the near-infrared if at all. Variability at all wavelengths can also be due to pulsation, persistent star spots, or eclipsing multiple systems.

Looking at the sun as the star which is best studied for multi-wavelength variability, we see much uncorrelated variability but also a particular kind of radio–X-ray correlation in the form of the Neupert effect which was observed towards a star other than the sun (the flare star UV Cet) for the first time by Güdel et al. (1996). For a discussion of multi-wavelength aspects of stellar coronae, see Güdel (2002a).

Until now, there have been few simultaneous multi-wavelength observations of YSOs, mainly targeting T Tauri stars and not class 0 or class I protostars: Feigelson et al. (1994) observed a magnetically active T Tauri star (V773 Tau) simultaneously at X-ray, ultraviolet, optical, and radio wavelengths, while Gullbring et al. (1997) and Stelzer et al. (2003) study simultaneous optical and X-ray variability of the classical T Tauri star BP Tau and the weak-line T Tauri star V410 Tau, respectively. Guenther et al. (2000) targeted pre-main sequence stars in the Taurus-Auriga region, specifically V773 Tau, in quasi-simultaneous X-ray, optical, and radio observations. In all cases, no correlated variability was found, based on relatively short observations lasting several hours. Bower et al. (2003) report the serendipitously simultaneous radio and X-ray observation of an enormous radio flare towards a supposed highly obscured weak-line T Tauri star (GMR-A) in Orion. The X-ray flux increased by a factor of 8 two days before the radio flare observation. In observations a few days after this outburst, the source was found to show also millimeter activity for 13 days while the infrared *K*-band magnitude remained unchanged (Furuya et al. 2003). The ρ Oph cloud complex and its pre-main sequence stars were selected for simultaneous radio and X-ray observations by Gagné et al. (2004), covering the largest amount of sources yet. However, none of the class I protostars were detected simultaneously in both wavelength regimes but interestingly, no correlated radio and X-ray variability was found towards several T Tauri stars. Targeting a candidate brown dwarf, Berger et al. (2005) attempted to constrain its magnetic properties by simultaneous radio, X-ray, and H α observations. They directly confirmed the large ratio of radio vs. X-ray luminosity towards this source which remained undetected in X-rays so that still only a lower limit to this ratio could be determined. Most recently, Stassun et al. (2006) presented a comprehensive optical

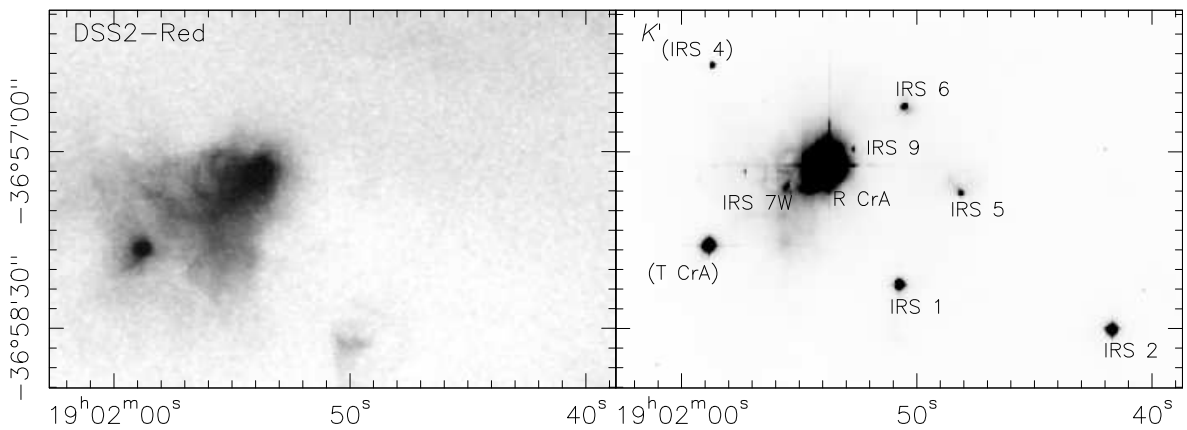


Figure 1.4: Optical (DSS2-Red, left) and near-infrared (K' , right) views of the *Coronet* cluster. T CrA, seen at left, is not covered by the radio data presented here. It is marginally detected in X-rays (Skinner et al. 2004). The K' image is from Hodapp (1994), coordinates are J2000.

variability study of Orion pre-main sequence stars, carried out simultaneously to the Chandra Orion Ultradeep Project. They find indication for time-correlated optical and X-ray variability in only 5% of their sources and conclude that there is little evidence for a causal link between variability at optical and X-ray wavelengths.

1.3 YSOs in the *Coronet* cluster

Given the effort necessary for simultaneous multi-wavelength observations of protostars, an ideal target region should contain several objects of interest within the field of view, which in our case was limited by the primary beam of the VLA, i.e. $5\frac{1}{4}$ full-width half-maximum (FWHM) at $\lambda = 3.5$ cm. The *Coronet* cluster in the Corona Australis (CrA) star-forming region is a unique target in this respect.

The CrA star-forming region is one of the nearest (about 3.5 times closer than the Orion Nebula Cluster) and most active regions of recent and ongoing star formation (e.g. Neuhäuser et al. 2000 or review by Neuhäuser & Forbrich 2007, *subm.*). It contains a loose cluster of a few dozen known YSOs, which cover a wide range of masses (from intermediate-mass Herbig AeBe stars down to very-low-mass brown dwarfs) and evolutionary stages (from pre-stellar cores through class 0 and class I protostars, class II T Tauri stars, to class III objects that have already cleared their dusty environment). This region also contains dozens of HH objects, tracing jets emanating from the YSOs.

The distance to CrA is relatively well known, based on distance determinations of two members. The optically brightest member, the B8e star TY CrA, is a well known eclipsing spectroscopic multiple system. An analysis of photometric eclipse data allowed Casey et al. (1998) to derive precise stellar dimensions of the system and to determine the distance to $D = 129 \pm 11$ pc. The B9e star HD 176386, located only about $1\frac{1}{5}$ to the south-west of TY CrA, forms a common proper motion pair with TY CrA (Teixeira et al. 2000), and shows signs of strong accretion (Grady et al. 1993). These arguments strongly suggest that HD 176386 also is a member of the star-forming region, and its Hipparcos distance of 136_{-19}^{+25} pc is fully consistent with the distance derived for TY CrA. We thus adopt a distance of 130 pc for the CrA star-forming region.

Taylor & Storey (1984) found a compact cluster of infrared sources in the densest part of the cloud complex close to the Herbig Ae star R CrA, calling it the *Coronet* cluster. Fig. 1.4 shows the DSS2-Red and K' -band views of its central region, clearly showing a number of deeply embedded sources. The *Coronet* cluster is the densest clustering of YSOs in CrA. Its

core contains at least six deeply embedded protostars (Wilking et al. 1986, 1992, 1997), mostly identified at radio as well as X-ray wavelengths. As already pointed out, this is the principal advantage of this region for observations of simultaneous multi-wavelength variability: It does not only contain a number of protostars detected over a broad wavelength range, these sources are additionally located in a sufficiently compact group to warrant simultaneous observability.

Koyama et al. (1996) reported the detection of hard X-ray emission towards five protostars in this region with ASCA, the first signs ever of class I protostars detected in X-rays. Three of these sources could be verified at higher angular resolution by ROSAT (Neuhäuser & Preibisch 1997), more ROSAT-detected YSOs were reported by Neuhäuser et al. (2000). First results from *Chandra*-ACIS observations of this region were presented by Garmire & Garmire (2003) who detected more than 70 sources in a 20 ksec exposure. An observation with XMM-Newton was presented by Hamaguchi et al. (2005a), including the discovery of strong X-ray emission towards a candidate class 0 source. Earlier observations were carried out with EINSTEIN (Damiani et al. 1994; Walter et al. 1997). All these observations, however, were several times less sensitive than the combined dataset analyzed in this work (see Chapter 4).

The *Coronet* cluster has been analyzed at radio wavelengths already several times. Brown (1987) carried out VLA observations at $\lambda = 6$ cm in 1985, identifying five sources associated with YSOs. Suters et al. (1996) analyze the radio variability of pre-main-sequence stars using archival VLA (1985-1987) and Australia Telescope (1992) data, while Feigelson et al. (1998) report on VLA observations at 3.5 cm, taken in 1997. They detect circular polarization toward the class I protostar IRS 5.

Studying dust emission from the region at $\lambda = 1.2$ mm, Chini et al. (2003) report several peaks, with the brightest one (called MMS 13 and already detected by Henning et al. 1994) in the vicinity of IRS 7 in the *Coronet* cluster. The dust mass of the entire cloud core around R CrA and the *Coronet* is reported as $\sim 200 M_{\odot}$ within a region with a projected typical diameter of $\lesssim 0.5$ pc. Millimeter emission is associated with IRS 1, 2 and 5 as well. The authors conclude that the MMS 13 peak is a deeply embedded source not related to any of the sources observed at other wavelengths. Based on millimeter continuum and molecular line data, Groppi et al. (2004) reach a similar conclusion. Nutter et al. (2005) present higher-resolution submillimeter continuum data resolving MMS 13 into two protostellar and one prestellar sources for which gravitational collapse has not yet started. This prestellar source is at the position of the class 0 source surmised earlier and is estimated to have a mass of 3.5 to 6.4 M_{\odot} (scaled to $d = 130$ pc), while the envelopes of the other protostars in this region all have dust masses of less than a solar mass. The two protostellar sources are associated with unresolved radio and X-ray sources (IRS 7E and IRS 7W).

Using near-infrared spectroscopy, Nisini et al. (2005) constrain the accretion rates and evolutionary stages of some *Coronet* protostars. They conclude that IRS 1 and IRS 2 appear to be mostly accretion-powered (accounting for 80% and 65% of the bolometric luminosity, L_{bol} , respectively), while IRS 5 – a binary source – appears to be a deeply embedded, more evolved object with accretion accounting for only 20% of the bolometric luminosity of one of the components, IRS 5a. IRS 3 and IRS 6a show no signs of accretion. Comparing their derived stellar luminosities and effective temperatures to different models of pre-main sequence evolution, IRS 1 emerges as the youngest object in this sample with an age of about 10^5 years, while IRS 2, 5a and 6a apparently have about the same age, closer to 10^6 years in spite of their different accretion properties.

1.4 Observatories

In the course of this work, data was collected from a number of observatories operating at very different wavelengths, with a variety of instruments. In the following, the most important of

them are briefly introduced:

Chandra and XMM-Newton These two X-ray satellites are the best currently available X-ray observatories for studies of stellar X-ray emission. Both satellites rely on Wolter-type grazing-incidence X-ray imaging telescopes, and both offer CCD imaging detectors that can be used for imaging spectroscopy since for every count the energy is recorded. Also high-resolution spectroscopy is possible. Principal differences between these two satellites concern the collecting area which is bigger for XMM-Newton and the angular resolution which is better for Chandra. XMM-Newton is described by Jansen et al. (2001) while information on Chandra can be found in Weisskopf et al. (2002).

The Very Large Array (VLA) The Very Large Array (VLA), situated near Socorro in New Mexico (USA), consists of 27 radio telescopes, each 25 m in diameter. These are combined into a connected-element interferometer with variable baselines. The antennas stand on three tracks arranged in a Y-shape and are regularly reconfigured in different configurations. The most extended configuration with baselines of up to 36 km is the so-called ‘A’ configuration, while the smallest is called ‘D’. The antennas are equipped with receivers for wavelengths between 7 mm and 4 m.

The Very Long Baseline Array (VLBA) The Very Long Baseline Array (VLBA) is a dedicated network for Very Long Baseline Interferometry (VLBI). It consists of ten radio telescopes, each 25 m in diameter, located across North America. For instance, the easternmost antenna is located on one of the Virgin Islands while the westernmost antenna stands close to the summit of Mauna Kea, Hawaii.

The High Sensitivity Array (HSA) The sensitivity of the VLBA can be improved by typically an order of magnitude by adding the VLA (phased into the sensitivity equivalent of a 130 m antenna) as well as the three biggest single-dish radio telescopes in the world, namely the Arecibo 305 m antenna on Puerto Rico, the 101 m Green Bank Telescope (GBT) in Virginia as well as the Effelsberg 100 m telescope in Germany.

The IRAM 30m telescope and the PdB interferometer The IRAM 30 m radio telescope belongs to the prime millimeter radio antennas in the world. Located at an altitude of 2920 m close to the summit of Pico Veleta in the Spanish Sierra Nevada, the observing conditions are excellent for observations at wavelengths between 1 mm and 3 mm.

The IRAM Plateau de Bure Interferometer (PdBI) The IRAM PdBI is located close to Grenoble (France) in the Alps. It consists of six connected radio telescopes, each having a diameter of 15 m, which are operating at wavelengths between 1 mm and 3 mm. It is the millimeter array with the largest collecting area.

Optical and infrared telescopes The optical and infrared telescopes used in this work are located in Chile and in South Africa. The 3.5 m New Technology Telescope (NTT) of the European Southern Observatory (ESO) is located on Cerro La Silla in Chile. The 0.9 m telescope of the Cerro Tololo Inter-American Observatory (CTIO) is located on Cerro Tololo, also in Chile. The Japanese Infrared Survey Facility (IRSF), a 1.4 m telescope whose specialty is the Simultaneous Infrared Imager for Unbiased Survey (SIRIUS) is located in South Africa.

1.5 Objectives of this work

Within the scope of this work, the role of magnetic fields and associated high-energy processes in star formation was studied using several different observational techniques. Chapters 2 and 3 deal particularly with radio and X-ray variability of YSOs, the latter chapter focusing on *simultaneous* X-ray, radio, infrared, and optical variability. Chapter 4 deals with X-ray emission of YSOs in more detail, based on one of the deepest X-ray observations yet of a star-forming region. In Chapter 5, high-resolution VLBI radio observations of protostars with unprecedented sensitivity are presented. In Chapters 6 and 7, two spectacular examples of radio variability of YSOs are shown and discussed. Finally, in Chapter 8, an attempt to detect weak linear polarization due to the Goldreich-Kylafis effect with new instrumentation at the IRAM 30 m telescope is presented and analyzed.

Chapter 2 – Radio and X-ray variability of Young Stellar Objects in the Coronet cluster In a preparatory study to subsequent simultaneous multi-wavelength observations of YSOs, multi-epoch VLA radio data as well as multi-epoch archival XMM-*Newton* and *Chandra* archival data are studied for an assessment of the variability of YSOs in the *Coronet* cluster.

Chapter 3 – Simultaneous X-ray, radio, near-infrared, and optical monitoring of Young Stellar Objects in the Coronet cluster The first simultaneous X-ray, radio, near-infrared, and optical monitoring of YSOs is presented, targeting the *Coronet* cluster in the Corona Australis star-forming region, which harbors at least one class 0 protostar, several class I objects, numerous T Tauri stars, and a few Herbig AeBe stars. Multi-wavelength (X-ray to radio) monitoring of YSOs can provide important information about physical processes at the stellar surface, in the stellar corona, and/or in the inner circumstellar disk regions.

Chapter 4 – Coronae in the Coronet: A very deep X-ray look into a stellar nursery To study the X-ray properties of YSOs, we analyze an exceptionally sensitive *Chandra* dataset of the *Coronet* cluster in the CrA star-forming region, consisting of the observations obtained during the simultaneous multi-wavelength campaign plus archival data. This dataset represents one of the most sensitive X-ray observations ever obtained of a star-forming region. The above-mentioned questions concerning protostellar X-ray emission are addressed.

Chapter 5 – Searching for small-scale nonthermal radio emission from protostars by VLBI In order to study the role of magnetic fields in the immediate vicinity of protostars, Very Long Baseline Interferometry of nonthermal centimetric radio emission is the method of choice since it is technically the only possibility to study magnetospheric emission at sub-AU resolution. VLBI observations of four nearby protostars were obtained in order to look for compact nonthermal centimetric radio emission. For maximum sensitivity, the High Sensitivity Array (HSA) was used where possible.

Chapter 6 – A 1.3 cm radio flare from a deeply embedded source in the Orion Nebula A spectacular radio outburst of a deeply embedded YSO in the Orion Nebula is presented. Within hours, it became the brightest source in the area with a peak flux density of nearly 50 mJy (at a wavelength of 1.3 cm), then starting to dim before the observation ended. This source does not have any infrared counterpart in images taken with the Hubble Space Telescope (HST) and the Very Large Telescope (VLT). Curiously, a *double* centimetric radio source was found at the position of the flare source. An X-ray counterpart was analyzed in the course of the *Chandra* Orion Ultradeep Project (COUP), leading to an assessment of the extinction towards the source as well as to the discovery of fluorescent iron line emission, probably from a circumstellar disk.

Chapter 7 – Synchrotron radio emission from the T Tauri binary system V773 Tau A The pre-main sequence binary system V773 Tau A shows remarkable flaring activity around periastron passage. The observation of such a flare at a wavelength of 3 mm (90 GHz) performed with the Plateau de Bure Interferometer is presented. Different possible causes for the energy losses are examined.

Chapter 8 – Searching for linearly polarized molecular line emission towards protostars The Goldreich-Kylafis (GK) effect causes molecular line emission to be weakly linearly polarized. The effect is explained using magnetic fields, and under certain circumstances the magnetic field structure of star-forming cores can be studied. Compared to polarized dust emission, the GK effect yields additional information along the line of sight by its dependence on velocity in the line. The XPOL correlation polarimeter at the IRAM 30m telescope was used in a search for polarized linear polarization in several bright molecular transition lines towards prominent star-forming regions. Additionally, the instrument response is modeled in order to quantitatively estimate the influence of instrumental vs. astronomical effects.

Chapter 2

Radio and X-ray variability of Young Stellar Objects in the Coronet cluster

(based on Forbrich, Preibisch, & Menten, *A&A* 2006, 446, 155)

2.1 Introduction

In this preparatory study for subsequent simultaneous multi-wavelength observations, a multi-epoch VLA dataset was analyzed together with multi-epoch archival X-ray data from the *Chandra* and *XMM-Newton* observatories. After the description of the observations in Section 2.2, the results are discussed in Section 2.3, including remarks on particular sources. Conclusions are given in Section 2.4.

2.2 Observations and data analysis

2.2.1 Radio observations

Here we present the results of a radio monitoring campaign at $\nu = 8.44$ GHz of the *Coronet* cluster, carried out with the NRAO Very Large Array (VLA) between 1998 September 19 and October 13. The sources, which are all within the 5.4 FWHM primary beam, were observed five times, separated by a few days each. Originally, these observations were scheduled to be simultaneous with X-ray monitoring, but ROSAT unexpectedly went out of operation before the campaign was to begin. The VLA was observing in the B configuration (program ID AM596) at $\nu = 8.44$ GHz with two intermediate frequency (IF) pairs, offset by each IF band's width, 50 MHz. One IF of each pair detected right circular polarization (RCP), the other one left circular polarization (LCP). The phase center was $(\alpha, \delta)_{J2000} = 19^{\text{h}}01^{\text{m}}48^{\text{s}}, -36^{\circ}57'59''$. These data are complemented by four additional epochs in 1998, also taken with the VLA in B/BnA configuration (program ID AK469) at $\nu = 8.44$ GHz, increasing the total to nine epochs, now starting on June 27, 1998. The source coverage is slightly different due to a different phase center, $(\alpha, \delta)_{J2000} = 19^{\text{h}}01^{\text{m}}55.6^{\text{s}}, -36^{\circ}57'09''.6$. Details on the dates and durations of the different observation epochs are given in Table 2.1. These data can be compared with measurements taken by Feigelson et al. (1998) on 1997 January 19 and 20 (see Table 2.4).

The VLA data were analyzed using NRAO's Astronomical Image Processing System (AIPS). An absolute flux density scale was established by observations of 3C286, the nearby phase calibrator 1924–292 was observed every ten minutes. At a declination of nearly -37° , the *Coronet* cluster is observable with the VLA only at very low elevations ($< 18^{\circ}$), increasing problems with phase instabilities caused by the atmosphere. Here, however, by using self-calibration, these effects could be minimized. All observation epochs were phase-only self-calibrated, as the low

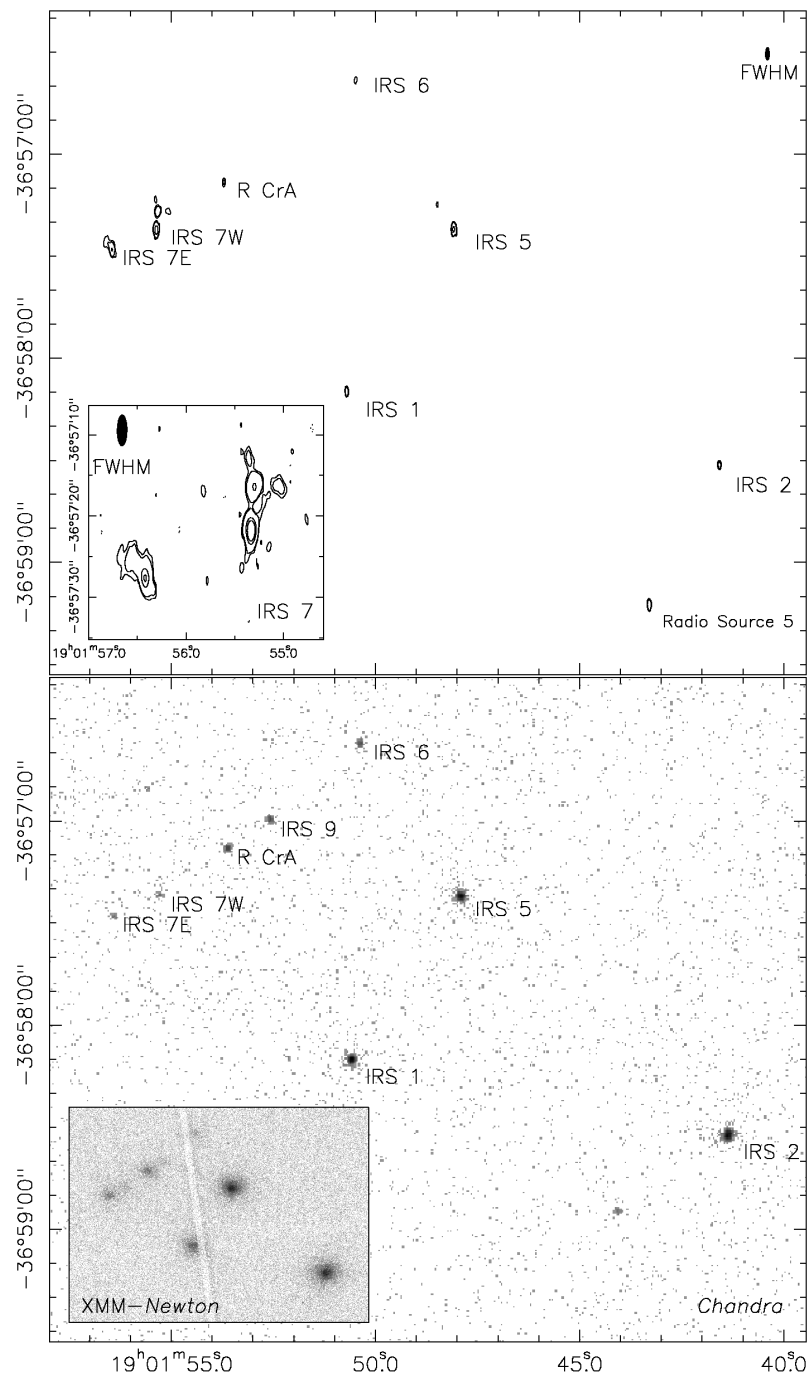


Figure 2.1: Upper panel: Image made from the combined uv data of all five VLA observation epochs. Contours shown are 5, 10 and 100 σ in the main plot and -3 (dashed), 3, 5, 50 and 100 σ in the inset showing IRS 7. Coordinates are J2000.0. Lower panel: The same view, showing the merged *Chandra* ACIS-I data. The inset shows approximately the same view in the merged XMM-*Newton* data (MOS+EPN, X1-X3).

flux densities did not warrant self calibration of, both, phases plus amplitudes. Following this, Stokes- I and Stokes- V were imaged separately, with the input uv -data split into different time intervals. The polarization of the secondary calibrator 1924–292 is $\lesssim 1\%$. Source positions and flux densities were determined, using the AIPS task SAD, by fitting Gaussians to each detection. The light curves thus derived are shown in Fig. 2.2. The root mean square (rms) noise level in the Stokes I and V maps for the different epochs is shown in Table 2.1. For the detection

Table 2.1: VLA *Coronet* observation dates

Epoch	Day	Date	IAT Interval	Duration	rms (μ Jy)
R1	1	1998 Jun 27	07:21:30 – 08:50:20	01:28:50	30
R2	23	1998 Jul 19	05:27:10 – 06:54:00	01:26:50	33
R3	73	1998 Sep 07	03:08:30 – 04:07:21	00:58:51	36
R4	85	1998 Sep 19	01:23:00 – 03:17:40	01:54:40	24
R5	93	1998 Sep 27	01:51:40 – 03:46:10	01:54:30	25
R6	98	1998 Oct 02	00:03:00 – 01:56:40	01:53:40	27
R7	102	1998 Oct 06	00:15:11 – 01:13:10	00:57:59	36
R8	106	1998 Oct 10	23:52:50 – 01:51:10(+1)	01:58:20	23
R9	109	1998 Oct 13	23:14:40 – 01:09:30(+1)	01:54:50	25

All epochs except for R1 (BnA) were observed with the B array.

Datasets R4-R6 and R8-R9 are from project AM596.

Datasets R1-R3 and R7 are from project AK469.

Table 2.2: Archival X-ray data used in this study

Satellite	Obs.	ID	Date	Time (UT)	Dur. (sec)	Pointing Center R.A./Dec. (J2000)
<i>Chandra</i>	19	C1	2000 Oct 07	17:01:59 – 23:11:01	19958	19 01 50.6 -36 57 30.0
<i>XMM-Newton</i>	0111120101	X1	2001 Apr 09	09:32:16 – 15:56:46	26445	19 01 49.4 -36 55 41.4
<i>XMM-Newton</i>	0146390101	X2	2003 Mar 28	08:50:45 – 18:32:49	36715	19 01 37.2 -36 51 02.3
<i>XMM-Newton</i>	0146390201	X3	2003 Mar 29	19:35:00 – 04:00:38(+1)	32211	19 01 37.2 -36 51 02.5
<i>Chandra</i>	3499	C2	2003 Jun 26	12:58:10 – 00:16:08(+1)	38126	19 01 50.6 -36 57 30.0

of weak sources, the five AM596 observations were combined, yielding a map with an rms of $< 12\mu$ Jy. The synthesized beam size for this combined data is $1''.93 \times 0''.63$ at position angle -0.51° .

2.2.2 Archival X-ray data

In addition to the radio data, we studied archival X-ray data of the *Coronet* sources. On 2000 October 7, this region was observed with *Chandra*, using the Advanced CCD Imaging Spectrometer in its imaging mode ACIS-I in order to search for X-rays from young stars in a 20 ksec exposure (Garmire & Garmire 2003). A second ACIS-I observation of this region, with a 38 ksec exposure, was carried out on 2003 June 26. Additionally, there have been three *XMM-Newton* observations of the *Coronet* region: On 2001 April 9 there was a 26 ksec exposure and on 2003 March 28/29 two consecutive observations of 36 ksec and 32 ksec were carried out. While the first *XMM-Newton* observation was taken through the “thin” filter, the “medium” filter was used for the latter two observations. Details on the X-ray data analyzed here are listed in Table 2.2. Our analysis of the archival X-ray data focuses on the three X-ray brightest sources among the sample discussed here, IRS 2, 5, and 1 because they are bright enough for a spectral analysis. These three sources are class I protostars.

Chandra X-ray data were analyzed using the Chandra Interactive Analysis of Observations (CIAO) 3.1 software package together with CALDB 2.28. Apertures used were three or five (IRS 2, 5, and 1) arcseconds in diameter. Spectra were prepared with the task *psextract*, including the creation of response matrices and ancillary response files. Finally, spectra bin sizes were determined by a minimum event number per bin of fifteen.

XMM-Newton data were analyzed using the Science Analysis System (SAS) 6.0.0. Due to the superior signal-to-noise ratio among XMM imaging instruments, we only make use of the EPIC-PN data here. We generally used apertures with a diameter of $32''$, but in cases of close neighbouring sources, we defined smaller ($14''$ diameter) non-overlapping extraction

Table 2.3: Positions and identification of *Coronet* radio and X-ray sources

No.	Position (J2000.0)	Source ID ^a
1	19 01 41.6 -36 58 31	IRS 2 (I)
2	19 01 43.3 -36 59 12	Source 5 ^b
3	19 01 44.2 -36 58 54	
4	19 01 48.1 -36 57 22	IRS 5 (I)
5	19 01 48.5 -36 57 15	
6	19 01 50.5 -36 56 38	IRS 6 (T)
7	19 01 50.7 -36 58 09	IRS 1 (I)
8	19 01 52.6 -36 57 01	IRS 9 (I)
9	19 01 53.7 -36 57 08	R CrA (H)
10	19 01 55.0 -36 57 16	
11	19 01 55.3 -36 57 16	Source 9 ^b
12	19 01 55.3 -36 57 22	IRS 7W (I)
13	19 01 55.4 -36 57 13	
14	19 01 56.4 -36 57 28	IRS 7E (0?)
15	19 01 56.5 -36 57 26	

Remarks:

^a YSO types:

(0)=class 0, (I)=class I, (T)=T Tau,

(H)=Herbig Ae,

^b as defined by Brown (1987)

regions. These apertures encircle approximately 66% and 40% of the point source flux¹, so that corresponding correction factors had to be taken into account in the luminosity determination. Spectroscopy involved the creation of response matrices and ancillary response files using the tasks *rmfgen* and *arfgen*, respectively. Finally, the spectra were binned with the same minimum event number criterion as was used for the *Chandra* data.

Models were fitted to all background-subtracted spectra with *Sherpa* from the CIAO 3.1 software package, using Monte Carlo multi-parameter fits. The spectral model consists of the Astrophysical Plasma Emission Code (APEC) with an absorption factor. This code calculates the emission spectrum from collisionally ionized diffuse gas. The main fit parameters are the plasma temperature, the absorbing hydrogen column density and the element abundances compared to solar values.

After a determination of elemental abundances from the Fe K line at 6.7 keV from one spectrum per source, an absorbed APEC emission model was fitted to the spectra. It turned out that the spectra can be well described with a single-temperature model; there was no need to assume two temperature components. However, due to the high absorbing column densities toward the sources, softer emission components might easily be extinguished. The uncertainties of the best-fit parameter values were estimated with the *Sherpa* task *uncertainty*. Based on these fits, the count rates in the light curves were converted into unabsorbed flux using the PIMMS software (Mukai 1993) and finally, into luminosity units (energy range 0.5 – 10 keV), assuming a distance² of $d = 130$ pc.

2.3 Results

After a general discussion of the 1998 VLA monitoring and the analysis of archival X-ray data, individual source properties will be summarized.

2.3.1 Radio monitoring

In Stokes-*I*, eight sources can be detected throughout all five AM596 observation epochs, taking a 5σ detection limit as the criterion for source existence. These sources are also detected throughout the AK469 data with the exception of IRS 2, not detected due to primary beam attenuation far from the observation's phase center. An image created from the combined AM596

¹as given in the XMM-Newton User's Handbook V2.2

²In the published version of this paper (Forbrich et al. 2006), $d = 150$ pc is assumed, based on a different evaluation of the literature. In order to ensure a uniform treatment in this work, $d = 130$ pc is used as the distance to the *Coronet* cluster throughout (see Introduction). This change does not affect any of the conclusions.

Table 2.4: *Coronet* sources, radio data

No.	R1 (mJy)	R2 (mJy)	R3 (mJy)	R4 (mJy)	R5 (mJy)	R6 (mJy)	R7 (mJy)	R8 (mJy)	R9 (mJy)	comb. ^a (mJy)	1997 ^b (mJy)
1	0.30	< 0.27 ^c	< 0.30 ^c	0.29	0.35	0.32	< 0.30 ^c	0.36	0.30	–	0.67
2	0.40	0.68	1.15	1.04	0.76	0.93	0.52	1.21	0.58	–	1.08
3	n.d.	n.d.	n.d.	n.d.	n.d.	n.d.	n.d.	n.d.	n.d.	–	n.d.
4	1.96	1.10	0.75	1.32	1.11	2.97	2.31	3.28	1.67	–	1.36
4V	< 0.09 ^c	0.22	0.15	0.25	0.26	0.29	0.34	0.65	0.36	–	0.23
5	n.d.	n.d.	n.d.	n.d.	n.d.	n.d.	n.d.	n.d.	n.d.	0.10	n.d.
6	n.d.	n.d.	n.d.	n.d.	n.d.	n.d.	n.d.	n.d.	n.d.	0.15	n.d.
7	0.42	0.36	0.59	0.44	0.47	0.45	0.55	0.49	0.46	–	0.45
8	n.d.	n.d.	n.d.	n.d.	n.d.	n.d.	n.d.	n.d.	n.d.	< 0.035 ^c	n.d.
9	0.16	0.21	0.17	0.22	0.17	0.23	0.24	0.20	0.26	–	0.23
10	n.d.	n.d.	n.d.	n.d.	n.d.	n.d.	n.d.	n.d.	n.d.	0.12	n.d.
11	0.93	0.78	0.89	0.85	0.78	0.72	1.04	0.94	0.84	–	1.58
12	4.26	4.15	5.01	4.27	4.31	4.11	5.29	4.52	4.31	–	3.74
13	n.d.	n.d.	n.d.	n.d.	n.d.	n.d.	n.d.	n.d.	n.d.	0.11	n.d.
14	1.38	1.53	2.10	1.66	1.83	1.54	2.04	1.75	1.62	–	2.03
15	n.d.	n.d.	n.d.	n.d.	n.d.	n.d.	n.d.	n.d.	n.d.	0.13	n.d.

^a sources detected in combined AM596 data (10h)

^b 3.5 cm flux density on 19/20 Jan 1997, as published by Feigelson et al. (1998)

^c local 3σ limit, in the case of IRS 2: accounting for primary beam attenuation

Table 2.5: *Coronet* sources, X-ray data

No.	Source ID	C1 ^a (cnts/ksec)	C2 ^a (cnts/ksec)	X1 ^a (cnts/ksec)	X2 ^a (cnts/ksec)	X3 ^a (cnts/ksec)
1	IRS 2	48.7 ± 1.6	26.6 ± 0.9	42.1 ± 1.5	49.4 ± 1.4	54.4 ± 1.5
2	Source 5	n.d.	n.d.	n.d.	n.d.	n.d.
3		0.5 ± 0.2	0.8 ± 0.2	n.d.	n.d.	n.d.
4	IRS 5	13.2 ± 0.9	31.0 ± 0.9	46.5 ± 1.6	40.3 ± 1.3	75.6 ± 1.7
5		n.d.	n.d.	n.d.	n.d.	n.d.
6	IRS 6	2.4 ± 0.4	1.5 ± 0.2	3.4 ± 0.8	0.9 ^c ± 0.5	0.5 ^c ± 0.5
7	IRS 1	22.9 ± 1.1	30.9 ± 0.9	31.7 ± 1.4	10.9 ^c ± 0.7	18.3 ^c ± 0.9
8	IRS 9	2.9 ^b ± 0.4	2.1 ± 0.3	1.3 ^d ± 0.4	2.8 ^d ± 0.4	1.2 ^d ± 0.4
9	R CrA	3.2 ± 0.5	3.1 ± 0.3	5.2 ^d ± 0.6	9.3 ^d ± 0.6	6.8 ^d ± 0.6
10		n.d.	n.d.	n.d.	n.d.	n.d.
11	Source 9	n.d.	n.d.	n.d.	n.d.	n.d.
12	IRS 7W	0.6 ± 0.2	0.6 ± 0.2	2.1 ^d ± 0.4	2.6 ^d ± 0.4	4.7 ^d ± 0.5
13		n.d.	n.d.	n.d.	n.d.	n.d.
14	IRS 7E	1.0 ± 0.3	0.3 ± 0.1	1.6 ^d ± 0.4	3.7 ^d ± 0.4	14.7 ^d ± 0.8
15		n.d.	n.d.	n.d.	n.d.	n.d.

^a background-subtracted count rates (0.5 – 10 keV) from X-ray datasets as listed in Table 2.2, *Chandra* and *XMM-Newton* count rates are not directly comparable. Additionally, different filters were used in the *XMM-Newton* observations: ‘thin’ for X1 and ‘medium’ for X2/X3.

^b flare

^c source partly covered by chip gap, loss estimated to be $\approx 20\%$

^d contamination from neighbouring source

uv data is shown in Fig. 2.1. Five weak additional sources only emerge from this integration of the five AM596 observation epochs, including the T Tauri star IRS 6. In Stokes-*V* only IRS 5 was detected, showing epoch-averaged circular polarization degrees between 0% and 23%. IRS 5 at the same time is the most spectacularly variable source in this dataset: Starting at a relatively high emission level, but interestingly without circular polarization, the source dims, then rises sharply towards two peaks at the end of the period covered, accompanied by changes in its polarization. Analyzing the data in shorter intervals, the Stokes-*V* emission of IRS 5 re-

Table 2.6: X-ray spectral fitting results for IRS 2, 1, 5, and R CrA: Absorbing column density and plasma temperature, with 1σ error margins

	IRS 2		IRS 5		IRS 1		R CrA	
	N_H	T	N_H	T	N_H	T	N_H	T
	[10^{22} cm $^{-2}$]	[MK]	[10^{22} cm $^{-2}$]	[MK]	[10^{22} cm $^{-2}$]	[MK]	[10^{22} cm $^{-2}$]	[MK]
C1	$2.43^{+0.11}_{-0.10}$	$45.9^{+3.3}_{-3.3}$	$3.02^{+0.25}_{-0.22}$	$26.7^{+2.5}_{-2.3}$	$3.75^{+0.31}_{-0.27}$	$63.1^{+9.2}_{-6.6}$	–	–
X1	$1.99^{+0.09}_{-0.08}$	$27.6^{+1.7}_{-1.7}$	$3.50^{+0.15}_{-0.13}$	$30.2^{+1.2}_{-1.2}$	$4.60^{+0.23}_{-0.21}$	$28.7^{+1.4}_{-1.4}$	$1.2^{+0.4}_{-0.3}$	106^{+209}_{-43}
X2	$1.76^{+0.06}_{-0.06}$	$28.8^{+1.4}_{-1.4}$	$4.80^{+0.17}_{-0.15}$	$26.1^{+0.9}_{-0.9}$	$3.21^{+0.31}_{-0.26}$	$48.9^{+7.7}_{-6.0}$	$1.4^{+0.2}_{-0.2}$	100^{+57}_{-26}
X3	$1.60^{+0.15}_{-0.16}$	$36.5^{+5.7}_{-4.2}$	$4.23^{+0.13}_{-0.12}$	$36.8^{+1.1}_{-1.1}$	$2.75^{+0.21}_{-0.18}$	$44.6^{+4.4}_{-4.3}$	1.3^a	110^{+145}_{-45}
C2	$1.53^{+0.07}_{-0.07}$	$37.5^{+2.7}_{-2.6}$	$4.07^{+0.16}_{-0.14}$	$33.3^{+1.4}_{-1.4}$	$2.36^{+0.09}_{-0.09}$	$32.6^{+1.7}_{-1.6}$	–	–

^a frozen parameter, otherwise $N_H = 2.6^{+0.5}_{-0.4} \times 10^{22}$ cm $^{-2}$, $T = 50^{+14}_{-9}$ MK; however this change appears unlikely since X3 is immediately following X2

mains variable at timescales of 0.5 h while this is not the case for any of the sources in Stokes-*I*. The remaining sources show diverse degrees of variability, but to a lesser extent (Fig. 2.2). All sources detected in single epochs have been detected at radio wavelengths before. The source flux densities derived from the VLA observations are summarized in Table 2.4, together with the 3.5 cm flux densities from Feigelson et al. (1998) for comparison.

2.3.2 Archival X-ray data

At X-ray wavelengths, nine sources are clearly detected, including an unidentified weak source (no. 3) only detected by *Chandra* (see Tables 2.3 and 2.5). Fig. 2.1 shows the combined *Chandra* data, with the combined XMM-*Newton* data shown as an inset. It is interesting to compare this X-ray view with the radio view in Fig. 2.1. The five weak radio sources only emerging in the complete VLA data all remain undetected in X-rays together with the Radio Sources 5 and 9 (Brown 1987). However, the class I protostar IRS 9 – clearly detected in X-rays, even with a flare in the C1 observation – remains undetected at radio wavelengths, together with the weak X-ray source no.3 not showing any counterpart at other wavelengths. Comparing the count rates for these sources derived from the five X-ray datasets shows that there is considerable variability in many cases (Table 2.5). For the three class I protostars IRS 2, 5 and 1, this is corroborated by the luminosity curves (Fig. 2.6) and the corresponding spectra (Fig. 2.4). All three sources have X-ray luminosities on the order of several 10^{30} erg/s. IRS 5 emerges again as the most variable source.

The elemental abundances for the three sources, as derived from the 6.7 keV Fe K line emission, are 0.5 ± 0.2 (IRS1,X1), 0.7 ± 0.1 (IRS2,X3) and 0.26 ± 0.05 (IRS5,X3) relative to solar abundances. There is no evidence for fluorescent emission of weakly ionized or neutral iron at energies below 6.7 keV. Fitting absorbed APEC emission models to the spectra leads to the results depicted in Fig. 2.5 and listed in Table 2.6. All three sources show high absorbing column densities (several 10^{22} cm $^{-2}$) and hot plasma emission (several 10^7 K). There are signs of long-term variability in the absorbing column densities, especially towards IRS 2 and IRS 1. Note that the X2 and X3 observations are consecutive while a total range of about 2.5 years is covered. Tentatively, there is a trend for the emission being harder when the sources are brighter, although the situation is inconclusive.

Interestingly, though, the hydrogen column densities as derived from the X-ray spectra for IRS 2, 5, and 1 are at around half the values derived by Nisini et al. (2005) from near-infrared colours³ (see Table 2.7). In order to check the significance of this discrepancy, we tried to fit the spectra while freezing the absorbing column density N_H to the value derived from NIR colours. This led to very poor fits (large χ^2) in all cases, demonstrating that the large N_H values are inconsistent with the X-ray spectra. Additionally, by using a Monte Carlo fitting

³adopting $A_V = 15.9 \cdot E(H - K)$ (Rieke & Lebofsky 1985)

Table 2.7: Comparison of column densities towards IRS 2, 5, and 1 derived from NIR and X-ray emission

Source	$N_H(\text{NIR})^a$ [10^{22} cm^{-2}]	$N_H(\text{X-ray})$ [10^{22} cm^{-2}]
IRS 2	4.0 ± 0.6	1.9 ± 0.4
IRS 5	9.0 ± 0.6	3.9 ± 0.7
IRS 1	6.0 ± 0.6	3.3 ± 0.9

^a A_V (from Nisini et al. 2005) converted into N_H using $N_H[\text{cm}^{-2}] \approx 2 \times 10^{21} \times A_V[\text{mag}]$, see text

Table 2.8: Bolometric and X-ray luminosities (derived from X-ray spectra)

Source	L_{bol}^a L_{\odot}	L_X $10^{-3} L_{\odot}$	$\log(L_X/L_{\text{bol}})$
IRS 2	12	0.70	-4.2
IRS 5	3	1.27	-3.4
IRS 1	14	0.56	-4.4
R CrA	99	0.13	-5.9

^a from Wilking et al. (1992) and Lorenzetti et al. (1999, R CrA; scaled to $d = 130 \text{ pc}$)

scheme, the parameter space was checked for multiple minima, but again no acceptable model was found for large N_H values. The empirical relation is $N_H[\text{cm}^{-2}] \approx 2 \times 10^{21} \times A_V[\text{mag}]$ (Ryter 1996; Vuong et al. 2003). A similar discrepancy has been observed previously towards the YSOs L1551 IRS 5 (Bally et al. 2003), EC 95 (Preibisch 2003a), and towards SVS 16 (Preibisch 2003b). Possible solutions to this ‘extinction problem’ are configurations in which the protostar and its X-ray emission become detached, so that the absorbing column densities for the infrared and X-ray emission become different. Scenarios include X-ray emission from jet shocks close to the protostar, X-rays scattered towards the observer by circumstellar material, and huge coronal structures.

For six of the YSOs studied here, it is possible to reliably determine X-ray luminosities based on their spectra. The radio and X-ray luminosities of these sources have been plotted into Fig. 2.7 together with an empirical relationship for active late-type stars from Guedel & Benz (1993, see also Benz & Güdel 1994). The underlying physics of this relation is that the acceleration of synchrotron-emitting electrons and the heating of the coronal plasma leading to X-ray emission are accomplished by the same mechanisms. The *Coronet* YSOs appear to be compatible with this relationship.

Comparing the X-ray luminosities to the bolometric luminosities (see Table 2.8), it turns out that IRS 2, 5, 1, and R CrA are all in the unsaturated regime $L_X/L_{\text{bol}} < 10^{-3}$ (Fleming et al. 1995), but a lot more active than the sun ($(L_X/L_{\text{bol}})_{\odot} \approx 10^{-6}$), IRS 5 being the most active source with a ratio of $\log(L_X/L_{\text{bol}}) = -3.4$.

2.3.3 Synthesis

2.3.3.1 The class I protostars IRS 2, IRS 5, IRS 1, and IRS 9

IRS 2 does not show significant radio variability in any time interval covered by our observations (Fig. 2.2 and Table 2.4). The flux density is, however, at about half the value determined by Feigelson et al. (1998). IRS 2 is one of the strongest X-ray sources among the objects studied here. The overall count rate in the C1 *Chandra* observation is twice as high as during the C2 observation which is clearly visible in the luminosity curves (Fig. 2.6). The XMM-Newton count rates are less diverse. Variability is seen also within observations, especially X1, showing a continuous increase, and X3, showing a sudden increase in the second half of the observation. Already the ROSAT data presented by Neuhäuser & Preibisch (1997) show variability on timescales of months. The X-ray spectra (Fig. 2.4), can be explained as the emission of hot plasma ($T \approx 4 \times 10^7 \text{ K}$), absorbed by a column density of $N_H \approx 2 \times 10^{22} \text{ cm}^{-2}$. Apparently, the absorbing column density towards IRS 2 has continuously diminished over two and a half years, the 3σ error bars of the first and the last measurements are clearly separated (Fig. 2.5 and Table 2.6). This could be caused by a clumpy circumstellar medium, probably involving the circumstellar disk. Nisini et al. (2005) find that accretion accounts for 60% of this

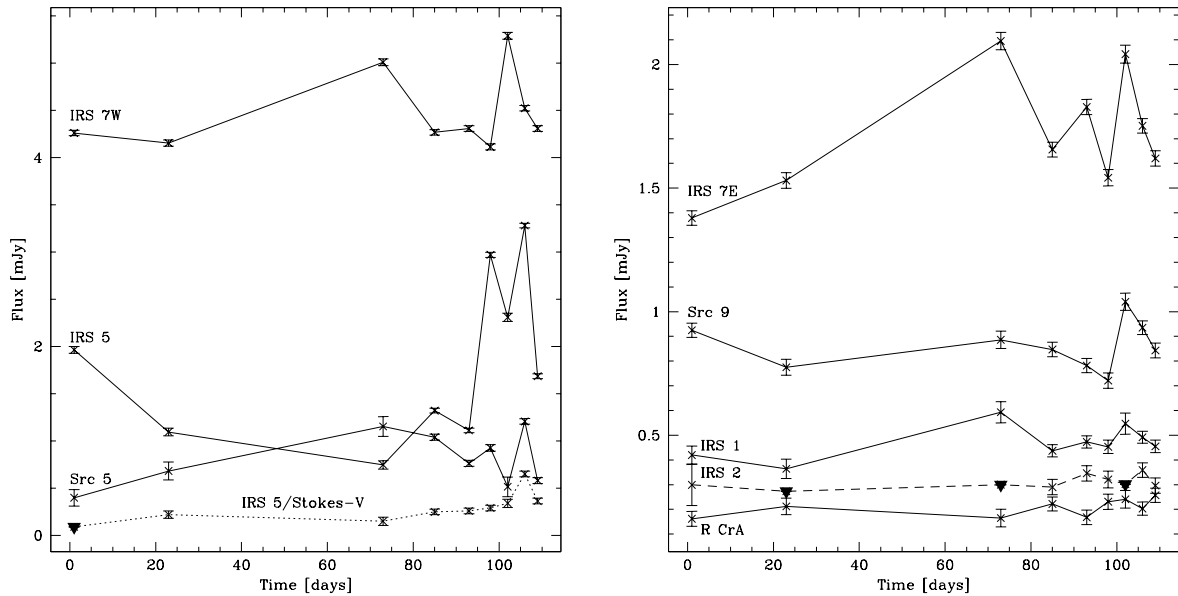


Figure 2.2: Radio flux density curves of sources identified in the 1998 VLA data. Error bars indicate the uncertainty estimates given by the AIPS task SAD, they are based on actual noise (1σ) rather than the quality of the fit. Filled triangles denote upper limits. Also shown is Stokes-V for IRS 5.

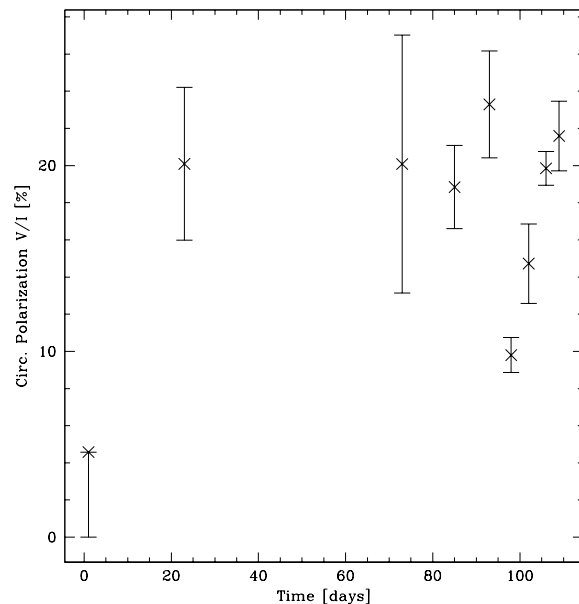


Figure 2.3: IRS 5 epoch-averaged polarization degrees in percent. Errors are propagated from those shown in Fig. 2.2. Note that the first data point is an upper limit, calculated with the 3σ upper limit for Stokes-V.

object's bolometric luminosity.

IRS 5 shows several flares in our VLA dataset (Figs. 2.2 and 2.3, Table 2.4) and has been observed flaring already once before at 4.9 GHz (Suters et al. 1996). In our data, the source starts at a relatively high flux density, dims, and then sharply rises towards two peaks, separated by about nine days. This source was previously reported to emit nonthermal radio emission (Feigelson et al. 1998). Interestingly, the initial high flux density of IRS 5 is accompanied by undetectable Stokes-V emission. Also when looking at the double peak towards the end of the period covered here, the Stokes-V flux density appears to be largely uncorrelated to the Stokes-I flux density:

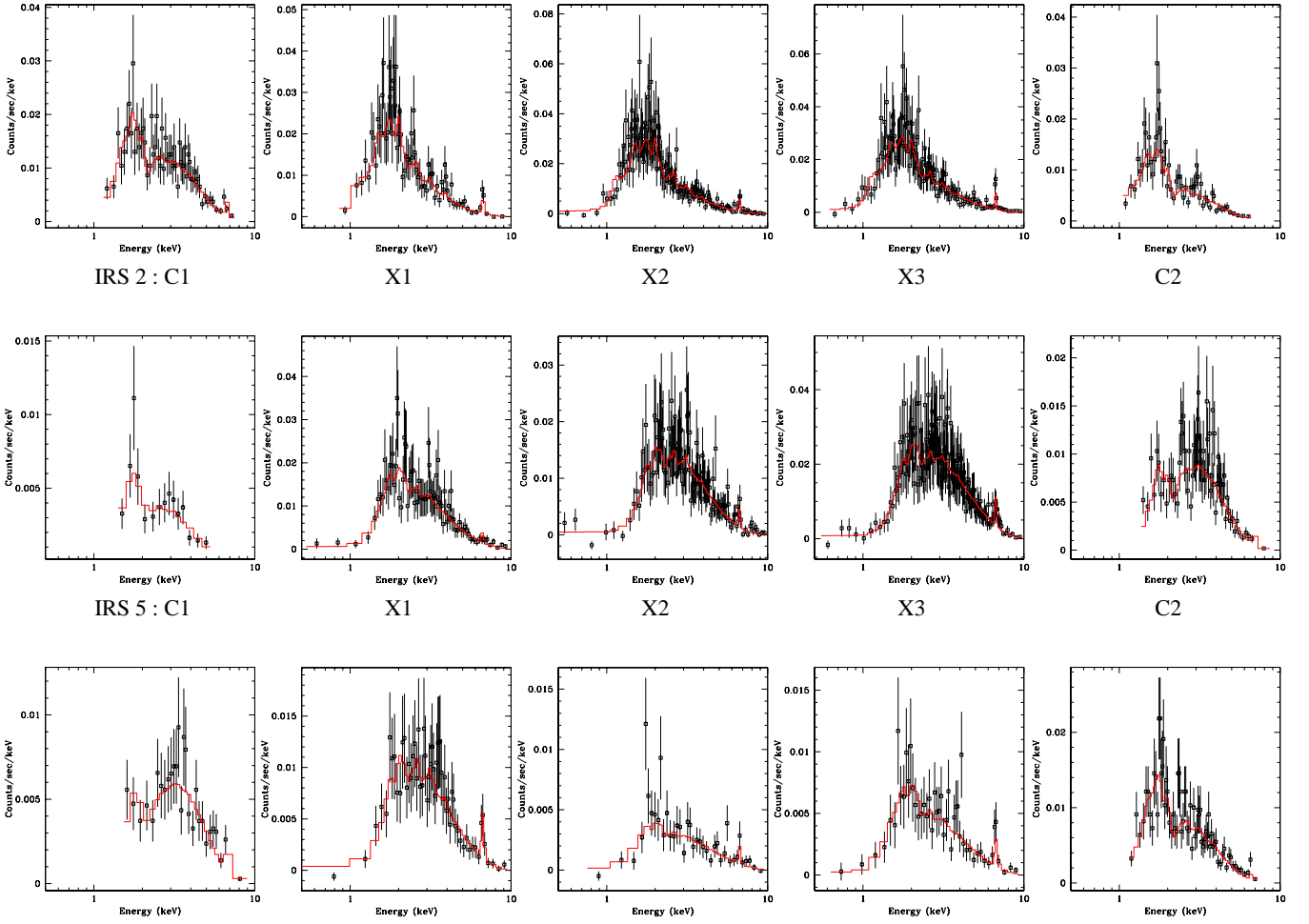


Figure 2.4: X-ray spectra of IRS 2, 5 and 1 derived from the five X-ray datasets, ranging from 0.5–10 keV. The line shows the result of fitting an absorbed APEC model.

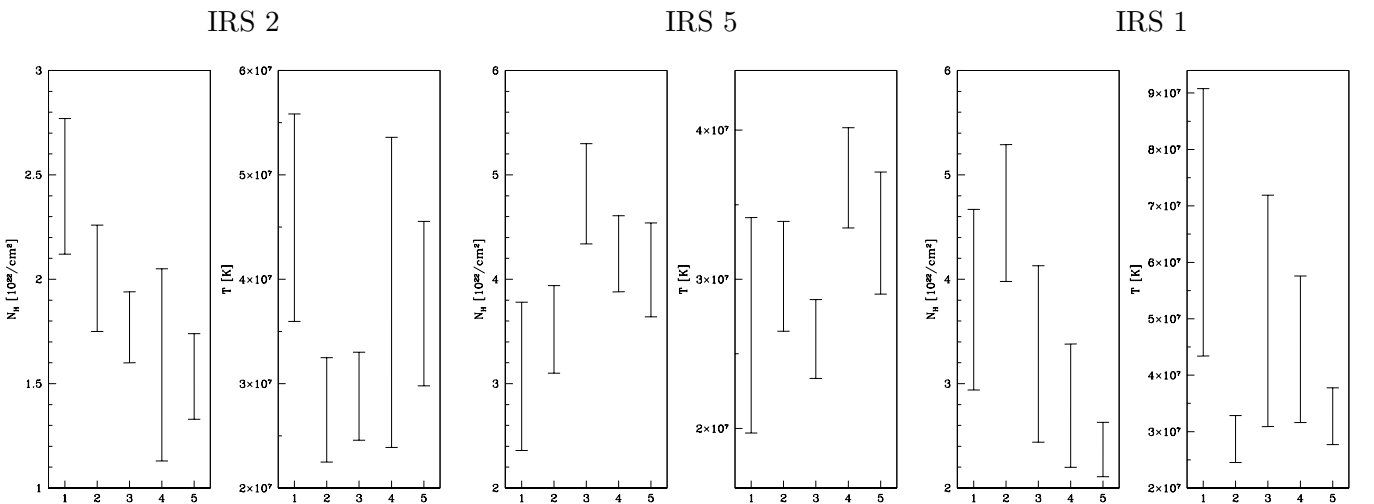


Figure 2.5: Results of fitting XSWABS×XSAPEC, fit parameters N_{H} [10^{22} cm^{-2}] (left) and kT [K] (right) for IRS 2, 5, and 1. Abundances set to values determined from best spectra. Error bars are 3σ . The X-ray datasets are numbered according to Table 2.2. The NIR-determined N_{H} column densities from Nisini et al. (2005) are $4 \times 10^{22} \text{ cm}^{-2}$ (IRS 2), $9 \times 10^{22} \text{ cm}^{-2}$ (IRS 5), and $6 \times 10^{22} \text{ cm}^{-2}$ (IRS 1).

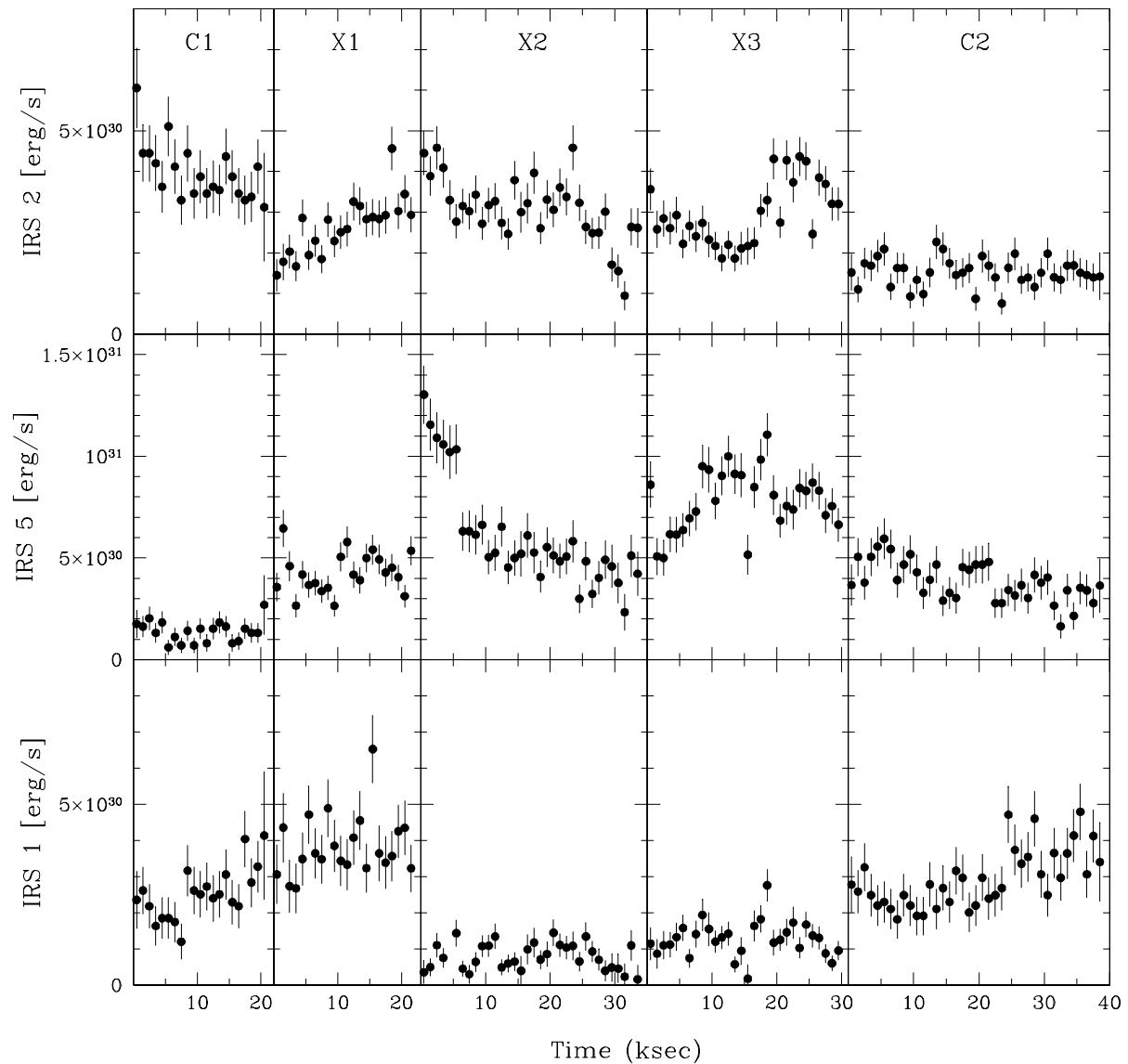


Figure 2.6: Kilosecond-binned, background-subtracted X-ray luminosity curves in temporal order for the three class I protostars IRS 2, 5, and 1. In the X2 and X3 observations, around 20% of the flux from IRS 1 is lost due to a chip gap in the source region.

Only in the second peak there is a rise in Stokes- V flux density. Possibly this different behaviour is at least partly due to an averaging effect, given the faster variability in Stokes- V : Contrary to the Stokes- I emission, Stokes- V in our data is variable down to timescales of 0.5h, a clear sign of nonthermal emission. In the epoch with the highest Stokes- V flux density (R8), for example, Stokes- V emission was only detected in the first quarter. Two epochs earlier, at the sharp rise in Stokes- I , the polarization degree drops from 23% to 10% because only the Stokes- I emission increases. In the subsequent epoch, the polarization degree is back at 20% while the total flux density increased even further. Feigelson et al. (1998) reported a polarization degree changing between 10% to 37% during a day.

In X-rays, IRS 5 is the most variable object when compared to IRS 1 and IRS 2, within our datasets as well as on longer time scales. The overall count rate in 2003 (C2) is nearly three times as high as in 2000 (C1). In the two consecutive observations X2 and X3, the X3 count

rate is nearly twice as high as the X2 count rate. The X3 luminosity curve (Fig. 2.6) starts with an increase followed by a slight diminution in emission towards the end of the observation. The high-luminosity points at the beginning of the X2 luminosity curve remain unexplained. The X-ray spectra (Fig. 2.4) show signs of high absorption ($N_H \approx 4 \times 10^{22} \text{ cm}^{-2}$), the temperature of the emitting plasma is at around $T \approx 3 \times 10^7 \text{ K}$. There appears to be no significant temporal evolution in these fit parameters (Fig. 2.5 and Table 2.6). Nisini et al. (2005) confirm earlier observations by Chen & Graham (1993), finding that IRS 5 is a binary object with only 78 AU separation. Thus, the attribution of X-rays to any of the components, or both is difficult. For IRS 5a, they find that accretion accounts for below 20% of the object's bolometric luminosity. While this suggests a deeply embedded object in a later evolutionary stage, Nisini et al. (2005), using standard evolutionary tracks, conclude that IRS 5a has about the same age as IRS 2 ($\approx 5 \times 10^5 - 10^6 \text{ yrs}$). Already Feigelson & Montmerle (1999) note that the radio properties of this source rather resemble a weak-line T Tauri star. Due to the compact grouping of protostars surrounding it, it remains unclear whether IRS 5 powers an outflow (e.g. Wang et al. 2004). The weak neighbouring radio source (no. 5 in Tables 2.3 and 2.4) has a very faint 2MASS counterpart within the nebulosity surrounding IRS 5.

IRS 1 was not found to be variable at radio frequencies of 4.9 GHz (Suters et al. 1996). In our data, this source does not show significant radio variability either (Fig. 2.2 and Table 2.4). The observed flux density is compatible with the value measured by Feigelson et al. (1998). There are, however, clear signs of X-ray variability in this relatively bright X-ray source – within the datasets as well as on longer time scales. The C2 count rate is 35% greater than the C1 count rate, and the XMM-Newton count rates also suggest variability even though the X2 and X3 count rates are affected by a chip gap in the source region, which causes a flux loss of about 20%. The X-ray luminosity curves (Fig. 2.6) show only slight variability within the single observations. The X-ray spectra (Fig. 2.4) can be modeled by highly absorbed ($N_H \approx 3.5 \times 10^{22} \text{ cm}^{-2}$) emission of hot plasma ($T \approx 5 \times 10^7 \text{ K}$). There is a significant difference in the absorbing column densities derived from the X1 and C2 observations. No such signs of differences in the fitted plasma temperatures are seen (Fig. 2.5 and Table 2.6). According to Wang et al. (2004), IRS 1 could be the powering source of four Herbig-Haro objects. Nisini et al. (2005) find that 80% of this object's bolometric luminosity is due to accretion (see also Nisini et al. 2004 who find evidence for an accelerating wind in the vicinity of IRS 1).

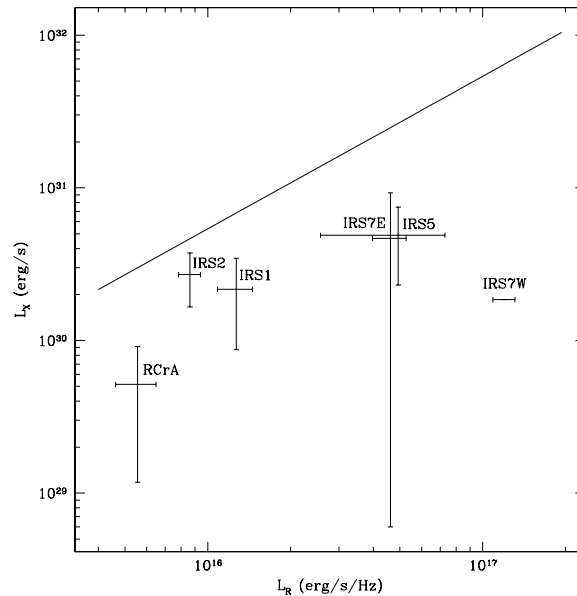
IRS 9 is detected as a weak X-ray source throughout all datasets studied here, shows an X-ray flare in the C1 *Chandra* data (not shown), however, was not detected at radio wavelengths ($S < 0.035 \text{ mJy}$). This is consistent with previous radio observations.

2.3.3.2 Radio Source 5 and IRS 6: A candidate brown dwarf and a T Tauri star

Radio Source 5, initially observed by Brown (1987), has not been detected at X-ray wavelengths. In our data, its radio intensity is variable on timescales of days to months (Fig. 2.2 and Table 2.4). Feigelson et al. (1998) report a radio flux density on a similar scale. Variability of this source at radio frequencies (4.9 GHz) was also reported by Suters et al. (1996) who argue against an extragalactic origin of the emission. Given its faint infrared counterpart, this source could be a brown dwarf (Wilking et al. 1997; Feigelson et al. 1998). If confirmed, the radio data presented here together with the data analyzed by Suters et al. (1996) would constitute an interesting dataset of long-term variability of brown dwarf radio emission.

IRS 6, detected as a weak X-ray source by *Chandra* as well as XMM-Newton, was only found in the combined AM596 *uv*-data: Its emission is very weak at 0.15 mJy. No radio emission from this source has been reported before. While this source is too weak for an analysis of short-timescale X-ray variability, the emission is somewhat weaker in the 2003 (C2) data when

Figure 2.7: X-ray vs. radio luminosity of identified YSOs for which X-ray luminosities can be derived from spectra. The error bars correspond to the standard deviation within the 1998 VLA and archival X-ray data, except for IRS 7E/W, where the X-ray luminosities are from Hamaguchi et al. (2005a). For IRS 7E, the X-ray error bars reflect the flare seen in X2/X3 while for IRS 7W, only a single luminosity was determined from the X2 data. The line shows the empirical relationship for active late-type stars from Guedel & Benz (1993, see also Benz & Güdel 1994).



compared to the 2000 (C1) level. The X2 and X3 count rates for IRS 6 are affected by a chip gap in the source region. Wang et al. (2004), looking for optical outflows, argue that IRS 6 could be the driving source of four Herbig-Haro objects. Nisini et al. (2005) resolve this source into a binary object with a separation of only 97 AU, making the attribution of X-rays difficult. However, they find no sign of ongoing accretion in the near-infrared towards IRS 6a. Thus, IRS 6 appears to contain at least one T Tauri star.

2.3.3.3 The IRS 7 complex with its two deeply embedded protostars

Two main sources can be detected in the IRS 7 region, at both radio and X-ray wavelengths, namely IRS 7E and IRS 7W. Another major radio source is located five arcseconds north of IRS 7W (Radio Source 9, as defined by Brown 1987). Three additional weak radio sources accompany IRS 7E/W.

There has been confusion about possible protostellar sources detected at different wavelengths around IRS 7, although some clarification was brought by Nutter et al. (2005), presenting submillimeter data where the single emission peak observed before at millimeter wavelengths (Henning et al. 1994; Chini et al. 2003; Groppi et al. 2004) is resolved into three subsources. A molecular outflow and a disk were detected in the IRS 7 region and analyzed by Anderson et al. (1997) and Groppi et al. (2004), although the latter showed that it is not yet possible to attribute these to any of the sources seen at higher angular resolution. IRS 7 is also the driving source of Herbig-Haro objects (Wang et al. 2004). Harju et al. (2001) find evidence for a jet emanating from IRS 7E at $\lambda = 6$ cm, using the ATCA radio interferometer. Choi & Tatematsu (2004) analyze the IRS 7 region at $\lambda = 6.9$ mm with the VLA. Interestingly, they only marginally detect IRS 7E while there is elongated emission around IRS 7W and Radio Source 9, although the connection remains unclear. The emerging picture is that of IRS 7W being an infrared-detected, deeply embedded protostar, probably a class I or II source, while IRS 7E could be a class 0 source although the source was detected at $4.8 \mu\text{m}$ by Pontoppidan et al. (2003). This would be one of the first class 0 sources detected in X-rays.

IRS 7E is quite variable on all timescales covered in the 1998 VLA data (Fig. 2.2 and Table 2.4), at a flux density level mostly below the value reported by Feigelson et al. (1998). The weak radio source detected in the eastern vicinity of IRS 7E (source 15) might be a sign for

extended radio emission. The radio sources detected around IRS 7E/W are shown in an inset of Fig. 2.1.

IRS 7E is the most variable X-ray source among the objects studied here. While IRS 7E was only marginally detected in the C1, X1, and C2 observations, the 2003 (X2, X3) datasets show IRS 7E as a strong and very hard X-ray source. This flaring has been studied by Hamaguchi et al. (2005a) who argue that this might be an X-ray detected class 0 source. They do not find any near-infrared counterpart down to a K -band magnitude of 19. However, Pontoppidan et al. (2003) detect both sources, IRS 7E/W, at $4.8 \mu\text{m}$ using VLT-ISAAC, arguing that IRS 7E remained undetected at $10 \mu\text{m}$ (Wilking et al. 1997) due to silicate absorption. It is tempting to attribute also the enormous flare observed by Koyama et al. (1996) to this source, although that remains unclear due to the limited angular resolution of their ASCA data. Since spectra of IRS 7E could only be taken from the XMM-Newton data, an estimated luminosity curve for this source was produced by assuming the same spectral characteristics, taken from Hamaguchi et al. (2005a), of $kT = 3 \text{ keV}$ (corresponding to a temperature of $\approx 35 \text{ MK}$, rather a lower limit) and $N_H = 2.8 \times 10^{23} \text{ cm}^{-2}$ for all five datasets, then determining the fluxes and luminosities following the procedure outlined above. To minimize contamination, Hamaguchi et al. (2005a) excluded IRS 7W from the IRS 7E source region in their analysis. The plot shows the enormous increase in luminosity (Fig. 2.8). In the two *Chandra* observations, only 19 and 13 – however highly energetic – photons were recorded from IRS 7E respectively. Given the high temperature of the plasma emission as well as the quick variability, especially when comparing the subsequent X2 and X3 datasets, it appears unlikely that the emission is due to an accretion shock. These characteristics rather point towards circumstellar magnetic activity.

IRS 7W is the brightest radio source in the sample considered here, mostly emitting at around 4.2 mJy, although in two epochs the source is detected at $> 5 \text{ mJy}$ (Fig. 2.2 and Table 2.4). This source shows only moderate radio variability within the 1998 monitoring, especially on timescales of days. Feigelson et al. (1998) report an 8.4 GHz flux density of 1.58 mJy, considerably higher than all flux densities measured in 1998 which are $< 1.1 \text{ mJy}$. Close to Radio Source 9, there are two weak radio sources (sources 10 and 13) which do not have counterparts at other wavelengths.

In the C1/C2 data, IRS 7W is detected as a weak X-ray source emitting energetic photons, similar to IRS 7E. Due to contamination caused by the flaring nearby source IRS 7E, a meaningful spectrum could only be extracted from the X2 dataset, leading to $kT = 4.7 \text{ keV}$ ($\approx 55 \text{ MK}$) and $N_H = 3.4 \times 10^{23} \text{ cm}^{-2}$ (Hamaguchi et al. 2005a).

2.3.3.4 The Herbig Ae star R CrA

R CrA is one of the optically brightest ($V \sim 11.5 \text{ mag}$) objects in the CrA cloud and it illuminates the reflection nebula NGC 6729. The stellar parameters are somewhat uncertain, especially because the optical spectrum seems to be variable and spectral types ranging from B8 to F7 have been reported (e.g. Bibo et al. 1992). Here we adopt the values listed in Lorenzetti et al. (1999), i.e. spectral type A5e, $L_{\text{bol}} = 132 L_{\odot}$, and $A_V = 1.9 \text{ mag}$. Comparison of these parameters to the pre-main sequence models of Palla & Stahler (1999) suggest a mass of $\sim 3.5 M_{\odot}$ and an age of slightly more than 1 Myr for R CrA.

The spectral energy distribution of R CrA rises very steeply between $0.6 \mu\text{m}$ and $3 \mu\text{m}$ (see, e.g. Acke & van den Ancker 2004), demonstrating the presence of large amounts of hot circumstellar material, presumably in the form of an optically thick circumstellar disk. This very large infrared excess suggests that R CrA is in a very early evolutionary state and thus we discuss it here together with the lower-mass protostars.

In the VLA data (Fig. 2.2 and Table 2.4), R CrA was detected as a weak and rather constant radio source with an average flux density of 0.23 mJy, the same level as measured by Feigelson et al. (1998). However, R CrA remained undetected at radio wavelengths several times before: in September 1985 (VLA, 6cm, $3\sigma=0.17 \text{ mJy}$, Brown 1987), in February 1990 (VLA, 3.6cm,

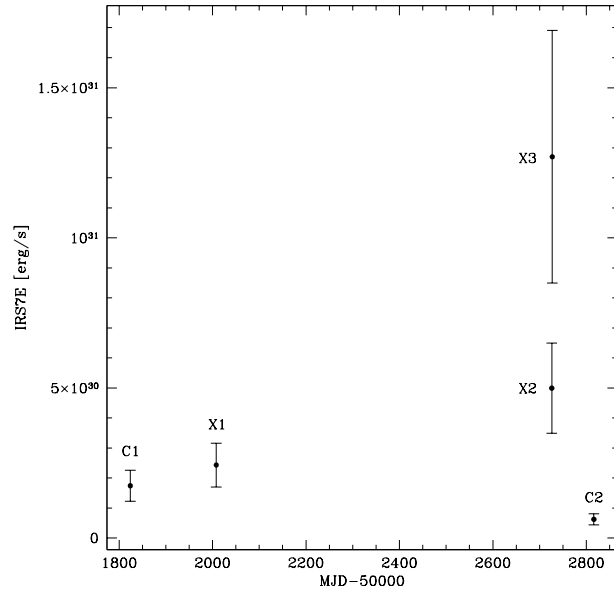


Figure 2.8: IRS 7E X-ray luminosity. Count rates for the five X-ray datasets were converted into luminosities without background subtraction, assuming a single-temperature spectrum of $kT = 3$ keV and $N_H = 2.8 \times 10^{23} \text{ cm}^{-2}$ (Hamaguchi et al. 2005a). The error bars denote errors of 30%. Note that the source is only marginally detected in C1 and C2.

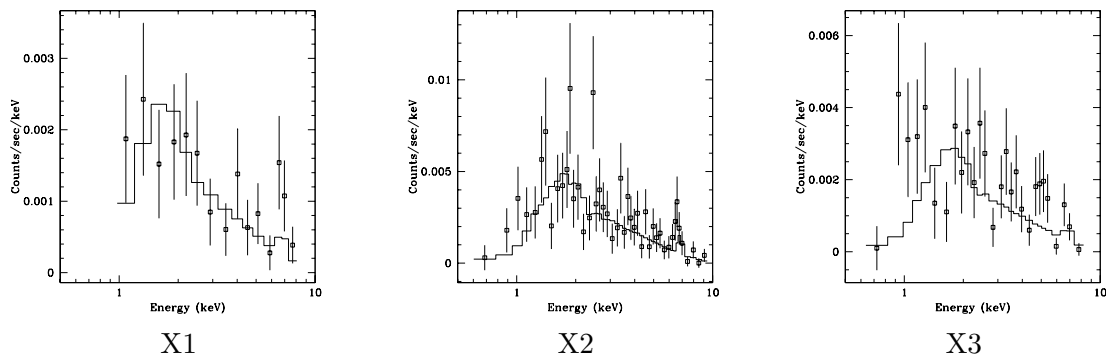


Figure 2.9: R CrA spectra, taken from an ellipse region avoiding the neighbouring source IRS 9. The results of fitting an absorbed APEC model are shown. In the X3 fit, the column density was frozen to the values from X1 and X2.

$3\sigma=0.10$ mJy, Skinner et al. 1993) as well as with the VLA and the AT in 1985-87 and 1992, respectively (Suters et al. 1996). Even though R CrA is quite close to the respective 5σ limits, this is suggestive of long-term variability.

X-ray observations of the *Coronet* region with EINSTEIN and ROSAT did not detect X-ray emission from R CrA (Zinnecker & Preibisch 1994; Damiani et al. 1994; Neuhäuser & Preibisch 1997; Walter et al. 1997). Koyama et al. (1996) detected hard X-ray emission near the location of R CrA with ASCA. However, due to the poor spatial resolution of the ASCA data (FWHM $\sim 2'$) the contributions of the individual YSOs R CrA, IRS 7, and IRS 9 could not be resolved. Nevertheless, since the intensity peak in the ASCA image was located close to the position of R CrA, it appears likely that R CrA produced a significant fraction of the observed hard X-ray emission. During this ASCA observation a strong flare was seen. The X-ray spectrum was found to be very hard and could be fitted with a $kT \sim 6 - 7$ keV plasma model and an absorbing hydrogen column density of $N_H \sim 4 \times 10^{22} \text{ cm}^{-2}$. During the flare, the spectrum showed a remarkable broadened or double emission line structure between 6.2 and 6.8 keV. However, it remained unclear which of the sources caused the flare.

X-ray emission from R CrA is clearly detected in all the *Chandra* and *XMM-Newton* datasets

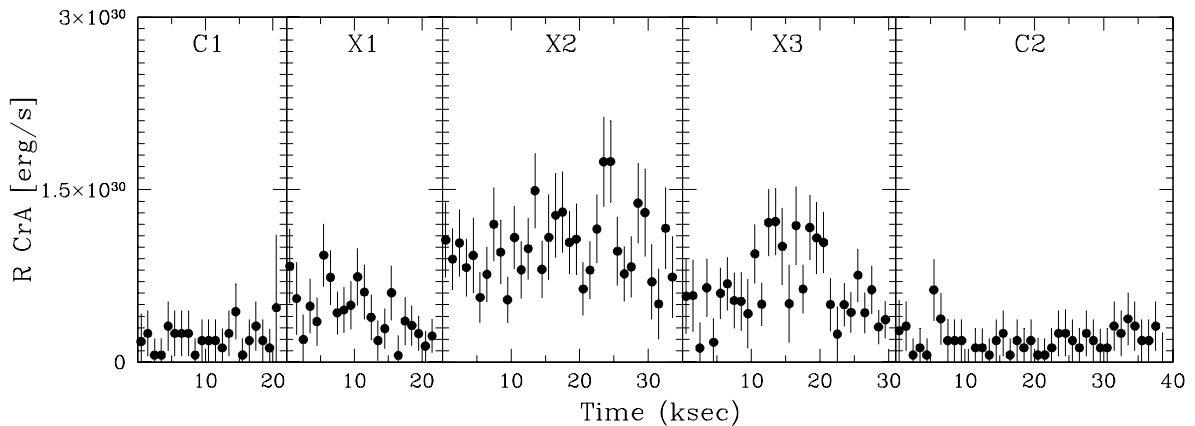


Figure 2.10: R CrA X-ray luminosity curves from the same elliptical region also used for the spectra. Luminosity calculated assuming spectral properties of the best spectrum (X2). Data is kilosecond-binned and background-subtracted, datasets are in temporal order as labeled.

used in this paper. The detection in the *Chandra* observation C1 was already noted by Skinner et al. (2004). During both *Chandra* observations R CrA is only seen as a rather weak source, yielding no more than ~ 100 counts, too few for detailed spectral analysis. During the first *XMM-Newton* observation the observed count rate for R CrA is well consistent with that in the *Chandra* observations, but during the *XMM-Newton* observations X2 and X3 the count rates were about a factor of two larger (see light curve in Fig. 2.10). The light curves show no indications of a flare, it appears rather as if the source has “switched” to a higher activity level during X2 and X3. A sudden drop of the count rate (by about a factor of two) is seen in the second half of observation X3. A possible interpretation for the general shape of the light curve would be the temporal presence of a dominant active region during X2 and X3. The sharp drop in X3 may then be explained by the occultation of such an active region when the stellar rotation moves it behind the stellar disk.

The X-ray spectra of R CrA extracted from observations X1, X2, and X3 show a very strong high-energy tail and a pronounced 6.7 keV emission line, providing clear evidence for very hot plasma. The spectral fits yield a plasma temperature of about 100 MK, the highest value of all sources in the *Coronet* region. The hydrogen column densities derived from the spectral fits are $\sim 1.3 \times 10^{22} \text{ cm}^{-2}$ and correspond to an optical extinction of $A_{V,X} \sim 6 - 8$ mag (Ryter 1996; Vuong et al. 2003). This is higher than the extinction estimate derived from the optical properties ($A_V \sim 2$ mag), but given the uncertainty of the optical parameters of R CrA, both values may well be in agreement.

The X-ray luminosity of R CrA derived from the spectral fits ranges from 1.9×10^{29} erg/sec in the C2 observation to 1.0×10^{30} erg/sec in the X2 observation. The fractional X-ray luminosity is thus $\log(L_X/L_{\text{bol}}) \sim -6.3 \dots - 5.6$.

The observed X-ray emission of R CrA is particularly interesting since, according to our current understanding of stellar X-ray emission mechanisms, one would not expect to see any X-ray emission from this star. Being an intermediate-mass A-type star, R CrA should neither possess a magnetically driven corona, which is the source of the X-ray emission from late type (F to M) stars, nor can it have a strong radiation-driven stellar wind, in which shocks cause X-ray emission observed in the more massive O- and early B-type stars (see e.g. Pallavicini 1989; Favata & Micela 2003). The theoretical expectation that late B and A stars should not be intrinsic X-ray emitters is well confirmed in the case of main sequence stars (e.g. Schmitt et al. 1993; Cassinelli et al. 1994). However, it is still unclear whether the Herbig Ae/Be stars, i.e. the class of very young intermediate-mass pre-main sequence stars, to which R CrA belongs, also fit to this scenario. In EINSTEIN, ROSAT, ASCA, and *Chandra* X-ray observations of

samples of Herbig Ae/Be stars (Damiani et al. 1994; Zinnecker & Preibisch 1994; Preibisch & Zinnecker 1996; Skinner et al. 2004; Hamaguchi et al. 2005a) some 30 - 50 % of the observed stars were detected as X-ray sources. Several possible explanations have been proposed for these findings (see Caillault et al. 1994; Preibisch & Zinnecker 1996; Skinner et al. 2004), but no final explanation has been found. There exist some ideas how an AeBe star may produce X-ray emission (e.g. the scenario of a nonsolar dynamo powered by rotational shear in very young intermediate mass stars; see Tout & Pringle 1995), but no really convincing evidence has yet been found for this. A possible explanation for the observed X-ray emission may be that the X-rays originate not from the AeBe stars themselves, but from close, unresolved, late type companions.

For our case of R CrA, we note that Takami et al. (2003) presented spectro-astrometric observations and found some evidence for the presence of a companion at a separation of about $\sim 0''.070 - 0''.10$, i.e. only 10–15 AU. If such a companion actually exists, it is probably a lower-mass YSO, i.e. a T Tauri star or a low-mass protostar, which could easily explain the observed X-ray emission.

What remains quite remarkable, however, is the extremely high plasma temperature of ~ 100 MK inferred from the X-ray spectra. Typical plasma temperatures in YSOs range from ~ 10 MK up to ~ 50 MK, reaching higher values usually only during large X-ray flares⁴. From other X-ray observations of star forming regions it seems that class I protostars show systematically higher plasma temperatures than the more evolved T Tauri stars (see, e.g., Imanishi et al. 2001a for the case of ρ Oph). This may be an indication that the companion of R CrA is a very young object (i.e. more likely a class I protostar than a T Tauri star). In this case, some (perhaps the largest) fraction of the infrared excess emission may come from the companion and not from the Ae star R CrA itself.

2.4 Conclusions

We presented the results of radio monitoring of protostars in the *Coronet* cluster together with archival X-ray data of these sources covering 154 ksec. The main results are:

1. Observing with the VLA in nine epochs spread over several months in 1998, we detect centimetric radio emission from 13 sources in the region around R CrA. Nine sources in this region are detected in X-rays, and eight sources are detected at both radio and X-ray wavelengths.
2. IRS 5, a class I protostar with nonthermal radio emission, shows an interesting increase and decrease in its radio emission on the order of days, accompanied by changes in its polarization properties. It is the most variable radio source in the 1998 VLA data. Among the three protostars bright enough for a detailed X-ray study, IRS 5 is also the most variable source in X-rays.
3. Not counting IRS 7W due to the unclear classification, we detect three out of four covered class I sources in radio emission, while we detect all four in X-rays. With IRS 7E, one candidate class 0 source is detected in X-rays as well as in radio emission.
4. The Herbig Ae star R CrA was detected at both radio and X-ray wavelengths. The X-ray spectrum of this source surprisingly contains emission from extremely hot plasma ($\approx 9 \times 10^7$ K). We suspect that a lower-mass companion is responsible for this emission.

⁴In the most comprehensive dataset on the X-ray emission from young stars, the Chandra Orion Ultradeep Project, only 2% of the optically visible T Tauri stars in the Orion Nebula Cluster showed plasma temperatures exceeding 100 MK (see Getman et al. 2005b; Preibisch et al. 2005a).

5. The spectra of IRS 2, 5 and 1 all can be explained by the absorbed emission of plasma having temperatures of several 10^7 K while the high absorbing column densities (several 10^{22} cm^{-2}) are all at about half the values determined from near-infrared colours. This has been observed before towards similar sources, but the effect remains unexplained. We discuss possible explanations.
6. While the X-ray light curves of the the class I protostars IRS 2, 5, and 1 all show varying degrees of variability, no flare events were observed. With no class II sources to compare with, it is impossible here to corroborate the conclusion of Imanishi et al. (2001a) that class I sources are intrinsically more X-ray-variable than later evolutionary stages, although the three class I sources studied here are not extremely variable.
7. The X-ray spectra are spread over about 2.5 years and also allow an analysis of variability in their main fit parameters, absorbing column density and plasma temperature. While mostly no significant variability can be seen, a significant change is observed in the absorbing column density towards IRS 2: It appears to have decreased continuously to a significantly lower level, from 2.4×10^{22} cm^{-2} to 1.5×10^{22} cm^{-2} , possibly due to a clumpy circumstellar medium towards this source.

Studying the *Coronet* cluster at radio and X-ray wavelengths has provided a number of interesting insights. In order to learn more about high-energy processes in these young stellar objects, we subsequently carried out simultaneous X-ray, radio, and near-infrared observations of the *Coronet* cluster in August 2005 with *Chandra*, the VLA, as well as infrared and optical telescopes. The results of this observing campaign are presented in Chapter 3.

Chapter 3

Simultaneous X-ray, radio, near-infrared, and optical monitoring of Young Stellar Objects in the Coronet cluster

(based on Forbrich, Preibisch, Menten, Neuhäuser, Walter, Tamura, Matsunaga, Kusakabe, Nakajima, Brandeker, Fornasier, Posselt, Tachihara, & Broeg, *A&A* 2007, in press)

3.1 Introduction

Multi-wavelength (X-ray to radio) monitoring of YSOs can provide important information about physical processes at the stellar surface, in the stellar corona, and/or in the inner circumstellar disk regions. Here we present the first simultaneous X-ray, radio, near-infrared, and optical monitoring of YSOs, targeting the *Coronet* cluster in the Corona Australis star-forming region which harbours at least one class 0 protostar, several class I objects, numerous T Tauri stars, and a few Herbig AeBe stars. The observations and the data analysis are presented in Section 3.2. After a discussion of single-wavelength variability in Section 3.3, multi-wavelength variability is analyzed in Section 3.4. This section also includes remarks on specific sources. Finally, conclusions are presented in Section 3.5.

3.2 Observations and data reduction

We present here the results of a multi-wavelength observing campaign targeting YSOs in Corona Australis, based on five epochs of *Chandra* observations. For the first time, protostars (class 0/I YSOs) were observed simultaneously at radio, X-ray, and near-infrared wavelengths. The field of view of the observations is shown in Fig. 3.1, their scheduling is shown in Fig. 3.2 as well as listed in Table 3.1.

Due to the far southern declination of the *Coronet* cluster (nearly -37°), the region is accessible for the NRAO¹ Very Large Array only during a few hours per day. Thus, the core experiment was designed around five 4h epochs of *Chandra* observations on five successive days (finally with a break in-between due to the satellite crossing a radiation zone). The instrument used was the Advanced CCD Imaging Spectrometer (ACIS). The *Chandra* observations were to be complemented by five epochs of simultaneous VLA observations around the *Coronet* Cluster's

¹The National Radio Astronomy Observatory is a facility of the National Science Foundation operated under cooperative agreement by Associated Universities, Inc.

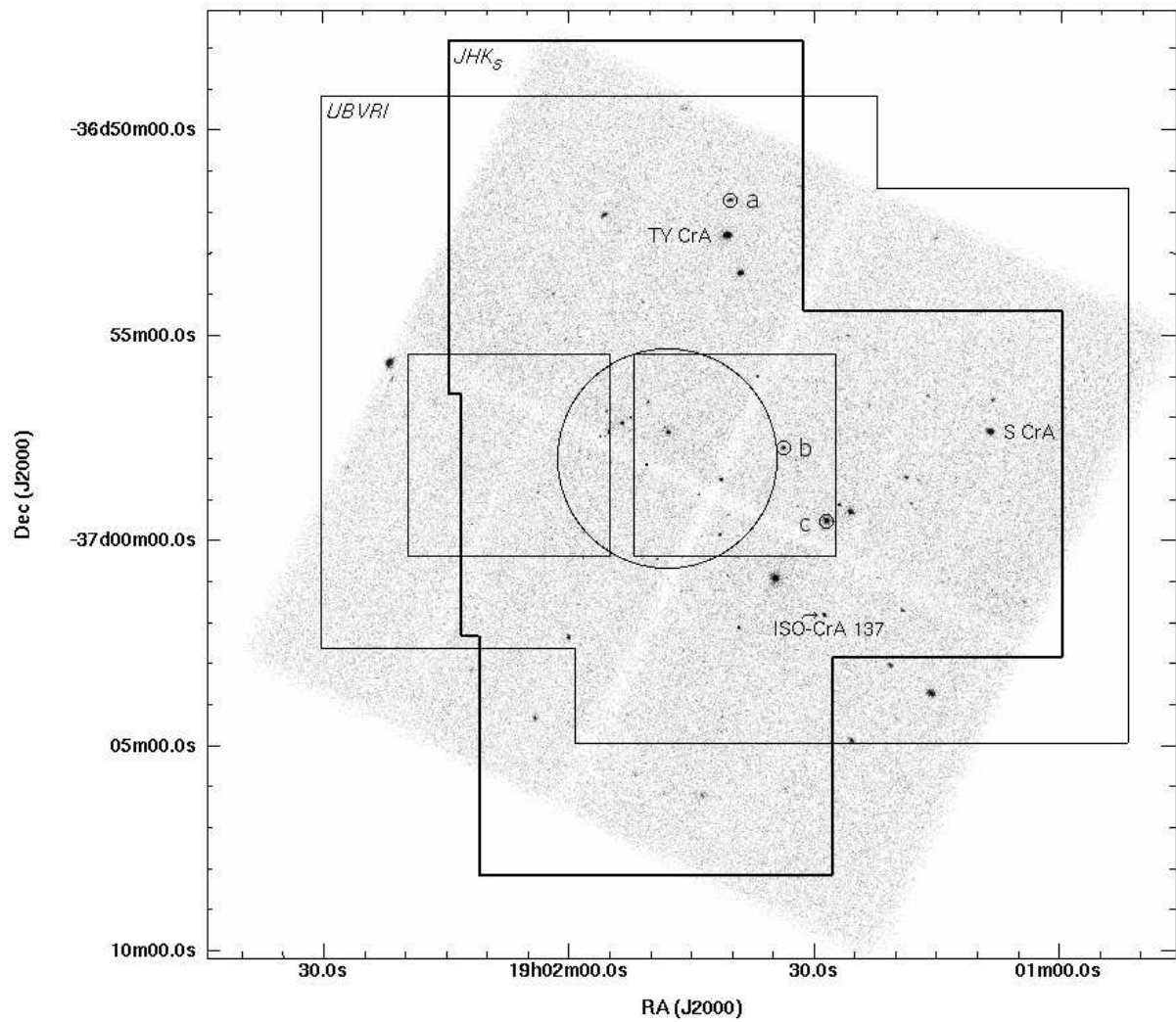


Figure 3.1: Plot of the *Coronet* region covered in this multi-wavelength dataset. The background image shows the combined X-ray data, the big circle indicates the half-power beam width of the VLA primary beam. The outer two boxes mark the coverage of the SMARTS-*UBVRI* and SIRIUS-*JHK_S* data (thick line). The two small boxes show the fields of view of the SofI observations. The central *Coronet* cluster is shown in detail in Fig. 3.3. Three 2MASS sources discussed in the text are marked as small circles: a) 2MASS J19014041-3651422, b) 2MASS J19013385-3657448, and c) 2MASS J19012872-3659317

meridian passage. To ease scheduling, blocks of 2h VLA time were to be scheduled within the 4h *Chandra* observations. A few simultaneous near-infrared observations were collected with ESO's 3.5m New Technology Telescope (NTT) in Chile, using the SofI imager in the *JHK_S* bands subsequently and in two fields east and west of R CrA. SofI is based on a 1024×1024 Hawaii HgCdTe CCD detector, providing a field of view of $4'.94 \times 4'.94$ with a pixel scale of $0''.288$ (using the Large Field Objective). The exposure time was set to the minimal possible value at 1.182 seconds.

Additional near-simultaneous observations were carried out with SIRIUS (Simultaneous Infrared Imager for Unbiased Survey) at the 1.4m telescope of the InfraRed Survey Facility² (IRSF)

²IRSF is operated by Nagoya University and SAAO (South African Astronomical Observatory) at Sutherland, South Africa.

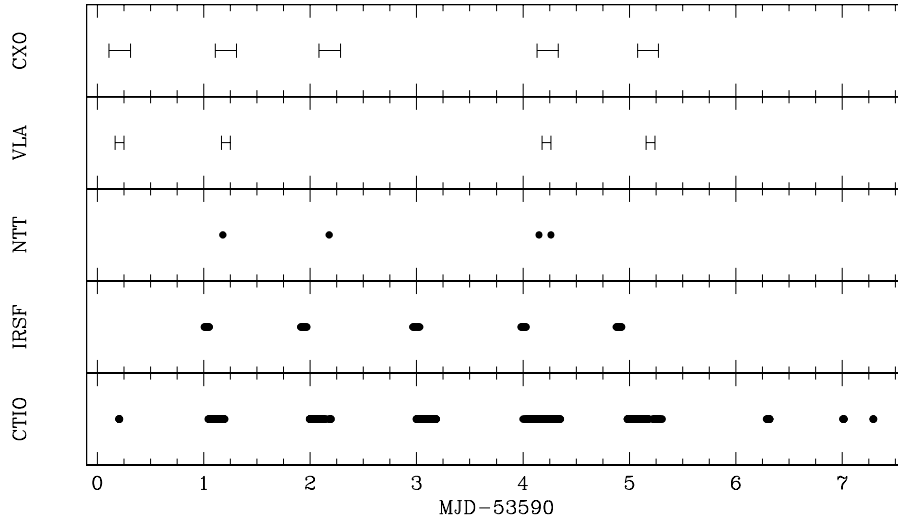


Figure 3.2: Graphical depiction of the observing times at the different observatories indicated on the lefthand side.

Table 3.1: Simultaneous observations of the *Coronet* with *Chandra* and the VLA (given in UT)

Day (MJD ¹)	<i>Chandra</i>	VLA
Aug 08, 2005 (0)	02:37:52 – 07:33:11	04:04:20 – 06:03:45
Aug 09, 2005 (1)	02:38:52 – 07:22:10	04:00:50 – 06:00:00
Aug 10, 2005 (2)	01:58:25 – 06:53:28	–
Aug 12, 2005 (4)	03:12:57 – 07:54:57	04:18:30 – 06:18:20
Aug 13, 2005 (5)	01:51:20 – 06:34:32	03:44:40 – 05:44:10

¹ MJD-53590

in South Africa (for a description of this simultaneous three-band NIR camera, see Nagayama et al. 2003). The SIRIUS camera has a field of view of $7'.7 \times 7'.7$ and a pixel scale of $0''.45$. Four different fields were observed, one centered on the *Coronet* cluster, and three more north, west, and south of the central field. The SIRIUS images typically consist of ten dithered exposures of 30 sec duration.

Last not least, simultaneous optical imaging (bands *UBVRI* successively) of the region was performed with the CTIO 0.9m telescope, operated by the SMARTS³ consortium, at the Cerro Tololo Inter-American Observatory in Chile. The detector used was a 2048×2046 quad-chip CCD camera providing a field of view of $13'.5 \times 13'.5$ with a pixel scale of $0''.396$. Again, two fields were observed, east and west of R CrA, but both overlapping to cover R CrA. The last three epochs including the last multi-wavelength epoch were increasingly compromised by bad weather. In all filters and both fields, long and short exposures were taken, e.g. for the *I*-band typically durations of 20 sec and 2 sec.

3.2.1 X-ray observations

The *Chandra* Interactive Analysis of Observations (CIAO) 3.3 software package together with CALDB 3.2.1 was used for the analysis of the *Chandra*-ACIS data. Apertures of 5 arcseconds

³Small and Moderate Aperture Research Telescope System

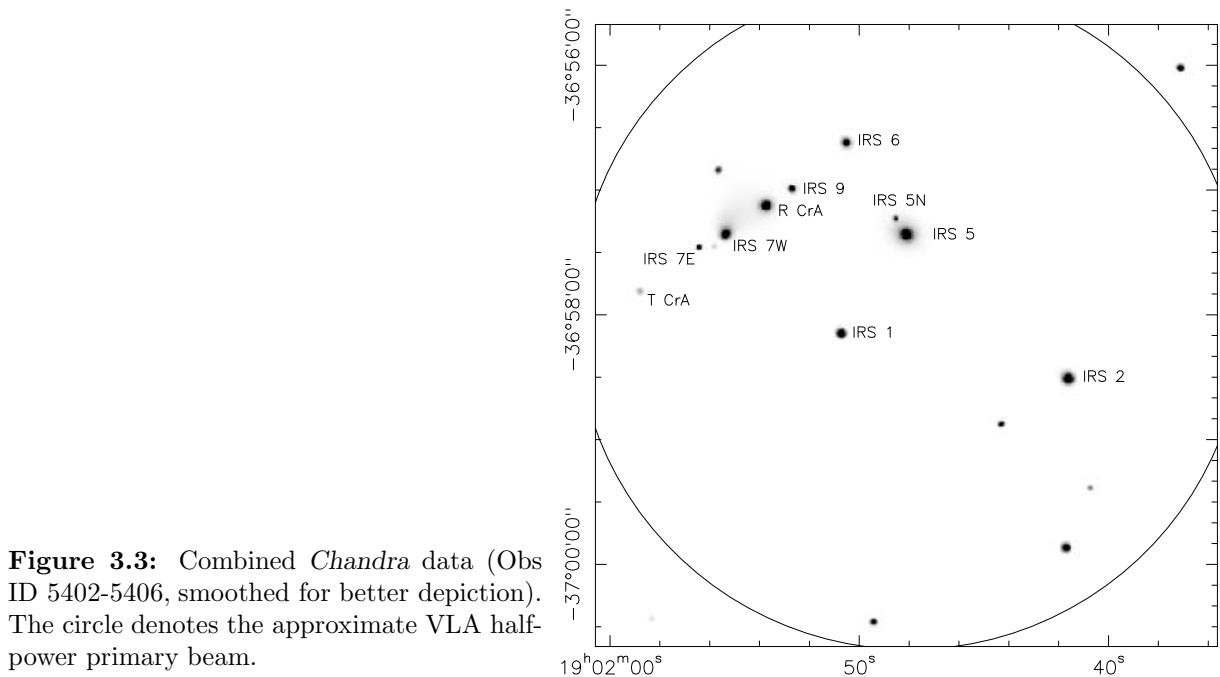


Figure 3.3: Combined *Chandra* data (Obs ID 5402-5406, smoothed for better depiction). The circle denotes the approximate VLA half-power primary beam.

in diameter were used for light curves and spectra alike. The spectra were compiled with the task *psextract* which includes the creation of response matrices and ancillary response files. Bin sizes in the spectra were determined by a minimum event number per bin of fifteen.

3.2.2 Radio observations

The VLA was observing in its D configuration (program ID S6 255) at $\nu = 8.44$ GHz with two intermediate frequency (IF) pairs, offset by the IF bandwidth of 50 MHz. One IF of each pair detected right circular polarization (RCP), the other one left circular polarization (LCP). The phase center was $(\alpha, \delta)_{J2000} = 19^{\text{h}}01^{\text{m}}48^{\text{s}}, -36^{\circ}58'00''$. The primary beam of the VLA antennas limits the field of view to approximately five arcminutes FWHM around the phase center position (Fig. 3.3). Compared to the other observations reported here, the radio observations cover the smallest field, centered on the *Coronet* cluster. Data were analyzed using the NRAO Astronomical Image Processing System (AIPS). Observations of 3C286, once per observing epoch, were used to establish an absolute flux density scale. The nearby phase calibrator 1924–292 was observed every seven minutes. We estimate that our absolute flux density scale thus derived is accurate to $\sim 15\%$.

Due to the low elevation ($< 19^{\circ}$), there are problems with phase instabilities caused by the atmosphere. After initial flagging of obviously faulty uv data, data were phase-only self-calibrated before imaging in Stokes-*I* and Stokes-*V* could be carried out for different time intervals. Source positions and fluxes were determined by fitting Gaussians to each detection, using the AIPS tasks SAD and JMFIT. Splitting the single observing epochs into intervals of approximately one hour, the root mean square (rms) noise level in the Stokes *I* and *V* maps is $\approx 40 \mu\text{Jy}$, for the entire uv data this value reduces to $17 \mu\text{Jy}$. The synthesized beam size for the combined four epochs is $6''.7 \times 2''.0$ at position angle 1.9° .

3.2.3 Near-infrared and optical observations, photometry

The SIRIUS-*JHK_S* data were processed using a reduction pipeline developed as an external package of the IRAF⁴ software package. Processing includes dark frame subtraction, flat-fielding, sky subtraction and finally combination of the dithered single images.

The SofI-*JHK_S* images, consisting of pairs of offset images, were processed using Eclipse 5.0.0. Dark frame subtraction, flat-fielding, and sky subtraction were performed.

The optical images in *UBVRI* bands were dark-subtracted and flat-fielded using IRAF. Slightly different properties of the four CCD chips in the array had to be accounted for using the quadproc procedures. The observations were partly affected by bad weather in the last three epochs.

By correlating the near-infrared and optical data with 2MASS positions, an overall astrometric accuracy of $< 0''.1$ was achieved.

Differential photometry was carried out for optical and near-infrared counterparts of X-ray sources using an algorithm described by Broeg et al. (2005). This procedure uses aperture photometry determined by the IRAF daophot package. For the aperture radii we chose values of around three times the radius of the point-spread function while the background was determined from surrounding annuli. The respective comparison stars are weighted down according to their variability as represented by their standard deviations, resulting in an optimum artificial comparison star. As an estimate of the errors in the resulting light curves, a linear model of the instrumental errors is self-consistently adjusted so that it reproduces the standard deviations of the least variable comparison stars before it is applied to the science source. For the sources analyzed here, measurements with resulting 1σ errors of more than 0.05 mag were discarded. Due to the different selections of comparison stars, the zero levels of the differential magnitude scales generally are not the same. Thus, the light curves are plotted with the respective median magnitudes subtracted. Sources observed outside the respective linear detector ranges were not analyzed photometrically.

3.2.3.1 S CrA

We undertook a separate analysis of the S CrA optical photometry in the context of our long term monitoring, which consists of over 200 observations between 2003 April and 2006 June, mostly obtained with the CTIO/SMARTS 1.3m ANDICAM dual-channel photometer. This detector is described in, for example, Walter et al. (2004). Out of this long-term monitoring, we include seven ANDICAM data points in our analysis here, obtained in the nights of 2005 August 14-17. For this analysis we do not make use of the short exposures. The data quality is poorer, and those images do not extend the temporal coverage.

S CrA is spatially resolvable under the typical observing conditions at CTIO. We measure the brightness of the individual components by fitting two Gaussians to the image. The separation and position angle are well-known, and are not free to vary. We constrain the two images to have the same point-spread function (PSF). The relative brightnesses of the two stars are then the relative amplitudes of the two Gaussians.

The seeing (measured as the FWHM of the Gaussian PSF) in the *I* band varied from $0''.7$ to $1''.4$, with a median value of $0''.9$. The seeing was stable for the first 4 nights, with a variance of $0''.06$, but went up in the remainder of the run, with the variance in the mean seeing ballooning to $0''.2$. There are no obvious seeing-dependent effects on the photometry.

We calibrate the brightness of the system in a three-step process. First, we determine the long-term brightness variations of the S CrA binary through differential photometry with respect to 9 other stars in the sparse field. We use an $8''$ aperture to enclose all the light from the S

⁴IRAF is distributed by the National Optical Astronomy Observatories, which is operated by the Association of Universities for Research in Astronomy, Inc. (AURA) under cooperative agreement with the National Science Foundation.

Table 3.2: Radio flux densities of the *Coronet* sources

Source ID	2005 flux density ¹ [mJy]	1998 flux density ² [mJy]
IRS 2	0.49 ± 0.02	0.29–0.36
Source 5	1.14 ± 0.02	0.40–1.21
IRS 5N	0.06 ± 0.02	0.10 ³
IRS 5	0.68 ± 0.02	0.75–3.28
IRS 6	0.07 ± 0.02	0.15
IRS 1	0.42 ± 0.02	0.36–0.59
R CrA	0.30 ± 0.02	0.16–0.26
IRS 7W ⁴	5.33 ± 0.02	4.11–5.29
IRS 7E	1.77 ± 0.02	1.38–2.10

¹ quoted errors are from Gaussian fitting. Our flux scale has an absolute uncertainty of $\sim 15\%$

² minima and maxima (if source detected in single epochs), see Forbrich et al. (2006)/Chapter 2

³ note that this source is not called IRS 5N in Forbrich et al. (2006)/Chapter 2 but is no. 5 in the tables

⁴ blended with Source 9

CrA binary. We assume that the weighted mean brightness of these nine stars does not vary significantly with time. The comparison brightness is heavily skewed to the flux of VSST 14, a pre-main sequence star, but not a known variable star, which is by far the brightest of the comparison stars in the field. To check whether our assumption of constancy is valid, we also compared the differential brightness against four other fainter stars singly. All yield the same long-term trends, suggesting that VSST 14 is not nearly as variable as S CrA and the assumption of constancy is warranted.

We then use the mean long-term magnitude of S CrA ($I=9.81$) from the Van Vleck Observatory T Tauri database⁵ to establish the mean I -band magnitude. We assume that the mean differential magnitude in our photometric monitoring program corresponds to the mean long-term magnitude. We determine this offset and apply it to all the differential measurements. Finally, we divide the light from S CrA between the two components based on the Gaussian fits.

3.3 Single-wavelength variability

After a discussion of the results by wavelength, we discuss multi-wavelength aspects for individual sources in section 3.4.

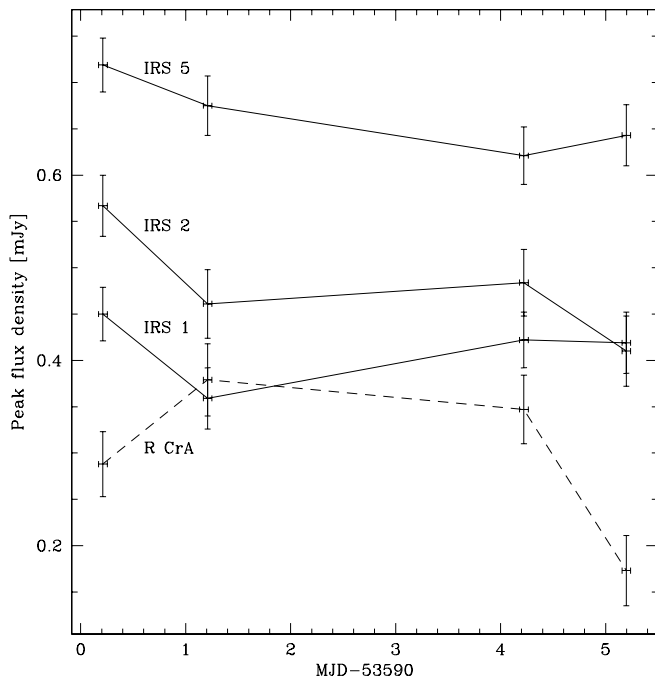
3.3.1 Radio data

The radio data show the same sources as in previous observations (Fig. 2 in Forbrich et al. 2006, Fig. 2.1 in the previous chapter), although the D array configuration of the VLA used this time results in lower angular resolution which is problematic only for IRS 7 and its immediate vicinity. The combined 2005 data is less sensitive than the combined 1998 data. No clear variability beyond an estimated uncertainty of $\sim 15\%$ in the absolute flux density scale is seen within these four epochs of observing which is why we only quote flux levels determined from the combined dataset in Table 3.2 while showing exemplary radio flux density curves for the three class I protostars as well as R CrA in Fig. 3.4. Also on timescales shorter than the duration of each epoch (2h), no variability was found. For comparison, the minimum and maximum flux densities from the 1998 monitoring are shown as well in Table 3.2. The most striking differences are IRS 5 – the above-mentioned only known class I protostar with circularly polarized nonthermal

⁵<http://www.astro.wesleyan.edu/~bill/research/ttauri.html>

Table 3.3: X-ray count rates for the five *Chandra* observations, 0.5-10 keV, corrected for effective exposure

Source ID	S1	S2	S3	S4	S5
	1/ksec	1/ksec	1/ksec	1/ksec	1/ksec
IRS 2	20.4	27.2	47.2	31.3	36.6
IRS 5N	0.1	1.0	0.8	0.8	0.0
IRS 5	16.1	27.0	49.0	17.1	11.7
IRS 6	1.3	2.4	2.2	2.7	2.0
IRS 1	25.3	14.5	14.5	18.3	26.7
IRS 9	0.5	2.5	0.7	2.3	0.9
R CrA	4.7	6.4	5.3	23.7	15.2
IRS 7W	1.0	6.1	5.1	1.6	1.9
IRS 7E	0.7	0.7	0.4	1.3	1.5

**Figure 3.4:** Exemplary VLA radio flux density curves for the three class I protostars IRS 1, 2, and 5, as well as for R CrA. Flux densities were derived by fitting Gaussians with the AIPS task SAD. The error bars mainly take into account actual noise (1σ) rather than the quality of the fit.

centimetric radio emission – showing a lower flux than before throughout this observation and R CrA with a higher radio flux. The flux of IRS 5 is in fact so low that we cannot detect Stokes- V emission which presumably is below the detection threshold, which would indeed be the case if the polarization degree was comparable to the values measured in 1998. The only X-ray flare of IRS 5 during this observing run took place during VLA maintenance time so that it could not be monitored simultaneously at radio wavelengths. R CrA was marginally detected in most of the previous data, now it is brighter and clearly detected. IRS 2 appears brighter than in the 1998 data, similar to levels reported before (Feigelson et al. 1998). When comparing the radio variability, it is important to note the different timescales probed in our 1998 and 2005 monitoring campaigns. While in 1998, observations span nearly four months, in 2005 only five days are covered. Our results suggest generally lower levels of variability on these shorter timescales.

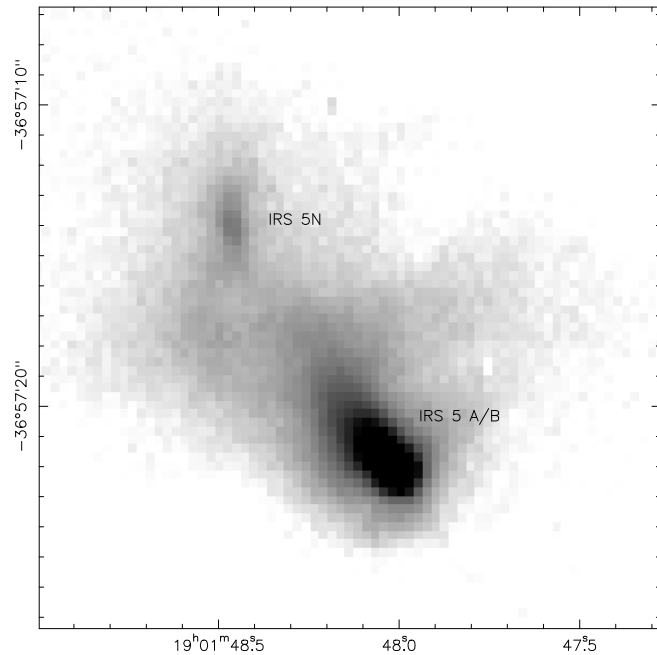


Figure 3.5: The double source IRS 5 (marginally resolved here) and its neighbouring source IRS 5N seen in K_S (SofI/NTT) on August 9, 2005.

3.3.2 X-ray data

Focusing on multi-wavelength variability here, a detailed X-ray census of the Corona Australis region is beyond the scope of this chapter and will appear in a separate paper (Forbrich & Preibisch 2007, see Chapter 4). Compared to the previous data presented by Forbrich et al. (2006)/Chapter 2, several new X-ray sources have been detected in the region of the *Coronet* cluster (Fig. 2 in Forbrich et al. 2006 vs. Fig. 3.3). With the exception of the source north-east of IRS 5 (IRS 5N, detected only in S2), none of these sources is detected simultaneously at radio, near-infrared or optical wavelengths. IRS 5N was detected as a weak radio source by Forbrich et al. (2006)/Chapter 2 and is also seen in the near infrared (Fig. 3.5).

Averaged count rates per observing epoch for the main *Coronet* sources also discussed by Forbrich et al. (2006)/Chapter 2 are summarized in Table 3.3. The count rates are similar to those previous *Chandra* count rates. The most variable sources by factors of about five are IRS 5, R CrA, and IRS 7W. IRS 5 appears to be in a decaying flare state in epoch S3. R CrA shows increased levels of X-ray emission in the last two epochs S4 and S5. No strong flare towards IRS 7E occurred during this observing run, but the source is detected on a low and slightly variable flux level (but cf. Hamaguchi et al. 2005a and Chapter 2). The class I source IRS 9 shows an X-ray flare in the second observing epoch S2. Both IRS 7E and IRS 9 are too weak for the analysis of meaningful light curves so that we only give the averaged count rates. Confirming the detection reported by Skinner et al. (2004), we also see T CrA in X-rays, south-east of IRS 7. We note that the spectral properties of the sources are similar to those reported by Forbrich et al. (2006)/Chapter 2.

There are a few interesting sources outside the VLA primary beam which merit attention in this context because they are variable and were observed in at least two wavelength regimes simultaneously: S CrA shows variability in the first half of the observations and 2MASS J19012872-3659317 shows a flare in the last *Chandra* observing epoch S5. The X-ray light curves are plotted in Figs. 3.7 and 3.8.

3.3.3 Near-infrared and optical data

In a first step, near-infrared and optical data were searched for counterparts of X-ray sources, then singling out those sources that were variable by more than 0.1 mag in the respective band.

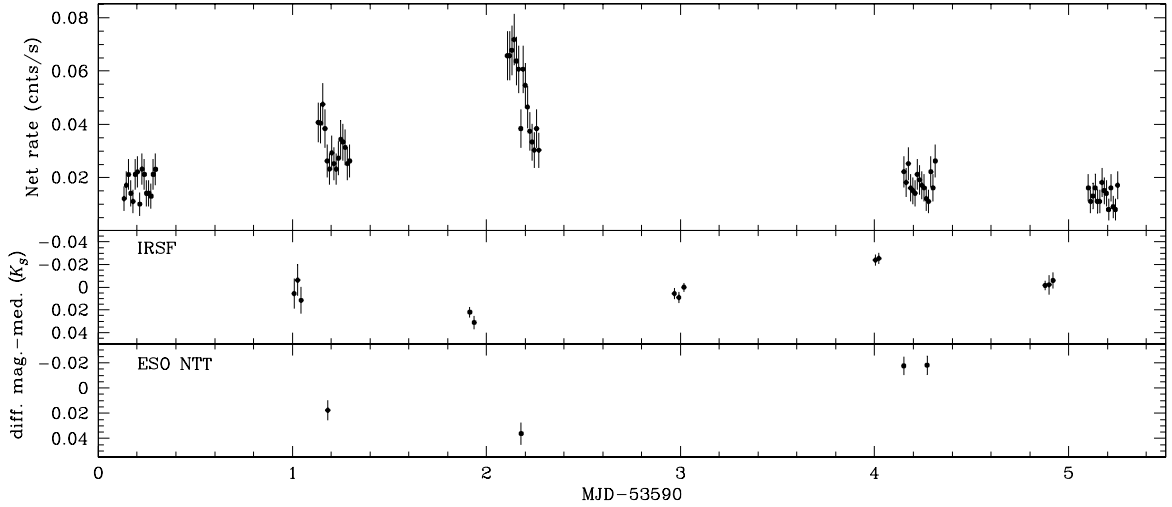


Figure 3.6: Top panel: *Chandra* X-ray light curves of IRS 5 for the five observations S1-S5, bin size is 1 ksec. Center and bottom panel: K_S -band differential photometry of IRS 5 taken with SIRIUS and SofI, respectively. If anything, the K_S -band flux appears to slightly *decrease* around the enhanced X-ray activity of IRS 5. Error bars are 1σ .

The discussion focuses on these variable sources. We note, however, that while a full discussion of all sources is beyond the scope of this paper, not all X-ray sources in this region have NIR or optical counterparts and vice versa. In general, only slow variability is seen at these wavelengths, with the notable exception of TY CrA which is showing an eclipse minimum.

Again, many sources are not covered by the VLA primary beam, but there is a good near-infrared/optical to X-ray correspondence in source coverage. Fifteen near-infrared counterparts of X-ray sources spread over the four different pointings of the SIRIUS imager were analyzed for variability in the J band, sparing seven sources which were too bright in the J band for analysis in the I band (see below, a few of them were in fact also too bright in the I band). Two class I protostars, namely IRS 5 and IRS 9, as well as the embedded source north-east of IRS 5 (i.e. IRS 5N), are undetected in J band and thus had to be analyzed in K_S band.

Among the selected SIRIUS J -band sources, four show variability of > 0.1 mag (see Fig.3.7), namely the two class I protostars IRS 1 and IRS 2 as well as 2MASS J19013385-3657448, and 2MASS J19014041-3651422. It is remarkable that this selection includes the two identified class I protostars which are detected at all in the J band. In the K_S band, IRS 9, IRS 5N and IRS 5 (Fig. 3.6) vary by less than 0.1 mag, the former two brightening steadily.

Most of the saturated J -band counterparts of X-ray sources except for HD 176386 ($m_V = 7.30$) were detected also in I band and available for photometry. Several sources show variability of > 0.1 mag, namely the Herbig Ae stars R CrA, T CrA, and TY CrA, as well as the T Tauri star S CrA and the embedded sources ISO-CrA 137 and HBC 680, an M3 dwarf WTTS (Neuhäuser et al. 2000). The light curves are shown in Fig. 3.8 and in Fig. 3.11.

3.4 Multi-wavelength variability

3.4.1 The class I protostars IRS 2, 5, 1, and 9

Class I protostars were for the first time covered in simultaneous multi-wavelength observations in this experiment. As stated above, no significant radio variability was observed during the four

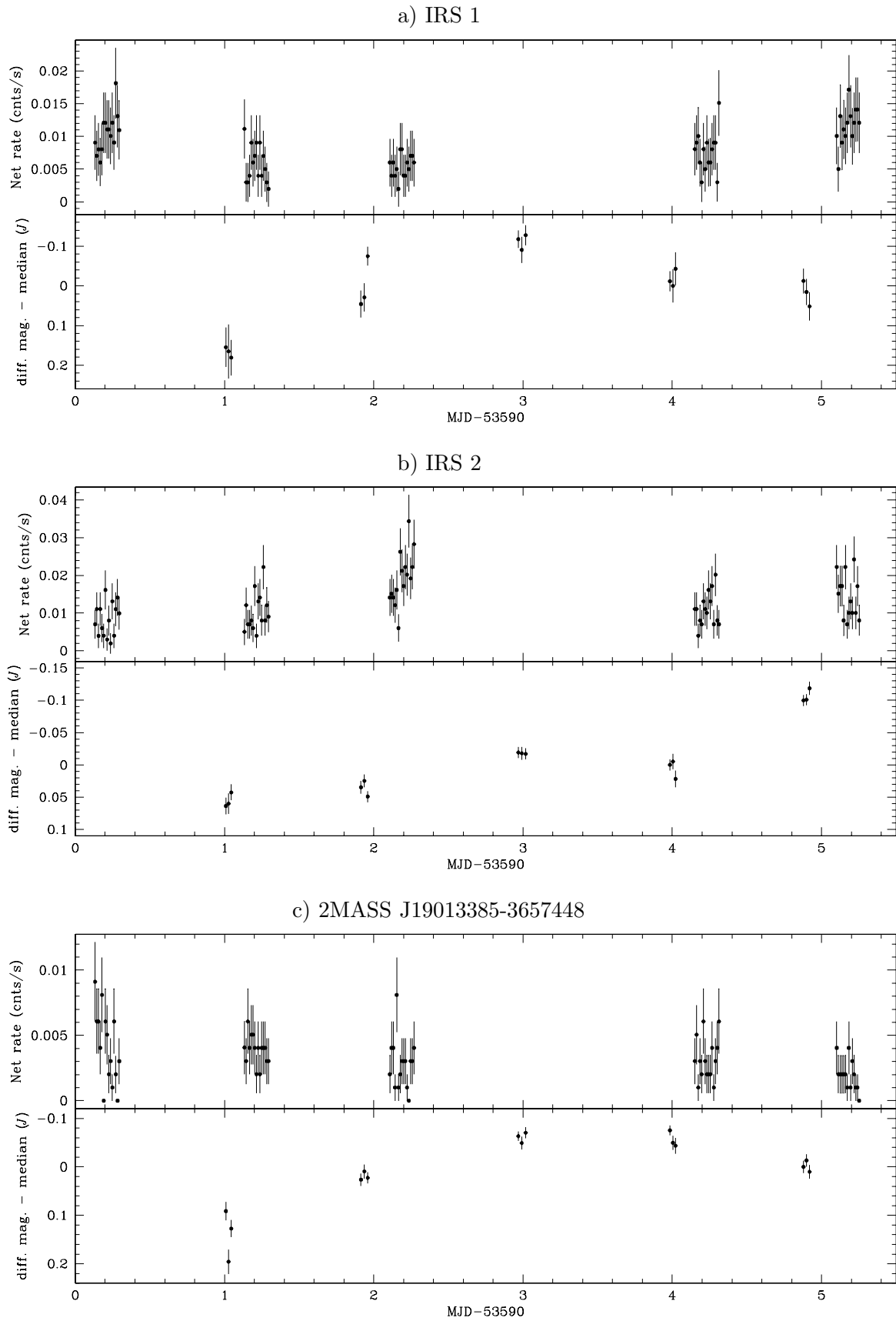


Figure 3.7: *Chandra* X-ray light curves for YSOs with near-simultaneous IRSF J -band data in the respective lower panels (with 1σ error bars).

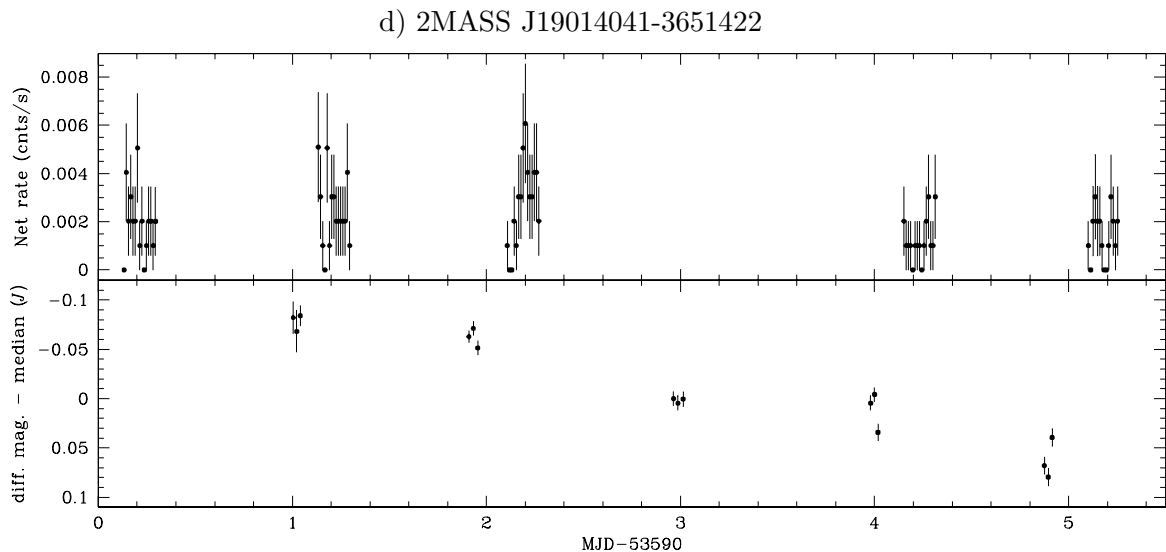


Fig. 3.7. Continued.

VLA observations. IRS 2 and IRS 1 show moderate X-ray variability (see Fig. 3.7), together with uncorrelated near-infrared variability, while IRS 5 is again the most variable class I protostar in X-rays with the enhanced activity in *Chandra* observation S3 not covered by simultaneous radio observations. The K_S -band flux of IRS 5 is slightly lower before and during the S3 observation (Fig. 3.6). The radio luminosity of IRS 5 is much lower during the observations reported here than before, in fact its Stokes- V emission is below the detection limit. IRS 5N, the weak X-ray source north-east of IRS 5 (Fig. 3.5) is detected in X-rays only in epoch S2. The source was simultaneously observed in the near-infrared with SofI/NTT, however no significant variability could be found compared to the SofI/NTT exposures taken later on except for a slight steady brightening by < 0.1 mag throughout the SIRIUS K_S -band observations. While the class I source IRS 9 shows an X-ray flare in the S2 *Chandra* observation, it remains undetected in the VLA observations as before. No significant near-infrared variability besides a slight steady brightening by < 0.1 mag is seen in the SIRIUS K_S -band data (the X-ray flare was not covered simultaneously at NIR wavelengths).

3.4.2 The Herbig Ae/Be stars R CrA, T CrA, and TY CrA

The three Herbig stars R CrA (type Ae), T CrA (type F0e), and TY CrA (type R8e) are among the most variable I -band sources in this dataset. R CrA which appeared to be in different X-ray activity stages in the data presented by Forbrich et al. (2006)/Chapter 2 is flaring continuously and is particularly active in the last two *Chandra* (S4-5) observations (Fig. 3.8). The X-ray emission of R CrA is again associated with an extremely high plasma temperature. Simultaneously, R CrA is quite continuously brightening by approximately 0.6 mag (I band) throughout the observation campaign. Optical data, however, are compromised by bad weather directly after the S4 *Chandra* observation. Still it seems that the brightening stops after the onset of enhanced X-ray activity, if only to resume later. The same brightening is observed in the U band (not shown). Given the earlier discussion on the origin of the X-ray emission towards R CrA (Forbrich et al. 2006, see Chapter 2), it is quite likely that two different objects are in fact observed here in optical and X-ray emission.

T CrA is quite variable at optical wavelengths (Fig. 3.11), however only barely detected as an X-ray source.

The multiple Herbig Be system TY CrA shows several eclipse minima during the observing run. While no minimum has been observed in different bands simultaneously, two primary

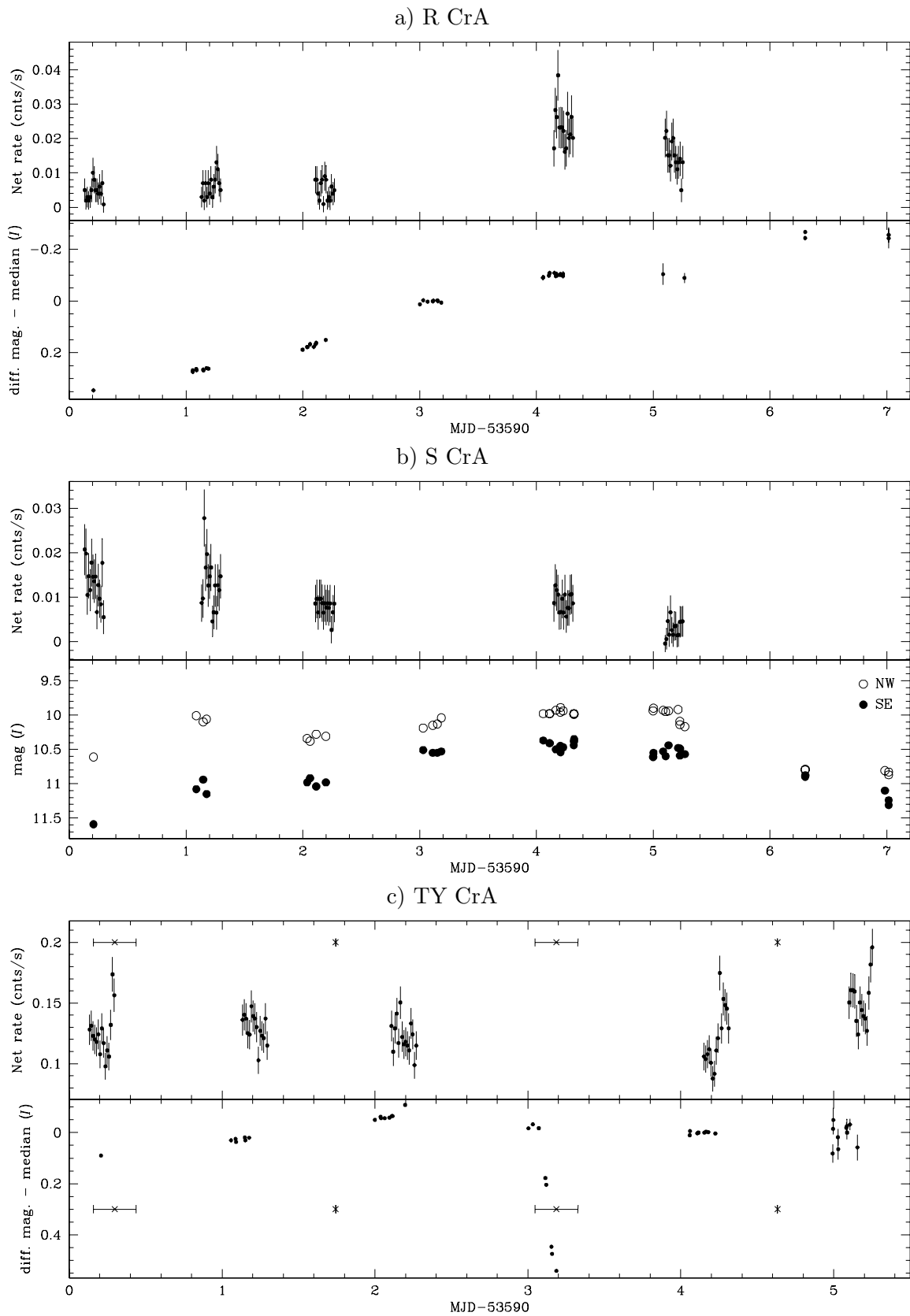


Figure 3.8: *Chandra* X-ray light curves for YSOs with simultaneous CTIO *I*-band data in the respective lower panels (with 1σ error bars). The *I*-band light curve for S CrA results from a special analysis involving Gaussian fitting to its two components NW and SE (see Fig. 3.9 and text). For TY CrA, the primary minima are marked as crosses with their durations indicated (orbital phase $-0.05..+0.05$), and the secondary minima are marked as asterisks (calculated according to Casey et al. 1998)

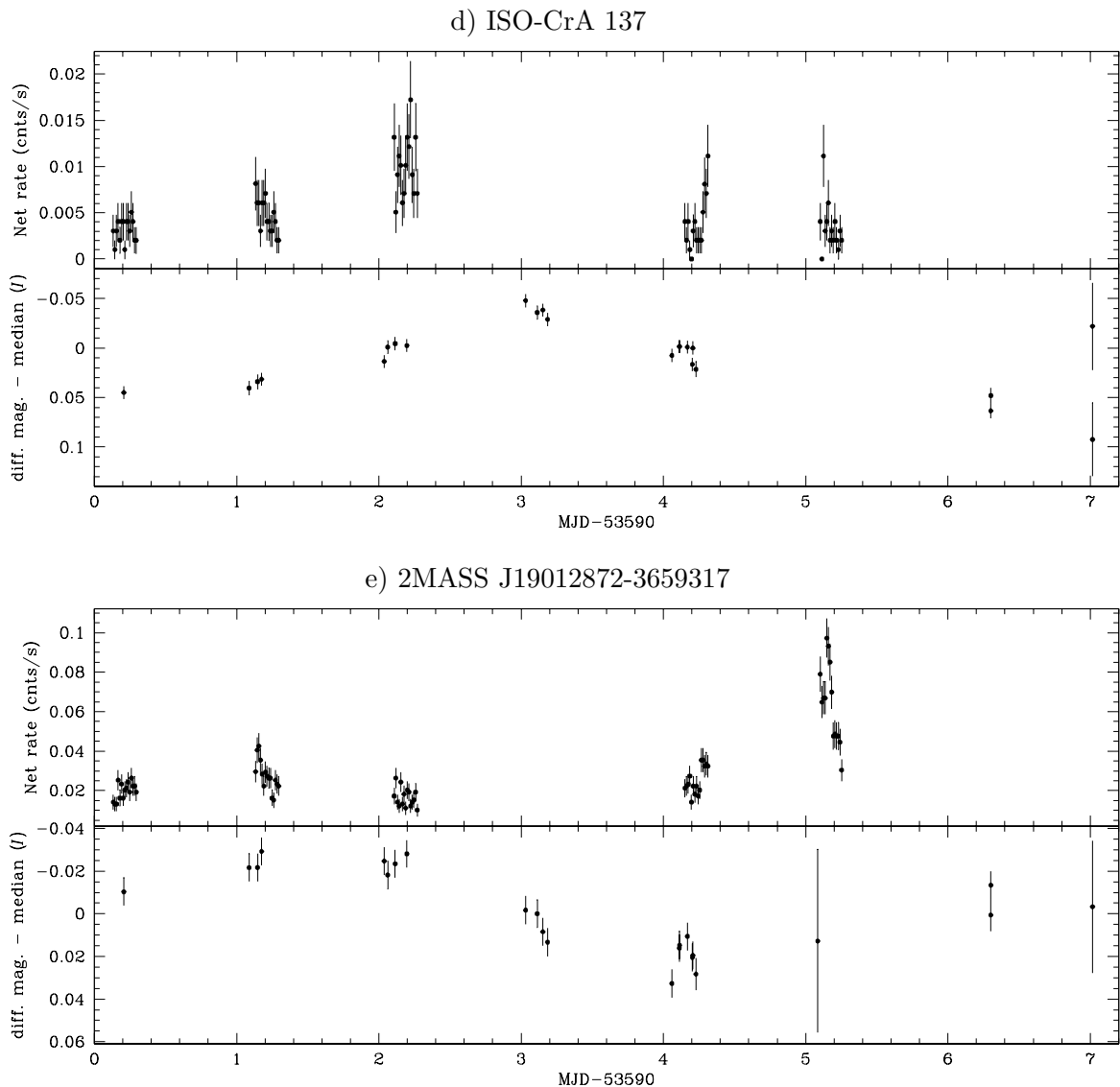


Fig. 3.8. Continued.

minima were observed in single bands, one at optical wavelengths and one in X-rays. It is interesting to note that the X-ray flux slightly *rises* during the descent to the calculated optical minimum in the first X-ray observation S1, an effect which was noted already by Hamaguchi et al. (2004) but which remains unexplained. However, as can be seen when looking at the remaining X-ray light curve, fluctuations like the one observed during primary eclipse also occur without eclipses.

3.4.3 The classical T Tauri stars S CrA and IRS 6

S CrA is a $1''3$ visual pair, varying by up to two magnitudes and showing variable inverse P Cygni profiles in the upper Balmer lines, indicative of mass accretion. Prato & Simon (1997) found that both components can be identified as T Tauri stars. The source remains unresolved in our X-ray data due to its off-axis location. Our X-ray light curve shows a quite slowly varying count rate with an apparently uncorrelated *I*-band light curve (see Fig. 3.8). The shape of the optical light curve is, however, quite complex even though not unusual.

The *I*-band light curves of the two components NW and SE are shown in comparison to the X-ray data Fig. 3.8 while Fig. 3.9 contains the full light curve discussed here (including

Table 3.4: X-ray count rates for discussed sources outside the VLA primary beam, from the five *Chandra* observations, 0.5-10 keV, corrected for effective exposure

Source ID	S1	S2	S3	S4	S5
	1/ksec	1/ksec	1/ksec	1/ksec	1/ksec
2MASS J19012872-3659317	21.3	28.5	17.5	26.5	67.4
2MASS J19012901-3701484 = ISO-CrA 137	3.8	6.2	11.8	4.8	4.1
2MASS J19013385-3657448	3.3	3.0	2.5	2.7	1.8
2MASS J19014041-3651422	4.0	4.7	5.2	2.5	2.9

the additional ANDICAM data) together with the magnitude difference of the two components. Both components of the binary are increasing in brightness throughout the time of the X-ray observations, before drastically fading. At peak the system is about 0.3 mag brighter than the historical mean, and within 0.1 mag of the maximum brightness we have observed. There is a 0.5 mag brightening in the NW component with a duration < 2 days, on the second day. The NW component is consistently brighter than the more volatile SE component. Historically (that is, in our database), the NW component is brighter than the SE component at I $89 \pm 2\%$ of the time, with a median brightness difference of 0.45 mag. We observed a median brightness difference of 0.48 mag. The rate of change of the stars is also well within the norms. The only oddity is the slow apparently coherent variations in the two stars. We would be concerned if the stars varied exactly in phase, but Fig. 3.9 shows that throughout this time the SE component is brightening relative to the NW component. Still, the concordance of the component light curves is unusual. The light travel time between the components, at a projected separation of 170 AU, is about one day. This makes it difficult to explain the rapid fading in terms of, say, a dust event in the system.

Even in this more detailed photometric analysis of the two components of S CrA, we find no apparent correlation between the X-ray light curve and the optical light curve. While the brightest X-ray points correspond closely to the 0.5 mag flare in the NW component, there does not seem to be a direct connection (see Fig. 3.10).

The T Tauri star IRS 6 is detected in centimetric radio emission, at a similar level as before (Forbrich et al. 2006, see Chapter 2). Low-level X-ray variability is met by insignificant changes in the near-infrared emission during the observation run.

3.4.4 Additional sources

Four more sources merit attention in this context because of peculiar X-ray or optical/NIR variability. 2MASS J19013385-3657448 is observed at low and barely changing X-ray count rates, however shows a maximum *J*-band magnitude approximately in the middle of the observations. 2MASS J19014041-3651422 drops continuously in *J*-band brightness, however shows fairly constant X-ray count rates. More variable X-ray emission with enhanced activity in epoch S3 is observed towards 2MASS J19012901-3701484 = ISO-CrA 137, a source showing a well-defined *I*-band emission maximum in-between *Chandra* observations S2 and S3. While towards 2MASS J19012872-3659317 the most pronounced X-ray variability within the data discussed here is observed, *I*-band light curve structure can be seen only below changes of 0.1 mag. Only one *I*-band measurement was taken during the enhanced X-ray activity, and this data point has a large error. The flare in epoch S5 is not covered in *U* band due to bad weather. The M dwarf HBC 680 is observed as a quickly variable *I*-band source (Fig. 3.11), however no X-ray emission was recorded (after previous detection – however, in the observation reported here, HBC 680 is very close to the limit of the field-of-view). The averaged X-ray count rates for these sources are listed in Table 3.4.

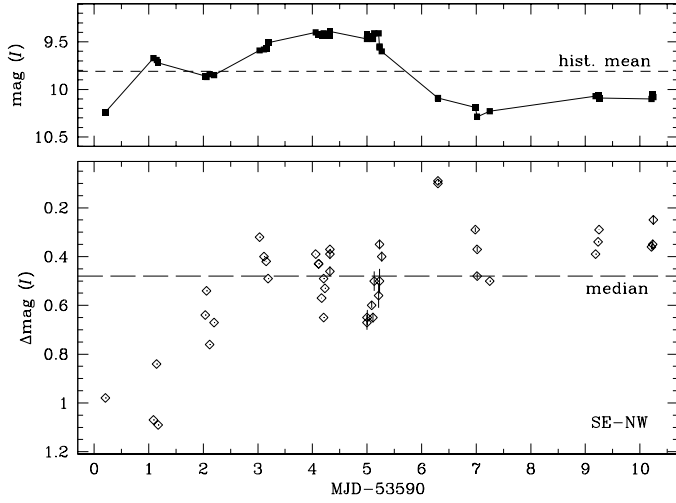


Figure 3.9: Upper panel: The total I -band magnitude of S CrA, determined as described in the text. The dashed horizontal line is the historical mean in the Van Vleck Observatory data base, used as the zero point here. Lower panel: The magnitude difference between the two components of S CrA. The dashed horizontal line is the median difference.

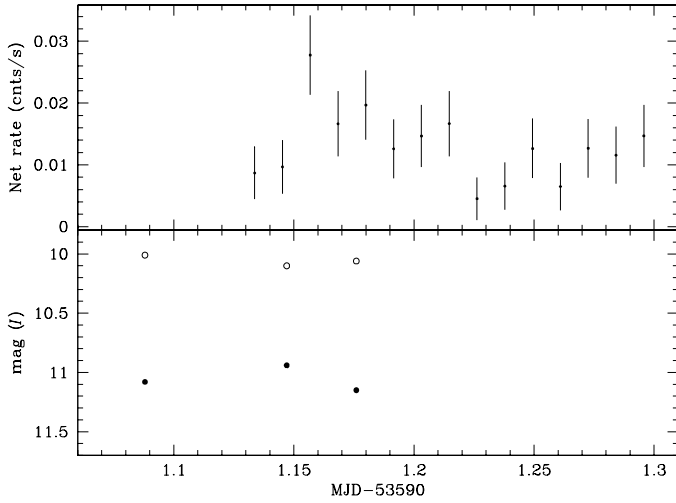


Figure 3.10: Detail of the X-ray and I -band light curves of S CrA, as shown in Fig. 3.8. The optical flare seen in the NW component in does not appear to directly correspond to the maximum in the X-ray light curve.

3.5 Conclusions

YSOs in and around the *Coronet* cluster in Corona Australis, including class I protostars, were observed simultaneously in multi-epoch X-ray, radio, near-infrared and optical observations. The main conclusions are as follows:

- The sources in the *Coronet* cluster are variable in X-rays and near-infrared/optical emission, however only barely significant variability at radio wavelengths could be detected even though the measured flux densities differ from previously measured values, indicating long-term variability.
- No clear multi-wavelength correlations in variability were found. The near-infrared variability of the class I protostars observed here appears to be uncorrelated to their X-ray variability (with the exception of a slight – possibly insignificant – drop in K_S band flux during enhanced X-ray activity of IRS 5). This is what would be expected in case of coronal X-ray emission – as opposed to X-rays due to accretion – which is also indicated by the very high plasma temperatures involved.
- Towards the Herbig Ae star R CrA, an apparent jump in X-ray emission is observed during continuous brightening in the optical regime. While the CTTS S CrA shows a complex

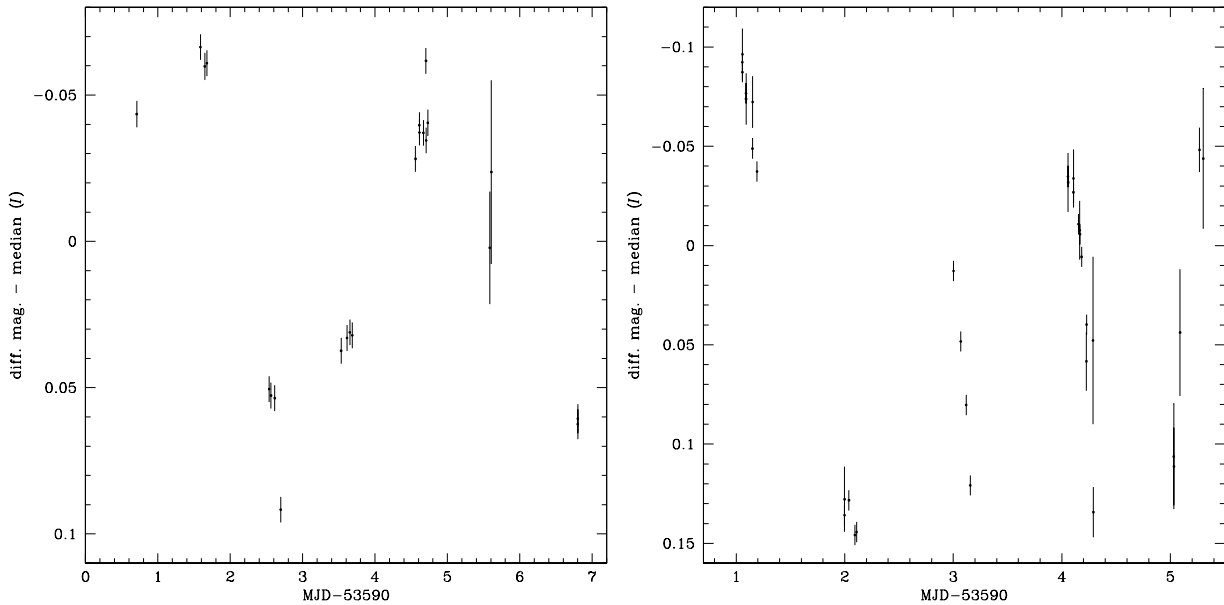


Figure 3.11: CTIO-*I* light curves for T CrA (left) and HBC 680 (right). While the former source is barely detected in X-rays, the latter remains undetected. Error bars are 1σ .

optical light curve, its X-ray emission is much less variable. Its two components were found to nearly vary synchronously in the *I* band.

- The radio behaviour of the polarized radio continuum source IRS 5, a class I protostar, could not be studied due to the low flux density of the source. The source shows, however, enhanced X-ray activity in one observation.
- Among the four sources with X-ray counterparts and an near-infrared (*J*) variability exceeding 0.1 mag, there are two class I protostars, a disproportionate share in spite of the low numbers. In case of the *I* band variability, six sources with variability exceeding 0.1 mag include three Herbig Ae/Be stars, one CTTS, as well as two additional embedded sources.

Chapter 4

Coronae in the Coronet: A very deep X-ray look into a stellar nursery

(based on Forbrich & Preibisch, A&A 2006, submitted)

4.1 Introduction

To study the X-ray properties of YSOs, we analyze an exceptionally sensitive *Chandra* dataset of the *Coronet* cluster in the CrA star-forming region, achieving a limiting luminosity of $L_{X,\min} \sim 5 \times 10^{26}$ erg/sec for lightly absorbed sources. This dataset represents one of the most sensitive X-ray observations ever obtained of a star-forming region. It consists of the data discussed in Chapter 3 as well as additional archival data and is presented in Section 4.2. The X-ray data are used to investigate the membership status of tentative members of the star-forming region (Section 4.3) and to derive plasma temperatures and X-ray luminosities of the YSOs, as well as to investigate their variability on the timescale of several years (Section 4.4). In the surroundings of R CrA, diffuse X-ray emission was detected which is discussed in Section 4.5. Finally, an X-ray census of the CrA star-forming region is presented in Section 4.6 before conclusions are summarized in Section 4.7.

4.2 Chandra observations and data analysis

We have performed a series of five individual ~ 15 ksec observations (separated by about one day) of the *Coronet* cluster and its surroundings with the ACIS camera on-board *Chandra* (Weisskopf et al. 2002; Garmire et al. 2003). The main aim of these observations was to monitor the X-ray emission of the YSOs simultaneously with optical, infrared, and radio observations, and the results of this multi-wavelength monitoring are described in Forbrich et al. (2007)/Chapter 3. On the other hand, this set of observations also provides rather deep X-ray data of the region. In order to optimize the sensitivity of the data, we included into our analysis three previous *Chandra* observations retrieved from the public archive, which have exposure times between 20 and 40 ksec. Details of the individual observations are listed in Table 4.1.

Our data analysis was performed with the Chandra Interactive Analysis of Observations (CIAO) software package version 3.3, combined with CALDB 3.2.1. Merging all eight individual observations results in a very deep dataset with a total exposure time of 156,470 sec. In our analysis we consider only results arising from the imaging array (ACIS-I) of four abutted 1024×1024 pixel front-side illuminated charge-coupled devices (CCDs) providing a field of view of about $17' \times 17'$ on the sky. As the aimpoints and the orientation of the camera on the sky (the “roll angle”) differed for the individual observations, the merged image covers a slightly larger area. Exposure maps and aspect histograms were computed for the single datasets as well as

Table 4.1: *Chandra* observations of the CrA star-forming region used in this study.

Obs	Expo. [ksec]	Aimpoint [J2000]			Start Date	
19	19.96	19 01 50.6	-36 57 30	2000-10-07	17:00:55	
3499	38.13	19 01 50.6	-36 57 30	2003-06-26	12:57:06	
4475	20.17	19 01 48.9	-36 59 23	2004-06-17	23:15:56	
5402	15.39	19 01 45.0	-36 58 09	2005-08-08	02:36:49	
5403	15.15	19 01 45.0	-36 58 09	2005-08-09	02:37:49	
5404	15.17	19 01 45.0	-36 58 09	2005-08-10	01:57:21	
5405	15.17	19 01 45.0	-36 58 09	2005-08-12	03:11:53	
5406	14.76	19 01 45.0	-36 58 09	2005-08-13	01:50:17	

for the merged dataset, allowing to determine the effective exposure time at each sky position, taking into account the spatial variation of the detector quantum efficiency, non-uniformities across the face of a detector, mirror vignetting, and bad pixels.

The detection limit of the *Chandra* data was determined in the following way: using the PIMMS¹ software developed by the NASA High Energy Astrophysics Science Archive Science Center and assuming an intrinsic source spectrum of a 10 MK thermal plasma with a metal abundance of 0.4 times solar, as typical for young stellar X-ray sources (e.g., Getman et al. 2005b), we find that one detected count in 156.47 ksec corresponds to an X-ray flux of 4.2×10^{-17} ergs/cm²/s in the 0.2–8 keV energy range. A five count source detection thus corresponds to an X-ray luminosity of $L_{X,\min} \sim 4.3 \times 10^{26}$ erg/s at the assumed distance of 130 pc and for no intervening extinction. Our dataset thus represents one of the most sensitive X-ray observations of a star-forming region ever obtained; it is about four times more sensitive than the data of the *Chandra* Orion Ultradeep Project (Getman et al. 2005b), which provided a detection limit of $L_{X,\min} \sim 2 \times 10^{27}$ erg/sec for lightly absorbed sources (Preibisch et al. 2005a). Many of the YSOs in the CrA star-forming region suffer from substantial extinction, up to $A_V \sim 45$ mag. The intervening extinction raises the effective detection limit; for $A_V = [3, 10, 20, 45]$ mag the detection limits are $[1.4, 6.5, 19, 58] \times 10^{27}$ erg/s. Note that these values are valid for the central ($\sim 5'$ radius) area of the *Chandra* image; source detectability degrades with off-axis angle, and is $\sim 2 - 3$ times lower near the edges of the *Chandra* field of view (at offaxis angles $8' - 11'$).

For locating the X-ray sources in our image, we used the wavelet transform detection algorithm implemented as the *wavdetect* program within the CIAO data analysis system (Freeman et al. 2002). With a significance limit of 1.6×10^{-7} and wavelet scales between 1 and 16 pixels the program located 91 sources. A careful visual inspection of the image revealed 8 additional sources, which were included in the final list of 99 X-ray sources.

After reprocessing all observations with CIAO 3.3 yielded a homogeneous set of “level 2” event files (without pixel randomization), the *acis_extract* package², version 3.94, was used for a variety of analysis tasks: Based on our source list, spectral extraction regions were defined in a way to include a specified fraction of the point-spread function at the respective positions (90% at an energy of 1.5 keV), independently for each observation. Then, the detected sources were masked out for the definition of background regions. Subsequently, a composite source spectrum was constructed by summing the single-observation spectra, taking into account appropriately scaled background spectra for each observation. In the grouping of the resulting spectra, the bins lie within the same fixed energy range for all sources while the binning otherwise is determined from the specified minimum significance of the background-subtracted spectrum in each bin. This targeted significance is iteratively lowered until there is a specified minimum number of

¹PIMMS is the Portable, Interactive Multi-Mission Simulator provided by the HEASARC Online Service at <http://heasarc.gsfc.nasa.gov/Tools/w3pimms.html>

²see http://www.astro.psu.edu/xray/docs/TARA/ae_users_guide/

groups so that the resulting significance per bin may differ between sources. For the bright sources, the resulting significance per bin is 5σ . In this multi-observation dataset, composite response matrix files (RMFs) and ancillary response files (ARFs) were constructed using the FTOOLS *addrmf* and *addarf*, weighting the single-observation source-specific RMFs and ARFs by their respective exposure times. In order to improve flux estimates, the ARFs for every source are corrected for source counts outside the extraction regions: The PSF is calculated at all available energies (using the CIAO task *mkpsf*), the respective extraction region is applied, and the ARF is multiplied by the interpolated energy-dependent PSF fraction thus derived in order to correct for source counts outside the extraction region. The composite datasets and ARFs are subsequently used for broad-band photometry. Furthermore, *acis_extract* was used for Maximum Likelihood reconstructions of source neighbourhoods (using the routine *max_likelihood.pro* from the IDL Astronomy Library). Spectral fitting with Monte Carlo techniques was then performed with the CIAO tool *Sherpa* (see Sect. 4.4.1).

Basic results of this analysis, namely a source list with total counts, median energy, source significance, hardness ratios, as well as incident flux estimates are listed in Table 4.5.

For those (putative) members of the CrA star-forming region that remained undetected in the *Chandra* data, we determined upper limits to the count rates and X-ray luminosities in the following way. We counted the observed number of photons in source regions centered at their optical/infrared positions and compared them to the expected number of background photons determined from several large source-free background regions. We used the Bayesian statistics method described by Kraft et al. (1991) to determine the 90% confidence upper limits for their count rates. From these count rate upper limits we computed upper limits for the extinction corrected X-ray luminosities in the 0.2–8 keV band assuming thermal plasma-spectra with a temperature of 10 MK and computing the absorbing hydrogen column density from the visual extinction according to the empirical relation $N_{\text{H}} \sim A_V \cdot 2 \times 10^{21} \text{ cm}^{-2}$ (Feigelson et al. 2005).

4.3 X-ray sources and cluster members

4.3.1 Source identification

In order to identify the X-ray sources, we inspected the source positions on optical images from the Digitized Sky Survey, near-infrared images from 2MASS, and near- to mid-infrared images from the *Spitzer* observatory. The *Spitzer* IRAC observations of the CrA star-forming region were obtained for the program ‘‘Structure and Incidence of Young Embedded Clusters’’ (PI: G. Fazio); a set of reduced mosaic images and IRAC photometry was kindly provided to us by Lori Allen. The *Spitzer* data characterize the broad-band infrared spectral energy distribution between $3.6 \mu\text{m}$ and $8 \mu\text{m}$, and were used to determine infrared classes of the objects as described in (Megeath et al. 2004; for a description of the classes, see Section 1.1.1).

The superb PSF of *Chandra*/ACIS and the high accuracy of the aspect solution, resulting in a positional accuracy of typically better than $1''$, allowed a clear and unambiguous identification of 48 of the 99 X-ray sources with optical and/or infrared counterparts. Figure 4.1 shows the location of the X-ray sources marked on the $3.6 \mu\text{m}$ and the $4.5 \mu\text{m}$ *Spitzer* images. Further information about the counterparts was obtained from the SIMBAD database and the literature. The results of the source identification are listed in Table 4.2.

51 X-ray sources have either no counterparts in any of the optical/infrared images mentioned above, or only extremely faint counterparts in the *Spitzer* images. Given the detection limits of $K_{\text{lim}} \sim 15$ for the 2MASS image and our estimate of $L_{\text{lim}} \gtrsim 15$ for the *Spitzer* $3.6 \mu\text{m}$ image, it is very unlikely that these objects are related to the CrA star-forming region: According to the Siess et al. (2000) pre-main sequence models, a 5 Myr old $0.1 M_{\odot}$ star at a distance of 130 pc would have un-reddened magnitudes of $K = 9.5$ and $L = 9.2$. An extinction of $A_V \sim 50$ mag would thus be required to prevent detection in the 2MASS K -band image, and an even higher

Table 4.2: Identification of *Chandra* X-ray sources with optical or infrared counterparts in the CrA star-forming region. Columns 2-4 provide information on counterparts to the X-ray sources in the optical DSS images, the 2MASS images, and the *Spitzer* images: “y”: counterpart, “n”: no counterpart, “f”: very faint, possible counterpart

Source CXO J	Counterpart DSS	2MASS	<i>Spitzer</i>	SED class	Name	SpT
190104.58–370129.6	f	y	y	III	CrA 453	M4
190108.60–365721.3	y	y	y	II	S CrA	G5e
190115.86–370344.3	n	n	y			
190116.26–365628.4	y	y	y	II	V667 CrA	M5
190118.90–365828.4	n	y	y	II	CrA 466	M4.5
190119.39–370142.0	n	n	y			
190120.86–370302.9	y	y	y	III	CrA 4111	M5
190122.40–370055.4	n	n	f			
190123.49–365641.3	n	y	y	III		
190125.61–370453.9	f	y	y	III	ISO-CrA 133	
190125.75–365919.3	f	y	y	II	ISO-CrA 134	
190127.15–365908.6	y	y	y	III	ISO-CrA 135	
190128.72–365931.9	y	y	y		ISO-CrA 136	
190129.01–370148.8	y	y	y	III	ISO-CrA 137	
190132.34–365803.1	n	y	y	II	TS 2.9 = ISO-CrA 139	
190133.84–365745.0	n	y	y	II	TS 2.8 = IRS 13	
190134.84–370056.7	y	y	y	III	V709 CrA	K1 IV
190139.15–365329.6	y	y	y		HD 176386-B	
190139.34–370207.8	y	y	y	III		
190140.40–365142.4	n	y	y	II		
190140.81–365234.0	y	y	y		TY CrA a/b/c/d	B8e/K2/F-K/M
190141.55–365831.6	n	y	y	I	IRS 2	K2
190141.62–365953.1	y	y	y	II	HBC 677	
190143.12–365020.9	n	n	y			
190148.02–365722.4*	n	y	y	I	IRS 5 a / b	K6 V / ?
190148.46–365714.5	n	n	y	I		
190149.35–370028.6	y	y	y	III	LS-RCrA 2	M6 (BD cand.)
190150.45–365638.1	n	y	y	II	IRS 6A	M2
190150.66–365809.9	n	y	y	I	V710 CrA = IRS 1 = HH 100 IR	K5-M0
190151.11–365412.5	n	y	y	II	IRS 8	
190152.63–365700.2	n	y	y	I	IRS 9	
190153.67–365708.3	y	y	y		R CrA	A5 IIe var
190155.31–365722.0	n	f	y	I	IRS 7W	
190155.61–365651.1	n	n	y	I		
190155.76–365727.7	n	n	y	I/II		
190155.85–365204.3	n	n	y			
190156.39–365728.4	n	n	y	0/I	IRS 7E	
190157.46–370311.9	n	y	y			
190158.32–370027.5	n	f	y	III		
190158.79–365750.1	y	y	y	II	T CrA	F0e
190200.11–370222.3	y	y	y	III	2MASS J19020012-3702220	M4
190201.92–370743.0	y	y	y	III	V702 CrA	G5
190201.94–365400.1	n	n	y		B185839.6-365823	BD cand.
190211.99–370309.4	f	y	y	II	ISO-CrA 143	BD cand.
190214.60–370032.0	n	y	y		ISO-CrA 145	
190222.13–365541.0	y	y	y	III	HBC 679	K2 IV
190227.05–365813.2	y	y	y	II	HBC 680	M
190233.07–365821.1	y	y	y	II	ISO-CrA 159	

* The X-ray emission of the 0'6 binary IRS 5a/b (Chen & Graham 1993; Nisini et al. 2005) is marginally resolved in the *Chandra* image (see Fig. 4.5).

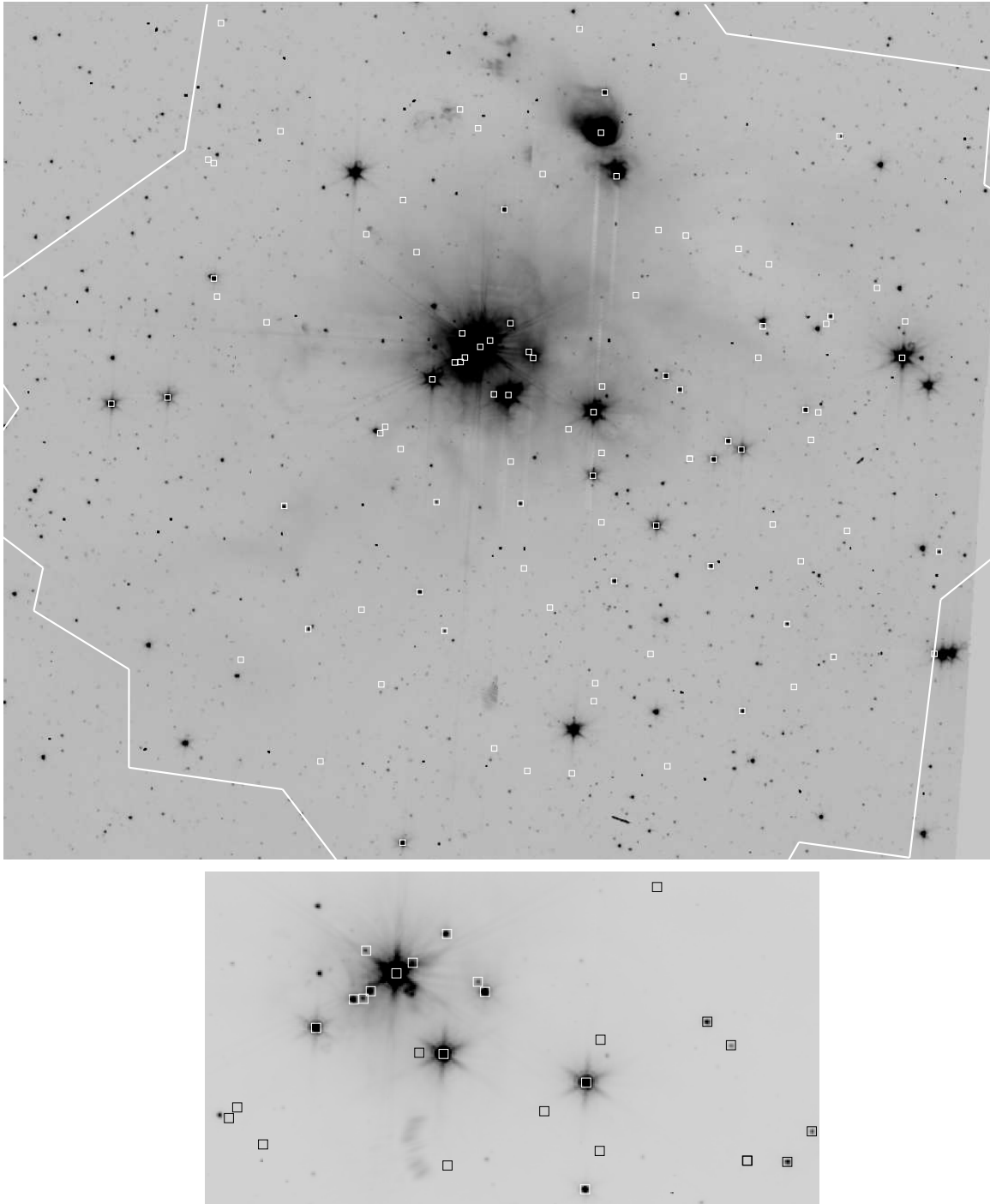


Figure 4.1: Above: 21.8×18.4 detail of the *Spitzer* IRAC $3.6 \mu\text{m}$ image of the *Coronet* region. The white line marks the boundaries of the field of view of the merged *Chandra* data. The positions of the *Chandra* X-ray sources are marked by the boxes. Below: The central 7.8×3.2 region of the *Spitzer* IRAC $4.5 \mu\text{m}$ image with X-ray source positions marked by boxes.

value of $A_V \sim 100$ mag to prevent detection in the *Spitzer* $3.6 \mu\text{m}$ image. We also note that the number of X-ray sources without counterparts is in good agreement with the expected number of (mostly extragalactic) background X-ray sources that has been derived from the deep X-ray source counts and other deep X-ray observations of star-forming regions. Furthermore, the

background nature of these sources is also supported by their uniform spatial distribution within the field of view.

We also searched for, but could not find any X-ray emission associated with the protostellar cores in the CrA star-forming region as listed by Nutter et al. (2005), unless these contain infrared objects. Finally, we also searched for X-ray sources at the positions of 43 Herbig-Haro objects in the CrA star-forming region as listed in Wang et al. (2004). From none of these objects X-ray emission is detected³.

Since the first detection of X-ray emission from HH 2 (Pravdo et al. 2001), it is clear that the shock-heated material in *some* jets can actually produce observable soft X-ray emission (e.g. Pravdo et al. 2004; Grosso et al. 2006; Favata et al. 2006). However, the vast majority of all HH objects remained undetected in X-ray observations. It is not clear whether this is due to the limited sensitivity of existing X-ray observations, or whether X-ray emission is created only in a small fraction (the fastest?) of all jets.

4.3.2 X-ray emission and membership in the star-forming region

The observed X-ray properties can provide crucial information for a clarification of the membership status of presumed members discussed in the literature. We can confidently expect to detect X-ray emission from (almost) any stellar member of the region, given the following considerations: The COUP data showed that *all* young late-type stars in the ONC show strongly elevated X-ray emission as compared to the Sun and solar-like field stars (Preibisch et al. 2005a): at least 98% of all late type YSOs in the ONC have fractional X-ray luminosities of $\log(L_X/L_{\text{bol}}) > -5$, and there are strong indications that the 2% of the stars below this value are not cluster members but field stars (see discussion in Preibisch et al. 2005a). Assuming the same lower limit to the fractional X-ray luminosities to hold for the YSOs in the CrA star-forming region, we thus expect to detect X-ray emission from any of its stellar members, unless the extinction is too high. To put this statement in a more quantitative way, we conservatively assume that the YSOs have fractional X-ray luminosities of $\log(L_X/L_{\text{bol}}) = -5$, and ages of 5 Myr. For the case of no extinction, the X-ray detections should then be 100% complete down to stars of $\sim 0.08 M_\odot$ or spectral type $\sim M7$. For an extinction of $A_V = 5$ mag, the limit of complete detections is at $\sim 0.2 M_\odot$ or spectral type $\sim M5$, and for $A_V = 10$ mag at $\sim 0.5 M_\odot$ or spectral type $\sim M0$. Note that the *typical* X-ray emission level of young stars is $\log(L_X/L_{\text{bol}}) = -3.6$, i.e. a factor of 25 higher than our assumed lower limit, so we expect to detect also the majority of lower mass objects, unless their extinction is very high.

4.3.2.1 Optically visible member candidates

Neuhäuser et al. (2000) list 34 previously known or suspected members of the CrA star-forming region. Among the objects in the field of view of the *Chandra* data, only two remain undetected. 2MASS J19010586-3657570 (= ISO CrA 113, spectral type G0) shows no near-infrared excess and the *Spitzer* photometry is consistent with purely photospheric emission. Neuhäuser et al. (2000) reported that no signs of 6708 Å Lithium absorption are seen in its spectrum, suggesting that it is not a young star. The second case is 2MASS J19014791-3659302 (= TS 13.4), which also shows no infrared excess and has a class III *Spitzer* SED. Together with the non-detection

³We note that the *Chandra* source 190205.84-365444.2 has neither optical nor infrared counterparts, but is located near a bow shock seen in the *Spitzer* images. However, a relation between the X-ray emission and the bow shock seems very unlikely. First, the positional offset of $8''$ is clearly much larger than the astrometric accuracy, and the offset is *not* along the flow direction, i.e. cannot be explained by the non-simultaneous nature of the X-ray and infrared images. Second, the distribution of energies of the 20 detected source counts is quite hard (no photons with energy ≤ 1 keV, 4 photons in the 1 – 2 keV, and 17 photons in the 2 – 8 keV range), in strong contrast to the very soft X-ray emission expected from jet shocks and observed in some cases (e.g. Pravdo et al. 2004; Grosso et al. 2006). We therefore believe that the X-ray emission comes from a background object and is not related to the bow shock.

in the *Chandra* data, these points strongly suggest that these two stars are not members of the CrA star-forming region but unrelated field stars.

4.3.2.2 Mid-Infrared excess sources as seen with the Infrared Space Observatory (ISO)

The results of a ISOCAM survey of the CrA star-forming region were reported by Olofsson et al. (1999). They identified 21 infrared sources with mid-infrared excess, 10 of which are located within the field of view of the *Chandra* data. Nine of these 10 objects are detected as X-ray sources, only ISO CrA 140 remains undetected. The 2MASS colors of ISO CrA 140 show a near-infrared excess, but the *Spitzer* photometry suggest a class III SED, and we note that this object was not detected in the ISOCAM 14.3 μm band, raising doubts about the presence of excess emission. The near-infrared colors of this objects suggest an extinction on the order of $A_V \approx 10$ mag. Since ISO CrA 140 is a relatively faint infrared source, we suspect that its low intrinsic luminosity in combination with strong extinction may have prevented the X-ray detection. Alternatively, it may be an unrelated background AGB star rather than a young star in the CrA star-forming region.

4.3.2.3 Very low-mass stars

López Martí et al. (2005) identified 13 candidate very low-mass members of the CrA star-forming region by optical spectroscopy. Six of these are in the field of view of the *Chandra* image, and five of them, CrA 453, 466, 468, 4110, and 4111, all with estimated spectral types around M5, are detected as X-ray sources, consistent with the assumption that they are young members of the CrA star-forming region. The X-ray detection of all these very low-mass star reinforces our expectation that our X-ray data should be complete for all stellar members of the *Coronet* region, unless they are particularly strongly obscured.

The remaining object is CrA 465, a brown dwarf candidate with estimated spectral type M8.5. It was not detected as an X-ray source by the automatic source detection, but as will be discussed in Section 4.4.2.5, inspection of the location of this object in the *Chandra* image yields indications of a tentative detection of very weak X-ray emission.

4.3.2.4 IRS 3: a background giant rather than a YSO

The bright infrared source IRS 3 (2MASS J19020491-3658564, $J=12.51$, $H=10.52$, $K=9.54$) is usually considered to be a YSO associated with the CrA star-forming region. For example, it was one of the targets in the spectroscopic and photometric study of YSOs in the *Coronet* by Nisini et al. (2005), who derived the following parameters: spectral type K5–M0 III, $L_\star = 0.3 L_\odot$, $A_V = 10$ mag, $M \sim 0.5 M_\odot$, age ~ 3 Myr, no significant near-infrared excess, and no signs of accretion. IRS 3 remains undetected in the *Chandra* data. Only a single count is detected in a 3'' radius aperture centered on its infrared position. Accounting for the local background yields a 90% confidence count rate upper limit of < 0.0158 counts/ksec. For the extinction of $A_V = 10$ mag this corresponds to an upper limit of $L_X < 3.2 \times 10^{27}$ erg/sec and $\log(L_X/L_{\text{bol}}) < -5.6$. This value would be most unusually low if IRS 3 was a YSO: we note that in the COUP data more than 99.5% of all young late-type stars in the ONC have fractional X-ray luminosities above this level. This non-detection therefore suggests that IRS 3 is *not* a young star, and this argument is supported by several other pieces of evidence: First, IRS 3 shows no strong infrared excess; the *Spitzer* photometry yields a class III SED. Second, the age of ~ 3 Myr, derived under the assumption that the object is located in the CrA star-forming region, is considerably larger than the ages of all other *Coronet* objects observed by Nisini et al. (2005). Third, IRS 3 is the only one of the CrA objects with luminosity class III; all other have luminosity class V (as expected for young stars). Taken together, these considerations strongly suggest that IRS 3 is *not* a YSO in the *Coronet* cluster, but rather a background giant behind the dark cloud.

4.3.2.5 YSO candidates from Spitzer-IRAC photometry

Spitzer IRAC colors were used to classify the infrared sources as described in Megeath et al. (2004). While class I or class II objects are probably YSOs, the class III objects are a mixture of YSOs which have already dispersed their (inner) disks and unrelated field stars. We thus consider objects with class I or class II SEDs and no previous identification as new YSO candidates. As discussed in Megeath et al. (2004), several factors may lead to incorrect classifications. For example, some of the objects identified as class I may be in fact strongly reddened class II objects, and background objects such as planetary nebulae, AGB stars, and galaxies may be misidentified as class I or class II objects. The detection of X-ray emission at levels typical for YSOs allows a clear distinction between YSOs and background objects of the above-mentioned kind.

Class I objects: *Spitzer* photometry reveals three objects in the *Chandra* field of view with class I SEDs that were not identified as YSOs before. Two of them, 190148.46–365714.5 and 190155.61–365651.1 (both remained undetected in the 2MASS images), can be identified with X-ray sources. Their X-ray detections strongly support the YSO status of these objects. With 22 and 41 source counts, respectively, these X-ray sources are too faint for detailed spectral fitting, but the high median energies of their source photons of 4.1 keV and 4.5 keV are fully consistent with the hard spectra expected for embedded class I objects.

The third new object with *Spitzer* class I SED is the infrared source B185836.1-370131 discovered originally by Wilking et al. (1997). It is invisible in the 2MASS *J*- and *H*-band images but is seen as a very faint source in the 2MASS *K*-band image. This object coincides with sub-mm source SMM 2 from Nutter et al. (2005), but remains undetected in the *Chandra* data. If it is truly a protostellar member of the CrA star-forming region, its non-detection in the *Chandra* data could be related to very strong extinction, as suggested by the non-detection in the 2MASS images. Since we cannot estimate the extinction to this object, no upper limit to the X-ray luminosity can be determined. However, we can ask how much extinction would be required to keep it undetected in the *Chandra* data, if one assumes that it has an X-ray luminosity of $\sim 3 \times 10^{30}$ erg/sec (the mean value for the X-ray detected *Coronet* class I objects IRS 1, 5, and 2). Using PIMMS and assuming a plasma temperature of 30 MK, we find that a hydrogen column density of 2.2×10^{24} cm⁻², corresponding to an extinction of $A_V \sim 1100$ mag, would be required for this object to escape detection in the *Chandra* data. This extreme extinction may perhaps be caused by occultation of a massive circumstellar disk seen exactly edge-on, or B185836.1-370131 may be very deeply embedded in a dense circumstellar envelope, and thus is perhaps a class 0 object. An alternative possibility would be that it is a background AGB star (which would not be a strong X-ray emitter); in that case, however, its location just behind a sub-mm cloud core would be a quite curious coincidence.

Class II objects: Three objects with class II *Spitzer* SEDs remain undetected in the *Chandra* data: LS CrA I and B185831.1-370456, two brown dwarf candidates which will be discussed in Section 4.4.2.5, and 2MASS J19020682-3658411. The later object is a relatively faint infrared source and shows a near-infrared excess. It may be a very-low luminosity (and correspondingly very-low mass, perhaps sub-stellar) member of the CrA star-forming region suffering from particularly strong extinction, or an unrelated background AGB star.

4.4 X-ray properties of the YSOs

4.4.1 X-ray variability and spectroscopic analysis

Since the short-term variability (as seen in the light curves of the individual observations) of the *Coronet* X-ray sources is discussed in Forbrich et al. (2006) and Forbrich et al. (2007) [see Chapters 2 and 3], we focus here entirely on the long-term variability defined by the temporal sequence of the *Chandra* observations, covering a period of nearly five years.

For the present analysis we determined for each source the mean count rates during each of the 8 individual *Chandra* observations. While many sources show only small and often statistically insignificant variations, strong variability is seen in some of the YSOs. The more interesting long-term light curves are shown in Fig. 4.2, and the variability of individual objects will be discussed below.

A detailed analysis of the X-ray spectra of all sources with optical/infrared counterparts was performed with the *Sherpa* package in CIAO. The spectra were fitted with one- and two-temperature optically thin thermal plasma models plus an intervening absorption term. We used the XSPEC models “apec”, assuming a uniform density plasma with 0.3 times solar elemental abundances, and “wabs” for the absorption model. Spectral fits were carried out ignoring energy bins outside an energy range of 0.2–10 keV. As X-ray spectral fits sometimes suffer from ambiguities in the spectral parameters, special emphasis was placed on a careful scanning of the parameter space in order to find the best fit model. For this, we employed the *monte-lm* algorithm implemented in *Sherpa*, which performs hundreds of fitting runs per spectrum, each one using a different set of randomly chosen starting values for the fitting parameters.

Spectra of sources with less than 1000 counts were generally well fitted with a single-temperature plasma model, for stronger sources and sources for which the single-temperature model did not provide an acceptable fit, a two-temperature model was employed. The spectral analysis yielded plasma temperatures and hydrogen column densities and was also used to compute the intrinsic (extinction-corrected) X-ray luminosity by integrating the model source flux over the 0.2–8 keV band. Some representative examples of spectra are shown in Fig. 4.3. For X-ray sources with less than ~ 50 counts, the spectral fitting procedure often does not allow to reliably determine the spectral parameters. In these cases, the incident flux⁴ at the telescope aperture as determined by *acis_extract* (see Table 4.5) provides at least a rough estimate of the *observed* (i.e. *not* extinction corrected) source luminosity.

4.4.2 X-ray properties of different object classes

4.4.2.1 B- to F-type stars

TY CrA: The B8e star TY CrA is (at least) a quadruple system: in addition to the two spectroscopic companions with separations of 0.07 AU and 1.2 AU and estimated spectral types of \sim K2 and late F to early K (Casey et al. 1995; Corporon et al. 1996; Casey et al. 1998), a visual companion at a projected separation of 41 AU ($0''.3$) and of spectral type \sim M4 was recently found by Chauvin et al. (2003). With 21086 counts, the TY CrA system represents the second-brightest X-ray source in the field of view. Since the individual components cannot be resolved it remains unclear which component (if not both) is an X-ray source. The X-ray properties (i.e. plasma temperatures of $T_1 = 10$ MK and $T_2 = 27$ MK and the X-ray luminosity of 5.0×10^{30} erg/sec) are in the typical range observed for G- and early K-type T Tauri stars (see, e.g., Preibisch et al. 2005a) and thus suggest that one (or both) of the spectroscopic companions is the source of the X-ray emission.

⁴The incident flux is determined from the net counts divided by the respective value of the ancillary response file and the exposure time (the ARF is treated differently to yield FLUX1 and FLUX2 in *acis_extract*; determined here for an energy range of 0.5–8 keV).

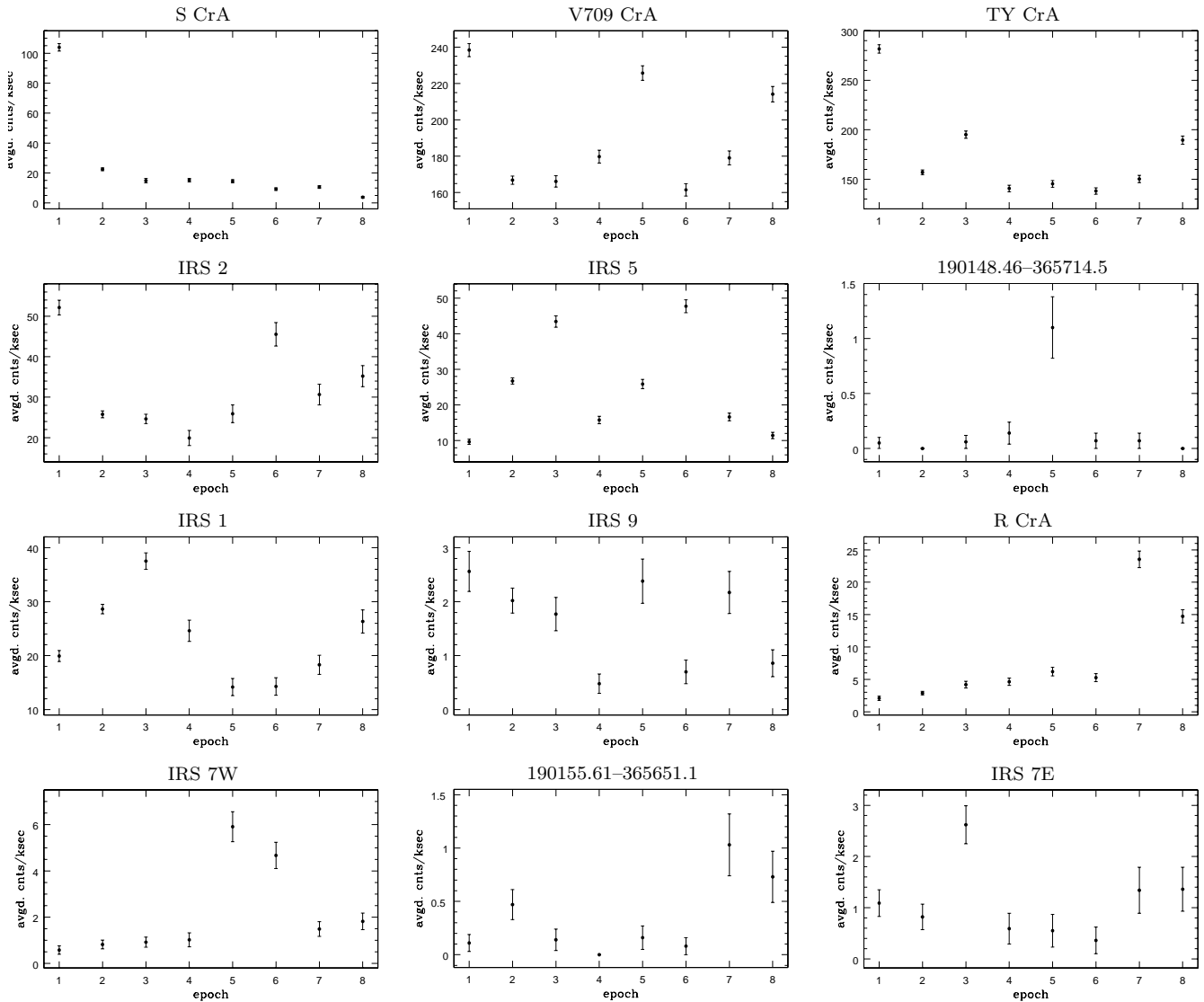


Figure 4.2: Long-term evolution of the X-ray emission of selected sources in the *Coronet* region derived from the *Chandra* observations obtained in October 2001 (epoch 1), June 2003 (epoch 2), June 2004 (epoch 3), and August 2005 (epochs 4 to 8). The dots show the mean count rates during each of the individual observations, which have exposure times between 15 and 40 ksec. The count rates were determined from counts between 0.2 keV and 8 keV and were corrected for effective exposure times using exposure maps.

HD 176386: This B9 IVe star has a visual companion at $\sim 4''$ separation (Jeffers et al. 1963). The strong decrease of the brightness ratio between primary and companion from optical to near-infrared wavelengths of $(\Delta[V, J, H, K] = [6.1, 0.76, 0.68, 0.45])$ mag according to Turon et al. (1993) and the 2MASS point-source catalog) suggests that the companion is of substantially later spectral type and thus most likely a low-mass ($M \lesssim 2 M_{\odot}$) star.

A strong X-ray source with 7772 counts is perfectly centered on the position of the companion to HD 176386, whereas there is no evidence for emission from the B star in our data. The spectral fit yields parameters ($T_1 = 9$ MK, $T_2 = 21$ MK, $L_X = 1.1 \times 10^{30}$ erg/sec) which are very typical for K- and early M-type T Tauri stars.

In order to derive an upper limit to the possible X-ray emission from the primary B-star

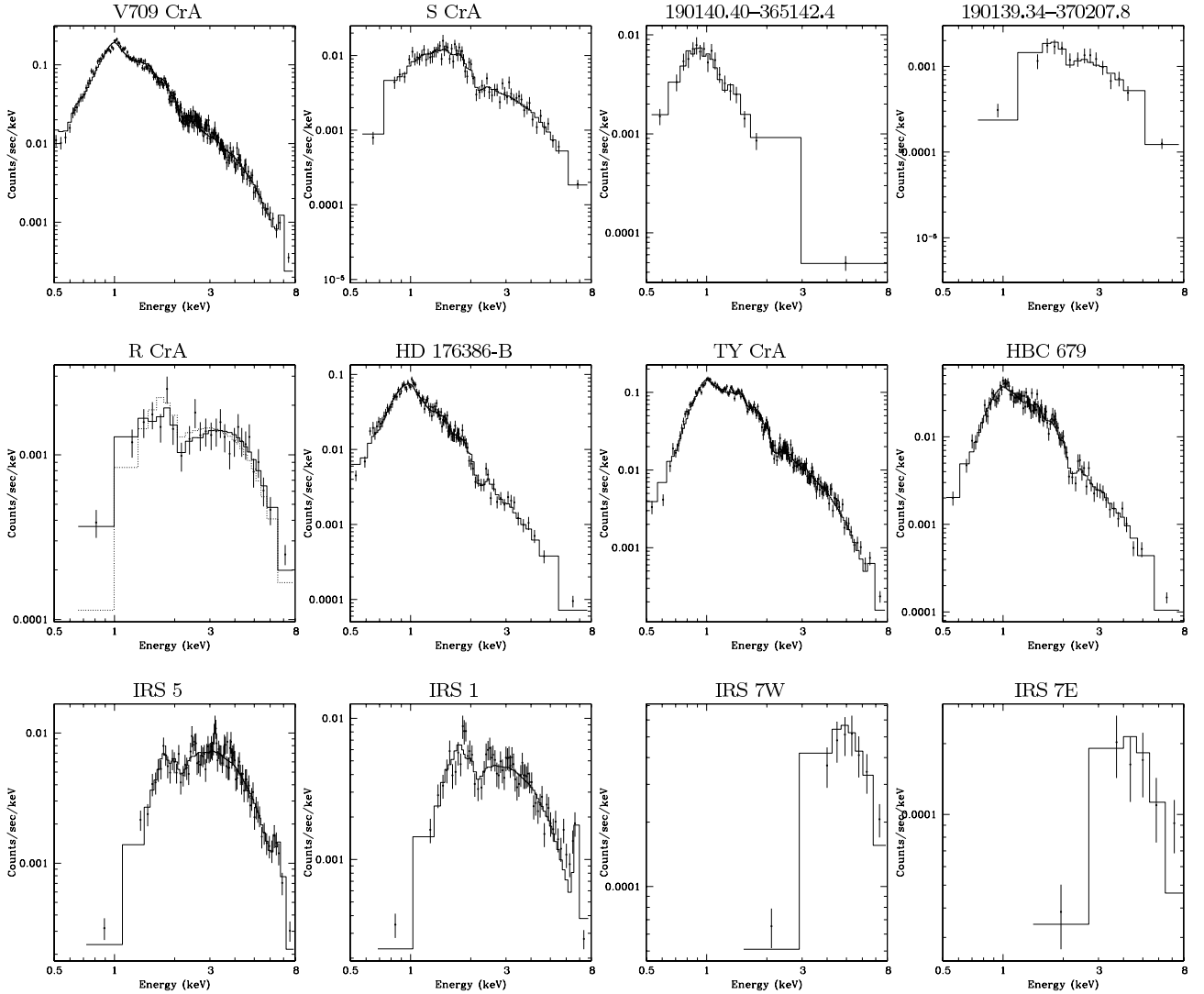


Figure 4.3: *Chandra* X-ray spectra of some YSOs in the *Coronet* region. The solid dots with error bars show the observed spectra, while the histogram lines show the best fit models. The first row shows two pairs of class III / II objects: V 709 (class III) & S CrA (class II), and 190140.40 (class III) & 190139.34 (class II), which illustrate the systematically harder spectra of the class II objects. The first plot in the second row shows the very hard spectrum of the Herbig Ae star R CrAr; the dotted line shows the one-temperature fit model, the solid line corresponds to the “two temperature – two absorption” model (for details see text). The next three panels compare the spectrum of the companion to the B star HD 176386 and the spectrum of the TY CrA multiple system to the spectrum of the class III T Tauri star HBC 687; the similarity of these spectra suggest that the true sources of X-ray emission apparently observed from these B stars are most likely young late-type stellar companions. The third row shows three class I objects and finally the likely class 0 protostar IRS 7E. The two last sources have significances per bin of 4.6σ and 3.2σ , respectively, compared to 5σ for the remainder.

HD 176386, we extracted counts in a $1''$ radius aperture centered on its optical position. There are 21 photons in this region, which however is strongly affected by the wings of the PSF of the X-ray emission from the companion. Comparison with nearby “background regions” at the same radial distance from the strong X-ray source yielded an expected background of 22 counts in a $1''$ radius aperture. The 90% confidence upper limit to the number of counts from HD 176386

Table 4.3: X-ray spectral fitting results for one- and two-temperature models. The fitting parameters are the absorbing hydrogen column density N_{H} , the plasma temperatures T , and the normalization factors from XSPEC (defined as $10^{-14}/(4\pi D^2) \int n_e n_{\text{H}} dV$). We also list the extinction-corrected (unabsorbed) X-ray luminosity L_{X} (integrated over the 0.2–8 keV band) derived from the model parameters, and the goodness-of-fit measure χ_{red}^2 . The fitting parameters for R CrA are given in the text.

Source	N_{H} [10^{22} cm^{-2}]	T_1 [MK]	T_2 [MK]	norm ₁	norm ₂	L_{X} [erg s^{-1}]	χ_{red}^2
190108.60–365721.3	0.72 ^{+0.02} _{-0.02}	49.4 ^{+3.1} _{-2.3}	6.8 ^{+0.5} _{-0.5}	(3.10 ^{+0.08} _{-0.08}) 10^{-4}	(1.67 ^{+0.16} _{-0.16}) 10^{-4}	1.23×10^{30}	0.93
190115.86–370344.3	0.22 ^{+0.03} _{-0.03}	77.5 ^{+17.3} _{-11.5}		(8.80 ^{+0.35} _{-0.35}) 10^{-5}		2.82×10^{29}	0.50
190118.90–365828.4	0.14 ^{+0.06} _{-0.05}	27.6 ^{+6.3} _{-5.3}		(1.18 ^{+0.12} _{-0.12}) 10^{-5}		2.70×10^{28}	1.09
190119.39–370142.0	0.54 ^{+0.14} _{-0.11}	33.1 ^{+10.1} _{-7.0}		(1.17 ^{+0.15} _{-0.15}) 10^{-5}		2.87×10^{28}	0.08
190120.86–370302.9	0 ^{+0.03}	14.9 ^{+2.2} _{-1.0}		(1.24 ^{+0.12} _{-0.12}) 10^{-5}		2.49×10^{28}	1.80
190125.61–370453.9	0.32 ^{+0.03} _{-0.03}	7.9 ^{+0.5} _{-0.3}		(4.06 ^{+0.31} _{-0.31}) 10^{-5}		8.79×10^{28}	1.96
190125.75–365919.3	1.07 ^{+0.02} _{-0.02}	7.2 ^{+0.2} _{-0.2}	25.6 ^{+1.2} _{-1.2}	(4.03 ^{+0.23} _{-0.23}) 10^{-4}	(2.39 ^{+0.09} _{-0.09}) 10^{-4}	1.37×10^{30}	0.57
190127.15–365908.6	0.04 ^{+0.01} _{-0.01}	3.4 ^{+0.2} _{-0.2}	13.8 ^{+0.6} _{-0.6}	(3.52 ^{+0.45} _{-0.45}) 10^{-5}	(4.26 ^{+0.21} _{-0.21}) 10^{-5}	1.33×10^{29}	1.22
190128.72–365931.9	0.53 ^{+0.01} _{-0.01}	24.6 ^{+0.8} _{-0.7}	8.8 ^{+0.5} _{-0.5}	(3.30 ^{+0.08} _{-0.08}) 10^{-4}	(1.41 ^{+0.09} _{-0.09}) 10^{-4}	1.03×10^{30}	0.75
190129.01–370148.8	0.15 ^{+0.01} _{-0.01}	3.5 ^{+0.2} _{-0.2}	14.2 ^{+0.6} _{-0.6}	(6.60 ^{+0.65} _{-0.65}) 10^{-5}	(4.95 ^{+0.26} _{-0.26}) 10^{-5}	1.89×10^{29}	0.93
190133.84–365745.0	1.63 ^{+0.06} _{-0.06}	26.1 ^{+1.3} _{-1.3}		(1.91 ^{+0.08} _{-0.08}) 10^{-4}		4.28×10^{29}	0.57
190134.84–370056.7	0.137 ^{+0.003} _{-0.003}	11.3 ^{+0.1} _{-0.1}	40.6 ^{+1.0} _{-1.0}	(6.23 ^{+0.10} _{-0.10}) 10^{-4}	(1.07 ^{+0.01} _{-0.01}) 10^{-3}	4.17×10^{30}	1.39
190139.15–365329.6	0.07 ^{+0.01} _{-0.01}	9.3 ^{+0.1} _{-0.1}	21.5 ^{+0.8} _{-0.8}	(2.41 ^{+0.06} _{-0.06}) 10^{-4}	(2.68 ^{+0.07} _{-0.07}) 10^{-4}	1.08×10^{30}	1.18
190139.34–370207.8	0.457 ^{+0.02} _{-0.02}	13.6 ^{+1.3} _{-1.3}	2.82 ^{+0.1} _{-0.1}	(3.03 ^{+0.30} _{-0.30}) 10^{-5}	(4.50 ^{+0.29} _{-0.29}) 10^{-4}	6.24×10^{29}	0.65
190140.40–365142.4	2.34 ^{+0.11} _{-0.10}	29.5 ^{+1.5} _{-1.5}		(1.78 ^{+0.09} _{-0.09}) 10^{-4}		4.19×10^{29}	0.65
190140.81–365234.0	0.357 ^{+0.004} _{-0.004}	27.6 ^{+0.5} _{-0.5}	10.2 ^{+0.1} _{-0.1}	(1.37 ^{+0.02} _{-0.02}) 10^{-3}	(8.68 ^{+0.16} _{-0.16}) 10^{-4}	5.01×10^{30}	1.13
190141.55–365831.6 ^[1]	2.42 ^{+0.05} _{-0.05}	33.8 ^{+0.9} _{-0.9}		(1.02 ^{+0.02} _{-0.02}) 10^{-3}		2.88×10^{30}	1.07
190141.62–365953.1	0.32 ^{+0.02} _{-0.02}	9.5 ^{+0.7} _{-0.6}	28.5 ^{+2.4} _{-2.4}	(3.98 ^{+0.33} _{-0.33}) 10^{-5}	(5.81 ^{+0.33} _{-0.33}) 10^{-4}	2.21×10^{29}	0.72
190148.02–365722.4 ^[2]	3.87 ^{+0.07} _{-0.07}	42.8 ^{+1.2} _{-1.2}		(1.13 ^{+0.02} _{-0.02}) 10^{-3}		3.09×10^{30}	0.90
190149.35–370028.6	0.24 ^{+0.04} _{-0.04}	4.6 ^{+0.3} _{-0.3}		(1.91 ^{+0.24} _{-0.24}) 10^{-5}		3.07×10^{28}	1.39
190150.45–365638.1	1.09 ^{+0.10} _{-0.09}	37.4 ^{+4.8} _{-4.3}		(3.86 ^{+0.28} _{-0.28}) 10^{-5}		9.97×10^{28}	0.69
190150.66–365809.9 ^[1]	2.75 ^{+0.07} _{-0.06}	48.2 ^{+1.6} _{-1.6}		(7.90 ^{+0.18} _{-0.18}) 10^{-4}		2.45×10^{30}	1.41
190152.63–365700.2	1.81 ^{+0.13} _{-0.11}	24.3 ^{+2.1} _{-1.9}		(6.39 ^{+0.48} _{-0.48}) 10^{-5}		1.39×10^{29}	1.11
190155.31–365722.0	27.67 ^{+1.66} _{-1.47}	99.3 ^{+25.1} _{-16.4}		(3.30 ^{+0.24} _{-0.24}) 10^{-4}		1.10×10^{30}	0.82
190155.85–365204.3	3.40 ^{+0.30} _{-0.26}	> 740 ₋₁₆₉		(9.84 ^{+0.60} _{-0.60}) 10^{-5}		2.71×10^{29}	0.96
190156.39–365728.4	14.81 ^{+1.98} _{-1.57}	79.4 ^{+32.1} _{-16.6}		(1.18 ^{+0.15} _{-0.15}) 10^{-4}		3.80×10^{29}	1.68
190200.11–370222.3	0.51 ^{+0.02} _{-0.02}	2.2 ^{+0.04} _{-0.04}	13.2 ^{+1.6} _{-1.5}	(9.87 ^{+0.68} _{-0.68}) 10^{-4}	(2.06 ^{+0.26} _{-0.26}) 10^{-5}	1.10×10^{29}	0.35
190201.92–370743.0	0.005 ^{+0.006}	9.4 ^{+0.2} _{-0.2}	22.2 ^{+0.9} _{-0.9}	(4.96 ^{+0.14} _{-0.14}) 10^{-4}	(6.02 ^{+0.17} _{-0.17}) 10^{-4}	2.35×10^{30}	1.30
190201.94–365400.1	2.63 ^{+0.92} _{-0.60}	406		(8.72 ^{+1.59} _{-1.59}) 10^{-6}		2.69×10^{28}	0.00
190211.99–370309.4	0.47 ^{+0.07} _{-0.06}	7.9 ^{+0.8} _{-0.8}		(1.35 ^{+0.19} _{-0.18}) 10^{-5}		2.92×10^{28}	2.36
190222.13–365541.0	0.25 ^{+0.01} _{-0.01}	9.5 ^{+0.2} _{-0.2}	25.6 ^{+0.9} _{-1.0}	(2.27 ^{+0.09} _{-0.09}) 10^{-4}	(4.66 ^{+0.11} _{-0.11}) 10^{-4}	1.53×10^{30}	0.96
190227.05–365813.2	0.16 ^{+0.04} _{-0.04}	39.7 ^{+6.7} _{-5.0}		(3.01 ^{+0.18} _{-0.18}) 10^{-5}		7.97×10^{28}	0.71
190233.07–365821.1	0 ^{+0.10}	> 740 ₋₂₄₆		(2.22 ^{+0.29} _{-0.27}) 10^{-5}		6.13×10^{28}	2.20

^[1] iron abundance adjusted to fit the 6.7 keV line; ^[2] fit including fluorescent iron line at 6.4 keV

is 8.4 source counts. After correction for the small extraction region, which would contain only about 30% of the flux from a point source at the off-axis angle of $\sim 6'$, we derive an upper limit of < 0.21 counts/ksec for the source count rate; with $A_V = 1$ mag and $L_{\text{bol}} = 58 L_{\odot}$ (Bibo et al. 1992) we derive upper limits of $L_{\text{X}} < 4.5 \times 10^{27}$ erg/sec and $\log(L_{\text{X}}/L_{\text{bol}}) < -7.7$.

R CrA: The Herbig Ae star R CrA is surrounded by a prominent reflection nebulosity and shows an extremely strong infrared excess (compared to the stellar photospheric emission). According to the analysis of Acke & van den Ancker (2004), the stellar luminosity, derived by fitting and integrating a model for the stellar photosphere to the de-reddened photometry, is only $0.65 L_{\odot}$, much less than the bolometric, i.e. the total integrated luminosity of the SED, for which they find $2800 L_{\odot}$. This shows that the object derives most of its luminosity from accretion of circumstellar matter. The fact that the derived stellar luminosity would place R CrA *below* the main-sequence in the HR-diagram, shows that the stellar parameters are very uncertain. Perhaps, the central star is deeply embedded in circumstellar material and seen only in scattered light. In that case, the stellar luminosity and also the derived extinction of $A_V = 1.33$ mag would be considerably underestimated.

The X-ray emission from R CrA is strongly variable and has risen to considerably higher levels in the last two epochs than in the earlier *Chandra* observations (Fig. 4.2, see also X-ray light curves in Forbrich et al. 2006/Chapter 2). The light curves of the individual August 2005 *Chandra* observations (shown in Forbrich et al. 2007/Chapter 3) reveal numerous flare-like peaks, suggesting the the source is more or less continuously flaring. We detect 982 source counts towards R CrA. The extreme hardness of the spectrum, providing clear evidence for the presence of very hot plasma, was already noted in Forbrich et al. (2006)/Chapter 2 and is clearly confirmed. A one-temperature model cannot produce an acceptable fit to the observed spectrum; while the hard part (> 2 keV) of the spectrum is rather well fitted, a clear excess of counts remains at and just below 1 keV (this model is shown by the dashed line histogram in the spectrum in Fig. 4.3). A two-temperature model provides a formally acceptable fit ($\chi_r^2 = 0.83$), but the resulting spectral parameters are very dubious: in addition to an extremely hot plasma component, for which only a lower bound to the temperature ($T_2 > 660$ MK) can be established, the fit yields an extremely strong and cool low-temperature component of 1.3 MK and strong extinction of $N_H = 2.3 \times 10^{22}$ cm². The emission measure of this alleged low-temperature plasma component would be more than 2000 times larger than that of the high-temperature component, and its (extinction-corrected) X-ray luminosity would be 1.6×10^{32} erg/sec, orders of magnitude higher than the luminosity of the high-temperature component of 4.3×10^{29} erg/sec. This extremely high X-ray luminosity makes it very unlikely that this very soft spectral fit component represents soft X-ray emission due to accretion shock emission. Rather, we strongly suspect that this fit result is an example of the highly nonlinear interaction of very low-temperature plasma components and strong extinction (see, e.g., the discussion in Getman et al. 2005b). For high hydrogen column densities, such a very low-temperature plasma component is almost entirely absorbed, and thus any uncertainties in the lowest energy bins of the spectrum can lead to large overestimates of the extinction-corrected X-ray luminosity.

In an attempt to find a spectral fit solution that avoids this kind of inference of a very luminous, but heavily absorbed, ultrasoft component, we considered a spectral model in which both of the two plasma components have individual extinction factors rather than a common extinction factor for both components (model = $wabs_1 \times apec_1 + wabs_2 \times apec_2$, instead of the “usual” model = $wabs \times [apec_1 + apec_2]$). This model provides a very good fit ($\chi_r^2 = 0.66$) for $N_{H,1} = (1.5 \pm 0.1) \times 10^{22}$ cm⁻² ($A_V = 7.25$ mag), $T_1 = (9.3 \pm 0.8)$ MK, and $N_{H,2} = (4.0 \pm 0.3) \times 10^{22}$ cm⁻² ($A_V = 20$ mag), $T_2 > 607$ MK. This model is show by the solid line histogram in the spectrum in Fig. 4.3. The extinction-corrected X-ray luminosities for the two spectral components are $L_{X,1} = 2.4 \times 10^{29}$ erg/sec and $L_{X,2} = 5.3 \times 10^{29}$ erg/sec.

These X-ray spectral fitting results for R CrA are in some respects similar to the case of FU Ori, for which Skinner et al. (2006) found that the hot plasma component also requires a considerably larger hydrogen column density than the low-temperature component to fit the observed spectrum. They argued that the hot component represents coronal emission that is strongly absorbed in accretion streams or a strong stellar wind. Why the cooler spectral component is less absorbed, remains unclear; perhaps it originates from a different location.

An alternative explanation would be that the X-ray emission comes from two different, close and thus unresolved objects (perhaps late type companions to R CrA) for which the extinction along the line-of-sight is different.

Although these explanations remain quite speculative, it is interesting that R CrA and FU Ori are both very strongly accreting, and their peculiar X-ray spectra may therefore be in some way affected by accretion processes. If the X-ray emission originates from R CrA (and not from an unresolved companion) the extinction derived from the X-ray spectrum ($A_V \geq 7$ mag) supports the suspicion that the optical extinction value of $A_V = 1.33$ mag is a serious underestimate.

T CrA: This F0e star is particularly interesting because its spectral type is very close to the upper boundary for stars with convective envelopes. For the stellar parameters of T CrA as listed in Acke & van den Ancker (2004), the models of Siess et al. (2000) suggest an extremely shallow convective envelope with relative thickness of $\Delta R_{\text{env}}/R_{\star} = 0.8\%$. An interesting question is whether a magnetic dynamo may work in such an extremely thin convection zone.

From an analysis of the first *Chandra* observation of the *Coronet* (ObsID=19), Skinner et al. (2004) reported a tentative X-ray detection of T CrA with 4 ± 2 counts in these data. In our much deeper dataset we clearly detect X-ray emission from T CrA, although again only as a rather faint source (14 source counts). A fit to the X-ray spectrum, with the hydrogen column density fixed at the value corresponding to the extinction of $A_V = 2.45$ mag as derived by Acke & van den Ancker (2004), suggests a plasma temperature of ~ 11 MK and yields an X-ray luminosity of $\sim 5 \times 10^{27}$ erg/sec. The corresponding fractional X-ray luminosity is $\log(L_X/L_{\text{bol}}) = -6.7$. This F0 star is thus clearly a much weaker X-ray emitter than the G type T Tauri stars. However, we note that its fractional X-ray luminosity is similar to those of early F-type main-sequence stars, which typically have $\log(L_X/L_{\text{bol}}) \sim -7$ (see, e.g., Schmitt & Liefke 2004). Of course, there exists the possibility that the X-ray emission comes from an unresolved late-type companion. That assumption, however, appears unlikely, because the observed X-ray luminosity is lower than typical even for a low-luminosity late M-type companion. For example, in the COUP data less than 1% of the T Tauri stars showed X-ray luminosities below the value we find here for T CrA (Preibisch et al. 2005a). This suggests that T CrA is the hottest object in the *Coronet* region with coronal X-ray activity driven by a dynamo in a very shallow convection zone.

4.4.2.2 T Tauri Stars

S CrA – This classical T Tauri star of spectral type K3 has a faint companion ($\Delta K = 3.27$), also a classical T Tauri star, with spectral type M0, located at a separation of $1''.3$ from S CrA (Prato et al. 2003; McCabe et al. 2006). The *Chandra* data yield 3026 source counts, and their spatial distribution is consistent with a single source at the position of the primary; there is no elongation along the direction toward the companion (along position angle 149°). The spectral parameters are prototypical for T Tauri stars.

HBC 679 – This weak-line T Tauri star of spectral type K5 has a companion of spectral type M3 at a separation of $4''.5$ (Prato et al. 2003). The *Chandra* source with 5485 counts is centered at the position of the primary, but there is an elongation in the direction of the secondary. Since the source is located close to the edge of the field of view of the *Chandra* image, where the PSF is already degraded, the contributions of the individual components cannot be reliably disentangled.

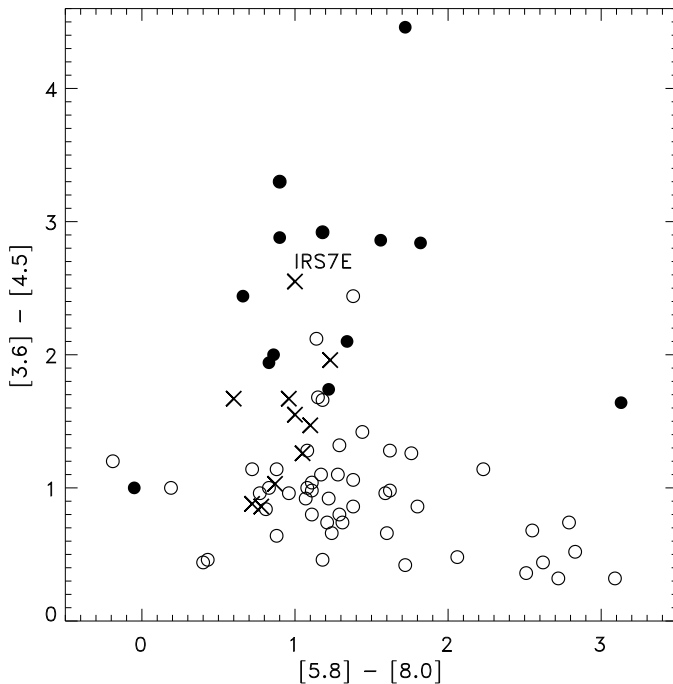


Figure 4.4: This plot shows the IRAC mid-infrared colors of the Perseus class I protostars as open circles and the candidate class 0 objects as filled circles (from Jørgensen et al. 2006). The embedded objects in the *Coronet* cluster are shown as crosses. The likely class 0 protostar IRS 7E is labeled.

4.4.2.3 The class 0 protostar candidate IRS 7E

The infrared source IRS 7E has many properties that are characteristic for class 0 protostars. Its SED is dominated by the strong submillimeter emission (Nutter et al. 2005), and possibly the source has a disk and an outflow (Anderson et al. 1997; Groppi et al. 2004), although a definitive attribution is currently difficult due to the high source density in the region and the comparably low angular resolution. Harju et al. (2001) find evidence for a radio jet emanating from IRS 7E. While all these results suggest that IRS 7E is a class 0 objects, they do not yet provide a definitive proof for this assumption.

IRS 7E is detected in all four IRAC bands of the Spitzer images. Although the Spitzer IRAC colours do not immediately allow to discern class 0 and class I objects, the IRAC colors of IRS 7E support the assumption that it really is a class 0 object based on the following considerations: Jørgensen et al. (2006) recently presented an analysis of *Spitzer* data of the Perseus molecular cloud complex, and suggested a promising method to distinguish between class 0 and class I objects by their IRAC colors. They found that the “candidate deeply embedded protostars” (class 0 candidates) have systematically redder [3.6]-[4.5] colors in the IRAC color-color diagram (their Fig. 17) than class I objects. In Fig. 4.4 we show the colors of the Perseus objects and have also included the embedded (class 0 or class I) objects in the *Coronet* cluster. The location of IRS 7E in this plot is well consistent with those of the class 0 candidates in Perseus and also clearly separated from the class I objects. This result supports the notion that IRS 7E is different (i.e. in an earlier evolutionary state) from the class I objects, and we will thus denote IRS 7E as a “likely class 0 protostar”.

The X-ray detection of IRS 7E (initially reported by Hamaguchi et al. 2005a) represents up to now the only reliable case for high-energy emission from a likely class 0 protostar. The long-term light curve (see Fig. 4.2) suggests considerable variability, but (probably due to the low count rate) no individual flares are detected in the individual *Chandra* observations.

The X-ray spectrum of IRS 7 E (see Fig. 4.3) is very hard; the spectral fit suggests an extinction of $A_V \sim 74$ mag, yields a plasma temperature of 80 MK, and gives an extinction-corrected X-ray luminosity of $\sim 4 \times 10^{29}$ erg/sec. These parameters are roughly consistent with those derived by Hamaguchi et al. (2005a) from their XMM-*Newton* data for the phase of “constant” emission before the flare.

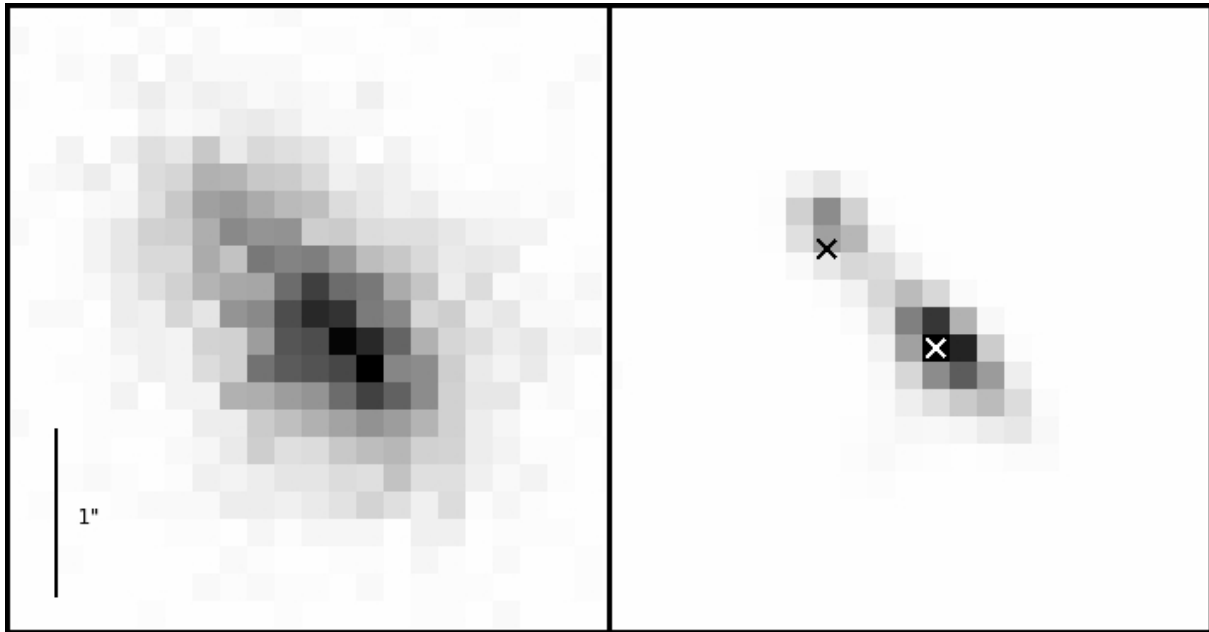


Figure 4.5: *Chandra* image of the IRS 5 a/b region, original data and maximum-likelihood-reconstructed super-resolution image (from 0.2–10 keV data). The crosses mark the positions of the double infrared source relative to the peak emission (from Nisini et al. 2005).

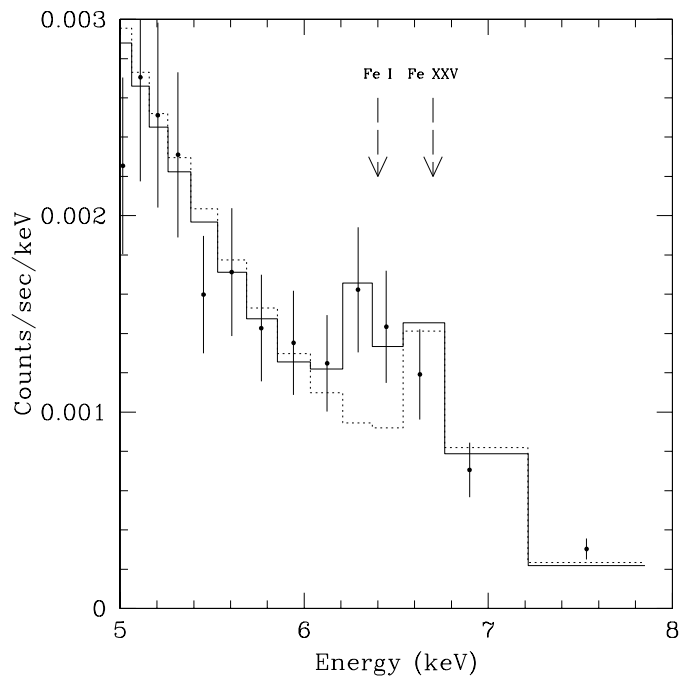


Figure 4.6: Detail of the X-ray spectrum of IRS 5 around the 6.7 keV iron line, showing the strong fluorescent emission at 6.4 keV. The dashed line shows the best-fit model without taking into account a line at 6.4 keV.

The very high plasma temperatures clearly show that the X-ray emission must be dominated by magnetic processes, showing that magnetic activity starts already in extremely early stages of (proto)stellar evolution.

4.4.2.4 Class I protostars

X-ray emission from seven class I protostars is detected in our dataset: IRS 1, 2, 5, 7W, 9, 190148.46–365714.5, and 190155.61–365651.1. The X-ray properties of these objects are similar to those of other X-ray detected class I protostars.

The class I object IRS 5 is especially interesting. First, the object is a close binary with a separation of $0''.9$ (Chen & Graham 1993; Nisini et al. 2005). The *Chandra* image (Fig. 4.5) shows that the X-ray emission is marginally resolved and that both components contribute to the observed X-ray emission. However, the strong overlap of the PSFs of the individual components does not allow the emission to be reliably resolved and thus we study here only the composite spectra and light curves. A closer look at the X-ray spectrum of IRS 5 reveals emission at 6.4 keV that can be well distinguished from the usual 6.7 keV K-line from highly ionized iron (Fe XXV). As 6.4 keV emission is the K-line from neutral to low-ionized, i.e. cool iron, the presence of 6.4 keV line can be explained as fluorescence emission from cool circumstellar material that is strongly irradiated by the hard X-ray emission from the central YSO (Fig. 4.6). Similar 6.4 keV iron fluorescence lines have been observed in some YSOs (e.g., Imanishi et al. 2001a; Tsujimoto et al. 2005) and provide direct evidence for the strong X-ray irradiation of circumstellar disk material that probably has important consequences for the physical properties of the circumstellar dust and gas and the evolution of proto-planets.

Class I objects are usually considered to be in a considerably younger evolutionary stage than class II objects (T Tauri stars) and are therefore often termed “protostars”. However, it is not fully clear to what degree the different SED classes truly correspond to significant evolutionary changes in the circumstellar material, or whether the classification is affected by other factors such as the inclination under which the YSO is seen. For example, White & Hillenbrand (2004) recently argued that the spectroscopically determined stellar ages of class I and class II sources appear indistinguishable, suggesting that the different SED slopes may (to some degree) be just the result of different viewing angles. However, two recent studies (Eisner et al. 2005; Doppmann et al. 2005) supported the conventional assumption that class I objects really represent an earlier evolutionary stage than class II objects and that class I objects truly are self-embedded protostars undergoing significant mass accretion, although the objects appear to span a broad range of mass accretion activity. The spectroscopic investigation of several class I objects in the *Coronet* cluster by Nisini et al. (2005) suggests that these objects actually are systematically younger than the T Tauri stars, although not by very much (ages ranging between 0.1 and 1 Myr were derived, larger than the canonically assumed 0.1 Myr). It was also found that IRS 2 and IRS 1 are dominated by accretion, while IRS 5 and IRS 6 are not.

Any systematic differences in the X-ray properties of the class I objects as compared to T Tauri stars would thus support a difference in nature. Such differences are actually seen in the *Chandra* data. First, we note that all class I objects display rather strong temporal variability in their long-term light curves (see Fig. 4.2). Although the small number of object prevents a rigorous statistical analysis, the data suggest that the class I objects display stronger levels of variability than class II and class III objects. Another difference is seen in the X-ray spectral properties, where we find that the class I objects show systematically higher plasma temperatures than class II and class III objects (see Fig. 4.7).

4.4.2.5 Brown Dwarfs

Sensitive X-ray studies have shown that stellar X-ray activity extends not only down to the stellar mass limit at $\sim 0.075 M_{\odot}$, but even beyond the stellar/substellar boundary and into the brown dwarf (BD) regime. While X-ray emission has been detected from numerous *young* BDs (e.g., Neuhäuser & Comerón 1998; Imanishi et al. 2001b; Preibisch & Zinnecker 2001, 2002; Tsuboi et al. 2003; Stelzer 2004; Preibisch et al. 2005b), just two older field BDs have been detected in X-rays up to now (Rutledge et al. 2000; Stelzer 2004). This is most likely related to the fact that the *young* BDs, during the first few Myr of their evolution, are warmer and orders of magnitude more luminous than at older ages. The nature of the X-ray emission from BDs and the origin of their activity is still not well understood.

The CrA star-forming region contains a number of very low-mass objects, some of which are

Table 4.4: Results for the Brown Dwarf candidates

Name	Ref	SpT	$\log\left(\frac{L_{\text{bol}}}{L_{\odot}}\right)$	M [M_{\odot}]	A_V [mag]	source counts	T_X [MK]	L_X [erg/sec]	$\log\left(\frac{L_X}{L_{\text{bol}}}\right)$
B185815.3-370435	1				~ 7	< 3.2		$< 2.6 \times 10^{27}$	
B185831.1-370456	1,2	M8.5	-2.6	~ 0.025	~ 0	9		$\sim 8.0 \times 10^{26}$	~ -4.1
B185839.6-365823	1		-3.1		~ 13	47	> 350	$\sim 2.7 \times 10^{28}$	~ -2.1
B185840.4-370433	1		-2.2		~ 12	6		$\sim 1 \times 10^{28}$	~ -3.4
B185853.3-370328	1		-2.2		~ 12	< 2.1		$< 4.5 \times 10^{27}$	< -3.7
LS-RCrA 1	3	M6.5-7	-2.6	$\sim 0.04-0.08$	~ 0.5	< 10		$< 1.1 \times 10^{27}$	< -3.9
LS-RCrA 2	3	M6	-1.5	~ 0.08	~ 1.2	113	4.5	3.1×10^{28}	-3.6
ISO CrA 143	4	\approx M8:	-2.0	~ 0.025	~ 2.3	88	8	2.9×10^{28}	-3.2

References: 1: Neuhauser et al. (1999); 2: López Martí et al. (2005); 3: Fernández & Comerón (2001); 4: Olofsson et al. (1999)

most likely young brown dwarfs (BDs). Several objects have been identified as BD candidates in different studies (Willing et al. 1997), but, unfortunately, in no case a fully reliable spectroscopic classification as BD is available, because either the spectral types were estimated from (narrow-band) photometry and are thus quite uncertain, or the objects are very close to the stellar/substellar boundary. Therefore, all objects discussed here are BD candidates, not bona-fide BDs.

There are eight BD candidates are in the field of view of the *Chandra* image. Three of them (B185839.6-365823, LS-RCrA 2, and ISO CrA 143) are among the X-ray sources detected by *wavdetect*. For the remaining five BD candidates we have performed a detailed investigation of the corresponding positions in the *Chandra* image. For each object we defined a source region centered at its optical position with a radius of $3''$ and a corresponding background region as annulus with inner radius $5''$ and outer radius $10''$. Then we determined the numbers of detected counts in the source and background regions and compared the number of background counts scaled by the corresponding area to the number of counts detected in the source regions. For two objects (B185840.4-370433 and B185831.1-370456) the number of counts in the source region exceeded the number of expected background counts with at least 90% confidence, tentatively indicating the presence of very weak X-ray emission. For the remaining 3 objects, upper limits to their count rates and (if information on extinction was available) also to their X-ray luminosities were determined as described above. The results of this analysis are listed in Table 4.4.

The X-ray luminosities and fractional X-ray luminosities of the young BD candidates in the CrA star-forming region are similar to those of the low-mass stars, and thus there is no evidence for changes in the magnetic activity around the stellar/substellar boundary. In two of the three objects which yielded enough counts for spectral analysis, the derived plasma temperatures are moderate and in the lower range of plasma temperature found for young stars, consistent with previous findings. On the other hand, the BD candidate B185839.6-365823 shows a rather hard spectrum and the fit suggests a very high plasma temperature. Although the S/N of the spectrum is rather low and thus no reliable determination of the spectral parameters is possible, the median photon energy of 3.4 keV already suggests a rather hard spectrum. We also note that this objects shows strong variability in the long-term light curve, so the hard spectrum may be related to X-ray flaring.

This result reinforces the conclusions of previous studies, that the key to the magnetic activity in very cool objects seems to be the effective temperature which determines the degree of ionization in the atmosphere (see, e.g., Preibisch et al. 2005b).

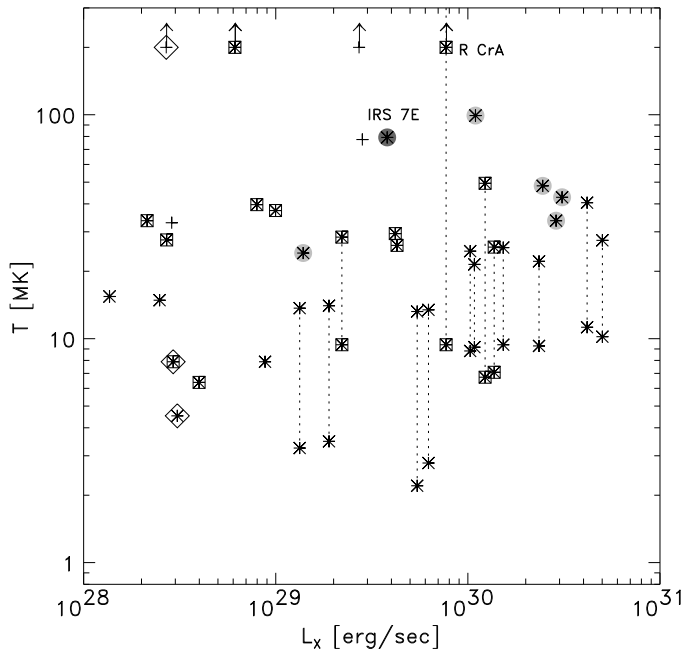


Figure 4.7: Plasma temperatures versus X-ray luminosities for the CrA members with sufficient counts for X-ray spectral fitting. The different SED classes are shown with different symbols: the likely class 0 protostar IRS 7E as asterisk with dark dot, class I objects as asterisks with grey dots, class II objects as asterisks surrounded by boxes, class III objects as asterisks, and objects without SED classification as crosses. For objects with 2T fits, the high and low-temperature values are connected by the dashed lines.

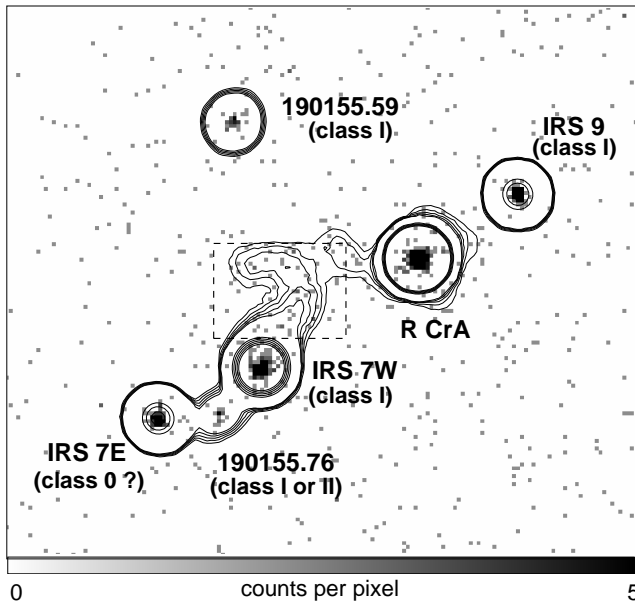


Figure 4.8: *Chandra* X-ray image of the central region ($78'' \times 68''$ field of view), showing the diffuse emission between IRS 7 W and R CrA. The greyscale shows the 3 – 6.5 keV band image with the original $0''.49$ pixels. The contours show the same image smoothed with a 10 pixel FWHM Gauss filter. Contours are drawn at levels of 0.07, 0.08, 0.09, 0.1, 0.11 (to trace the diffuse emission) and 0.6, 0.7, 0.8, 0.9, 1.0 (to outline point sources.)

4.4.2.6 Comparison of the X-ray properties of different object classes

In Fig. 4.7 we plot the plasma temperatures versus X-ray luminosities derived from the fits to the X-ray spectra. Objects in different evolutionary stages are distinguished by different plot symbols. As already described above, class I objects show systematically higher plasma temperatures than class II and III T Tauri stars. Furthermore, the plot also reveals that class II objects show systematically hotter plasma temperatures than class III objects. This effect is also illustrated in the comparison of the spectra for V709 CrA (class III) to S CrA (class II) and 190139.34 (class III) to 190140.40 (class II) in Fig. 4.3. We note that a similar spectral difference was found by Flaccomio et al. (2006) for the YSOs in the NGC 2264 star-forming region.

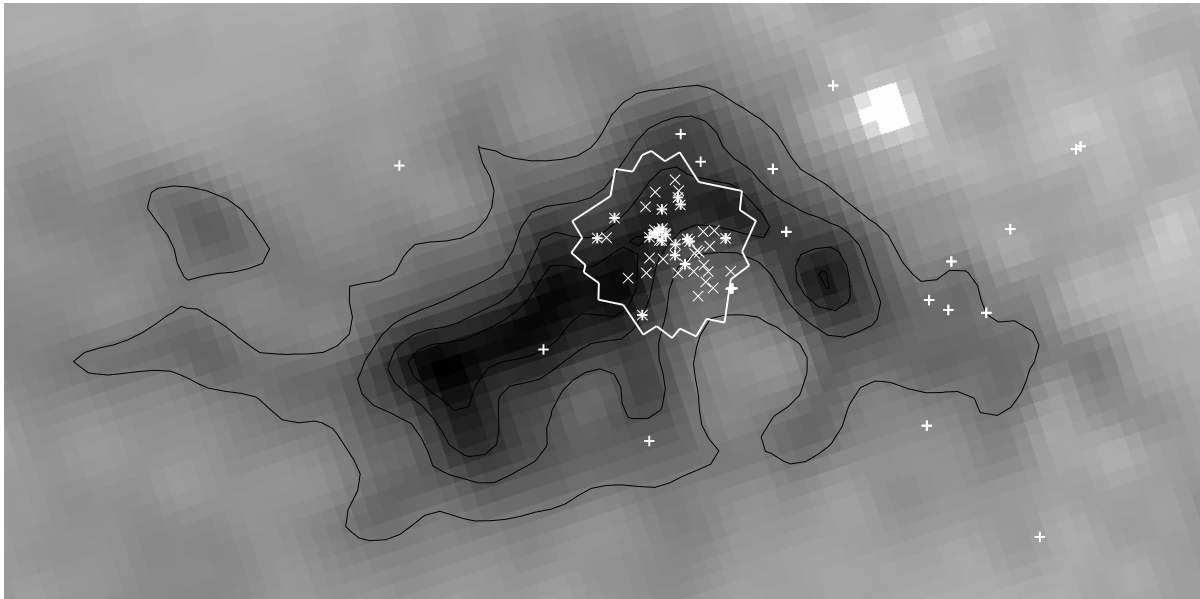


Figure 4.9: The extinction map of the CrA star-forming region from Dobashi et al. (2005) is shown as greyscale image and with contours at levels of $A_V = [1, 2, 3, 4]$ mag. The polygon shows the field of view of the *Chandra* image, the X symbols mark the positions of the X-ray sources with optical/infrared counterparts in the *Chandra* field of view, and the + signs mark the positions of previously known members of the CrA star-forming region (Walter et al. 1997; Neuhäuser et al. 2000).

4.5 Diffuse X-ray emission

Inspection of the *Chandra* image reveals an excess of counts in a region north of the class I object IRS 7 W and east of R CrA (see Fig.4.8). The box-shaped region contains 102 counts, whereas the local background, estimated from two nearby source-free regions, should contribute only ~ 38 counts. The excess of 64 counts apparently represents diffuse X-ray emission. Comparing the distribution of photon energies within this region to that in the background regions reveals a statistically significant excess in the 3 – 6.5 keV band.

The available optical and infrared images show obvious structures that may be related to this emission. We note that the continuum-subtracted [S II] image presented by Wang et al. (2004) shows a small arc of emission that seems to roughly coincide with the diffuse X-ray emission. As there is much stronger and extended [S II] emission to the east of this patch, it is not clear whether the X-ray emission is actually related to this [S II] emission.

The nature of the observed diffuse emission remains unclear. If the emission were related to one of the several known jets and outflows in this region, one would expect a quite soft X-ray spectrum, with most of the detected photons at energies of $\lesssim 1$ keV and not $\gtrsim 3$ keV as observed. Another possibility would be that we see scattered X-rays originating from one of the embedded sources in this area. The source of the emission could be IRS 7 W, R CrA or perhaps another, extremely deep embedded protostar in this area.

4.6 An X-ray census of young stars in the Coronet region

Since their strongly elevated X-ray emission provides an easy discriminant between young stars and older field stars, deep X-ray imaging is a very effective tool to establish a complete census of young stars in nearby star-forming regions. X-ray imaging is particularly effective in recovering the population of young stars which have their (inner) disks already dissipated, and which thus

display neither excess emission nor signs of accretion at optical and near-infrared wavelengths. The combination of optical, infrared, and X-ray observations is thus ideally suited to reveal the *full* population of young stars in star-forming regions (to mention just a few recent studies of this kind, we refer to Preibisch & Zinnecker 2002; Feigelson & Lawson 2004; Getman et al. 2005a; Flaccomio et al. 2006). A good knowledge of the complete stellar content of star-forming regions is essential for any reliable determinations of their IMF and star formation history, which eventually can yield detailed insight into the nature of the star formation process.

As determined above, the deep *Chandra* image should reveal all late-type stellar members of the *Coronet* region unless the extinction is too high: we expect the X-ray detections to be 100% complete for $\geq 0.08 M_{\odot}$ stars without extinction, for $\geq 0.2 M_{\odot}$ stars with $A_V \leq 5$ mag, and for $\geq 0.5 M_{\odot}$ stars with $A_V \leq 10$ mag. The X-ray detections should be 50% complete for $\geq 0.08 M_{\odot}$ stars with $A_V \leq 14$ mag, for $\geq 0.2 M_{\odot}$ stars with $A_V \leq 19$ mag, and for $\geq 0.5 M_{\odot}$ stars with $A_V \leq 24$ mag. We thus expect that our X-ray data reveal nearly all YSOs in the region and miss at most a very small number of YSOs with exceptionally strong extinction. The number of 48 X-ray sources with counterparts should thus be either identical or very close to the number of YSOs inside the field of view of the *Chandra* image. We add to this the three known companions of TY CrA, the undetected Be star HD 176386, and the companion of IRS 5 and arrive at a total number of 53 YSOs. Since the CrA star-forming region is very well observed in the optical and infrared regime, it is very unlikely that there is a substantial number of further, still undetected YSOs, perhaps with the exception of very deeply embedded protostars.

We now consider the IMF of the region. The lack of reliable mass estimates for most of the objects prevents a detailed IMF analysis, but we can gain at least some insight by investigating the number ratio of YSOs above and below $2 M_{\odot}$. There are three object above this limit in the field of view of the *Chandra* data⁵ TY CrA ($3.16 M_{\odot}$), R CrA ($\sim 2 - 3.5 M_{\odot}$), and HD 1763865 ($2.25 M_{\odot}$), while the remaining 48 objects should be low-mass ($M < 2 M_{\odot}$) members. Given a number of three stars in the $2 - 3.5 M_{\odot}$ mass range, analytic representations of the field IMF (Scalo 1998; Kroupa 2002) predict $\sim 100 - 120$ associated low-mass ($0.1 - 2.0 M_{\odot}$) stars. This is about twice as large as the number of known members within the *Chandra* field of view. Does this imply a deficit of low-mass stars in the central region of the CrA star-forming region?

The *Chandra* image covers an area with ~ 0.3 pc radius, and does not include the full spatial extent of the CrA star-forming region (see Fig. 4.9). Some fraction of the stellar population is expected to be outside the field of view. There is direct evidence for a wide distribution of members: Nine of the X-ray identified CrA WTTS from Walter et al. (1997) are outside the *Chandra* field of view. Furthermore, Neuhäuser et al. (2000) identified an even more widely dispersed population of 19 T Tauri stars around the *Coronet* region, all of which are outside the *Chandra* field of view. The ISOCAM study of Olofsson et al. (1999) showed that the density of YSOs (tentatively identified by their mid-infrared excess) is clearly larger in the *Chandra* field of view than in adjacent regions to the east and west, suggesting a clear concentration of the young stellar population in the central region. Taking these arguments into account, it appears reasonable to assume that roughly half of the YSOs of the CrA star-forming region should be located in the *Chandra* field of view. In that case, the agreement between the number of known low-mass members and the expectation from the field IMF provides no evidence that the IMF of the CrA star-forming region differs from the field IMF.

Finally, we consider the distribution of stellar ages. Lacking reliable age estimates for most individual objects, we compare here the number of YSOs in different evolutionary stages. There are 10 class 0/I/flat-spectrum objects, 13 class II objects, and 13 class III objects. The typically assumed ages of a few times 10^5 yr for class I objects, $\sim 1 - 3$ Myr for class II objects, and

⁵It should be noted that there are two additional B stars in the *Coronet* region, HD 176269 (B9V) and HD 176270 (B8 IV-V), both of which are just outside the field of view of the *Chandra* image. The membership status of these two stars is not fully clear, but if they are also cluster members, this would increase the estimate of the expected low-mass population to ~ 170 members.

$\gtrsim 3$ Myr for class III objects, suggest differences of more than one order of magnitude in the ages of the individual objects. This is confirmed by the spectroscopic ages estimates of ~ 0.1 Myr for some of the class I objects (Nisini et al. 2005) and $\sim 6 - 10$ Myr for most of the X-ray selected WTTS detected by Walter et al. (1997). If star formation in the CrA region would have been a continuously ongoing process during the last ~ 10 Myr, one would expect to see a much larger number of class III objects (and these should definitely be detected as X-ray sources) than class I objects. The observed number ratio therefore clearly suggests a strong temporal variation of the star formation rate, rather than a long period of constant star formation activity. For example, there may have been several discrete peaks in the star formation rate: a first star formation episode around $6 - 10$ Myr ago that created the apparently older WTTS and perhaps the intermediate-mass stars TY CrA as well as HD 176386, and another one during the last ~ 1 Myr, that created the embedded protostars.

4.7 Conclusions

Based on the X-ray results for the surroundings of the *Coronet* cluster in the CrA star-forming region, the answers to the questions raised in the introduction as well as the results on X-rays from Herbig-Haro objects can be summarized as follows:

1. What is the dominant X-ray emission process in T Tauri stars? The observed X-ray properties of the YSOs in the *Coronet* region are fully consistent with coronal magnetic activity. We find no evidence for X-ray emission from accretion shocks. This is in line with previous results and suggests that only in a small fraction of YSOs accretion processes contribute significantly to the observed X-ray emission. This finding is not very surprising when detailed models of accretion shocks are considered. Although hot accretion shocks should be present on basically any accreting star, this does *not* imply that one should expect *detectable* X-ray emission from the shocks in all cases: according to theoretical models of the shock structure (e.g., Calvet & Gullbring 1998), the material above the shock has typical column densities of $\gtrsim 10^{23} \text{ cm}^{-2}$ and should completely absorb and thermalize the soft X-rays (mostly at energies $\lesssim 0.5$ keV) emitted from the shock plasma within or close to the shock zone. This problem has also been highlighted by Drake (2005), who argued that for the typically estimated accretion rates in protostars and T Tauri stars ($\dot{M} \approx 10^{-7} - 10^{-6} M_{\odot}/\text{yr}$), the shock is buried too deeply in the (proto-)stellar atmosphere to allow the soft X-ray emission to escape and be detected; only for very low accretion rates ($\dot{M} \lesssim 10^{-9} M_{\odot}/\text{yr}$) detectable soft X-ray emission can be expected. Thus, the non-detection of accretion shock related X-ray emission is not very surprising.

The observed tendency that the class I objects exhibit a higher degree of X-ray variability than the older class II and III objects may be a consequence of magnetic reconnection events in the proto(star)-disk magnetic fields, causing frequent strong flares. The observed systematic differences in the X-ray properties of class I versus class II/III objects supports the assumptions that class I objects are truly in an earlier evolutionary stage. Finally, the high plasma temperatures of the class 0 and class I protostars clearly show that the X-ray emission of these extremely young objects must be dominated by magnetic processes.

2. How early in the protostellar evolution does X-ray activity start? The *Coronet* class I objects with relatively well determined spectroscopic ages as young as 0.1 Myr are clearly detected as X-ray sources. The likely class 0 protostar IRS 7E is so far the only case of a reliable X-ray detection of an object in earlier evolutionary stage than class I objects. The X-ray properties of this object are similar to those of the class I objects, showing that hot coronae and thus magnetic activity exist already in extremely young protostellar objects.

3. What is the origin of the observed X-ray emission from young intermediate-mass (Herbig Ae/Be) stars? For HD 176386 we show that the X-ray emission originates not from the Be star, but from a late type companion. The X-ray emission observed from the TY CrA multiple system has characteristics suggesting a coronal origin related to one (or several) of the low-mass companions. The case of R CrA remains unclear; its extremely hard X-ray spectrum clearly suggests a magnetic origin of the emission. One or several yet undiscovered and spatially unresolved late-type companions may provide the most straightforward explanation, although even in that case the extraordinarily high plasma temperature is very unusual. In any case, our data provide no indication for accretion-related X-ray emission in any of the young intermediate-mass stars, because in all cases the X-ray spectra are much too hard for this scenario.

4. How common is X-ray emission from HH objects? None of the numerous HH objects in the CrA star-forming region is detected in the *Chandra* data despite the very high sensitivity. X-ray emission at levels similar to those of the X-ray detected HH objects in the other star-forming regions should have been easily detected in our data.

The further results can be summarized as follows:

- X-ray emission is detected from about half of the brown dwarf candidates in the observed region.
- The class II objects in the *Coronet* region star-forming region show systematically higher plasma temperatures than class III objects.
- Diffuse X-ray emission is tentatively detected in the central part of the *Coronet* cluster, but its nature and origin remains unclear.
- Finally, the X-ray census of the stellar population of the *Coronet* region suggests that the IMF of the region is consistent with the field-star IMF and shows that the star formation process in the region must have proceeded in a non-steady way (with strong temporal variations of the star formation rate).

Table 4.5: CrA acis_extract source list

Src ID	Total counts ¹	Median E [keV] ¹	Source signif. ¹	HR1 ²	HR2 ²	HR3 ²	FLUX1 ² cm ⁻² s ⁻¹	FLUX2 ² cm ⁻² s ⁻¹
190104.58–370129.6	76	1.3	4.9	-0.98 ^{+0.09} _{-0.02}	-0.73 ^{+0.13} _{-0.10}	-3.05 ^{+0.51} _{-6.51}	1.99E-06	1.94E-06
190105.05–370340.2	28	1.2	4.0	-0.64 ^{+0.21} _{-0.17}	-0.42 ^{+0.24} _{-0.23}	-0.28 ^{+0.39} _{-0.39}	1.41E-05	1.80E-05
190108.31–365634.7	112	2.8	8.5	0.27 ^{+0.10} _{-0.10}	0.45 ^{+0.14} _{-0.14}	0.14 ^{+0.11} _{-0.12}	2.49E-06	3.35E-06
190108.60–365721.3	3026	1.8	53.7	-0.17 ^{+0.02} _{-0.02}	-0.22 ^{+0.02} _{-0.02}	-0.03 ^{+0.02} _{-0.02}	7.24E-05	9.55E-05
190111.30–365551.9	47	2.7	4.5	0.34 ^{+0.18} _{-0.17}	0.45 ^{+0.24} _{-0.23}	0.07 ^{+0.20} _{-0.20}	8.96E-07	1.32E-06
190114.54–370102.3	29	2.9	3.2	0.37 ^{+0.24} _{-0.23}	0.31 ^{+0.38} _{-0.39}	0.35 ^{+0.26} _{-0.25}	4.62E-07	8.20E-07
190115.32–365237.2	63	2.8	5.8	0.52 ^{+0.14} _{-0.13}	0.63 ^{+0.20} _{-0.16}	0.09 ^{+0.16} _{-0.16}	2.05E-06	2.54E-06
190115.86–370344.3	877	1.7	28.2	-0.21 ^{+0.03} _{-0.03}	-0.29 ^{+0.04} _{-0.04}	-0.04 ^{+0.05} _{-0.05}	2.87E-05	3.47E-05
190116.26–365628.4	70	1.2	6.5	-0.85 ^{+0.10} _{-0.07}	-0.59 ^{+0.11} _{-0.11}	-1.32 ^{+0.15} _{-0.15}	2.27E-06	1.76E-06
190116.65–365638.9	37	3.3	4.1	0.75 ^{+0.18} _{-0.13}	0.99 ^{+0.28} _{-0.30}	0.17 ^{+0.21} _{-0.21}	6.67E-07	8.26E-07
190117.52–365831.9	46	3.3	5.1	0.75 ^{+0.14} _{-0.11}	1.08 ^{+0.19} _{-0.03}	0.26 ^{+0.17} _{-0.17}	9.85E-07	1.26E-06
190118.29–365906.7	58	2.1	6.0	0.08 ^{+0.15} _{-0.15}	0.26 ^{+0.18} _{-0.18}	-0.19 ^{+0.17} _{-0.18}	1.24E-06	1.56E-06
190118.90–365828.4	162	1.4	11.4	-0.53 ^{+0.07} _{-0.07}	-0.49 ^{+0.08} _{-0.08}	-0.30 ^{+0.14} _{-0.14}	3.62E-06	4.43E-06
190119.39–370142.0	93	1.8	8.0	-0.26 ^{+0.11} _{-0.11}	-0.12 ^{+0.13} _{-0.13}	-0.33 ^{+0.16} _{-0.15}	2.01E-06	2.76E-06
190120.07–370422.9	41	3.0	3.9	0.44 ^{+0.20} _{-0.18}	0.32 ^{+0.30} _{-0.30}	0.25 ^{+0.22} _{-0.22}	1.10E-06	1.21E-06
190120.86–370302.9	177	1.1	11.8	-0.86 ^{+0.05} _{-0.04}	-0.77 ^{+0.06} _{-0.05}	-0.73 ^{+0.21} _{-0.15}	7.35E-06	6.24E-06
190122.40–370055.4	35	2.5	4.3	0.10 ^{+0.20} _{-0.20}	-0.51 ^{+0.26} _{-0.23}	0.52 ^{+0.26} _{-0.23}	6.57E-07	1.11E-06
190122.84–365522.0	24	3.4	3.2	0.64 ^{+0.24} _{-0.19}	0.70 ^{+0.54} _{-0.33}	0.54 ^{+0.25} _{-0.22}	4.81E-07	5.62E-07
190123.49–365641.3	17	1.9	2.5	-0.51 ^{+0.30} _{-0.27}	0.02 ^{+0.32} _{-0.34}	-0.80 ^{+0.43} _{-0.21}	2.04E-07	3.83E-07
190123.95–365721.5	18	3.3	2.8	0.72 ^{+0.27} _{-0.19}	0.32 ^{+0.59} _{-0.63}	0.64 ^{+0.29} _{-0.23}	2.70E-07	4.40E-07
190125.61–370453.9	267	1.1	14.7	-0.91 ^{+0.03} _{-0.03}	-0.70 ^{+0.05} _{-0.05}	-0.94 ^{+0.11} _{-0.05}	1.09E-05	9.58E-06
190125.75–365919.3	2101	1.6	44.8	-0.38 ^{+0.02} _{-0.02}	-0.28 ^{+0.02} _{-0.02}	-0.31 ^{+0.03} _{-0.03}	4.40E-05	6.13E-05
190126.10–365501.9	96	2.4	8.4	0.21 ^{+0.11} _{-0.11}	0.20 ^{+0.15} _{-0.15}	0.10 ^{+0.13} _{-0.13}	2.57E-06	2.48E-06
190127.15–365908.6	890	1.0	28.8	-0.83 ^{+0.02} _{-0.02}	-0.80 ^{+0.02} _{-0.02}	-0.49 ^{+0.09} _{-0.09}	3.33E-05	2.61E-05
190128.72–365931.9	3706	1.5	59.8	-0.50 ^{+0.01} _{-0.01}	-0.42 ^{+0.02} _{-0.02}	-0.32 ^{+0.03} _{-0.03}	7.52E-05	1.02E-04
190129.01–370148.8	986	1.1	30.3	-0.81 ^{+0.02} _{-0.02}	-0.75 ^{+0.02} _{-0.02}	-0.45 ^{+0.08} _{-0.07}	3.19E-05	2.69E-05
190131.25–365931.1	15	3.0	2.6	0.66 ^{+0.30} _{-0.22}	0.87 ^{+0.55} _{-0.16}	0.27 ^{+0.32} _{-0.32}	2.76E-07	3.40E-07
190131.28–365931.0	15	3.0	2.6	0.66 ^{+0.30} _{-0.22}	0.87 ^{+0.55} _{-0.16}	0.27 ^{+0.32} _{-0.32}	2.79E-07	3.43E-07
190131.73–365445.4	9	1.0	1.5	-0.98 ^{+0.46} _{-0.18}	-0.82 ^{+0.49} _{-0.20}	-0.14 ^{+0.99} _{-1.35}	3.36E-07	2.01E-07
190132.01–365121.7	40	3.1	3.6	0.62 ^{+0.20} _{-0.17}	0.34 ^{+0.33} _{-0.33}	0.31 ^{+0.23} _{-0.23}	7.21E-07	7.84E-07
190132.34–365803.1	24	1.6	3.8	-0.81 ^{+0.20} _{-0.12}	-0.37 ^{+0.23} _{-0.23}	-0.68 ^{+0.40} _{-0.28}	3.69E-07	6.28E-07
190133.61–370606.2	42	1.9	3.8	-0.08 ^{+0.20} _{-0.21}	-0.23 ^{+0.24} _{-0.24}	-0.05 ^{+0.28} _{-0.30}	4.78E-07	1.16E-06
190133.84–365745.0	843	2.1	28.0	0.08 ^{+0.04} _{-0.04}	0.13 ^{+0.04} _{-0.04}	-0.07 ^{+0.04} _{-0.04}	1.61E-05	2.21E-05
190134.65–365438.4	11	2.6	1.8	0.24 ^{+0.40} _{-0.41}	-0.37 ^{+0.53} _{-0.53}	0.39 ^{+0.52} _{-0.51}	3.08E-07	2.25E-07
190134.84–370056.7	25568	1.3	158.9	-0.56 ^{+0.01} _{-0.01}	-0.56 ^{+0.01} _{-0.01}	-0.24 ^{+0.01} _{-0.01}	6.03E-04	6.89E-04
190135.42–370340.9	47	1.8	5.2	-0.26 ^{+0.17} _{-0.17}	-0.24 ^{+0.20} _{-0.20}	0.03 ^{+0.23} _{-0.24}	7.58E-07	1.18E-06
190137.07–365601.9	115	3.8	9.7	0.83 ^{+0.07} _{-0.05}	0.58 ^{+0.22} _{-0.19}	0.67 ^{+0.08} _{-0.07}	3.54E-06	3.37E-06
190139.15–365329.6	7772	1.1	87.1	-0.79 ^{+0.01} _{-0.01}	-0.73 ^{+0.01} _{-0.01}	-0.44 ^{+0.02} _{-0.02}	2.19E-04	2.17E-04
190139.34–370207.8	719	1.0	25.8	-0.89 ^{+0.02} _{-0.02}	-0.84 ^{+0.02} _{-0.02}	-0.63 ^{+0.11} _{-0.10}	2.37E-05	1.96E-05
190140.40–365142.4	598	2.6	23.0	0.41 ^{+0.04} _{-0.04}	0.39 ^{+0.05} _{-0.05}	0.03 ^{+0.05} _{-0.05}	1.33E-05	1.70E-05
190140.63–365758.9	6	0.5	1.5	-1.35 ^{+0.94} _{-0.65}	-1.08 ^{+0.82} _{-0.11}	0.52 ^{+2.14} _{-0.00}	3.35E-07	1.03E-07
190140.67–365923.9	14	3.5	2.7	0.58 ^{+0.30} _{-0.25}	-1.09 ^{+0.84} _{-0.12}	1.02 ^{+0.30} _{-0.01}	2.42E-07	3.61E-07
190140.70–370052.9	72	2.8	7.4	0.19 ^{+0.13} _{-0.13}	-0.11 ^{+0.18} _{-0.19}	0.38 ^{+0.15} _{-0.14}	1.39E-06	1.84E-06
190140.81–365234.0	21086	1.4	144.1	-0.57 ^{+0.01} _{-0.01}	-0.52 ^{+0.01} _{-0.01}	-0.31 ^{+0.01} _{-0.01}	4.87E-04	6.18E-04
190141.35–370419.3	37	1.9	4.2	-0.21 ^{+0.20} _{-0.20}	-0.52 ^{+0.24} _{-0.23}	0.32 ^{+0.30} _{-0.30}	5.29E-07	8.10E-07
190141.49–370441.7	40	2.1	4.3	0.05 ^{+0.20} _{-0.20}	-0.31 ^{+0.23} _{-0.23}	0.11 ^{+0.27} _{-0.28}	4.64E-07	9.07E-07
190141.55–365831.6	3041	2.7	54.1	0.40 ^{+0.02} _{-0.02}	0.38 ^{+0.02} _{-0.02}	0.16 ^{+0.02} _{-0.02}	9.61E-05	1.14E-04
190141.62–365953.1	1040	1.3	31.2	-0.61 ^{+0.03} _{-0.02}	-0.60 ^{+0.03} _{-0.03}	-0.25 ^{+0.06} _{-0.06}	2.28E-05	2.87E-05
190143.12–365020.9	62	3.1	5.2	0.71 ^{+0.14} _{-0.11}	0.81 ^{+0.26} _{-0.15}	0.39 ^{+0.16} _{-0.15}	9.41E-07	1.44E-06
190143.80–370614.0	173	2.2	11.1	0.07 ^{+0.08} _{-0.08}	-0.04 ^{+0.10} _{-0.11}	0.02 ^{+0.11} _{-0.11}	3.81E-06	4.75E-06
190144.22–365853.6	73	2.8	7.6	0.34 ^{+0.12} _{-0.12}	0.46 ^{+0.17} _{-0.16}	0.14 ^{+0.14} _{-0.14}	2.08E-06	2.56E-06
190145.91–364929.3	138	3.5	9.3	0.76 ^{+0.07} _{-0.06}	0.64 ^{+0.18} _{-0.15}	0.57 ^{+0.09} _{-0.09}	3.82E-06	4.45E-06
190146.18–370241.8	23	3.0	3.5	0.59 ^{+0.23} _{-0.20}	0.71 ^{+0.35} _{-0.23}	0.11 ^{+0.25} _{-0.26}	5.74E-07	5.83E-07
190147.01–365326.9	26	3.7	3.7	0.74 ^{+0.20} _{-0.15}	0.04 ^{+0.53} _{-0.61}	0.77 ^{+0.21} _{-0.15}	4.84E-07	6.83E-07
190148.02–365722.4	3606	3.3	59.0	0.72 ^{+0.01} _{-0.01}	0.63 ^{+0.02} _{-0.02}	0.40 ^{+0.02} _{-0.02}	8.42E-05	9.26E-05
190148.46–365714.5	22	4.1	3.7	1.02 ^{+0.15} _{-0.01}	1.18 ^{+1.12} _{-0.48}	0.83 ^{+0.20} _{-0.12}	4.77E-07	5.43E-07

¹ in band (0.2–8 keV)² in band (0.5–8 keV), in accordance with the COUP (HR = hardness ratio, FLUX1/2 = incident flux, see text)

CrA acis_extract source list cntd.

Src ID	Total counts ¹	Median E [keV] ¹	Source signif. ¹	HR1 ²	HR2 ²	HR3 ²	FLUX1 ² cm ⁻² s ⁻¹	FLUX2 ² cm ⁻² s ⁻¹
190148.53–370611.2	67	3.9	5.7	0.70 ^{+0.13} _{-0.10}	0.54 ^{+0.30} _{-0.26}	0.58 ^{+0.14} _{-0.13}	2.44E-06	1.56E-06
190148.97–370151.7	9	2.8	1.9	0.82 ^{+0.40} _{-0.18}	0.56 ^{+0.53} _{-0.51}	0.22 ^{+0.42} _{-0.45}	2.75E-07	2.85E-07
190149.35–370028.6	113	0.9	9.6	-0.94 ^{+0.05} _{-0.03}	-0.87 ^{+0.06} _{-0.05}	-0.86 ^{+0.42} _{-0.16}	5.04E-06	3.11E-06
190150.38–365935.3	11	4.1	2.4	0.84 ^{+0.33} _{-0.15}	1.10 ^{+0.82} _{-0.13}	0.45 ^{+0.35} _{-0.32}	2.80E-07	2.96E-07
190150.45–365638.1	260	2.1	15.1	0.04 ^{+0.06} _{-0.06}	-0.03 ^{+0.08} _{-0.08}	0.05 ^{+0.08} _{-0.08}	5.18E-06	6.83E-06
190150.66–365809.9	2623	3.1	50.2	0.57 ^{+0.02} _{-0.02}	0.49 ^{+0.03} _{-0.03}	0.29 ^{+0.02} _{-0.02}	8.70E-05	9.74E-05
190151.11–365412.5	61	1.9	6.6	-0.10 ^{+0.14} _{-0.14}	0.05 ^{+0.16} _{-0.16}	-0.27 ^{+0.18} _{-0.18}	1.04E-06	1.63E-06
190152.10–370542.4	80	3.4	6.7	0.69 ^{+0.11} _{-0.09}	0.40 ^{+0.24} _{-0.23}	0.55 ^{+0.12} _{-0.11}	1.20E-06	1.99E-06
190152.20–365809.0	16	5.1	3.0	1.02 ^{+0.21} _{-0.01}	-0.08 ^{+1.20} _{-0.00}	1.01 ^{+0.21} _{-0.00}	5.60E-07	4.86E-07
190152.63–365700.2	249	2.2	14.8	0.13 ^{+0.07} _{-0.07}	0.29 ^{+0.08} _{-0.08}	-0.16 ^{+0.08} _{-0.08}	4.99E-06	6.45E-06
190153.67–365708.3	982	3.3	30.3	0.50 ^{+0.03} _{-0.03}	0.18 ^{+0.05} _{-0.05}	0.43 ^{+0.03} _{-0.03}	2.34E-05	2.59E-05
190153.92–365228.8	29	3.5	3.5	0.73 ^{+0.20} _{-0.15}	0.84 ^{+0.46} _{-0.18}	0.48 ^{+0.22} _{-0.21}	6.05E-07	7.05E-07
190155.31–365722.0	254	5.2	14.9	0.97 ^{+0.02} _{-0.01}	0.78 ^{+0.41} _{-0.22}	0.95 ^{+0.03} _{-0.02}	1.00E-05	7.54E-06
190155.61–365651.1	41	4.5	5.4	0.96 ^{+0.10} _{-0.03}	0.65 ^{+0.56} _{-0.38}	0.81 ^{+0.14} _{-0.10}	1.56E-06	1.24E-06
190155.76–365727.7	20	4.4	3.5	1.02 ^{+0.17} _{-0.00}	1.06 ^{+0.57} _{-0.06}	0.60 ^{+0.20} _{-0.20}	7.67E-07	7.15E-07
190155.85–365204.3	380	3.7	18.1	0.78 ^{+0.04} _{-0.03}	0.53 ^{+0.10} _{-0.09}	0.61 ^{+0.05} _{-0.04}	1.14E-05	1.12E-05
190156.39–365728.4	107	4.7	9.4	0.98 ^{+0.04} _{-0.01}	0.36 ^{+0.69} _{-0.73}	0.96 ^{+0.05} _{-0.02}	6.32E-06	5.01E-06
190157.46–370311.9	29	1.4	3.9	-0.47 ^{+0.22} _{-0.20}	-0.48 ^{+0.24} _{-0.22}	-0.15 ^{+0.38} _{-0.40}	4.04E-07	6.64E-07
190158.32–370027.5	24	1.8	3.9	-0.19 ^{+0.23} _{-0.23}	-0.22 ^{+0.26} _{-0.27}	-0.11 ^{+0.32} _{-0.34}	4.48E-07	6.49E-07
190158.79–365750.1	14	1.3	2.7	-0.78 ^{+0.29} _{-0.17}	-0.58 ^{+0.29} _{-0.24}	-1.37 ^{+0.95} _{-0.71}	3.11E-07	5.39E-07
190200.11–370222.3	538	1.0	22.1	-0.92 ^{+0.02} _{-0.02}	-0.86 ^{+0.03} _{-0.02}	-0.55 ^{+0.15} _{-0.13}	2.05E-05	1.47E-05
190200.49–365507.2	27	3.4	4.0	0.96 ^{+0.15} _{-0.04}	0.79 ^{+0.53} _{-0.25}	0.62 ^{+0.21} _{-0.17}	7.74E-07	6.92E-07
190201.92–370743.0	5966	1.1	76.1	-0.78 ^{+0.01} _{-0.01}	-0.74 ^{+0.01} _{-0.01}	-0.39 ^{+0.03} _{-0.03}	5.79E-04	4.93E-04
190201.94–365400.1	47	3.4	5.5	0.76 ^{+0.13} _{-0.10}	0.56 ^{+0.28} _{-0.24}	0.42 ^{+0.17} _{-0.16}	1.08E-06	1.18E-06
190202.16–365919.1	14	4.6	2.7	0.88 ^{+0.30} _{-0.11}	1.97 ^{+2.37} _{-4.13}	0.87 ^{+0.29} _{-0.13}	3.65E-07	3.18E-07
190203.82–365851.0	41	4.1	5.3	0.92 ^{+0.12} _{-0.06}	0.55 ^{+0.42} _{-0.35}	0.70 ^{+0.15} _{-0.12}	1.22E-06	1.08E-06
190204.22–370420.9	183	2.3	12.0	0.16 ^{+0.08} _{-0.08}	0.01 ^{+0.10} _{-0.10}	0.13 ^{+0.09} _{-0.09}	4.10E-06	5.40E-06
190204.34–365859.0	14	4.2	2.6	0.90 ^{+0.28} _{-0.10}	1.25 ^{+0.91} _{-0.43}	0.57 ^{+0.30} _{-0.25}	3.73E-07	3.48E-07
190205.84–365444.2	21	2.9	3.0	0.65 ^{+0.25} _{-0.20}	0.64 ^{+0.46} _{-0.33}	0.33 ^{+0.28} _{-0.27}	4.21E-07	4.76E-07
190206.33–370244.8	29	2.6	3.7	0.15 ^{+0.25} _{-0.25}	-0.19 ^{+0.36} _{-0.38}	0.44 ^{+0.29} _{-0.27}	9.57E-07	5.69E-07
190210.72–370559.2	53	2.4	5.2	0.10 ^{+0.17} _{-0.17}	-0.47 ^{+0.22} _{-0.20}	0.53 ^{+0.21} _{-0.18}	2.67E-06	2.50E-06
190211.99–370309.4	86	1.2	7.5	-0.76 ^{+0.09} _{-0.08}	-0.79 ^{+0.10} _{-0.07}	-0.07 ^{+0.30} _{-0.32}	2.87E-06	2.30E-06
190214.60–370032.0	24	2.9	3.2	0.39 ^{+0.25} _{-0.24}	-0.19 ^{+0.40} _{-0.43}	0.52 ^{+0.30} _{-0.26}	3.13E-07	5.41E-07
190215.00–365232.2	39	1.8	4.1	-0.29 ^{+0.20} _{-0.19}	-0.75 ^{+0.23} _{-0.16}	0.63 ^{+0.30} _{-0.23}	1.19E-06	1.48E-06
190216.54–365637.8	34	3.7	3.9	0.84 ^{+0.17} _{-0.10}	0.43 ^{+0.51} _{-0.48}	0.71 ^{+0.19} _{-0.15}	6.36E-07	7.70E-07
190219.19–370346.3	67	3.4	5.7	0.77 ^{+0.12} _{-0.09}	0.72 ^{+0.28} _{-0.19}	0.51 ^{+0.14} _{-0.13}	1.31E-06	1.91E-06
190221.22–365013.5	63	2.7	5.8	0.24 ^{+0.15} _{-0.15}	-0.11 ^{+0.20} _{-0.21}	0.26 ^{+0.18} _{-0.18}	4.18E-06	4.32E-06
190221.79–365604.2	73	4.4	6.1	0.85 ^{+0.10} _{-0.07}	0.03 ^{+0.34} _{-0.37}	0.79 ^{+0.11} _{-0.09}	1.94E-06	1.78E-06
190222.12–365313.2	28	1.9	3.1	-0.24 ^{+0.25} _{-0.25}	-0.02 ^{+0.27} _{-0.28}	-0.55 ^{+0.33} _{-0.28}	7.58E-07	1.22E-06
190222.13–365541.0	5485	1.3	72.9	-0.63 ^{+0.01} _{-0.01}	-0.55 ^{+0.01} _{-0.01}	-0.38 ^{+0.02} _{-0.02}	1.89E-04	2.25E-04
190222.71–365308.5	28	2.5	3.3	0.17 ^{+0.24} _{-0.24}	0.11 ^{+0.32} _{-0.34}	0.16 ^{+0.28} _{-0.29}	1.26E-06	1.46E-06
190227.05–365813.2	377	1.6	17.6	-0.43 ^{+0.05} _{-0.05}	-0.37 ^{+0.06} _{-0.06}	-0.20 ^{+0.08} _{-0.08}	8.68E-06	1.15E-05
190233.07–365821.1	109	2.2	9.1	0.01 ^{+0.10} _{-0.10}	-0.48 ^{+0.13} _{-0.12}	0.50 ^{+0.13} _{-0.12}	8.05E-06	8.62E-06

¹ in band (0.2–8 keV)² in band (0.5–8 keV), in accordance with the COUP (HR = hardness ratio, FLUX1/2 = incident flux, see text)

Chapter 5

Searching for coronal radio emission from protostars by VLBI

5.1 Introduction

The first YSO observations using Very-Long-Baseline Interferometry (VLBI) were reported in the late 1980s. Felli et al. (1989) reported the VLBI detection of radio emission from the young stellar object θ^1 Orionis A. André et al. (1991) reported nonthermal gyrosynchrotron radiation towards the young magnetic B star ρ Oph S1. André et al. (1992) report on a VLBI survey of the ρ Oph star-forming region, showing that several T Tauri stars have nonthermal radio emission, although detections did not include protostellar embedded sources (like IRAS 16293–2422). The very active system HD 283447 (= V773 Tau), located in the Taurus-Auriga molecular cloud complex at a distance of $d=140$ pc, could be resolved at VLBI scales (Phillips et al. 1991, 1996). It consists of two class III objects and therefore does not have a disk. The VLBI observations have shown that the emission arises from regions of some tenths of an AU. In particular, Phillips et al. (1996), who also conducted simultaneous VLA observations (see below), were able to map a source of ~ 10 mJy which shows one fourth of the total intensity contained in a component of $\gtrsim 0.5$ AU, approximately the size of the binary system. The bulk of the radiation comes from two small unresolved components related to the two stars. The reason of the large flares observed in this system is different from the mechanisms listed above; the flares are clustered around the periastron passage of the binary system and therefore probably due to colliding interbinary stellar coronal structure involving helmet streamers (Massi et al. 2002, 2006, see Chapter 7). As a matter of fact, Phillips et al. (1991, 1996) have performed several other VLBI observations of this source outside the periastron flaring window and observed a source of a size of a few stellar radii, much smaller than the dimensions of the binary system.

As explained in the Introduction (Section 1.2.4), compact nonthermal emission from YSOs easily is concealed by thermal radio emission from ionized plasma, for example at the base of outflows (e.g. André 1987). The VLBI observations of the class II protostar T Tau-S by Smith et al. (2003), in which the VLBA, the VLA, and the Effelsberg 100m telescope were used at a wavelength of 3.6 cm, are very important in this respect: Weak and variable emission (between 1.4 and 3.8 mJy) was finally detected, even if unresolved with the 1 mas FWHM beam. From multi-epoch VLBI observations of the same source, Loinard et al. (2005) confirm the detection of a compact radio source and derive a parallax yielding a precise distance ($141.5^{+2.8}_{-2.7}$ pc).

In Section 5.2, the target selection procedure is described. Then in Section 5.3, the actual VLBI observations and their analysis are presented. The results are described in Section 5.4 and finally, the results are summarized in Section 5.5.

Table 5.1: Journal of observations¹

Source	d [pc]	Phase ref.	Project	Date	Time (UTC)	On-source ²	VLA ³
YLW 15	130	J1625-2517	BF083 ⁴	30 Apr 2005	06:15–10:15	142.0 min	B
HL Tau & L1551	140	J0431+1731	BF084a ⁵	03 Jul 2005	12:30–16:30	64.1 min	BnC
EC 95	310	J1838+0404	BF084b	29 Jul 2005	01:00–04:00	90.4 min	C
HL Tau & L1551	140	J0431+1731	BF089 ⁶	24 May 2006	15:00–19:00	65.5 min	AnB

¹ HSA observations except for BF83 (VLBA+VLA+GBT)

² scan minutes, not taking into account the number of antennas observing

³ configuration of the VLA during the observation

⁴ VLBA without LA

⁵ Arecibo data lost

⁶ BF84a reobserved

5.2 Target selection

In order to establish the role of the disk or star/disk interaction, we planned to observe nearby protostars at an earlier stage than class III at $\lambda = 3.6$ cm by VLBI, trying to detect nonthermal radio emission. Given the difficulties described, we first had to define a good sample of target sources. We selected class I and class II protostellar sources which were detected in centimetric radio as well as in (variable) X-ray emission as a tracer of coronal magnetic activity. Preferably, the centimetric radio detections show signs of nonthermal emission by variability or spectral index. These criteria already produce only few candidate sources so that an additional distance criterion in order to ensure an optimal physical resolution was not applied. In our actual observations (see below), synthesized beam sizes of down to 0.2×0.1 AU were realized. We chose an observing frequency of 8.4 GHz ($\lambda = 3.6$ cm) as a compromise between a reduced influence of free-free-absorption compared to longer wavelengths and ensuring a good sensitivity by using a standard frequency allowing the use of the Arecibo 305m telescope.

Our sample consists of the class 0/I binary protostar YLW 15, the class I binary protostar L1551 IRS5, the class II source HL Tau, as well as the proto-Herbig Ae/Be star EC 95. Distances range from 130 pc to 310 pc (see Table 5.1). As noted above, YLW 15 was observed with VLBI before (Girart et al. 2004). Except for this source (YLW 15), all sources are in the declination range accessible to the Arecibo 305m telescope and thus were observed with the full High Sensitivity Array (HSA), consisting of the VLBA, the phased VLA, Arecibo, GBT, and Effelsberg.

5.2.1 The binary protostar YLW 15

YLW 15 is a binary protostar whose components are in the class 0/I stages. It is located in the ρ Oph dark cloud at a distance of 130 pc (Rebull et al. 2004), and it shows X-ray as well as radio emission. It was found to be a radio binary (with components named VLA 1 and VLA 2, Girart et al. 2000), whose orbital parameters were estimated by Curiel et al. (2003) from multi-epoch VLA observations. After an early VLBI attempt to detect nonthermal radio emission from the YLW 15 system yielded an upper flux density limit of 1 mJy (André et al. 1992), recent VLBI observations were reported by Girart et al. (2004) who observed at a wavelength of 6 cm and achieved an upper limit of 0.2 mJy (4σ). However, the authors note that both the non-detection of the source on the VLA-Goldstone baseline and their finding that the source has a non-variable radio spectrum point towards an extended source of thermal free-free emission at this wavelength. Interestingly, their additional near- and mid-infrared data indicates that VLA 1 is more deeply embedded (or less luminous) than VLA 2 while the orbital motion indicates that VLA 1 is the more massive object.

VLA 2 is responsible for strong quasi-periodic X-ray emission explained as due to the fast rotation of the star with respect to the disk (Tsuboi et al. 2000; Montmerle et al. 2000). The

consequent star-disk shearing of the magnetic field lines gives rise to magnetic reconnection and therefore creation of energetic electrons producing the quasi-periodic X-ray emission. nonthermal radio emission is therefore expected. The integrated flux at 3.6 cm, derived from VLA measurements, is $S_{3.6\text{cm}} = 0.64 \dots 0.78$ mJy (Girart et al. 2004). When comparing the VLBA-only non-detection at a wavelength of 6 cm with VLA data at the same wavelength, it seems that at least two thirds of the total emission is thermal emission from a collimated outflow partially resolved at VLA scales (Girart et al. 2004). The nonthermal contribution is thus embedded in an absorbing thermal medium.

5.2.2 The binary protostar LDN 1551 IRS 5

This source, located at a distance of 140 pc in Taurus, is one of the best-known deeply embedded young stellar objects. It drives one of the most spectacular bipolar outflows, the first ever detected (Snell et al. 1980), extending $> 10'$ (e.g. Moriarty-Schieven & Snell 1988) and also an optically visible jet very close to the position of the hidden driving source (Mundt & Fried 1983). The dark cloud LDN 1551 itself is one of the nearest and most active regions of ongoing low-mass stars formation. IRS 5 is the most luminous YSO in this region ($L = 40 L_{\odot}$), though deeply embedded ($A_V \approx 150$ mag, e.g., White et al. 2000). Rodríguez et al. (1998) discovered that IRS 5 is a protobinary separated by 40 AU (see also Rodríguez et al. 1986). Based on VLA observations at $\lambda = 7$ mm, they detected two protoplanetary disks with semimajor axes of about 10 AU. The integrated flux densities at $\lambda = 3.6$ cm are 0.78 mJy and 0.70 mJy for the northern and southern component, respectively (Rodríguez et al. 1998). Most recently, Lim & Takakuwa (2005) analyze the source at 7 mm using the VLA combined with the Pie Town VLBA antenna, and find that L1551 IRS 5 may actually be a triple system.

Favata et al. (2002) detected a faint X-ray source near IRS 5 in an observation carried out with XMM-Newton. Bally et al. (2003), presenting *Chandra* X-ray data of higher angular resolution, conclude that an X-ray source is located at the base of the jet. The source, named ACIS 31, is located about $0''.5$ west of IRS 5 with 60 counts registered in the 0.5 – 8 keV band in a 79 ksec exposure, 47 of them coming from within $1''.7$ of the source. Due to the difference in angular resolution between the XMM-Newton and *Chandra* data, it cannot be excluded that the X-ray emission is instead due to the protostar itself (although that appears to be unlikely, see Favata et al. 2006 who interpret morphological changes in the source as due to jet motion).

5.2.3 The class I/II transition protostar HL Tau

HL Tau is a strong-emission (‘classical’) T Tauri star, deeply embedded in dusty nebulosity associated with a reflection nebula. In the evolutionary sequence, it is in a transition phase between class I and class II. There is strong extinction towards the central source ($A_V > 22$ mag, Stapelfeldt et al. 1995), although the star is detected in the near-infrared (Weintraub et al. 1995; Beckwith & Birk 1995). The morphology of the optical and NIR reflection nebula as well as the flat spectral energy distribution of HL Tau can be explained by scattering and thermal emission from an infalling, dusty protostellar envelope typical of Taurus class I sources (Calvet et al. 1994). The star is associated with the outflow system HH 266. At centimeter radio wavelengths, HL Tau has been analyzed by Rodríguez et al. (1992, 1994), using the VLA. At $\lambda = 1.3$ cm, they observe an elongated structure (about $1''.4 \times 0''.6$, or about 200×80 AU at a distance of 140 pc) surrounding the star. The authors argue that the size and the integrated flux density of this source (2.9 ± 0.4 mJy) at $\lambda = 1.3$ cm indicate that the emission originates from dust in a protoplanetary disk. At $\lambda = 3.6$ cm, the picture is strikingly different: Here, the observed structure is elongated approximately in the east-west direction (with an integrated flux density of 0.52 ± 0.02 mJy) while the structure seen at $\lambda = 1.3$ cm is elongated approximately in the north-south direction. The authors argue that in contrast to the emission at $\lambda = 1.3$ cm, the emission at $\lambda = 3.6$ cm is dominated by free-free radiation from an ionized outflow. In order

to study the structure of its circumstellar material, HL Tau has been studied extensively at millimeter and submillimeter wavelengths (Lay et al. 1994; Mundy et al. 1996; Lay et al. 1997; Looney et al. 2000). Favata et al. (2003) discuss X-ray data of HL Tau. While the source seems to have been quiescent during XMM-Newton observations, there are *Chandra* data containing evidence for a short-duration flare.

5.2.4 The Proto-Herbig Ae/Be star EC 95

EC 95 is a very young intermediate-mass star (i.e., up to $5 M_{\odot}$), presumably a precursor of a Herbig AeBe (HAeBe) star, therefore not a low-mass protostar like our other sources. It is located in the Serpens cloud core at a distance of 310 pc.

The source has an X-ray luminosity of $2 \times 10^{33} \text{ erg s}^{-1}$ (Preibisch 1998). Radio emission has been detected (with peak flux densities $S_{8.4\text{GHz}} \sim 0.6 \text{ mJy}$ and $S_{5\text{GHz}} \sim 0.8 \text{ mJy}$) by Smith et al. (1999). The slightly negative spectral index (in $S \propto \nu^{\alpha}$) is inconsistent with thermal emission from an optically thick wind, where rather $\alpha = +2$ is expected (Simon et al. 1983). There is also evidence for variability on timescales of years. Eiroa et al. (2005) report a peak flux density of $1.65 \pm 0.1 \text{ mJy}$ on October 24th, 1993, also from 3.5 cm observations carried out with the VLA in CnD configuration. Only about one month earlier (in the observations reported by Smith et al. (1999), the source was more than three times fainter.

Although intermediate-mass stars are thought to be fully radiative, and therefore should not have a corona, previous detections of X-rays from HAeBe stars have been made (e.g. Zinnecker & Preibisch 1994). Tout & Pringle (1995) suggested that radially differential rotation in intermediate-mass stars could lead to the formation of a temporary convective layer and hence a corona. They estimated that the lifetime of such a corona would be of order 10^6 years, approximately the timescale for intermediate-mass objects to evolve onto the main sequence. On the other hand, a companion star responsible for the corona cannot be excluded. Another explanation of X-ray emission from Herbig Ae/Be stars involves star-disk interactions (Hamaguchi et al. 2005b). See also the discussions on R CrA in Chapters 2 to 4.

5.3 Observations and data analysis

In order to reach the highest possible sensitivity we used the world's biggest radio telescopes besides the 10-antenna NRAO Very Long Baseline Array (VLBA), mainly the High Sensitivity Array (HSA) consisting of the Arecibo 305 m, the Effelsberg and Green Bank (GBT) 100 m radio telescopes, the phased Very Large Array (VLA) as well as the VLBA (ten antennas of 25 m diameter each). The usage of the phased VLA, equivalent in sensitivity to a large single-dish telescope of 130 m diameter, has the additional advantage of providing regular VLA data as well. Thus, the source positions can be checked before correlation. All runs were phase-referencing observations in dual polarization (RCP & LCP) taken at 256 MBit/s, eight baseband channels of 8 MHz bandwidth covering an aggregate bandwidth of 32 MHz, and 2-bit sampling (mode 4cm 256-8-2-UL). Each observation was correlated with 16 channels per IF. The field of view is limited by time-smearing due to the correlator averaging time. Its size is estimated to be $\sim 1''.8$ for YLW 15 and $\sim 3''.3$ otherwise. Basic observation parameters including the phase reference sources used are listed in Table 5.1. The phase reference sources were within $52'$ (YLW15), $\sim 40'$ (HL Tau & L1551 IRS5), and 3.6° (EC 95) of the program sources; cycle times of a few minutes were used.

In order to confirm the correlator positions, the VLA data for all sources were analyzed separately (Fig. 5.2, see text below). Confirming the position was especially important in case of YLW 15 due to the apparent orbital motion of its components. YLW 15 and EC 95 were calibrated using a standard total flux density of 3C286 of 5.22 Jy while HL Tau and L1551 IRS 5 was calibrated using a model of J0530+1331 derived from self-calibration and yielding a flux

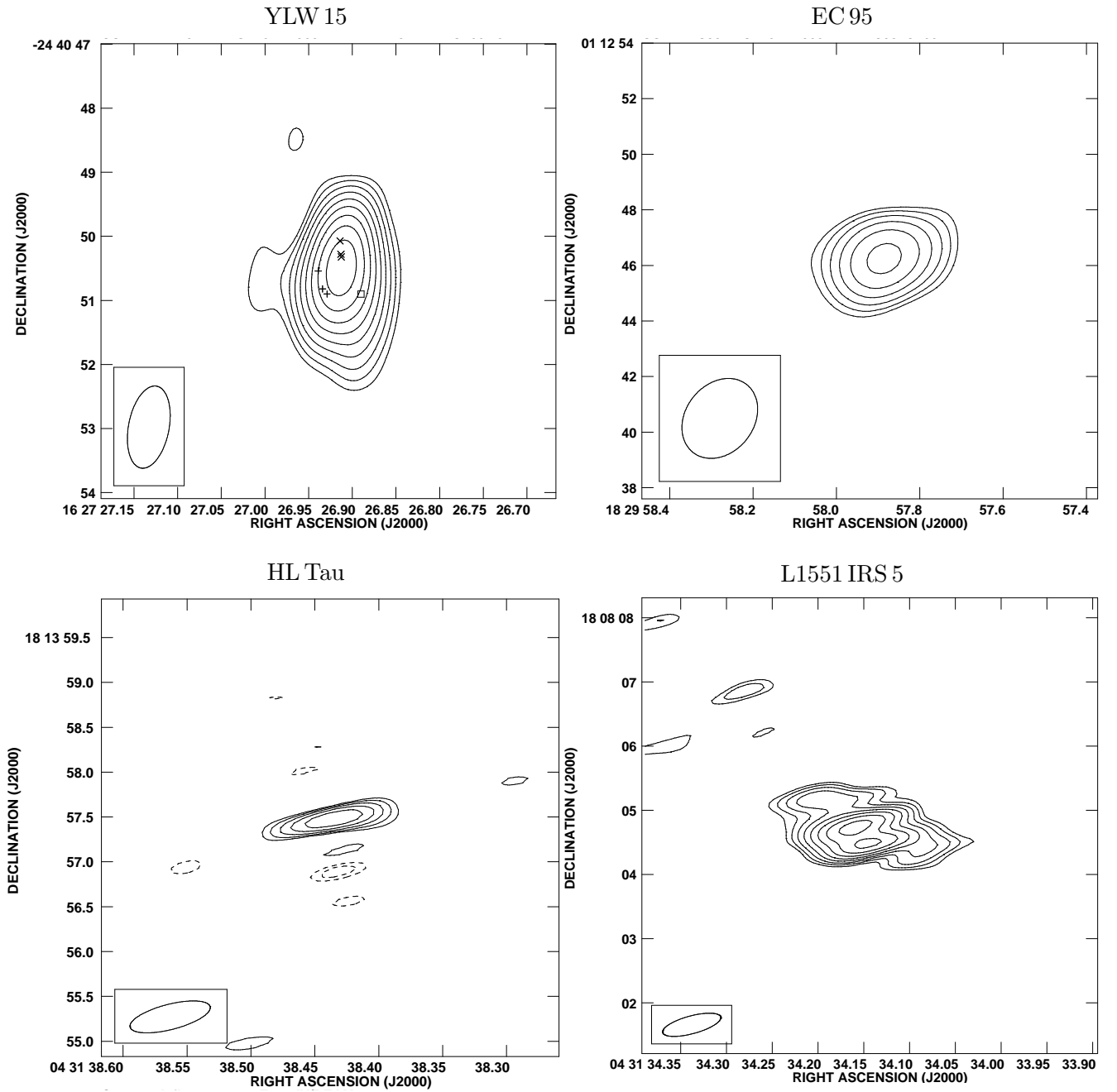


Figure 5.1: VLA-only maps of the four program sources YLW 15-VLA2, EC95, HL Tau, and L1551 IRS5. Note that YLW 15 is dominated by VLA 1 (see also Fig. 5.2 for an image restored with a smaller beam). For the two components of YLW 15, the proper motions as read from Fig. 2 in Curiel et al. (2003) are shown (‘x’ for VLA 1 and ‘+’ for VLA 2) together with the correlation position (‘o’), see text. For all sources the contour lines delineate multiples of the 3σ image noise, $(-2, -\sqrt{2}, -1, 1, \sqrt{2}, 2, \dots) \times 3\sigma$, increasing by factors of $\sqrt{2}$. The respective 3σ levels are $72 \mu\text{Jy}$ (YLW 15), $79 \mu\text{Jy}$ (EC 95), $72 \mu\text{Jy}$ (HL Tau), and $74 \mu\text{Jy}$ (L1551).

density of 3.62 Jy . While EC 95 and HL Tau were correlated simply at the positions of the singular emission peaks, and L1551 IRS 5N was correlated at the position of the northern component, YLW 15-VLA2 was correlated at a position in the south-western appendix to the main source as seen more clearly in a VLA-only image restored with a circular $0''.4$ beam, smaller than the synthesized beam (Fig. 5.2). The correlation parameters used are listed in Table 5.2 for all sources.

Figure 5.2: VLA-only map of YLW 15, restored with a circular $0''.4$ beam. The proper motions of the two components as determined by Curiel et al. (2003) are indicated (years 1990, 2000, and 2002 form north to south for both sources) together with the chosen VLBI correlation position (box). The contour lines delineate multiples of 0.1 mJy ($\sim 4\sigma$), increasing by factors of $\sqrt{2}$ (as explained for Fig. 5.1).

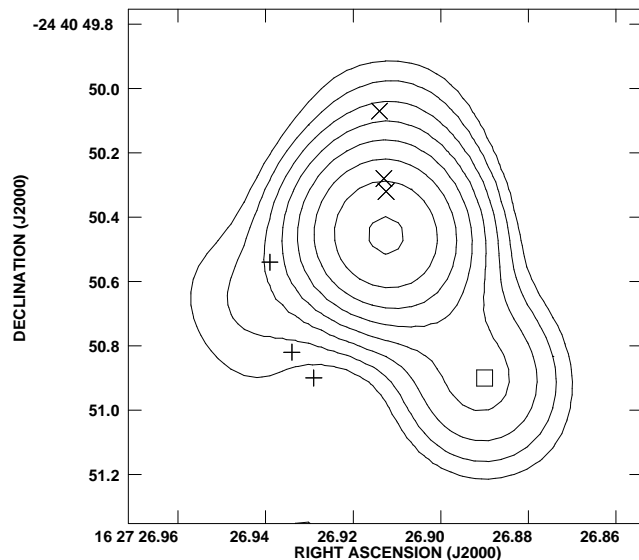


Table 5.2: VLBI correlator parameters

Source	RA (J2000)	Dec (J2000)	coravg ¹
YLW 15 VLA 2	16h27m26.89s	-24°40'50''.9	4s
EC 95	18h29m57.92s	+01°12'46''.0	2s
HL Tau	04h31m38.432s	+18°13'57''.485	2s
L1551 IRS 5	04h31m34.158s	+18°08'04''.760	2s

¹ correlator averaging time

All VLA and VLBI data were analyzed with the NRAO Astronomical Image Processing System (AIPS). After correcting the antenna parallactic angles recorded in horizontal coordinates and after applying the latest Earth Orientation Parameters, the dispersive delays caused by electrons in the earth's ionosphere were accounted for using Global Positioning System (GPS) models of the electron content of the ionosphere. Before amplitude calibration, the T_{sys} and gain curves of the phased VLA (which is recording ratios of antenna to system temperatures) were read, and the flux density scale was set using a calibrator source. Scans taken during telescope slewing were flagged. After correcting sampler voltage offsets using autocorrelation total-power spectra, the *a priori* amplitude calibration was applied based on the T_{sys} and gain tables. Then, in order to remove instrumental residual delays, phase corrections had to be applied, ideally using pulse-cal information inserted into the data during the observations. Since there is no such information in the VLA and Arecibo data, these corrections had to be derived from the fringes on a strong source for baselines involving these telescopes. From them, the residual delay and phase can be computed, which can then be taken into account. Finally, global time-dependent phase errors have to be corrected (e.g. phase gradients between the IFs). These are mainly due to inaccuracies in the geometrical delays assumed during correlation, causing phases varying rapidly with time. They were corrected with a fringe-fitting algorithm devised by Schwab & Cotton (1983). Before the final application of calibration information, the program sources were phase-referenced to their respective calibrator sources. As a check of global calibration quality, the calibrator sources were referenced to themselves and subsequently imaged (see Fig. 5.3). No polarization calibration was attempted because of the very weak flux densities detected. Maps were created without a uv taper, setting the ROBUST parameter in IMAGR to zero.

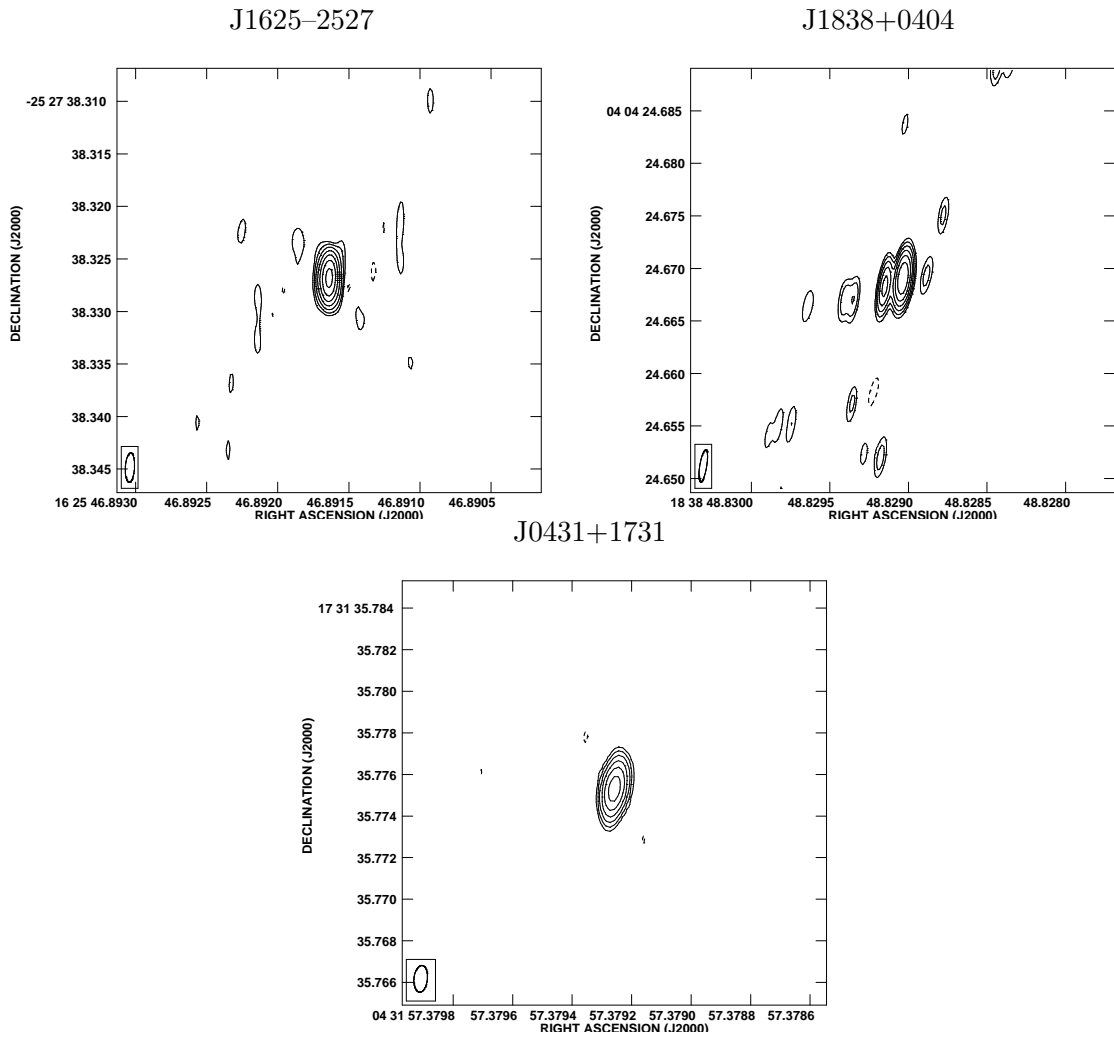


Figure 5.3: VLBI maps of the phase calibrators used in the experiments. Contour lines start at 7σ , increasing by factors of 2 like $(-2, -1, 1, 2, 4, 8, \dots) \times 7\sigma$; The 1σ image rms noise levels are 1.38 mJy (J1625-25, used for YLW 15), 0.20 mJy (J1838+04, used for EC 95), and 0.40 mJy (J0431+17, used for HL Tau and L1551), as determined from images of 1024×0.2 mas side length, respectively.

Table 5.3: VLA-only results

Source	synth. beam	map peak ¹	map rms ¹
YLW 15	$1''.3 \times 0''.6$, PA -10.3°	1.48 mJy ²	0.024 mJy
EC 95	$3''.1 \times 2''.4$, PA -38.5°	0.55 mJy	0.026 mJy
HL Tau	$0''.9 \times 0''.3$, PA -74.2°	0.40 mJy	0.024 mJy
L1551 IRS 5	$0''.9 \times 0''.3$, PA -74.2°	0.99 mJy ³	0.025 mJy

¹ peak flux densities and rms

² at position of main source (VLA 1)

³ northern component

5.4 Results

5.4.1 VLA data

As stated above, we analyzed the VLA-only data taken of each source as part of the VLBI experiments in order to refine the source positions for the correlator. All sources were detected (Table 5.3). The VLA results for the program sources are presented in Fig. 5.1 and in Table 5.3.

YLW 15 For YLW15 with its previously analyzed proper motion it was especially difficult to extract the position of YLW15-VLA2 out of the VLA data where VLA1 and VLA2 are blended. We chose the south-western appendix to the main source VLA1, as seen more clearly in an image of our VLA data restored with a circular $0''.4$ beam (Fig. 5.2). It remains unclear whether this emission is due to VLA 2. This position is unexpected given the predictions of (Curiel et al. 2003 – the positions from their Fig. 2 are plotted into our VLA maps in Fig. 5.1 and Fig. 5.2) – but the angular resolution of our VLA data is not good enough to decide this issue. On the other hand, the predictions are based on only three positions, thus the orbit is not yet fully determined. Given that the observations discussed by Curiel et al. (2003, see also Girart et al. 2004) were carried out in 1990, 2000, and 2002, the big change seen since then in only about three years – if VLA2 is in the above-mentioned appendix – could possibly be explained by the periastron passage of VLA 2. More observations are needed in order to reliably determine the orbit.

The integrated flux densities of the two components (VLA 1 and 2) as given by Girart et al. (2004) are 2.18 mJy and 2.14 mJy in 2000 and 2002, respectively, whereas the integrated flux density of VLA 1 is 1.40 mJy and 1.51 mJy for the two epochs. In our case, the integrated flux density for both sources is 2.18 mJy. Assuming therefore no significant long-term variability, the flux density of VLA 2 is 0.67–0.78 mJy.

LDN 1551 IRS 5 Both components of LDN 1551 IRS 5 are of similar flux density. We found the northern component, of special interest here, to be slightly brighter than the southern component in our VLA data while Rodríguez et al. (1998) found the opposite in 1996 data. The peak flux density in our data of 0.99 mJy at the position of the northern component compares to a peak flux density of ~ 0.5 mJy at the position of the southern component in their data (Rodríguez et al. 1998, Fig. 2). The source morphology in both datasets is similar, and differences in the observed source positions are much smaller than the beam size.

HL Tau The peak flux density of HL Tau, as determined from our VLA-only data is 0.40 mJy which is compatible with the peak flux density of ~ 0.3 mJy determined by Rodríguez et al. (1994, Fig. 2). Since their measurement in 1992, the source has shifted eastward by about $0''.5$. However, this displacement is along the major axis of the elongated synthesized beam in our data which also prevents a confirmation of the slight east-west elongation of HL Tau apparent in the 1992 data.

EC 95 In 1995, EC 95 was observed twice at peak flux densities of 0.64 ± 0.02 mJy (May 1st, D array) and 0.62 ± 0.02 mJy (July 20th, A array), respectively; an observation carried out on September 21st, 1993 (in CnD array configuration) yields a peak flux density of 0.5 ± 0.1 mJy (Smith et al. 1999). These flux density is very close to the 0.55 ± 0.07 mJy found in our data, although different from the 1.65 ± 0.1 mJy reported by Eiroa et al. (2005) for October 1993.

5.4.2 VLBI data

While all four target sources were detected with the VLA (observing in various configurations, see above), the clean maps produced from the VLBI data contain only one detection. Basic results for each source, including the rms noise level achieved, are listed in Tab. 5.4.

In the VLBI data of YLW 15-VLA 2, we find a persistently detected weak source of $\sim 7 - 9\sigma$ (see Fig. 5.4). In particular, the detection is reproduced when using different cell sizes in image reconstruction, different weighting parameters in the uv plane (ROBUST parameter in AIPS or using a uv taper to reduce the weights of the visibilities with the longest baselines).

The peak flux density of this unresolved source is 0.145 ± 0.016 mJy, therefore almost 20% of the flux density of VLA 2 is due to compact emission of $< 0.4 \times 0.1$ AU (FWHM beam size).

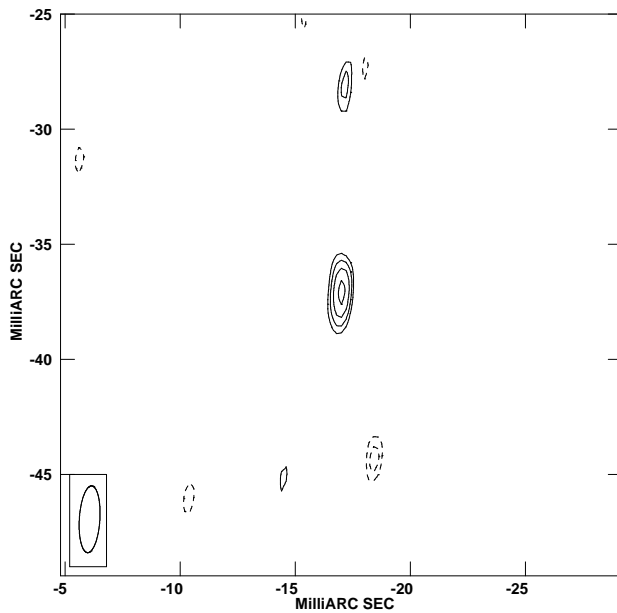


Figure 5.4: Weak source found in the VLBI data close to the putative position of YLW 15 YLW 2 at RA 16h27m26.88875s, Dec $-24^{\circ}40'50''.937$. The source reaches a significance of $\sim 9\sigma$. The contour lines delineate multiples of 3σ , as explained for Fig. 5.1. The 1σ rms noise level is $15.4 \mu\text{Jy}$.

No compact emission was detected towards VLA 1. Interestingly, the direction of the outflow towards YLW 15 as seen in CO appears to be quite close to the direction of the line of sight because the integrated line wing emission overlaps considerably (Bontemps et al. 1996). This may cause a favourable viewing geometry onto the central source along the jet.

YLW 15 has been observed in the near-infrared using ISAAC at the ESO Very Large Telescope (VLT) only 1.5 months after our VLBI run (16 June 2005). Since only VLA 2 is supposedly detected in J band (e.g. Allen et al. 2002; Girart et al. 2004), these data can help assessing the position of this source independently. Six exposures of 15 sec duration were obtained from the ESO Science Archive (program code 075.C-0561, PI: B. Nisini). They were reduced using the *jitter* algorithm implemented in the ESO Eclipse package. The accuracy of the astrometry was improved using a fit to the five 2MASS PSC sources in the field of view. With such a low number of reference sources, however, it is difficult to judge the astrometric accuracy, especially since all sources presumably are members of the star-forming region. The general astrometric accuracy of 2MASS is $< 0''.1$. A neighbouring source to YLW 15, some $8''$ away, is fitted to $\lesssim 0''.1$ while the remaining 2MASS sources, all quite close to the limits of the field of view though in different directions from YLW 15, are fitted to $\lesssim 0''.2$. The astrometric precision of the infrared data is thus estimated to be $\lesssim 0''.2$, or at least $< 0''.3$. Fig. 5.5 shows the vicinity of the detected infrared source together with the positions from previous proper motion analysis (Curiel et al. 2003; Girart et al. 2004, see above) and the position of the weak VLBI source indicated by circles of $0''.1$, $0''.2$, and $0''.3$ radius. The infrared emission appears to be unrelated to the VLBI source. However, the observed near infrared ($1-2 \mu\text{m}$) emission from deeply embedded objects often is not directly due to the protostar, but rather a combination of stellar light scattered at circumstellar material as well as line emission from shock heated regions in jets and outflows (Weigelt et al. 2006). Thus, the position in the J -band image might be just light scattered off the dust.

For all sources discussed here, it follows from our observations that the main radio emission observed with the VLA does not come from sub-AU scales around these protostellar sources. This can be explained by radio emission due to an optically thick thermal emission region which is resolved out at VLBI resolution. In fact, while there are some indications of partially nonthermal radio emission in our target sources, there are also clear signs of thermal emission (see source descriptions above).

Figure 5.5: Archival VLT-ISAAC *J*-band data of YLW 15 (grey scale), obtained only 1.5 months after our VLBI run (16 June 2005). Only VLA 2 is supposedly seen in this band. The VLBI source (marked by circles with radii of $0''.1$, $0''.2$, and $0''.3$; see text for discussion of astrometric accuracy of the infrared data) is apparently unrelated to the infrared emission. For reference, the positions from previous proper motion analyses are shown as well (Curiel et al. 2003; Girart et al. 2004, see text).

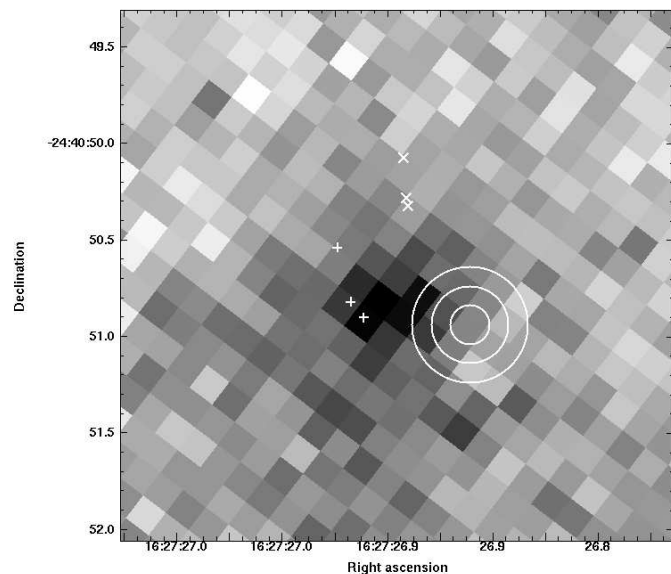


Table 5.4: VLBI results

Source	Distance	synth. beam (FWHM)	map rms ¹	
YLW 15	130 pc	2.9 mas \times 0.9 mas, PA -3.6°	0.4 AU \times 0.1 AU	15.4 μ Jy
EC 95	310 pc	2.6 mas \times 0.7 mas, PA -7.7°	0.8 AU \times 0.2 AU	14.3 μ Jy
HL Tau	140 pc	1.3 mas \times 0.7 mas, PA -6.3°	0.2 AU \times 0.1 AU	11.0 μ Jy
L1551 IRS5	140 pc	1.3 mas \times 0.7 mas, PA -6.1°	0.2 AU \times 0.1 AU	11.4 μ Jy

¹ determined from a Stokes-*I* clean map with $0''.2$ side length (1024×0.2 mas)

5.5 Summary

We present the results of a search for nonthermal radio emission on sub-AU scales towards a specially selected sample of protostars showing signs of potentially nonthermal centimetric radio emission. The observations, partly carried out with the NRAO High Sensitivity Array, involving the largest radio telescopes in the world, are the most sensitive yet towards this class of objects. While all sources in this sample are detected in VLA-only observations, we fail to detect compact emission in VLBI observations except for a persistent detection of compact radio emission towards the putative position of YLW 15-VLA 2 with a significance of $7 \dots 9\sigma$ depending on the imaging parameters. In this case, the size of the corona can be constrained to $< 0.4 \times 0.1$ AU. Given the apparently fast orbital movement of YLW15 VLA-2 around VLA-1, more observations will soon enable a much better determination of the orbit. A plausible explanation for the non-detections of the other sources is that thermal free-free emission from ionized regions (e.g. due to stellar winds or jets) is seen in the VLA observations which is resolved out in our VLBI data. Since this thermal radio emission easily becomes optically thick, it can effectively conceal nonthermal radio emission from underneath also in our sample of sources. André (1987) estimates how easily emission from underneath this region can be entirely concealed by ionized material: A mass-loss wind of only $10^{-11} M_\odot/\text{yr}$ suffices to entirely absorb 5 mJy of flux density of $T_b > 10^7$ K from underneath. It seems that the only means to overcome this problem is to look for target sources which have favourable lines of sight (as it is the case apparently towards YLW 15) allowing a more direct view of the innermost nonthermal emission, e.g. by ensuring the clear detection of nonthermal radio emission already in VLA data. Since VLBI observations offer the possibility to study the active coronae and thereby the magnetic fields of protostars at high angular resolution down to < 0.1 AU, we look forward to observations for other candidate sources in the future.

Chapter 6

A 1.3 cm radio flare from a deeply embedded source in the Orion Nebula

6.1 Introduction

While protostellar variability has recently been extensively studied at X-ray wavelengths (e.g. Getman et al. 2005b and references therein), still little is known about short-term protostellar radio variability and even less about multi-wavelength correlations. Bower et al. (2003) presented the first observation of a millimeter radio flare of a Young Stellar Object in Orion. This observation was simultaneously covered in X-rays. The X-ray flux increased by a factor of 8 two days before the radio flare observation. In observations a few days after this outburst, the source was found to show also millimeter activity for 13 days while the infrared *K*-band magnitude remained unchanged (Furuya et al. 2003). Massi et al. (2006, see Chapter 7) present a millimeter flare of the binary T Tauri system V773 Tau, interpreted as synchrotron radiation due to interacting coronae. While longer-term radio variability of Young Stellar Objects has been known for some time (e.g. Feigelson & Montmerle 1999), there are only few radio observations of YSOs in the course of which the target sources vary significantly. Here, we present another such source in Orion. We observed a spectacular outburst of this source at a wavelength of 1.3 cm.

6.2 Observations and results

6.2.1 Radio data: VLA observations

We made several epochs of observations at different VLA frequency bands. The data concerning us here were made in X-band (8.4 GHz) and K-band (22.285 GHz). The Orion region was observed in K band on July 5th, 1991 with the NRAO¹ Very Large Array in its highest-resolution ‘A’ configuration.

6.2.1.1 Basic calibration and imaging

Given the weakness of the sources – in the K band, 16 sources have a total flux density of ~ 80 mJy – “conventional” self-calibration is impossible at K band. We therefore calibrated the data in the same way as first described by Reid & Menten (1990, see also the Appendix of Reid & Menten 1997 for a detailed description). In short, a dual intermediate frequency (IF) band setup was used with a narrow IF band (of width 3.125 MHz) covering the $6_{16} \rightarrow 5_{23}$ H₂O maser line (rest frequency 22238.08 MHz) and a broad IF band (of width 50 MHz) centered at a 50 MHz

¹The National Radio Astronomy Observatory (NRAO) is operated by Associated Universities, Inc., under a cooperative agreement with the National Science Foundation.



Figure 6.1: The 1.3 cm sources detected here overlaid onto a *JHK* color composite of the region as seen by the Very Large Telescope (VLT) in a detail of ESO PR Photo 03a/01. The box shows the field of view of the Hubble-Space-Telescope (HST) image in Fig. 6.2. The entire field of view as seen in the mid-infrared is also shown in Fig. 6.2.

higher frequency on a line-free portion of the spectrum. A position near the infrared source IRc 2 was observed in the $0^{\text{h}}30\text{--}10^{\text{h}}30$ LST interval in both bands simultaneously. Observations of the quasars 0501–019 and 0535+135 were interspersed alternately every ~ 30 minutes to determine electronic phase offsets between the bands. The target position was $(\alpha, \delta)_{\text{J2000}} = 05^{\text{h}}35^{\text{m}}14^{\text{s}}479, -05^{\circ}22'30.''568$.

To image the H_2O maser emission, several scans of the H_2O line in spectral line mode were interspersed. The known velocity range of the H_2O line was covered. Scans of the strong extragalactic continuum sources 3C84 and 3C273 provided bandpass calibration. The H_2O spectral line data will not be considered further in this work.

Absolute flux calibration was obtained from observations of 3C286 using fluxes interpolated from the values given by Baars et al. (1977). The uv data were edited, removing obviously faulty

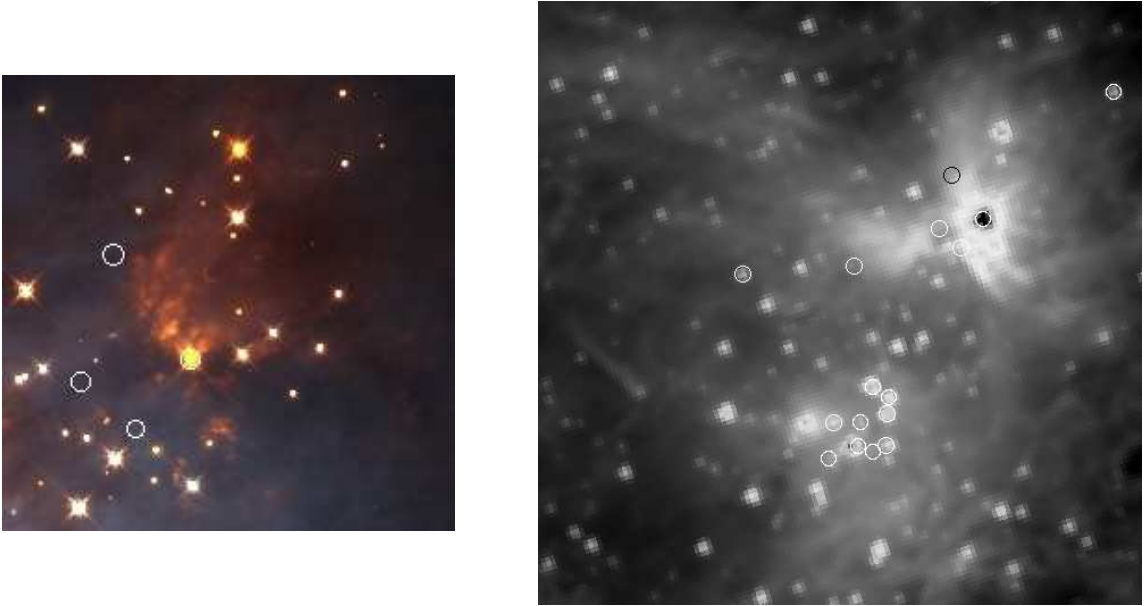


Figure 6.2: Left: HST-NICMOS observation (NASA/Luhman et al., detail of STScI-PRC00-19) of the region marked by the box in Fig. 6.1, composite image of $1.1 \mu\text{m}$ and $1.6 \mu\text{m}$ data. The latter data have a limiting magnitude of 17. The upper left (north-eastern) of the four marked sources is the flare source. Right: Archival *Spitzer*-IRAC 3.6μ data of the same field of view as Fig. 6.1. The saturated source is BN (there is also saturation in the Trapezium south of the image center). The radio sources are shown as circles, and the position of the flare source is marked with a black circle, but the source remains undetected in all four *Spitzer*-IRAC channels.

visibilities.

The narrow-band data were then “self-calibrated” with the very strong maser signal as a phase reference. The so-determined phase and amplitude corrections were then applied to the broadband data, with which the a high-quality map of the continuum emission was produced. A detailed description of the multi-step calibration procedure can be found in Reid & Menten (1997). Once the continuum data were “cross-self-calibrated” the data were imaged in the “usual” way with NRAO’s Astronomical Image Processing System (AIPS), setting the ROBUST parameter to zero. The half-power beam-width of the synthesized beam, as determined by IMAGR, is 109×97 milliarcseconds (mas), at a position angle 37° (E of N). The map size was 8192×8192 times 20 mas pixels, or $164''$ squared.

6.2.1.2 Further Processing

After a continuum map was produced as described above, we noted an uneven noise distribution over parts of the map. After checking our calibration and editing we found no apparent error in our processing. We then produced two images, one from the first (temporal) half of the uv data and one from the second. Comparing the source distribution, we noted that one source, in the following called KBS for “K-band burst source”, had different flux densities in each of the maps, suggesting significant variability. This variability was causing the excess noise, since “usual” AIPS processing is incapable of properly addressing such a situation. We then split the cross-selfcalibrated uv data in ~ 1 hour long chunks (using UVCOP), which then were mapped successively. A preliminary analysis using the AIPS task SAD showed that in each map, within statistical uncertainties all sources apart from KBS have a roughly constant flux density. All these sources are point-like or of size ≤ 2 times the synthesized beam. We then used UVMOD to subtract a point source model with the position and flux density determined for source KBS in each of the chunks of uv data before using DBCON to concatenate the resulting uv data into

Table 6.1: Sources detected in entire dataset after subtraction of the flare source (see text). 6σ detections in a map with an rms noise level of 0.18 mJy (1σ). The formal Gaussian-fitting positional errors as given by JMFIT range from 0.8 mas for BN and KBS to ~ 30 mas for the weak off-axis source GMR 15 and scale with $\sim 0.5 \times \text{HPBW}/\text{SNR}$, where HPBW is the half-power beam width and SNR is the signal-to-noise ratio of the respective source (e.g. Boboltz et al. 2003). Flux densities were corrected for primary-beam attenuation. If applicable, the COUP source number is given (if within $< 0''.3$).

	Position (1.3cm, J2000.0)	Pos. err. (mas)	Flux dens. (peak, mJy)	ID	COUP	X-ray - 1.3cm [']
1	5 35 11.801 -5 21 49.15	2.4	9.0	GMR A	450	0.08
2	5 35 14.116 -5 22 22.81	0.8	13.1	BN	-	-
3	5 35 14.507 -5 22 30.40	2.7	3.9	GMR I	-	-
4	5 35 14.665 -5 22 11.18	0.8		KBS ^b	647	0.09
5	5 35 14.895 -5 22 25.30	5.4	1.8	GMR D	662	0.10
6	5 35 15.769 -5 23 09.81	8.5	1.9	(2MASS)	732	0.14
7	5 35 15.820 -5 23 14.01	1.3	12.5	GMR 12	745	0.23
8	5 35 15.836 -5 23 22.38	5.8	4.7	GMR 11	746	0.16
9	5 35 16.065 -5 23 24.20	7.0	3.4	GMR 8	-	-
10	5 35 16.070 -5 23 06.97	29.0	1.3	GMR 15	766	0.19
11	5 35 16.288 -5 23 16.49	7.0	3.8	GMR 7	787	0.06
12	5 35 16.326 -5 23 22.53	6.0	3.8	GMR 16	-	-
13	5 35 16.398 -5 22 35.23	4.2	2.7	GMR K	-	-
14	5 35 16.750 -5 23 16.36	4.8	6.8	GMR 6	826	0.11
15	5 35 16.846 -5 23 26.12	17.4	3.6	GMR 5	-	-
16	5 35 18.367 -5 22 37.36	1.3	14.5	GMR F	965	0.17

^a mainly referring to sources listed by Garay et al. (1987)

^b The position of KBS was determined separately at the flare maximum. No emission was found towards the neighbouring north-eastern X-band source (see Table 6.3). A reasonable upper limit to its flux density is the 3σ rms noise level at its position in the combined, KBS-subtracted map which is 1.14 mJy in a box with a side length of $0''.4$ (influenced by the residuals of the KBS source removal).

a dataset subsequently imaged in order to study the detections other than KBS with the highest possible sensitivity (rms map noise 0.18 mJy). SAD was used to find all sources exceeding six times the noise level in that map. The 16 detections were then studied using JMFIT (see Table 6.1), allowing to perform all flux density, size, and position determinations with the same AIPS task. Fig. 6.1 shows the detected sources overlaid onto a deep near-infrared view of the region. For a discussion of the infrared data, see Section 6.2.4.

A note on SAD is in order: SAD is used to search for sources with peak and integrated intensities above a certain threshold, $t = n s$, where s is the rms noise and n is, say, 6. Since it is only meaningful to use SAD on maps that are not corrected for primary beam response, specifying $t = 6s$ will find sources at or near the phase center that have flux densities above t/a , where a is the attenuation due to the Gaussian drop-off in the primary-beam response. At the half-power point ($1'$ in K-band) a equals 0.5. Some of the sources are at the limit of fulfilling our criterion, being “found” in one 6σ -cutoff map, but not in others with higher noise levels. Thus, all flux density determinations were confirmed using JMFIT: For sources that were detected in at least one of the sub-maps and whose position was returned by SAD, JMFIT was used with a search area around that position in order to determine the flux densities of that source in the other sub-maps. For comparison, flux densities were then finally corrected for primary-beam attenuation.

Source	a	Δa	b	Δb
BN	-0.37	0.13	18.5	2.3
GMR A	-0.92	0.19	24.2	3.4
GMR 12	-0.62	0.21	21.9	3.7
GMR 6	-0.50	0.19	14.6	3.3
GMR F	-0.57	0.25	22.8	4.5

Table 6.2: Results of fitting linear functions $S(t) = ax + b$ to the light curves shown in Fig. 6.3, weighing the data points according to their error bars. $S(t)$ is the dependency of source flux density on time. The asymptotic standard errors for the two parameters are given as well.

6.2.1.3 Results: Time variability

Six sources are bright enough for a study of time variability, including the flare source KBS (as well as BN, GMR A, GMR 12, GMR 6, and GMR F). For this purpose, we mapped the entire dataset in different time intervals, starting with the chunks having durations of about one hour which were described in Section 6.2.1.2. The flare source turned out to be bright enough for imaging in intervals of about 15 min (at noise levels of typically 1 mJy). When analyzing especially the data around the flare maximum in Stokes- I and V using SAD, no circular polarization was found towards any source.

The light curves for these six bright sources are shown in Fig. 6.3 with a time resolution of about 30 min. KBS is indeed the most variable source while BN is the least variable one (to within 30%). Fitting a linear function to the data yields the results shown in Table 6.2. In all cases, a slightly negative slope is observed which may indicate an instrumental effect. However, the slope of the GMR A light curve, reaching nearly a significance of 5σ according to the fit parameter error estimate, is probably real (this is the flare source reported by Bower et al. 2003). Together with the relatively high flux density of BN, the fact that this source has the smallest rms compared to a source of constant flux density is the reason for analyzing only KBS with BN as a reference at twice the time resolution of about 15 min, as shown in Fig. 6.4. The source elevation corresponding to the light curves is shown in Fig. 6.5. It varies between 15° and 50° .

The flare source KBS is detected as a weak source already at the beginning of the observation, however the identification may be uncertain for the first datapoints of the light curve. Maps of the source and its surroundings are shown in Fig. 6.6. Following the steep rise of the flare, the maximum is reached about five hours after the beginning of the observation with a clear rise seen during about four hours. A first maximum in flux density is reached at 47 mJy. Subsequently, the flux density falls to values of 40 mJy, rises back to a peak value of 48 mJy only to decrease steadily afterwards with the exception of a precipitous drop lasting for about 30 min at around 20:30 IAT. At the end of the observation, the flux density still is at 69% of the peak value. At all times, the source is unresolved. The steep rise of the flare implies that the emitting region is smaller than 15 light minutes, i.e. < 2 AU, also indicating a peristellar origin.

Whether the drop around 20:30 IAT is real or due to observational effects remains unclear. The source elevation at this time still is $\sim 35^\circ$. Since nearby BN experiences a similar drop at the same time, this probably has nothing to do with the sources themselves, but instead may be due to clouds passing the telescope beam.

6.2.2 Radio data: VLA 8.4 GHz archival data

While the discovery observation on July 5, 1991, was not accompanied by observations at other frequencies, the Orion region has been frequently re-observed since then. One subsequent observation was carried out on September 6, 1991, in X-band (8.4 GHz), again in the high-resolution A configuration of the VLA. In this observation, an X-band radio counterpart to the 22 GHz flare source was discovered together with another previously unreported slightly weaker source separated by $0''.45$ (M. Reid, priv. comm.), the coordinates are listed in Table 6.3. Using the best position determination from its flare maximum, the source KBS appears to be associated

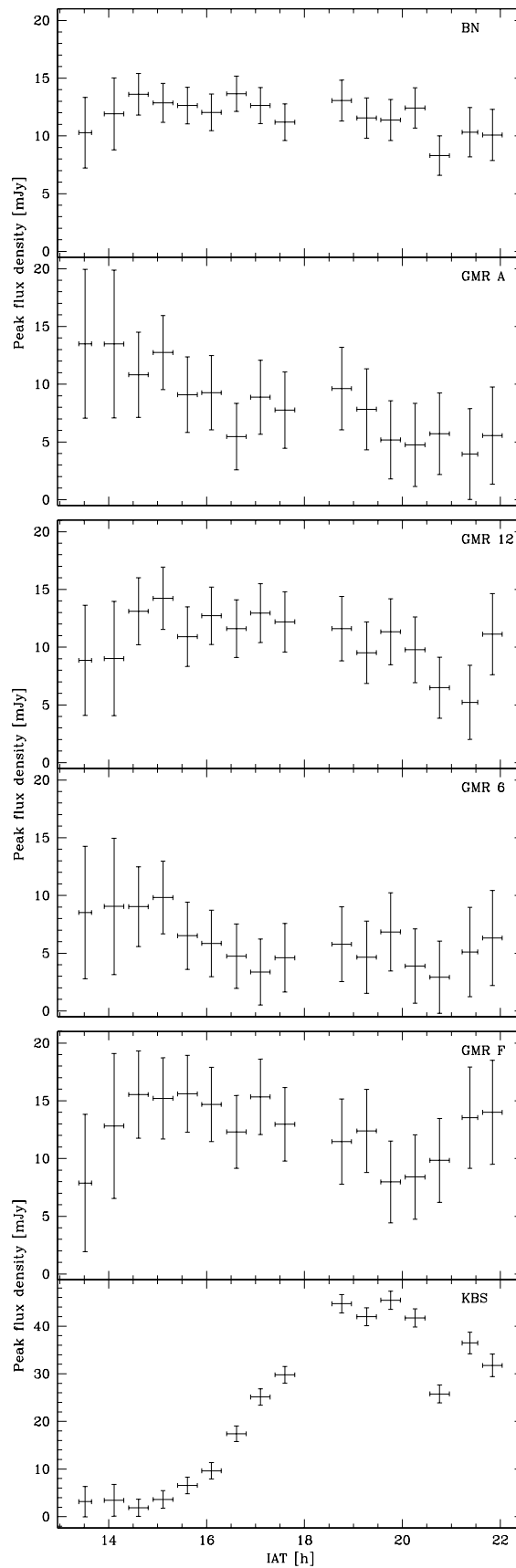


Figure 6.3: 1.3 cm flux density curves for the six brightest sources (as labeled). Error bars indicate the timeranges considered and three times the flux density error given by JMFIT (which is approximately equivalent to the map rms noise), i.e. 3σ in flux density. For flux curves of BN compared to the flare source KBS at twice the time resolution, see Fig. 6.4.

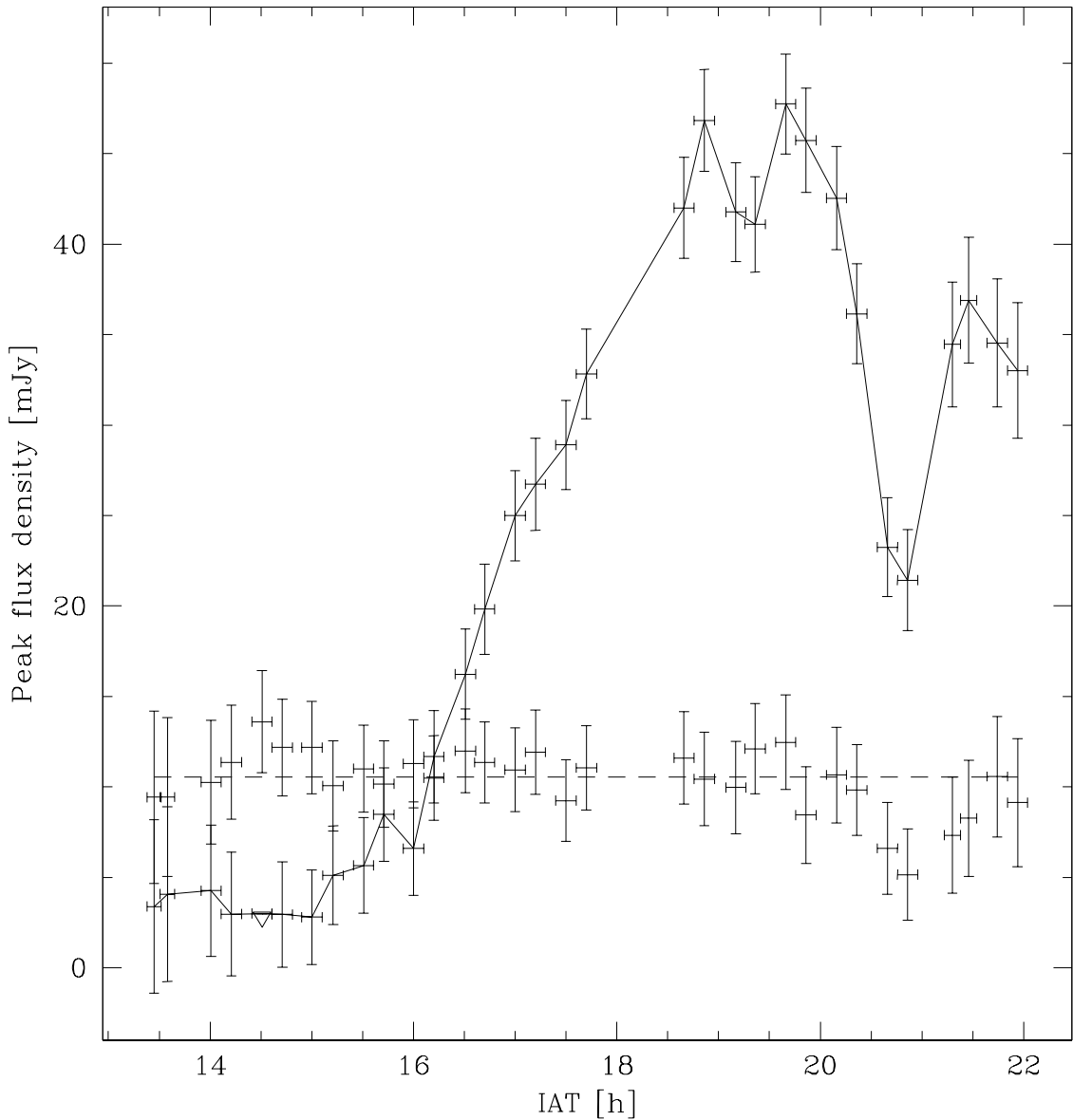


Figure 6.4: Light curves of the flaring source KBS and BN for comparison. Data was taken on July 5th, 1991. Error bars are defined as in Fig. 6.3. The triangle denotes a 3σ upper limit, and the dashed line indicates the median peak flux density of BN.

to the south-western component of the double X-band source (see Fig. 6.7).

While a full discussion of all subsequent observations is beyond the scope of this work, we note that X-band (8.4 GHz) observations carried out on April 29, 1994, Menten & Reid (1995, see their Fig. 1 in the upper left corner) detect this double source again. Interestingly, while all other sources discussed here and listed in Table 6.1 have X-band counterparts in multi-epoch data ranging from 1994–1997 discussed by Zapata et al. (2004), these two sources are not reported. This may be due to the fact that their flux densities in the two epochs during which they were detected at X-band are close to the significance threshold.

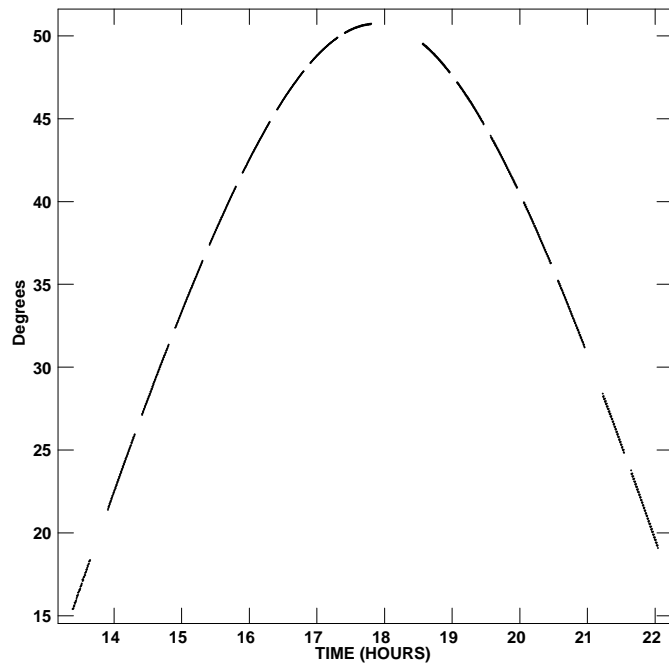


Figure 6.5: Source elevation during the discussed 1.3 cm observation.

Table 6.3: The double 8.4 GHz counterpart as observed on September 6, 1991 (M. Reid, priv.comm.). The synthesized beam size for this observation is 299×216 mas at position angle -39.2° . The corresponding rms map noise is ~ 0.04 mJy, and the positional Gaussian fitting error is $\sim 0.5 \times \text{HPBW}/\text{SNR} \approx 20$ mas (see Table 6.1).

Component	Position (J2000.0)	Flux density
1 (SW)	05 35 14.664 -05 22 11.16	0.28 mJy
2 (NE)	05 35 14.688 -05 22 10.89	0.23 mJy

6.2.3 X-ray data: Archival Chandra observations

The Orion Nebula Cluster and OMC 1 have been extensively studied at X-ray wavelengths recently, most notably in the Chandra Orion Ultradeep Project², an 838 ksec observation carried out with *Chandra* within a period of 13.2 days in January 2003. Interestingly, our flare source KBS has an X-ray counterpart which has been catalogued as X-ray source COUP 647 or CXO ONC J053514.6-052211. Fig. 6.7 shows an image of the source from the COUP data, together with the two 8.4 GHz sources and the position of the flare source. The radio flare source seems to be associated to the X-ray flare source to within $0''.10$. The COUP light curve shows a weak X-ray source with a quiescent flux corresponding to count rates of around 1 ksec^{-1} and a considerable flare shortly before the end of the observation, reaching 17 ksec^{-1} (Fig. 6.8). The observation ends with the count rate still at about half the maximum level. With 808 net counts from this source, especially this flare allowed to determine the absorbing column density towards the source which is $\log(N_{\text{H}})=23.51$ (corresponding to $A_V \approx 160$ mag, ruling out any observable infrared counterpart), showing that this is a deeply embedded source. The X-ray emission is quite hard with a derived plasma temperature of $kT = 5.5 \text{ keV}$ or 64 MK. The total X-ray luminosity (0.5 – 8 keV) corrected for absorption is $10^{30.9} \text{ erg s}^{-1}$. Tsujimoto et al. (2005) find that COUP 647 is one out of only seven sources in the entire COUP sample with detectable fluorescent 6.4 keV iron line emission and among these the only source without a near-infrared counterpart. This emission is interpreted as reprocessed radiation e.g. from a circumstellar disk.

²see the ApJS COUP Special Issue, October 2005

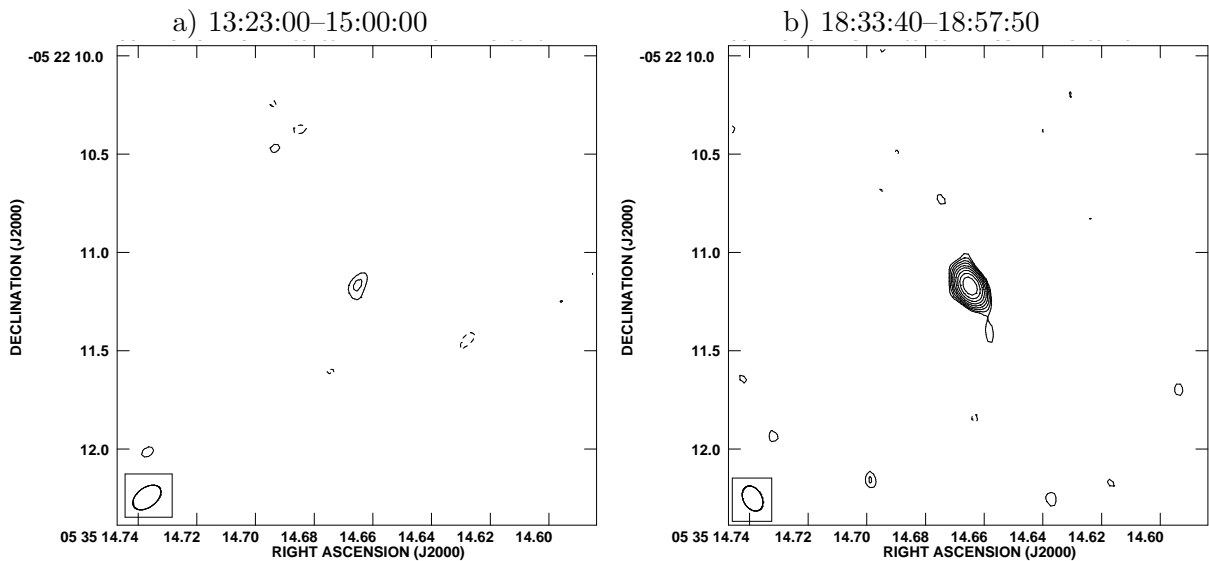


Figure 6.6: Maps of the flare source, using (a) all the data up to 15:00, i.e. combining the data where the source is weakest, and (b) the data corresponding to the first light curve maximum in Fig. 6.3. The contour lines denote multiples of each map’s 3σ rms noise level, namely 1.52 mJy and 1.79 mJy. Level spacing is $-2, -\sqrt{2}, -1, 1, \sqrt{2}, 2, \dots \times 3\sigma$.

Feigelson et al. (2002) analyze two older *Chandra* ACIS-I datasets from 1999 and 2000, covering 86 ksec in total. They detect a weak source (ID 428) with a total of 74 counts and classify it as long-term variable due to differences between the two observations (see also Garmire et al. 2000 for the first of the two datasets). Flaccomio et al. (2003) detect the source in *Chandra* HRC observations in February 2000, they find 15 counts in a 63 ksec exposure.

Thus, in a total of 987 ksec (i.e. 11.4 days) of *Chandra* X-ray observations, only a single flare was observed. Unfortunately, in archival XMM-*Newton* data, the source region is only covered close to the limits of the respective field of view.

6.2.4 Infrared data: Archival HST, VLT, and Spitzer data

The source remains undetected in near-infrared *JHK* data taken with the ESO Very Large Telescope (see Fig. 6.1; as quoted in the COUP Atlas, Getman et al. 2005b). This is certainly due to the high absorbing column density causing an extinction of $A_V \approx 160$ mag (see above). The source remains undetected as well in even deeper HST-NICMOS observations³ performed at wavelengths of 1.1 μm and 1.6 μm , reaching a limiting magnitude of ~ 17 mag in the latter band (see Fig.6.2). No detection was as well reported by Robberto et al. (2005) from their mid-infrared observations at 10 μm and 20 μm . Also in *Spitzer*-IRAC mid-infrared observations, no source is detected at the position of the flare source (although the sensitivity is limited by the very bright neighbouring BN object, see Fig. 6.2).

Out of the other 15 sources, twelve have near-infrared counterparts. Apart from the flare source, only GMR I, D, and K do not have counterparts. Interestingly, two of these sources (GMR I and D) are close to BN and the flare source. Their positions are marked in the HST image in Fig 6.2.

³http://nicmosis.as.arizona.edu:8000/TRAPEZIUM/TRAPEZIUM_DOWNLOAD.html

6.3 Summary

We report the observation of a 1.3 cm radio flare of a deeply embedded source in the surroundings of Orion BN. The flare source (KBS) was observed to rise within four hours to become the strongest source in the field. Afterwards, the flux density decreased slowly, disrupted by a sharp drop and rise affecting also the reference source BN, possibly due to a cloud passing the telescope beam.

The source does not have a near-infrared counterpart in VLT and HST data, but an X-ray counterpart was found (a flaring COUP source) allowing to determine the absorbing column density (corresponding to $A_V \approx 160$ mag). Also in the mid-infrared, the source remains undetected although deep observations of the region are hampered by the bright neighbouring BN object.

There are 15 additional sources detected at 1.3 cm, including GMR A, towards which a 86 GHz flare was reported by Bower et al. (2003). Apart from KBS, only GMR A appears to be slightly variable in the observation reported here. All 16 sources detected at 1.3 cm have counterparts at 3.5 cm, including the flare source which is a double source separated by $0''.45$. These weak sources have been reported for two different observations, but in further observations they have not been found which is possibly due to variability.

This is now the second YSO in Orion known to be very active at radio as well as at X-ray wavelengths. It is much deeper embedded than the first example, GMR A (Bower et al. 2003), and thus probably in an even earlier evolutionary stage. With the X-ray variability of YSOs now well studied, details on the radio variability of these sources and possible correlations to X-ray emission remain mostly unknown.

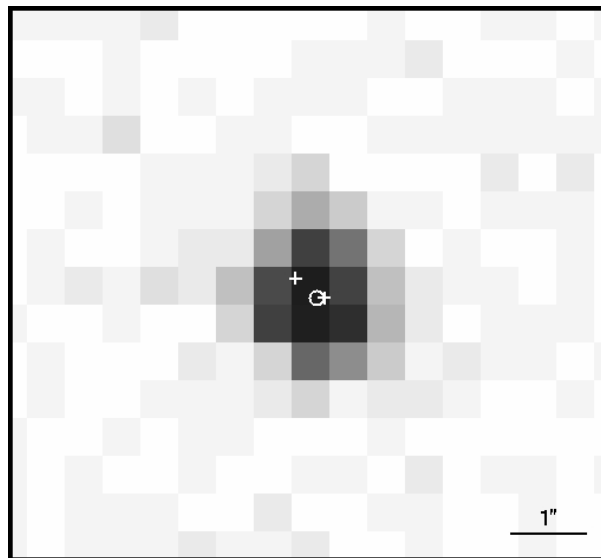


Figure 6.7: The COUP X-ray image of COUP 647. The peak positions of the two 8.4 GHz radio sources are shown as crosses, the 1.3 cm flare source is shown as a circle. Symbols are larger than the positional accuracies.

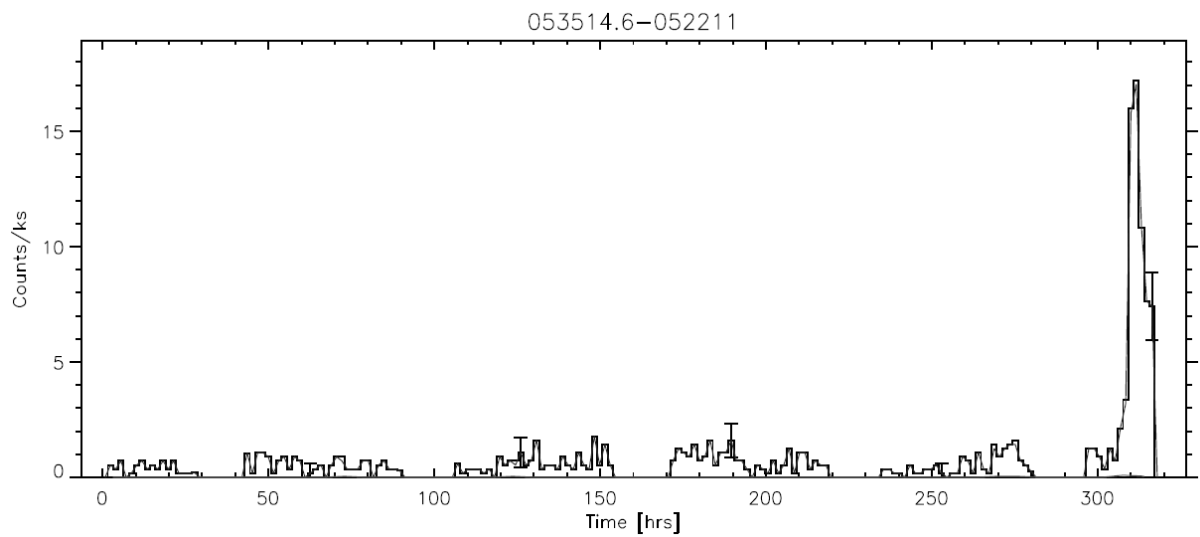


Figure 6.8: X-ray light curve of the flaring source COUP 647 – coincident with KBS – from the COUP experiment. The observation was made in January 2003 with the ACIS instrument onboard *Chandra*. The source is clearly detected already before the flare. The gaps in the light curve are due to non-continuous coverage. From Getman et al. (2005b).

Chapter 7

Synchrotron millimeter radio emission from the T Tauri binary system V773 Tau A

(based on *Massi, Forbrich, Menten, Torricelli-Ciamponi, Neidhöfer, Leurini, & Bertoldi, A&A 2006, 453, 959*)

7.1 Introduction

The dynamo theory (Parker 1955) explains how differential rotation generates a toroidal field in the interior of a star from an initial stellar dipole field, and how convection, bringing this field up to the surface, creates the coronal magnetic arc-like structures called loops. A close relationship between magnetic loops and flares exists. In fact, the physical mechanism invoked to explain solar and stellar flares today is magnetic reconnection, which occurs when different loops interact with each other or when field lines of the same loop are stretched. The released magnetic energy accelerates a part of the thermal electrons trapped in the loops to high energies, causing the flare (Golub & Pasachoff 1997; Priest & Forbes 2002).

We have observed a strong flare at millimeter wavelengths toward the T Tauri binary system V773 Tau A. In the context of the outlined scenario, our aim is to investigate: *a*) the flare location and hence the geometrical structure of the involved magnetic field, and *b*) the nature of the observed emission, i.e. whether the magnetic field intensity and the electron Lorentz factor can be derived, yielding information on the emission mechanism.

Concerning the first issue, *a*, one can distinguish among three possible origins for flares:

1. In a *single* star, flares occur when new emerging loops from below the stellar surface move into older, already-existing loops (Heyvaerts et al. 1977; Massi et al. 2005). Such intruding loops have indeed been observed on the Sun in high-resolution maps obtained with the Nobeyama Radio Interferometer (Nishio et al. 1996).
2. In protostars or young (pre-main sequence) stellar systems, which are still surrounded by a dense accretion disk, flares can occur because of stretching, disruption, and reconnection of magnetic field lines between the star and its disk (Feigelson & Montmerle 1999).
3. In close binary systems consisting of late spectral type stars, much higher magnetic activity is expected compared to the Sun (because tidal synchronism increases the rotation rate and therefore the dynamo efficiency). Moreover, the coronal loops of the two stars can interact with each other, as for RS CVn (close) binaries (Uchida & Sakurai 1983; Graffagnino et al. 1995). Observational evidence for inter-binary loop “collisions” was also recently found

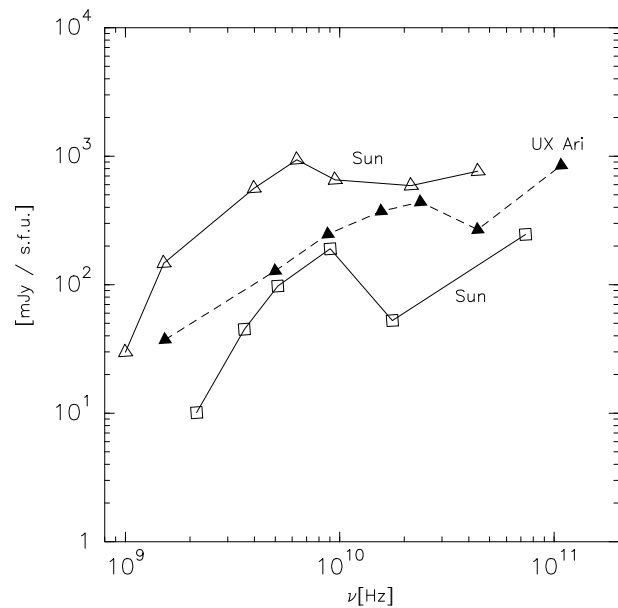


Figure 7.1: Examples of spectra of the Sun (squares: Akabane et al. (1973); empty triangles: Zirin & Tanaka (1973) and UX Arietis (filled triangles: Beasley & Bastian 1998) exhibiting a “flattening” towards millimeter wavelengths. Notice that the vertical scale is in both solar flux units (for the solar spectra) and mJy (for UX Arietis).

for the young binary system V773 Tau A, which shows a high rate of radio flares around the periastron passage (Massi et al. 2002).

Concerning the second issue (*b*), the usually observed radio emission from stellar coronae shows spectra peaking around 10 GHz and is consistent with the gyro-synchrotron process (Mutel et al. 1985; Bastian et al. 1998; Güdel 2002b). However, some solar and stellar flares can also be observed at millimeter wavelengths (Fig. 7.1), and the spectra are thought to be due to the superposition of a gyro-synchrotron spectrum with a synchrotron spectrum, the last one peaking in the shorter submillimeter to the far-infrared range (Kaufmann et al. 1986, 2004). Gyro-synchrotron emission, associated with mildly relativistic particles, i.e., with a Lorentz factor of $\gamma < 10$, is circularly polarized. In contrast, synchrotron emission comes from highly relativistic particles ($\gamma \gg 1$) and is linearly polarized (Dulk 1985; Phillips et al. 1996; Tsuboi et al. 1998).

To probe the existence of relativistic electrons in the V773 Tau A system and to constrain their energy and the strength and topology of the magnetic field, we observed it at millimeter wavelengths using the IRAM Plateau de Bure Interferometer.

The chapter is organized as follows. Section 7.2 reviews previous results on V773 Tau A, and in Section 7.3 our new observations and results are presented. In Section 7.4 we evaluate which kind of energetic processes may cause the trapped electrons to lose their energy and derive the Lorentz factor and magnetic field strength. These deductions are confirmed in Section 7.5 by the analysis of the flare rising time. Section 7.6 discusses the magnetic field configuration, while Section 7.7 presents our conclusions.

7.2 The V773 Tau A binary system

V773 Tau, at a distance of 148 ± 5 pc (Lestrade et al. 1999), is a quadruplet of T Tauri stars within an area of radius less than 100 AU (Woitas 2003). The system has two stars with orbital periods of years and two shorter period inner stars. The object of our studies is the V773 Tau A binary, with an orbital period of only 51.075 days (Welty 1995). The orbit of V773 Tau A is moderately eccentric ($e=0.3$) and the epoch of periastron passage, corresponding to orbital phase $\Phi = 0$, is $t_0=2449330.94$ JD. The stars, both very active, have similar radii ($R_* = 2.4 R_\odot$) and rotation periods (about 3 days), but seem to have different masses (see Welty 1995).

The system possesses only weak hydrogen emission lines in its spectrum, which implies that

its components are weak-line T Tauri stars with mass loss. This follows from the presence of forbidden emission lines (Cabrit et al. 1990). The presence of a disk is controversial (Skinner et al. 1997) since the observed infrared excess may also be attributable to V773 Tau D, the fourth member of the quadruplet (Duchêne et al. 2003). Also, it is difficult to establish any thermal component in the millimeter emission (which would imply a disk), since it is strongly dominated by a variable nonthermal component typical of flaring coronal activity (Skinner et al. 1997). At 2.7 mm, variability was found with the flux density changing from 30 mJy to less than 3 mJy in a period of a few months (see Skinner et al. 1997). Beckwith et al. (1990) measured a flux density at 1.3 mm, $S = 42 \pm 6$ mJy, whereas an observation several years later gave $S = 24 \pm 4$ mJy (see Skinner et al. 1997). With the Effelsberg 100-m telescope, Massi et al. (2002) observed a flare at 7 mm with $S = 68 \pm 13$ mJy, and three months later they only obtained an upper limit (3σ) of 23 mJy.

V773 Tau A is not the only pre-main sequence object with millimeter-flaring emission. For example, Bower et al. (2003) observed a giant outburst at 86 GHz in the Orion source GMR-A, also a weak-line T Tauri star. Long-lasting (13 days) millimeter activity in that source was observed by Furuya et al. (2003). However, V773 Tau A is the only known system with coronal solar-like magnetic activity where linearly polarized emission together with the more common circularly polarized emission was measured (Phillips et al. 1996). The high level of variable millimeter emission together with the presence of linear polarization indicates that a quite energetic electron population is present. The fact that these energetic electrons have rather short lifetimes is worthy of note for the following analysis. Phillips et al. (1996) find that total intensity variations at different wavelengths and epochs share common time scales and establish a recurring interval for the decay of radio events with a typical $1/e$ time scale of only about 1 hour.

The two components of V773 Tau A are both active (Welty 1995); flares on both of them are expected due to mechanism *a-1* discussed in the introduction. In addition, however, there is evidence for mechanism *a-3* (inter-binary loop collision): by folding the data, monitored over 522 days, with the orbital period (51.075 days), the flares appear to be clustered at periastron passage (Massi et al. 2002). Around the periastron, more than one interbinary interaction seems to occur: three consecutive flares, separated by a time interval of 3 – 4 days, have been observed during a continuous observation around periastron passage (Fig. 7.3 in Massi et al. 2002). The hypothesis of a stable active region simply eclipsed by the body of the star during each rotation ($P_{\text{rot}} = 3$ days) is ruled out by the short lifetimes (1 – 2 hours only) of the energetic electrons. On the contrary, a large asymmetric structure rooted on one of the two rotating stars could explain the occurrence of the three consecutive flares, as repeated collisions (at each rotation) with the corona of the other star. The extent, H , of this magnetic structure must be large enough to allow the observed consecutive collisions around periastron passage. The periastron separation is 56 solar radii, R_{\odot} , which for a stellar radius, $R_* = 2.4 R_{\odot}$ (Welty 1995), corresponds to $23 R_*$. Indeed, a large magnetic structure has been imaged by using Very Long Baseline Interferometry (VLBI, Phillips et al. 1996; orbital phase $\phi = 0.1$) at $\lambda = 3.6$ cm, with two peaks of different intensity separated by 0.17 AU ($15 R_*$). Observational constraints for the size of the emitting region are therefore in the range 15 – 20 R_* .

The fact that linear polarization has been observed implies that Faraday depolarization is not effective and puts an upper limit to the density ($n < 10^9 \text{ cm}^{-3}$) of the plasma confined in this extended magnetic structure (Phillips et al. 1996). X-ray observations give evidence not only of a density much above this limit, but also of the existence of smaller, solar-like, coronal loops in V773 Tau A. Skinner et al. (1997) interpreted the light curve of a hard X-ray flare in V773 Tau A as being due to the rotational modulation of the emitting flaring region, determining a size of $H \leq 0.6 R_*$. Tsuboi et al. (1998) interpreted the decay of another hard X-ray flare as being due to radiative cooling, obtaining a size of $1.4 R_*$. Therefore, radio and X-ray emission come from spatially separated regions: denser and smaller ones associated with X-ray emission

Table 7.1: Flux density of V773 Tau in November 2003

Day	$S_{1\text{mm}}$ (mJy)	$S_{3\text{mm}}$ (mJy)
13	5.0 ± 1.2	3.0 ± 0.4
14	6.0 ± 1.2	5.0 ± 0.3

and larger and more diffuse ones associated with radio emission. Further confirmation of the presence of two structures comes from the multiwavelength campaign on V773 Tau A carried out by Feigelson et al. (1994) showing radio variability combined with a steady X-ray flux. Using our millimeter observations, the following sections are aimed to better define what kind of extended magnetic structure might confine the radio-emitting plasma, the intensity of the magnetic field, and the energy of the trapped particles.

7.3 Observations and data reduction

V773 Tau A was observed with the IRAM Plateau de Bure Interferometer at 1 mm and 3 mm around the two periastron passages in August and November 2003. The configuration was 5D (five antennas) in August and 6Cp (the six-antenna configuration) in November. Observations were done in LCP for the 3 mm observations and in RCP for the 1 mm observations. The continuum was measured with four correlator units per receiver, twice with a bandwidth of 320 MHz and twice with a bandwidth of 160 MHz. Cyclical observations (every 20 minutes) of the sources 0528+134 and 3C286 were used for phase and amplitude calibrations. The data were reduced with the programs CLIC and MAPPING of the GILDAS software package developed by the Grenoble Astrophysics Group. The source was always unresolved. A complete flare (Fig. 7.2) was observed on August 6 ($\Phi = 0.1$). With about 12 mm of precipitable water vapor in the atmosphere, no observations at $\lambda = 1$ mm were possible, and those at $\lambda = 3$ mm had the high rms noise level of 17 mJy; the 3 mm receiver was tuned to 90 GHz and had a system temperature around 1000 K. The best power-law fit to the decay part of the light curve shown in Fig. 7.2 gives an e-folding time of $\tau = 2.31 \pm 0.19$ hour. Around the periastron passage in November, we were able to observe under very good weather conditions for two consecutive days at $\Phi = 0$. The flux density was at a quiescent constant level with a nearly flat spectrum (Table 7.3).

7.4 Rapid flare decay: leakage of the emitting particles

As outlined in the introduction, the emission observed at 3.3 mm (90 GHz) can be interpreted as synchrotron radiation. In synchrotron radiation, the emission of each relativistic electron with Lorentz factor γ moving in a magnetic field B (in Gauss) is centered around a peak spectral frequency, ν_0 (Ginzburg & Syrovatskii 1965) of

$$\nu_0 = 1.8 \times 10^6 B \gamma^2 \text{ Hz.} \quad (7.1)$$

This implies that, to reproduce the observed emission at $\nu = 90$ GHz, electrons must exist for which the following relationship holds:

$$B \gamma^2 = 5 \times 10^4. \quad (7.2)$$

The temporal evolution of the flux density shown in Fig. 7.2 clearly indicates that the emitting electron distribution, responsible for the observed synchrotron emission, is subject to

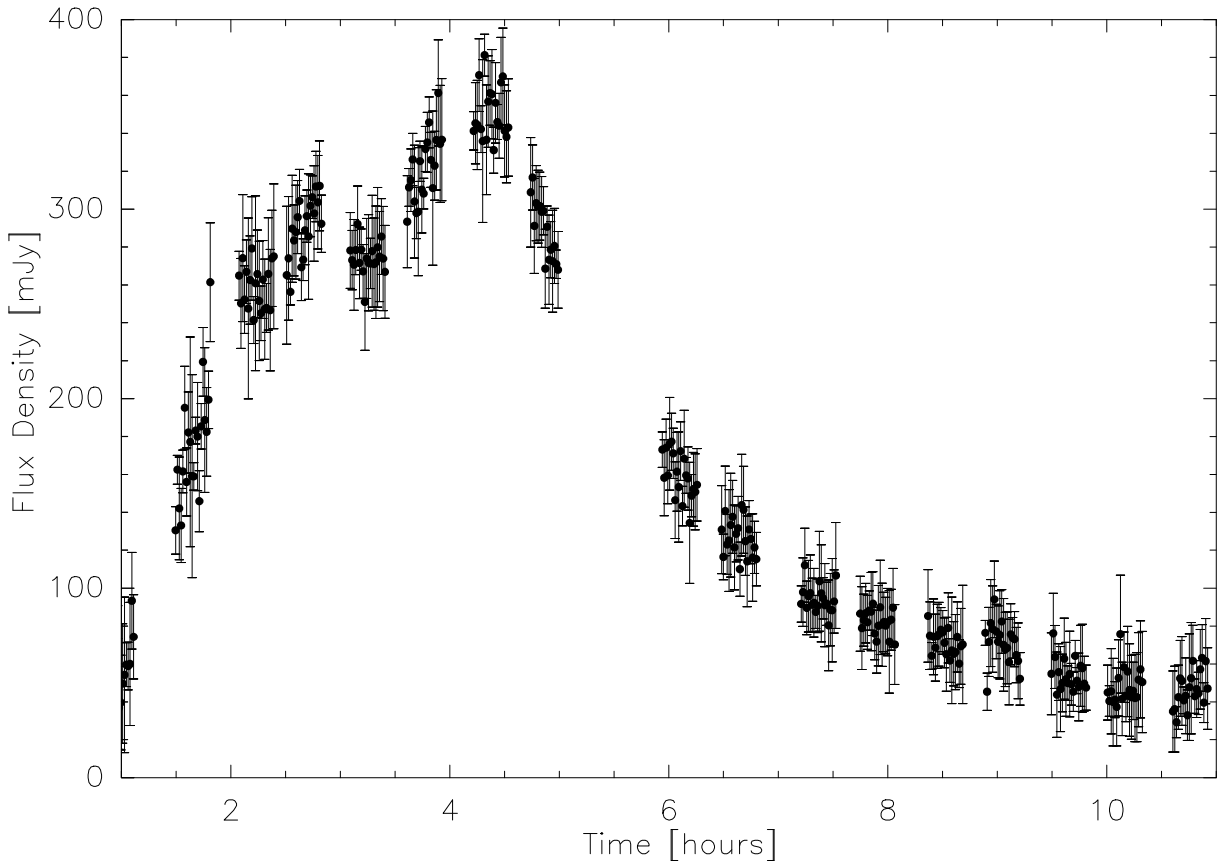


Figure 7.2: V773 Tau A flare observed August 6, 2003 ($\Phi = 0.1$) with the Plateau de Bure Interferometer at $\lambda = 3$ mm. The error bars indicate the 2σ rms noise.

some losses. In particular, the derived e-folding time of 2.31 hours for the millimeter flare is of the same order of that measured by Phillips et al. (1996) for cm emission (about one hour). This time scale implies that the electrons must be at least partially trapped in the emitting region, which would otherwise be rapidly depleted in a time equal to the size of the region divided by the speed of the electrons: $20R_*/c \sim 112$ s. It is well-established that particles trapped in magnetic structures spiral around field lines to a point (the “mirror point”) where the magnetic field lines converge and the field strength is sufficient to cause the particles to reverse direction and travel back to the other mirror point. Reflected back and forth between mirror points (known as “bounce” motion), the particles remain trapped and, continuously spiraling, emit synchrotron radiation until they have lost their energy (Roederer 1970).

However, the decay time of 2.31 hours is not attributable to synchrotron losses. As derived in the appendix to this chapter (Section 7.8), synchrotron losses would explain an intensity decay time of that duration only for an emitting region of size $\leq 3.8R_*$, whereas the observed size is $H \geq 15R_*$ (Section 7.2). Neither inverse Compton losses, due to the radiation field of the star, and/or to the synchrotron emission of the flare (Synchrotron Self-Compton, SSC), can be responsible for the observed decay; Compton losses are even lower than synchrotron losses (see appendix in Section 7.8). On the other hand, even collisional losses cannot account for the observed decay time, since collisions are important only for high density plasmas (see appendix in Section 7.8) in contrast to the upper limit on the plasma density $n < 10^9 \text{ cm}^{-3}$ derived from Faraday depolarization (Section 7.2).

Since the fast decay of the emission cannot be attributed to energetic losses of the electrons, it may be caused by leakage of the particles themselves, meaning that at each bounce motion at one mirror point, some of the electrons are able to leave the trapping region and escape into

free space. This is possible for electrons having a pitch angle, θ (the angle between their velocity direction and the magnetic field vector), smaller than the loss cone angle

$$\sin \theta < \sin \theta_0 = \left(\frac{B_1}{B_0} \right)^{1/2}. \quad (7.3)$$

Here, B_1 is the magnetic field intensity far out in the corona at a distance (H_1), while B_0 is that at a lower distance (H_0). Pitch angle scattering, also known as “pitch angle diffusion” (Melrose & Brown 1976), is one of the main processes by which trapped particles are lost. Weak and strong diffusion have been introduced by Melrose & Brown (1976). However, in order to be effective, weak diffusion demands a high-density medium ($n > 10^9 \text{cm}^{-3}$), in contrast to what we discussed above. Also, Lee et al. (2002) found that for the microwave decay of a solar flare, the assumption of strong diffusion seems to be the most appropriate. In this scenario, the emission decreases by a factor of $1/e$ if the precipitation rate

$$\nu_p = \frac{1}{2} \theta_0^2 \frac{c}{(H_1 - H_0)} \quad (7.4)$$

(Melrose & Brown 1976; Lee et al. 2002) times the decay time (2.31 hours, in our case) equals unity. This condition, valid for small θ_0 values, implies:

$$742 \times \frac{B_1}{B_0} \frac{R_*}{H_1 - H_0} = 1. \quad (7.5)$$

For a magnetic dipole field, $B_1/B_0 = [H_0/H_1]^3$, possible solutions of Eq. (7.5) are values in the ranges $H_0 \sim (2 - 5)R_*$ and $H_1 \sim (10 - 20)R_*$. Assuming a magnetic field strength at the stellar surface of the order of 1 kG (see appendix in Section 7.8), the corresponding values of the magnetic field intensity are in the range 125 – 8 G for H_0 and 1 – 0.12 G for H_1 . This scenario is consistent with synchrotron emission, since from Eq. (7.2), the corresponding Lorentz factor of relativistic electrons emitting at 90 GHz is $20 < \gamma < 632$.

This scenario is also in accordance with the VLBI observation of Phillips et al. (1996), since the analogon of Eq. (7.5) derived for the decay time of one hour and solved for $H_1 - H_0 = 15R_*$ with $H_1 \sim 20R_*$ gives B in the range of 4.6 – 0.12 G. These values of the magnetic field for $\nu = 8.2$ GHz (Phillips et al. 1996) correspond (see Eq. 7.1) to $31 < \gamma < 195$ indicating, therefore, the presence of relativistic electrons in agreement with the observed linear polarization.

7.5 The flaring phase: a propagating shock

In the previous section, we established the most likely physical process responsible for the rapid flare decay. The aim of this section is to test whether the additional constraint set by the flare rising time confirms the previously obtained results.

Recent solar flare studies (Tanuma & Shibata 2005; Asai et al. 2004) have shown that the observed downflow motions can create fast shocks that are related to observed nonthermal bursts, since shocks are supposed to be sites of electron acceleration (Aschwanden 2002). In our scenario, in which reconnection takes place far out where the two stars’ magnetospheres interact (i.e. at H_1), the shock induced by magnetic reconnection can propagate down to H_0 along the magnetic structure at the local Alfvén velocity

$$v_A(H) = \frac{B(H)}{\sqrt{4\pi m_H n(H)}} \simeq 7 \cdot 10^9 \left(\frac{H}{R_*} \right)^{-2} \text{ cm/sec} \quad (7.6)$$

(for a dipole magnetic field with $B(R_*) = 1000$ G and a particle density $n \sim 10^9 (H/R_*)^{-2} \text{cm}^{-3}$), thus inducing successive particle acceleration events. The shock propagation speed can

be related to the flare rise time, t_{rise} ,

$$t_{\text{rise}} = \int_{H_0}^{H_1} \frac{dH}{v_A(H)}, \quad (7.7)$$

from which the following relationship can be derived:

$$\left(\frac{H_1}{R_*}\right)^3 = 452 \left(\frac{t_{\text{rise}}}{\text{hour}}\right) \left(\frac{B(R_*)}{10^3 \text{G}}\right) \left(\frac{n(R_*)}{10^9 \text{cm}^{-3}}\right)^{-\frac{1}{2}} + \left(\frac{H_0}{R_*}\right)^3, \quad (7.8)$$

For $t_{\text{rise}} \simeq 4.5$ hours and H_0 between $(2 - 5) R_*$, the resulting height H_1 is in the interval of $(13 - 27) R_*$, assuming that $B(R_*)$ is in the range 1000-3000 G (see appendix in Section 7.8) and the density is in the range $10^8 - 10^9 \text{ cm}^{-3}$, as in Fig. 7.3.

This range for H_1 is well-consistent with the scenario of a reconnection event at a large stellar distance and in agreement with the resulting interval $(10 - 20)R_*$ from the leakage model.

7.6 Magnetic configuration

In the previous sections, in the context of our leakage model, we established magnetic field values in the range 125 – 8 G (for $H_0 = 2 - 5 R_*$) and 0.12 G (at $H_1 = 20 R_*$) at the two mirror points of the confining magnetic structure. Also, we determined values of 4.6 G (at $H_0 = 6 R_*$) and 0.12 G (at $H_1 = 20 R_*$) for the centimeter observations of Phillips et al. (1996). In both cases, in a high-resolution image of the source brightness distribution, the two mirror points would correspond to two peaks (displaced by $H_1 - H_0$) of rather different intensity, because of the relationship between emissivity and B (Dulk 1985). This predicted morphology finds its confirmation in the Very Long Baseline Array (VLBA) image of Phillips et al. (1996). The VLBA image, given in the small box of Fig. 7.3, shows a strong brightness distribution peak, which we may identify with the first mirror point, P_0 , separated by $15 R_*$ from a second weaker peak, which may be coincident with the second mirror point, P_1 .

Let us assume the scenario of two stellar coronae interacting at periastron passage. One of the two coronae must be very asymmetric, in accordance with the asymmetric magnetic field configuration implied by the Massi et al. (2002) observations of three consecutive flares around periastron (see Section 7.2). On the other hand, a single giant stellar loop is ruled out by X-ray observations which, on the contrary (see Section 7.2), provide evidence for a stellar-sized coronal loop (Skinner et al. 1997; Tsuboi et al. 1998). However, in the case of the Sun, extended magnetic structures are sometimes present above coronal loops. Indeed, when the Sun is observed with white-light coronagraphs, one can see that above the top of some coronal loops (Fig. 7.4), a dome-shaped structure (the “helmet”) is formed, extending out to 2 – 4 solar radii, with streamers that can extend out to many solar radii (Suess & Nerney 2004; Endeve et al. 2004). A helmet streamer is therefore a plausible physical model for the elongated asymmetric structure implied by the previous observations of Massi et al. (2002). Moreover, a helmet streamer structure with its two mirror points at P_0 and P_1 (Fig. 7.4) matches the results of our leakage model based on PdBI data, as well as the appearance of the source in the VLBA image.

Finally, we point out that the helmet streamer in the simplified sketch of Fig. 7.4 is represented, for simplicity’s sake, by a straight structure. In real highly conducting stellar plasmas, where the ionized gas is frozen to the field lines, more complex morphologies will occur: wherever magnetic pressure exceeds gas pressure, the fluid moves only along the field lines. In contrast, when gas pressure dominates, the magnetic field lines do move or bend, depending on the fluid motion. In a rotating star with mass loss rate \dot{M} and terminal wind velocity v_∞ , the distance (called Alfvén radius, R_A) where the corotation of the wind can no longer be enforced by the

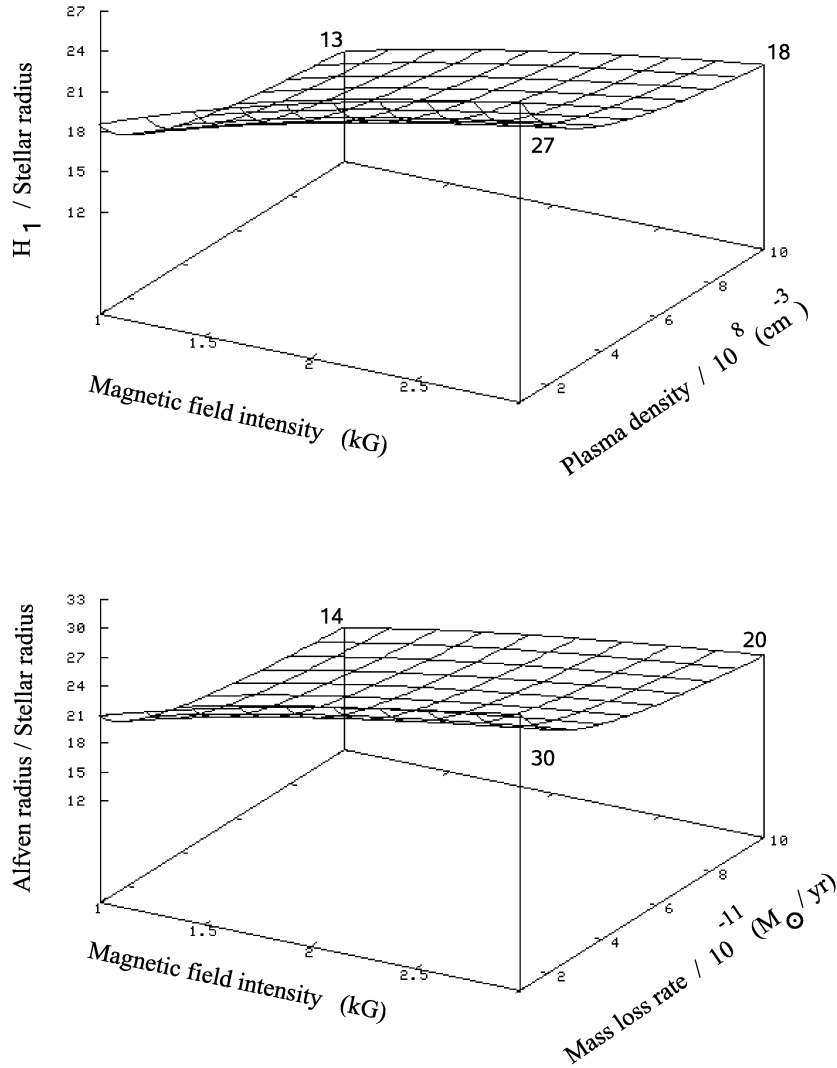


Figure 7.3: Top: Variations of the height H_1 (Eq. 7.8), where magnetic reconnection occurs, as a function of magnetic field intensity and plasma density (see Section 7.5). Bottom: Alfvén radius (Eq. 7.9) as a function of magnetic field intensity and mass loss rate (see Section 7.6)

magnetic field and the magnetic field lines become curved is, as given by André et al. (1988),

$$\frac{R_A}{R_*} = 26 \left(\frac{B_*}{10^4 \text{G}} \right)^{\frac{1}{3}} \left(\frac{\dot{M}}{10^{-10} M_\odot \text{ yr}^{-1}} \right)^{-\frac{1}{6}} \left(\frac{v_\infty}{10^3 \text{ km s}^{-1}} \right)^{\frac{1}{6}} \left(\frac{P}{1 \text{d}} \right)^{\frac{1}{3}}. \quad (7.9)$$

Adopting a range 10^{-11} – $10^{-10} M_\odot \text{ yr}^{-1}$ for the mass loss rate of a weak T Tauri star (André et al. 1992), and a wind terminal velocity of 300 km/sec (Ardila et al. 2002), we can conclude that the Alfvén radius for $P = 3 \text{ d}$ (Fig. 7.3 bottom) is in the range of (14 – 30) R_* .

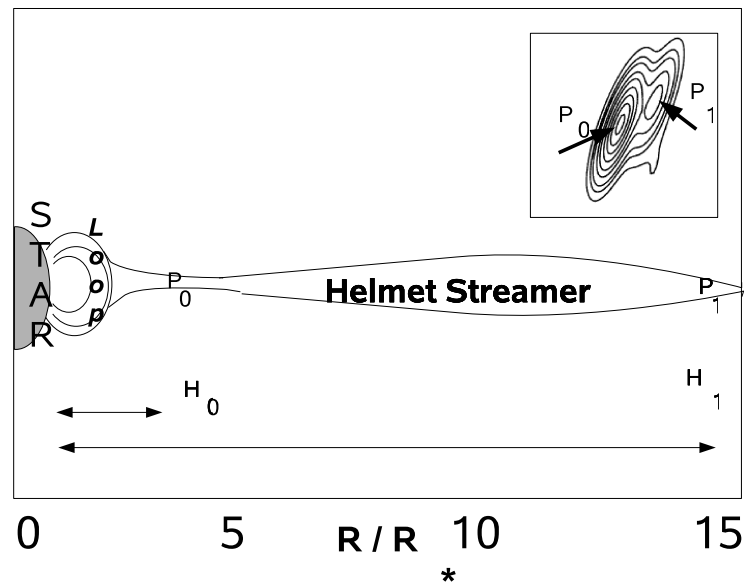


Figure 7.4: Sketch of the magnetic structure of a helmet streamer, above a coronal loop, as treated in magnetohydrodynamic models (Endeve et al. 2004). The small box contains the VLBA image by Phillips et al. (1996).

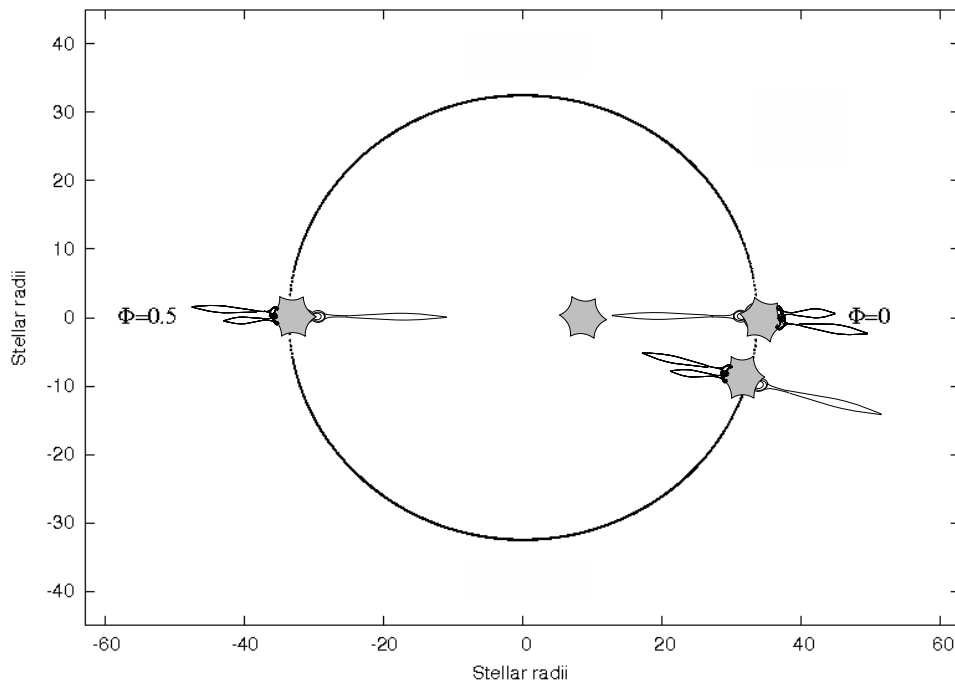


Figure 7.5: Sketch of the binary system with the orbit parameters of Welty (1995). One star with helmet streamers is shown at different positions along the orbit. Interbinary collisions may occur at periastron passage (see text).

7.7 Conclusions

Our previous observations of the binary system V773 Tau A (Massi et al. 2002) have shown inter-binary loop collisions at periastron passage. We performed millimeter wavelength observations

aimed to better define the extended magnetic structure confining the radio-emitting plasma, its topology, strength, and the energy of particles trapped in it. Based on our results, we propose the following scenario.

Radio and X-ray emission from V773 Tau A arise from spatially separated volumes: X-ray emission arises from denser and smaller regions (size $\lesssim 1R_*$) like the closed loop region underneath P_0 in the sketch of Fig. 7.4 (see Section 7.2). The radio emission emerges from larger and more diffuse regions that are similar to the solar helmet streamers. A helmet streamer from one of the stars, formed at the top of a coronal loop, as in the case of the Sun, could interact with the corona of the other star and could produce the strong radio flares observed around periastron passage (Massi et al. 2002). In this scenario, the lack of flares at some periastron passage (as in the PdBI observations of Table 7.3) could be explained as the absence of a collision, possibly because no large enough helmet streamer was emerging on the hemisphere facing the other star. As shown in Fig.7.5, because of the slightly eccentric orbit ($e \simeq 0.3$, Welty 1995) the distance at periastron ($23 R_*$) is appreciably less than at apoastron ($40 R_*$). The size of the helmet streamer should therefore be comparable with the periastron distance, but still be less than $40 R_*$. In this work, where we report a flare at 3 mm with $S_{\text{peak}} = 360 \pm 17$ mJy, we have derived the size “ H_1 ” of the emitting region (i.e. the helmet streamer) in three completely independent ways. Interpreting the rising time of the flare in terms of propagation towards the low corona of a shock due to a magnetic reconnection event occurring at large height, we have determined a height H_1 in the range of $(13 - 27) R_*$. This size agrees with that determined for the Alfvén radius, i.e. in the range $(14 - 30) R_*$. By interpreting the rapid decay of the flare as leakage of the emitting electrons from the trapping magnetic structure of size H_1 , we determine H_1 in the range $(10 - 20) R_*$. As a result, one of the two stars of the system might have a corona of a few stellar radii only, and interbinary collisions can still occur because of a large (i.e. average size $H_1 \sim 19R_*$) helmet streamer located on the other star.

The leakage model has shed light on the nature of the electrons responsible for the flare. We state that interbinary collisions are able to accelerate electrons to relativistic velocities. In fact, we determine a Lorentz factor γ of up to 632. This confirms that the emission in this pre-main sequence system is synchrotron radiation, as postulated from the observed linear polarization (Phillips et al. 1996).

In particular, streaming back and forth between the two mirror points (P_0 and P_1 in Fig. 7.4) of the helmet streamer, with magnetic fields between 0.12 G and 125 G, the relativistic electrons produce the observed synchrotron radiation. The trapping by the helmet streamer is, however, only partial and during each reflection particles escape and the emission fades out relatively quickly. Leakage explains the puzzling finding that flares have similar decay times (1 – 2 hours), not only in different radio bands, but also in the millimeter band. The latter similarity would be difficult to explain on the basis of any loss mechanism dependent on the electron energy.

7.8 Appendix: Energetic considerations

Accelerated nonthermal electrons are subject to energy losses both because synchrotron radiation is emitted and because of collisions with thermal electrons. In addition, energy losses are also due to the interaction of nonthermal electrons by inverse Compton (IC) processes with the stellar radiation field (external IC) and even with photons emitted by the synchrotron process itself in the radio band (Synchrotron Self-Compton, SSC).

If synchrotron losses are responsible for the observed decay (τ , in hours), the following relationship holds between magnetic field intensity B (in Gauss) and Lorentz factor γ (Blumenthal & Gould 1970):

$$\gamma B^2 = \frac{2.2 \times 10^5}{\tau_{\text{synchrotron}}}. \quad (7.10)$$

From Eqs. (7.10) and (7.2), with $\tau_{\text{synchrotron}} = 2.31$ hours, the value of the magnetic field strength in the emitting region and the value of the Lorentz factor of the emitting electrons can be derived as: $B = 56$ G and $\gamma = 30$.

A magnetic dipole field, with $B(R_*)$ at the stellar surface, attains the intensity of 56 G at a distance $H/R_* = [B(R_*)/56]^{1/3}$. In the literature, there are very few estimates of the magnetic flux $B(R_*)$ in weak-line T Tauri stars. Basri et al. (1992) determined the upper limit of 1500 G for the product Bf , where $f < 1$, for TAP 35. An even higher value ($Bf > 2000$ G) is derived by Guenther et al. (1999) in the source LkCa 16. Basri et al. (1992) exclude fields above 3000 G, and more recently (Bower et al. 2003), the value of $B = 2600$ G has been measured in a weak-line T Tauri star in the Orion Nebula. Therefore, 1000 – 3000 G seems to be a likely range. For $B(R_*) \leq 3000$ G, the magnetic dipole field attains the intensity of 56 G at a distance $H/R_* \leq 3.8$ from the stellar surface. This scenario cannot account for the observed extended radio emission (Section 7.2). We also exclude synchrotron losses as being responsible for the life time of $\tau = 1$ hour in the Phillips et al. (1996) observations at $\nu_0 = 8.2$ GHz. The application of Eqs. (7.1) and (7.10) would give $B \sim 223$ G and $\gamma = 4$, and hence emission coming from a region relatively close to the stellar surface ($H/R_* \leq 2.4$) and from mildly relativistic electrons, in contrast with previously reported considerations (Section 7.1 and 7.2).

IC losses cannot account for the observed emission decay either. In fact, as derived hereafter, IC losses are even lower than synchrotron losses because the radiation energy density (U) is smaller than the magnetic energy density i.e.,

$$U < B^2/8\pi. \quad (7.11)$$

A dipole magnetic field, with the intensity at the surface of the star in the range quoted above (say $2 \cdot 10^3$ G), has $B^2/8\pi \simeq 1.6 \times 10^5 (H/R_*)^{-6}$ erg cm $^{-3}$, while $U = L_*/4\pi cH^2 = 0.86 (H/R_*)^{-2}$ erg cm $^{-3}$ for known values of radius and luminosity of V773 Tau A ($R_* \sim 2.4R_\odot$, $L_* \sim 3L_\odot$) (Skinner et al. 1997; Welty 1995). Hence, if the radiation of the star is the source of the seed photons (IC), condition (7.11) holds for $H \leq 21R_*$. On the other hand, for SSC, the related flare luminosity is $L_{\text{flare}} = 6.4 \times 10^{26}$ erg sec $^{-1}$, which, supposing that the flare takes place in a spherical region of radius aR_* , with $a > 0.01$, gives $U = 6 \cdot 10^{-8} a^{-2}$ erg cm $^{-3}$. Hence, condition (7.11) holds throughout the region of interest, since $(H/R_*) \leq 118 a^{1/3}$ is verified for every $(H/R_*) \leq 25$.

Finally, the thermalization time due to collisions of relativistic electrons in an ionized gas of density n is given by (Petrosian 1985; Massi & Chiuderi-Drago 1992):

$$\tau_{\text{collisions}} \simeq 4.16 \times 10^8 \frac{\gamma}{n}, \quad (7.12)$$

where n is in cm $^{-3}$ and τ is expressed in hours. Therefore, collisions would be important only for $n \sim \gamma \cdot 1.8 \times 10^8$ cm $^{-3}$, which, for the relativistic electrons ($\gamma \gg 1$) implied by the linear polarization, does not match the condition derived from Faraday depolarization ($n < 1 \cdot 10^9$ cm $^{-3}$; see Section 7.2).

Chapter 8

Search for weak linear polarization in molecular line emission towards protostars with the IRAM 30m telescope

8.1 Introduction

Partial polarization in rotational emission lines of molecules was first predicted by Goldreich & Kylafis (1981, 1982). Additionally, Kylafis & Shapiro (1983) and Kylafis (1983a) also predict polarized absorption lines. Already a very weak magnetic field causes the rotational levels to split into magnetic sublevels. Unequal populations of the different sublevels lead to partial linear polarization. This is the case when there is a gradient in the line optical depth, e.g. due to a velocity gradient or an anisotropic radiation field. In this model, the polarization percentage depends on several factors: the degree of anisotropy, the ratio C/A of the collisional rate to the radiative decay rate, i.e. the ratio of the density compared to critical density of the transition, the optical depth of the line, and the angle between the line of sight, the magnetic field, and an assumed axis of symmetry of the velocity field. The maximum polarization percentage is on the order of a few percent and is expected for $C/A \approx 1$ – i.e. a density close to the critical density for the transition – and $\tau \approx 1$. At smaller optical depths, it becomes difficult for an anisotropic optical depth to have any effect on the observed radiation, while at higher optical depths, collisions increasingly dominate radiative transitions, tending to equalize magnetic sub-level populations. Since optical depth varies across a line profile, an optical depth of order unity usually is found only in certain parts of a spectrum.

Detailed predictions of the GK effect and its observables are model-dependent. Trying to predict the polarization percentage, Goldreich & Kylafis (1981, 1982) used a large velocity gradient (LVG) model with two molecular rotational levels, resulting in values of up to 14%. An extension of this model to include more levels, developed by Deguchi & Watson (1984), resulted in lower polarizations of about 7%. Morris et al. (1985) discuss line polarization in expanding circumstellar envelopes – in fact the environment in which the effect was first observed later on. Lis et al. (1988), abandoning the LVG approximation, concluded that polarizations of a few percent should be observable. According to them, polarization should be greatest for molecules that have large permanent dipole moments. Therefore, polarized emission from CS emission would be more likely to be observable than from CO (2.0 D vs. 0.1 D), even though CS emission may be fainter. Kylafis (1983b) and e.g. Lis et al. (1988) note that linear polarization is expected to be stronger at the *edge* of molecular clouds rather than at their centers due to more anisotropic optical depth. We will see in Section 8.3.1 that such observations are technically

Table 8.1: 30m observations, April 2005: Source coordinates

Source	RA/Dec (J2000.0)	v_{LSR} [km s ⁻¹]	d [kpc]
DR21(OH)	20h39m00.9s +42°22'48"0	+3	3 ^a
G34.3+0.2	18h53m18.6s +01°15'00"0	+58	2.0 ^b
W3(OH)	02h27m03.9s +61°52'25"0	-48	3.8 ^c
UYSO 1	07h05m10.85s -12°19'02"4	+12	1.0 ^d

a) Campbell et al. (1982), b) Reid & Ho (1985)

c) Hachisuka et al. (2006), d) Forbrich et al. (2004)

very difficult with a single-dish telescope because it is very likely that emission then falls onto polarized sidelobes.

The observed polarization direction is linked to the orientation of the magnetic field projected onto the plane of the sky. According to Kylafis (1983b), the polarization is either perpendicular or parallel to the magnetic field lines in case of simple velocity fields (1D or 2D), even for quite low field strengths ($B \approx 1\mu\text{G}$).

While polarization observations of thermal dust emission have been possible for many years, the low polarization levels expected for molecular lines were discovered only recently. Following earlier attempts towards young stellar objects (Wannier et al. 1983; Barvainis & Wootten 1987; Glenn et al. 1997b), the first observation of linearly polarized molecular line emission was made by Glenn et al. (1997a) towards the envelope of the evolved star IRC +10216 in CS(2-1) and HCN(1-0). They measured polarizations of $p = 5.1 \pm 1.5\%$, as of now the highest polarization interpreted as due to the Goldreich-Kylafis effect, and $p < 0.9\%$, respectively. Then, Greaves et al. (1999) observed two molecular clouds and the “2 pc ring” around the Galactic center in CO(2-1) and CO(3-2), and found polarizations at a level of 0.5%–2%. The Goldreich-Kylafis effect has also been observed in interferometric observations towards the outflow of the young stellar system NGC 1333 IRAS 4A (Girart et al. 1999), as well as in the outflow of NGC 2024 FIR 5 in single-dish observations (Greaves et al. 2001). Also, gas flows near the galactic center were studied (Greaves et al. 2002). Lai et al. (2003) measured polarized continuum and CO line emission in the star-forming region DR21(OH), confirming the prediction that the two polarizations are either parallel or orthogonal to each other. Cortes et al. (2005) find that towards the same source, the linear polarization of the CO(1-0) transition is perpendicular to that of the CO(2-1) transition, an unexpected result which they explain by anisotropic excitation. In subsequent studies, weak linear polarization of CO(2-1) was found in G30.79 FIR 10 and NGC2071IR (Cortes & Crutcher 2006; Cortes et al. 2006, both observations carried out with BIMA).

When compared to dust polarization, line observations have the advantage of containing velocity information. Continuum and line polarization observations thus are complementary, covering a wide parameter space of density and temperature. Our aim here is to establish whether observations of the GK effect are feasible with the correlation polarimeter XPOL at the IRAM 30m telescope and to study how the measurement is influenced by extended emission in the surroundings of the compact sources studied.

8.2 Observations and data analysis

We used the XPOL polarimeter at the IRAM 30m telescope to search for linearly polarized molecular line emission. XPOL operates at the intermediate frequency of the telescope. The signals of two orthogonally linearly polarized receivers observing simultaneously are correlated to yield all four Stokes parameters simultaneously. The instrument is an upgrade of the one

Table 8.2: 30m observations, April 2005: Molecular transition lines, integration times, and hour angle ranges

Source	Transition	t_{int}	HA range
DR21(OH)	$^{13}\text{CO}(1-0)$	144 min	-1.097 ... 6.610 h
DR21(OH)	$\text{C}^{18}\text{O}(1-0)$	62 min	-5.316 ... -2.051 h
DR21(OH)	CS(2-1)	72 min	-2.258 ... 8.001 h
G34.3+0.2	$^{13}\text{CO}(1-0)$	79.5 min	1.861 ... 4.290 h
G34.3+0.2	$\text{C}^{18}\text{O}(1-0)$	64 min	0.271 ... 2.037 h
G34.3+0.2	CS(2-1)	64 min	-2.727 ... -1.060 h
W3(OH)	$^{13}\text{CO}(1-0)$	64 min	3.244 ... 4.998 h
W3(OH)	$\text{C}^{18}\text{O}(1-0)$	63.5 min	-4.961 ... -2.822 h
W3(OH)	CS(2-1)	66 min	-1.542 ... 0.400 h
W3(OH)	$\text{C}^{34}\text{S}(2-1)$	88 min	4.457 ... 6.973 h
UYSO 1	$^{13}\text{CO}(1-0)$	72 min	-3.139 ... -0.676 h

described in detail by Thum et al. (2003). Before the start of the observations, both receivers were tuned to the same local oscillator standard. A linearly polarized signal generator is used to calibrate phase variations across the bandpass and to determine the instrumental phase which is subsequently monitored throughout the observation. The minute changes in the instrumental phase that occur during the observations are corrected using a phase shifter.

We observed the star-forming regions DR21(OH) and a hot molecular core near the ultra-compact H II region W3(OH), as well as the cometary H II region G34.3+0.2 mainly in $^{13}\text{CO}(1-0)$, $\text{C}^{18}\text{O}(1-0)$, and CS(2-1) in order to detect linear polarization due to the Goldreich-Kylafis effect. In addition, the candidate massive protostar UYSO 1 (Forbrich et al. 2004) was observed in $^{13}\text{CO}(1-0)$. The sources were mainly selected for their bright line emission and their compactness compared to the telescope beam ($22''$ FWHM for CO(1-0)). These observations were carried out in April 2004 and from April 22 to April 23, 2005. However, the alignment of the two receivers was considerably improved in-between the two observing campaigns, reducing instrumental polarization, and we discuss only the 2005 data here. Details about the observations are listed in Tables 8.1 and 8.2. Pointing was checked approximately hourly while focus was checked about every two hours.

While previous polarimetric observations of DR21(OH) in ^{12}CO (Lai et al. 2003) are sensitive only to the outermost material or foreground material along the line of sight (while extended emission is filtered out by the interferometer), our choice of CO isotopologues with a lower optical depth should improve the comparability with dust polarization measurements. With CS, the same region is also traced using a molecule with a larger dipole moment (2.0 vs. 0.1 Debye) and thus higher critical density (by about two orders of magnitude). The maximum linear polarization in CO(2-1) reported by Lai et al. (2003) is 2.4%.

We analyzed the data with the XPOL software version 3.0, developed in the CLASS environment of the GILDAS software¹. In the data reduction, an elevation-dependent part of the instrumental polarization is taken into account, as determined from observations of Venus at different elevations. This leads to an efficiency correction for horizontal polarization in Nasmyth coordinates of typically $< 1\%$ (for elevations between 13° and 62°).

In order to discuss the role of extended emission in our data, on-the-fly maps of source neighbourhoods were obtained on August 16–18, 2006 at the 30m telescope. Mapping was performed in molecular line transitions which were also used in the previous polarimetric observations. Two molecular lines were observed simultaneously towards each of the three sources W3(OH), G34.3+0.2, and DR21(OH). In case of W3(OH), the mapping was done in $\text{C}^{18}\text{O}(1-$

¹<http://www.iram.fr/IRAMFR/GILDAS>

0) and $^{13}\text{CO}(1-0)$ while for the latter two sources the transitions $^{13}\text{CO}(1-0)$ and $\text{CS}(2-1)$ were chosen.

8.3 Results and discussion

The resulting Stokes spectra as well as the derived linear and circular polarizations and the polarization angle are shown in Fig. 8.1 for all sources and transitions. Since instrumental or telescope-related effects are best revealed in the coordinates of the Nasmyth focus while an astronomical signal is best studied in equatorial coordinates, the plots of the Stokes spectra are shown for both coordinate systems. These rotate relative to each other during the observation, depending on the hour angle range. Based on the Stokes spectra, the linear polarization $p_L = \sqrt{(Q^2 + U^2)}/I$, the circular polarization $p_C = V/I$ and the position angle of the linear polarization $\chi = \arctan(U/Q)/2$ (E from N) are calculated. The polarization angle has an ambiguity of 180° . The polarizations p_L and p_C are independent of the coordinate system, they only differ in χ . All error bars represent 1σ baseline noise from the four Stokes spectra propagated throughout the analysis.

Looking at the single observations of DR21(OH) in detail, we note significant variations in the Stokes- I line profiles, mainly in ^{13}CO . Since the interferometric ^{12}CO data reported by Lai et al. (2003) clearly show two emission peaks separated by $8''$, i.e. about a third of the beam size in our observations, this may be due to marginally resolved source structure. In this case, the different line profiles could be explained by small pointing inaccuracies. The same effect, though to a lesser degree, is also observed towards W3(OH), again mainly in ^{13}CO . In Fig. 8.1, we still plot the combined data for each source and transition because some effects can also be seen in these spectra.

In all cases, weak linear polarization, varying across the line profiles, is detected while the circular polarization is zero within the uncertainty of the measurement across the entire line profiles. The degrees of linear polarization are below 4%, and this value is reached only in few cases, e.g. for G34.3+0.2 in $\text{CS}(2-1)$. The polarization angles mostly have well-defined values, smoothly varying or even nearly constant across parts of the line profile. This does not necessarily have to be a property of the sources, though (see discussion of instrumental effects below). It is interesting to note that the observed polarization appears to be systematically higher in the line wings, even when taking into account the lower signal to noise ratio.

When a linearly polarized source is observed across a wide hour angle range, its measured polarization properties rotate against the coordinate system of the Nasmyth focus in a well-defined way, thus analyzing the dependance on hour angle in this reference frame can in principle help distinguishing astronomical polarization from instrumental effects if the signal is strong enough and the geometry is favorable. Among our sources, DR21(OH) was observed with the widest hour angle coverage. However, because of the above-mentioned time-variable line profile, we do not attempt to study the behaviour of the polarized signal as a function of hour angle. For the other sources, a wider hour-angle range would be required for such a type of analysis to become meaningful.

Even in the case of the ^{13}CO spectra with time-variable and thus unreliable line profiles due to source structure (namely DR21(OH) and W3(OH)), it is interesting to note that the linear polarization as well as especially the polarization angle χ are still well defined. The polarization angle χ remains roughly constant over large parts of the spectrum. In the case of W3(OH), the $^{13}\text{CO}(1-0)$ and the $\text{CS}(2-1)$ transitions display nearly the same polarization angle dependency on frequency while there is no clear correlation in case of DR21(OH). The spectrum of G34.3+0.2 will be discussed in more detail below: Here, there is a difference of 90° in part of the spectrum.

Since DR21(OH) was successfully searched before for the GK effect (Lai et al. 2003), though with an interferometer and in $^{12}\text{CO}(1-0)$, it is interesting to compare the results. With the 30m

telescope, we can detect polarized line emission on spatial scales of about the size of the main beam. Looking at previous results of millimeter continuum and heterodyne polarimetry, the assumption that magnetic fields are detectable on these large spatial scales seems reasonable (e.g. Ward-Thompson et al. 2000), even though it is important to keep in mind that this is only part of the picture. The opposite problem occurs in observations using an interferometer without zero-spacings correction yielding information on large-scale emission. Lai et al. (2003) find a maximum degree of linear polarization of 2.4 ± 0.6 % in $^{12}\text{CO}(1-0)$ and a polarization angle rapidly varying with velocity. How these results based on the much more optically thick $^{12}\text{CO}(1-0)$ compare in detail to our single-dish observations of less optically thick isotopologues, when filtering out large-scale emission by the use of an interferometer, remains unclear. In our data, a comparison is further hampered by the observed variable line profile.

8.3.1 Simulating the instrumental response

There is always an instrumental contribution to the observed linear polarization. A clear sign of instrumental polarization is the leakage of power from Stokes- I to other Stokes parameters, especially Stokes- Q and U . While in some cases (e.g. DR21(OH) in ^{13}CO) the Stokes- Q spectra resemble scaled copies of the Stokes- I spectra at first sight, possibly a sign of this leakage effect, the correspondence is not exact, leading to considerable residuals when trying to correct this by subtraction. This non-correspondence can be explained by velocity structure of the source which would lead to the observation of slightly different source parts in the different Stokes parameters. One consequence of this polarization leakage can be a mostly constant polarization angle χ : If the Stokes- Q and $-U$ spectra are scaled copies of the Stokes- I spectrum to some degree, their ratio and, thus, χ will tend to stay constant over the spectrum. A phase jump of 90° could then be due to a change of sign in either Q or U .

In order to determine the order of magnitude of the instrumental part in the polarized signal more quantitatively, including the role of extended emission, we have attempted to simulate the linear polarization based on real source geometries but assuming that the sources are *not* intrinsically polarized. How the telescope beam looks like in the different Stokes parameters is best probed by observations of bright unpolarized sources. We acquired such beam maps in all four Stokes parameters by continuum observations of Venus on August 30th, 2004, at a wavelength of 3 mm (Fig. 8.2). At this time, Venus had an apparent size of $20''.9$. The alignment of the receivers was not changed between this date and our second run of polarization observations in April 2005. The signal-to-noise ratio in the Stokes- I map is ~ 500 . The linear polarization at the (0,0) position (i.e. the map center) is 0.74 % and stays < 1 % within reasonable pointing accuracies. These beam maps contain information on the instrumental polarization, for instance the effects due to ‘beam squint’, i.e. due to the two receivers looking at slightly different positions on the sky leading to polarized sidelobes. Therefore the presence of extended emission can significantly alter the measurements. Such a simulation thus yields a good estimate of the instrumental limits when observing low percentages of linear polarization, although a detailed error analysis of the simulation would require independently measured beam maps and is not attempted here. Obviously, the real beam shape at the time of the observation remains unknown, but our simulation should give a good order-of-magnitude estimate.

As noted above, the maps of the source geometries on the order of several beam sizes were obtained by on-the-fly mapping in two molecular transitions for DR21(OH), G34.3+0.2, and W3(OH) (Fig. 8.3). While the emission is well concentrated in the main source peaks there is (of course) still considerable emission in the surroundings.

In order to simulate the dependency of the linear polarization p_L on frequency (i.e. velocity), first a series of velocity-integrated maps in intervals of 0.5 km s^{-1} was computed. After resampling to the same resolution, these were then convolved with the beam maps of the 30m telescope in order to simulate a polarization observation. Since the observed maps are already

convolved with the telescope beam, this is not entirely accurate, but the additional smoothing due to a second application of the beam should not interfere with the estimates of instrumental effects on linear polarization that we seek to derive. Also, a simple convolution of source and model beam does not take into account the rotation of the source structure with regard to the horizontal telescope reference system which necessarily occurs in an observation covering a certain hour angle range. Subsequently, maps of simulated linear polarization were computed, and the value of p_L at the map center was taken as the simulated linear polarization. In general, the simulated polarization increases with distance from the map center because the main source emission then falls onto the polarized sidelobes. In real life, pointing errors occur, and we note that within $\pm 10''$ of the map center, the polarization varies by about $\pm 0.2\%$.

The resulting simulated spectra are shown in Fig. 8.4. First of all, it is important to note that the simulated linear polarizations assuming intrinsically unpolarized sources are on the same order of magnitude as the actual observations. The simulated linear polarization is considerably higher than the value of 0.74% from the beam map alone (see above), clearly demonstrating the influence of extended emission on the result of the measurement. While there is mostly no apparent correlation of simulated and measured polarization, the observed polarization behaves approximately as predicted for an unpolarized source with the same source geometry in case of DR21(OH) for the CS(2-1) transition. We note again that the simulations do not have the aim to exactly reproduce the measured polarizations but just to help in the interpretation.

8.3.2 G34.3+0.2: Intrinsically polarized?

The measurements yielded values above the simulated polarizations only in a few cases. The averaged simulated linear polarization is lowest for G34.3+0.2 in CS(2-1), arguably the most centrally concentrated source in this sample (Fig. 8.3). In the blueshifted line wing, measured polarizations of up to 3.6% contrast to simulated polarizations of slightly below 2%. If we take the simulation as an estimate for the instrumental polarization, then after its subtraction the intrinsic polarization reaches values of up to $\sim 1.5\%$. The measurements are also above the simulated values for DR21(OH) and W3(OH) in the $^{13}\text{CO}(1-0)$ transition, however these two datasets are unreliable due to the above-mentioned variable line profiles.

Thus, G34.3+0.2 emerges as the best detection of intrinsically polarized radiation within our sample. Additionally, the source appears to be sufficiently unresolved so that the line profile remains constant in the individual scans in both CS(2-1) and $^{13}\text{CO}(1-0)$, allowing a detailed comparison of the different transitions.

The spectra of G34.3+0.2 show two peaks in ^{13}CO and CS, apparently due to self-absorption at the line center (see the discussion of optical depth at the end of this subsection). In C^{18}O , only a single, broad line profile is seen. The observed linear polarization is strongest for CS and ^{13}CO with values of up to $\sim 4\%$ while in C^{18}O , values $\lesssim 2\%$ were measured. The velocity dependence of the linear polarization is similar especially for $^{13}\text{CO}(1-0)$ and CS(2-1). The most notable feature is that the polarization is highest in the blue-shifted line wing of the main velocity component, steadily falling off towards the red-shifted line wing. Interestingly, the offset between the velocity dependencies of the polarization angle χ between ^{13}CO and CS is 90° to within the error bars across the main velocity component. The situation is less clear for the weaker component. This differs from W3(OH) where there is no significant offset between the polarization angles in $^{13}\text{CO}(1-0)$ and CS(2-1) in nearly the entire spectrum. While differences of $\pm 90^\circ$ are reminiscent of the results of Cortes et al. (2005) who, as noted above, observed such a difference between the CO(1-0) and CO(2-1) transitions, this effect can easily be mimicked by instrumental effects in our case, so that the data remain inconclusive on this point.

The measurement of both $^{13}\text{CO}(1-0)$ and C^{18}O during this project allows to estimate the optical depth of the $^{13}\text{CO}(1-0)$ transition from the line ratio $^{13}\text{CO}/\text{C}^{18}\text{O}$ based on a number of assumptions. Among others, the beam filling factors are assumed to be the same, and the

ratio of optical depths is assumed to be $\tau_{13} = 5.5\tau_{18}$ (e.g. Vilas-Boas et al. 1994). Since the Goldreich-Kylafis effect is expected to be most prominent for $\tau \sim 1$, this is interesting to analyze. Fig. 8.5 shows the observed line ratio $^{13}\text{CO}/\text{C}^{18}\text{O}$ for G34.3+0.2, together with indications of the inferred optical depth of the ^{13}CO transition. The optical depth is indeed close to unity throughout most of the blue-shifted line wing where the observed polarization is highest.

8.4 Summary

We presented results of a search for weak linear polarization in molecular line emission towards protostellar sources, as expected if the Goldreich-Kylafis effect occurs. The project was carried out with the correlation polarimeter XPOL at the IRAM 30m telescope in different molecular line transitions. In order to interpret the spectra, we simulated the instrument response by convolving maps of the sources integrated in small velocity intervals with the telescope beam in all Stokes parameters. This way, the expected measured linear polarization when observing unpolarized sources of the same geometry was estimated. It turns out that the simulated linear polarizations are considerably higher than the value determined out of the beam maps for an unresolved source, thus only containing telescope-related effects. In fact, it is on the same order of magnitude as are the actually observed polarizations. This clearly shows that the role of extended emission in the surroundings of the sources has to be taken into account at least in this kind of single-dish polarimetric observations. In the case of G34.3+0.2 in the CS(2-1) transition, the best evidence for intrinsically polarized line emission was found, it is $p_L \lesssim 1.5\%$.

In preparing future single-dish observations of this kind, the sources and transitions have to be selected in a way that the sources are entirely unresolved with a minimum level of extended emission. This precludes the search for polarized emission at the edge of molecular clouds where, as noted above, the polarization may be more easily observable because of more anisotropic optical depth.

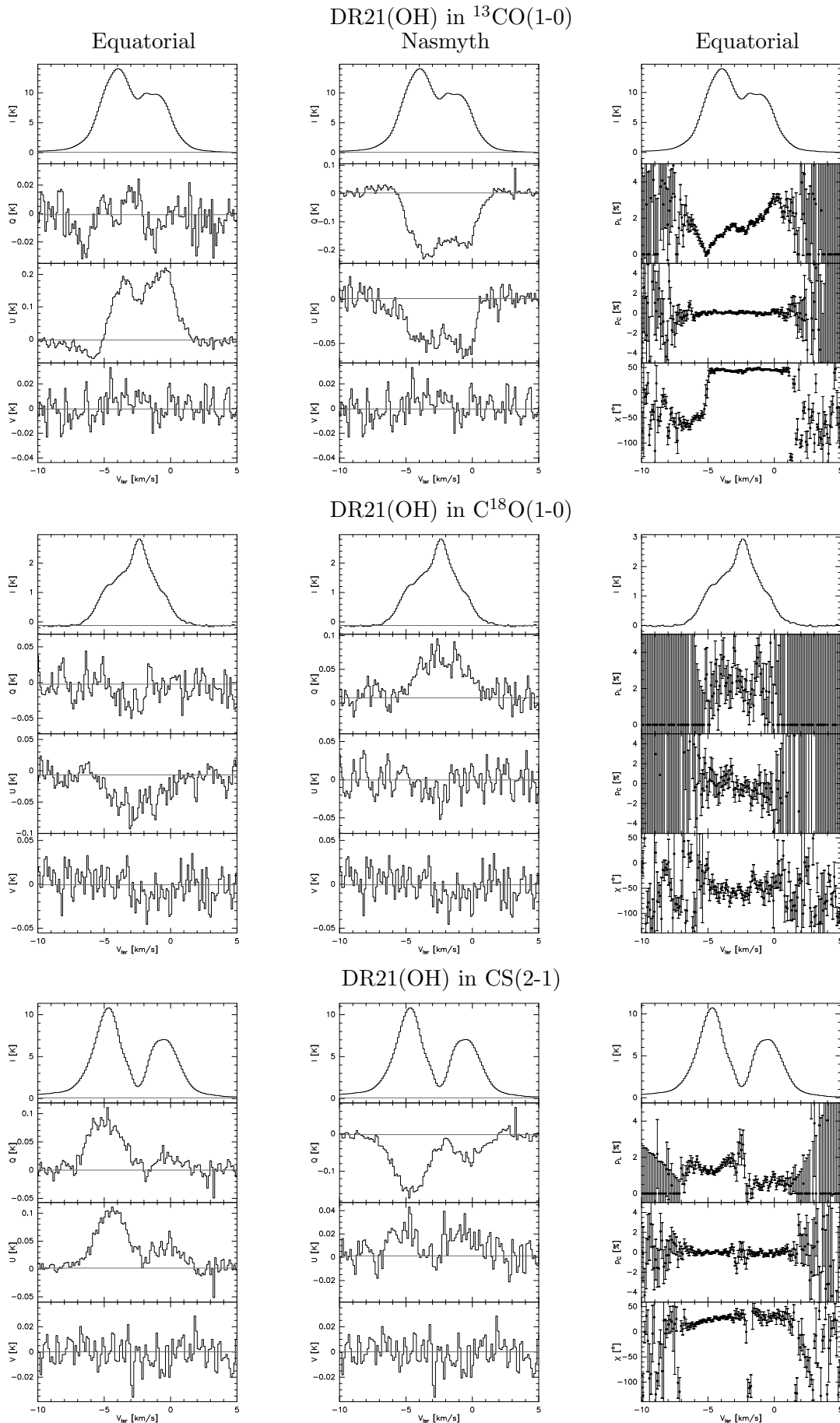


Figure 8.1: Stokes spectra (I, Q, U, V) [K] and resulting linear (p_L, χ) as well as circular (p_C) polarizations [%]. In the Stokes spectra, depicted in equatorial (left) as well as Nasmyth coordinates (center), the entire emission is shown while for the polarization plots (right) a baseline was subtracted (indicated in the Stokes spectra). A few single-channel spikes were blanked. Sources and transitions are indicated.

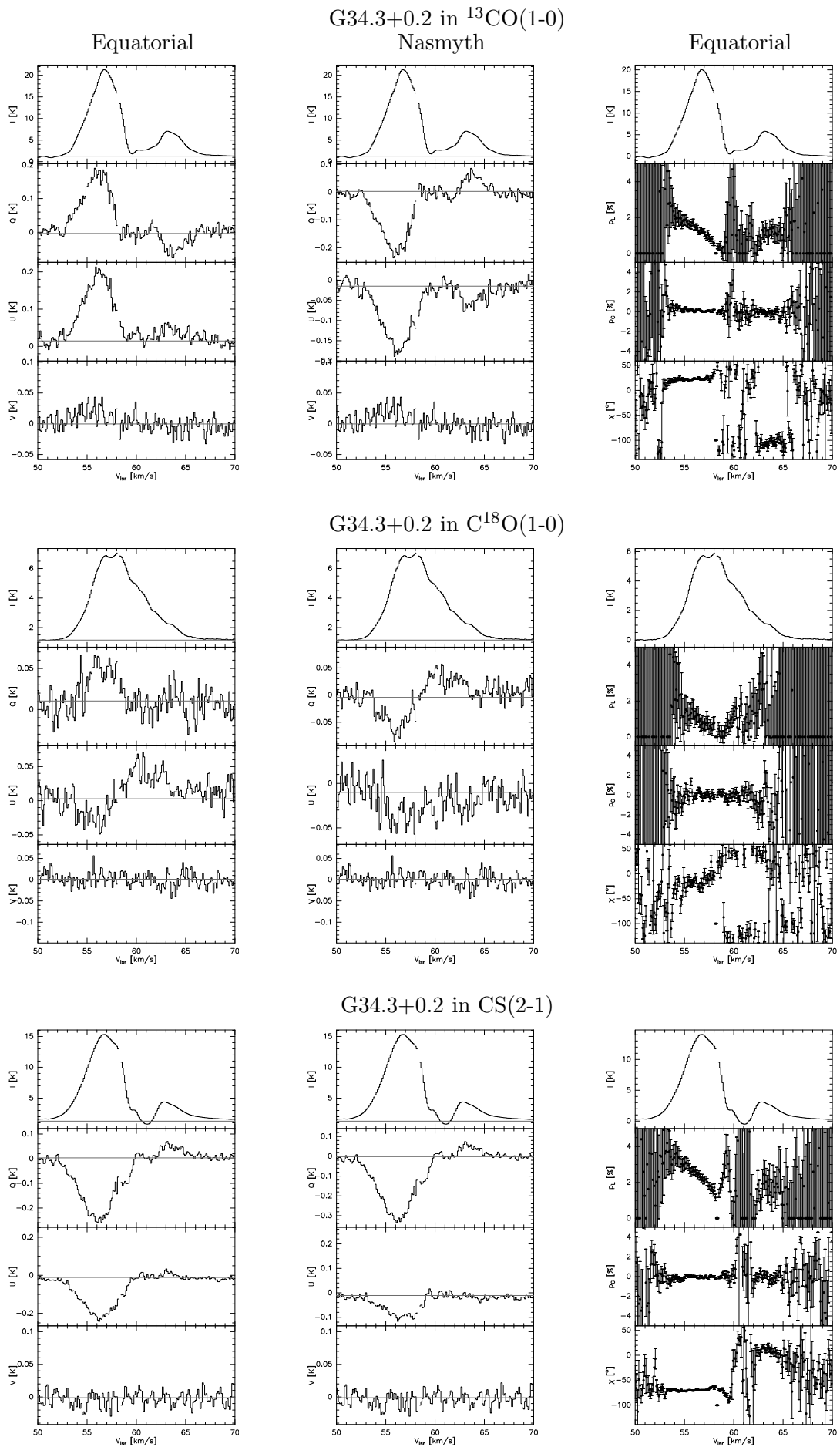


Fig. 8.1 cntd.

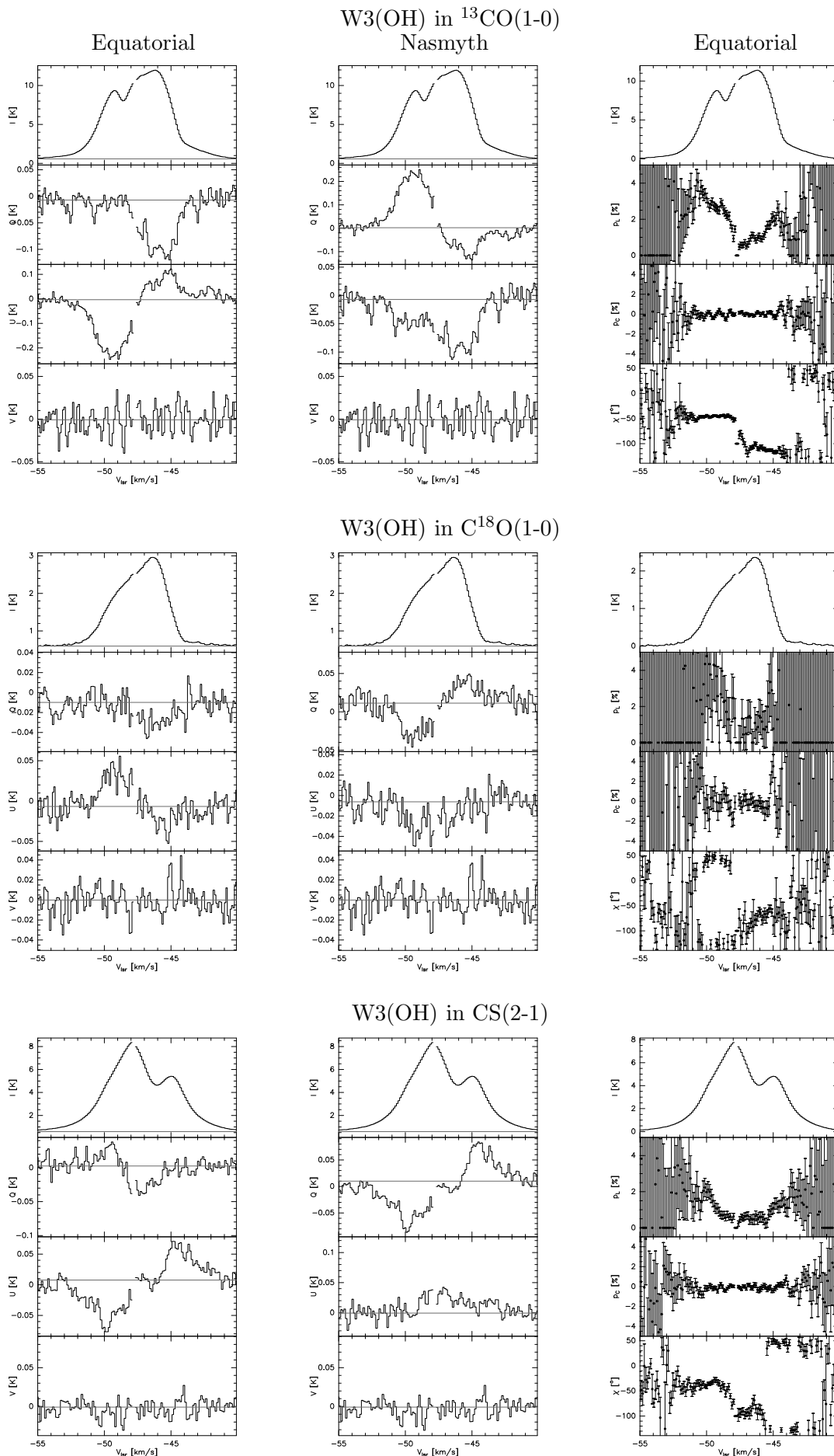


Fig. 8.1 cntd.

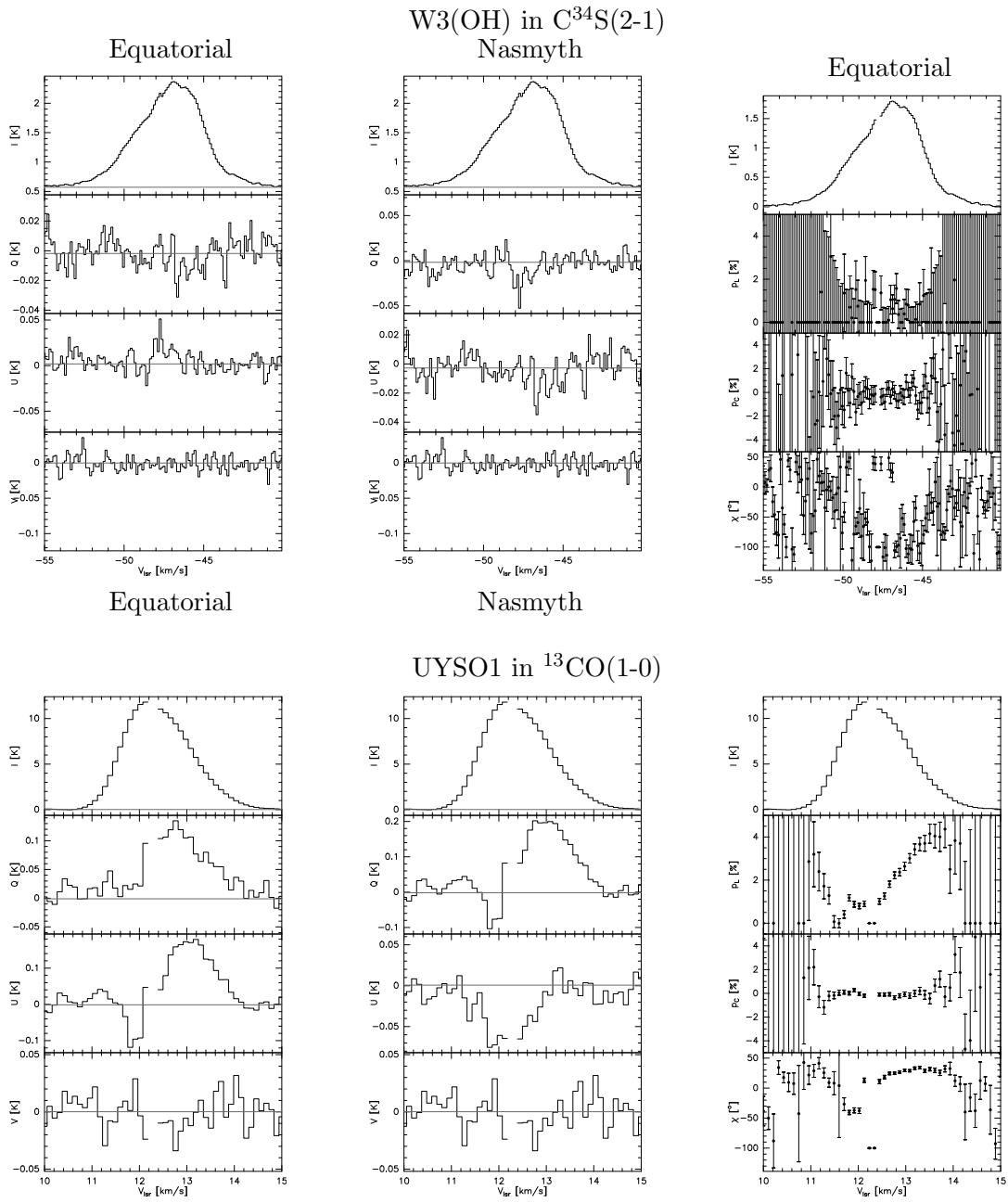


Fig. 8.1 cntd.

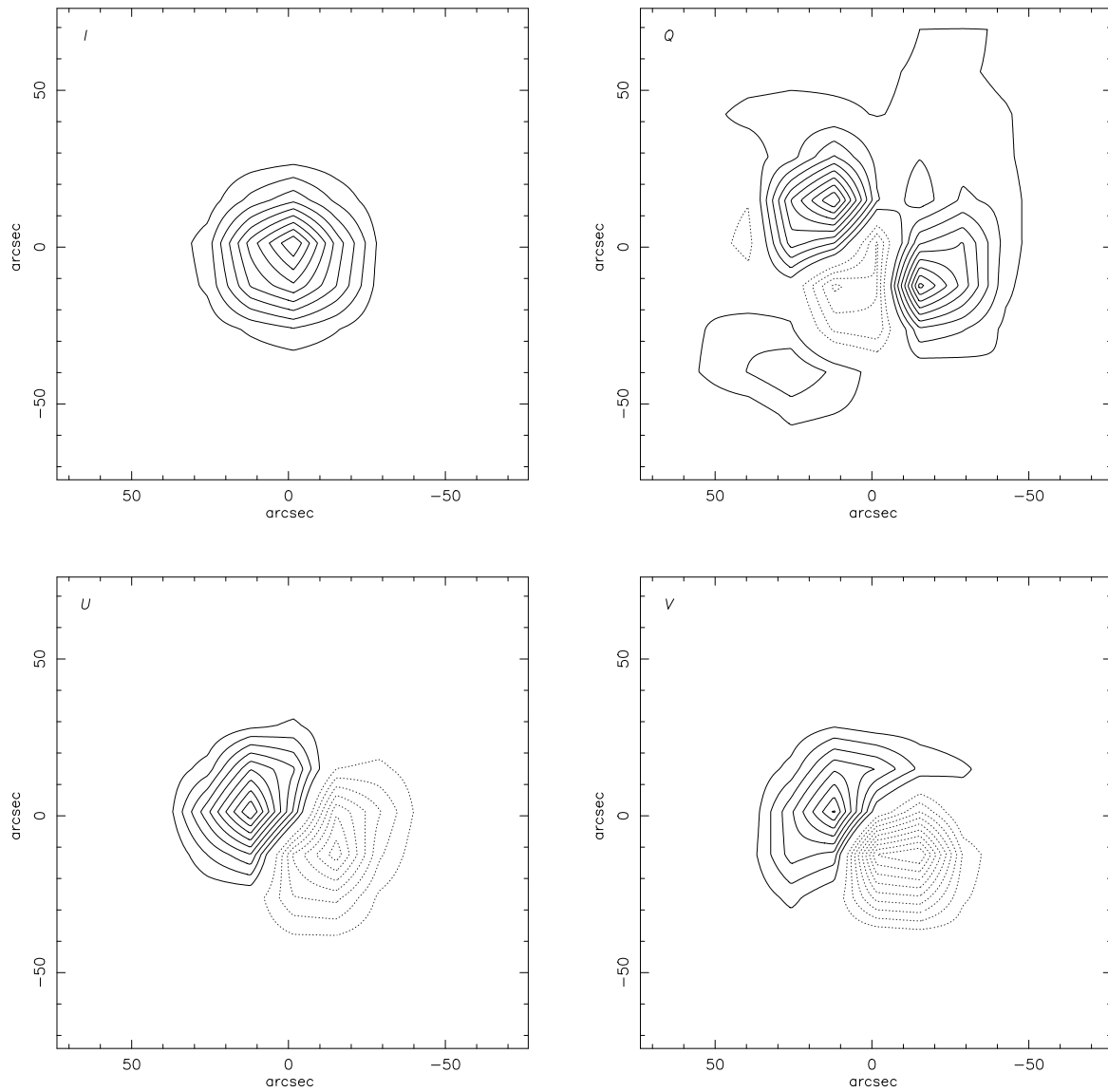


Figure 8.2: Beam maps of the 30m telescope (Stokes- I , Q , U , and V), acquired by observations of Venus and used in the simulations. The contour lines delineate multiples of 10% intensity, negative values are marked as dotted lines. The maxima of the Stokes- Q , $-U$, and $-V$ maps, in relation to the peak in Stokes- I , are at 2.1%, 1.3%, and 0.8%, respectively (not generally at the image center).

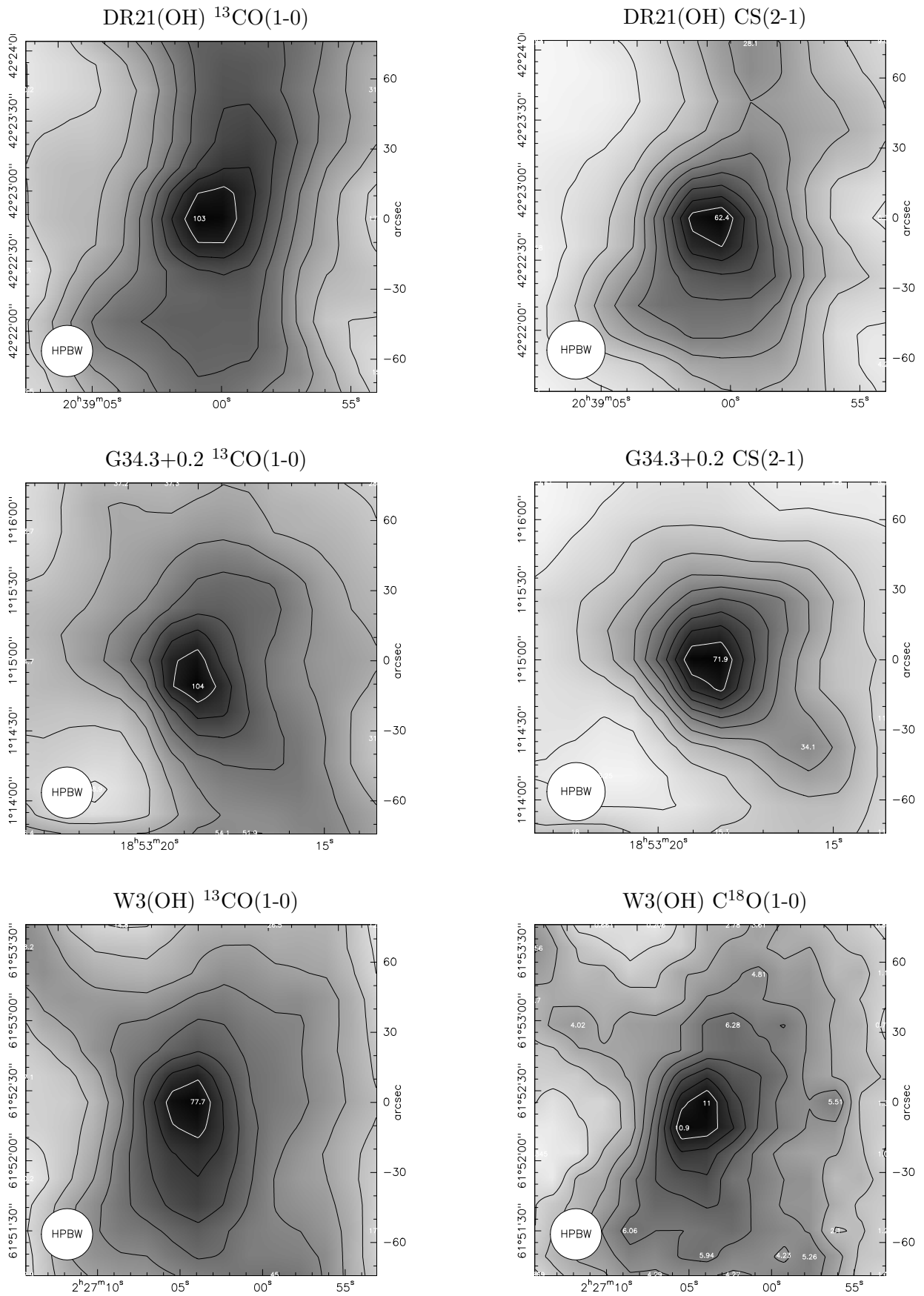


Figure 8.3: On-the-fly maps of DR21(OH), G34.3+0.2, and W3(OH), obtained with the IRAM 30m telescope, in two molecular transitions per source (as labeled). The contour lines delineate multiples of 10% of the map maximum which is indicated (the 90% contour line is shown in white for clarity). Map unit is K km s^{-1} (T_A^* integrated over the entire line profile).

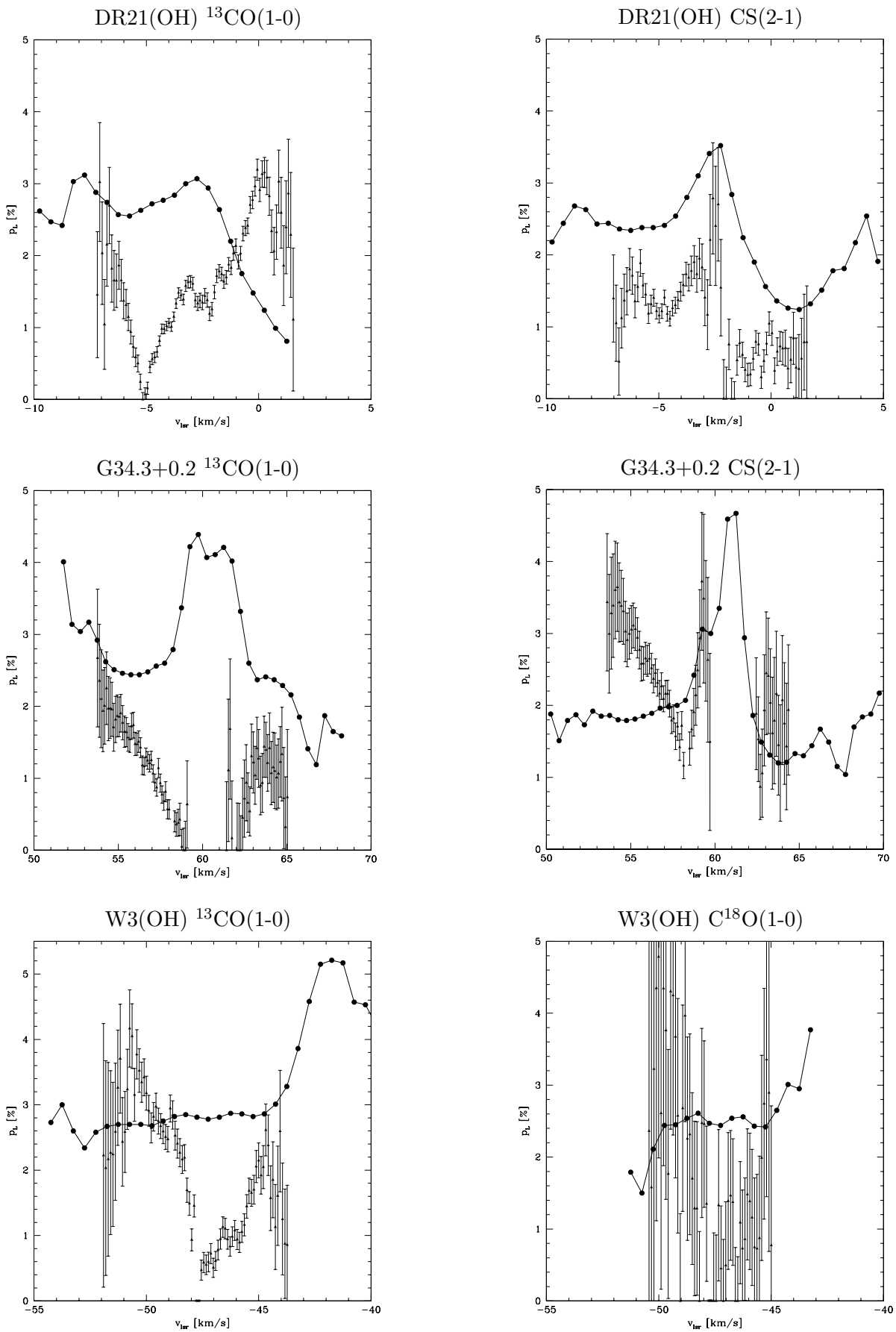


Figure 8.4: Simulated linear polarization after convolving the measured maps of the line integrated source environments with the Stokes beam maps (big points connected by a line, with actual data shown as triangles). For clarity, only measured datapoints with errors $< \pm 1\%$ are shown. For the full data and the line profile, see Fig. 8.1.

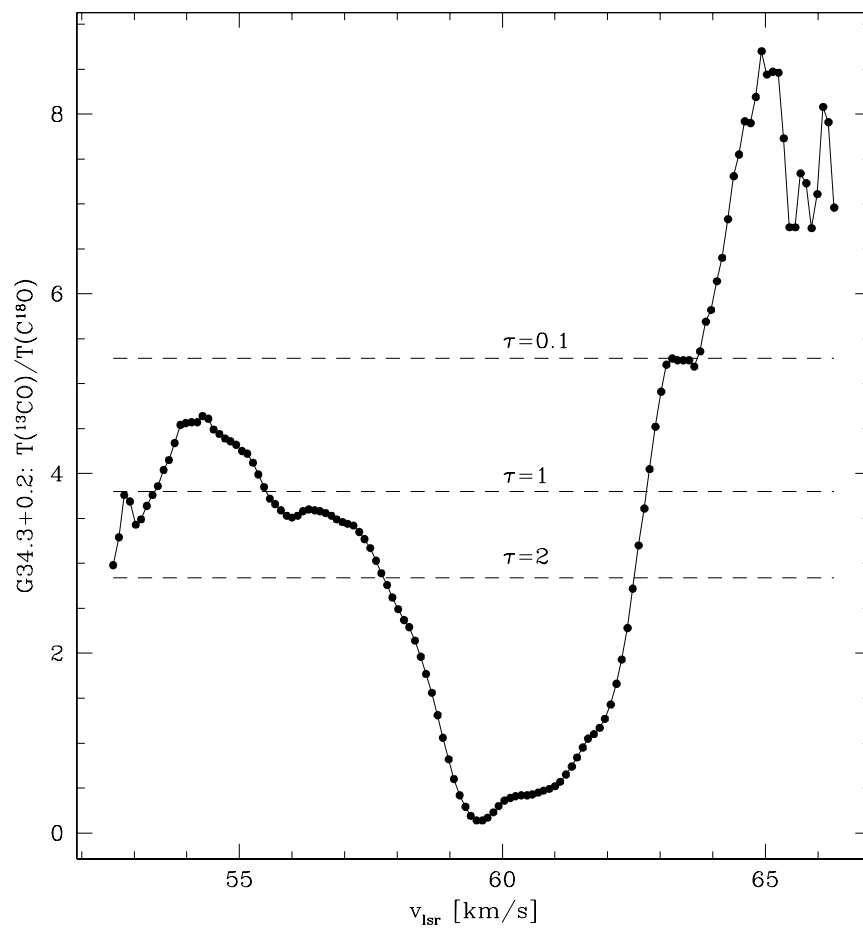


Figure 8.5: Line ratio $^{13}\text{CO}(1-0)/\text{C}^{18}\text{O}(1-0)$ for G34.3+0.2 (where both lines have $T_a > 0.1$ K) with inferred optical depth τ of the $^{13}\text{CO}(1-0)$ transition indicated (see text).

Chapter 9

Summary

In the following, the most important results of this work are summarized for every chapter, in the order of presentation.

Chapter 2 – Radio and X-ray variability of Young Stellar Objects in the Coronet cluster

The *Coronet* cluster in the nearby R CrA dark cloud offers the rare opportunity to study at least four “class I” protostellar sources as well as one candidate “class 0” source, a Herbig Ae star, and a candidate brown dwarf within a few square arcminutes – most of them detected at radio- and X-ray wavelengths. These sources were observed with the Very Large Array (VLA) at $\lambda = 3.5$ cm on nine occasions in 1998, spread over nearly four months. The source IRS 5, shown earlier to emit circularly polarized radio emission, was observed to undergo a flux increase accompanied by changes in its polarization properties. Comparison with VLA measurements made in January 1997 allows some analysis of longer-term variability. In addition to this radio monitoring, we analyze archival *Chandra* and *XMM-Newton* X-ray data of these sources. Three class I protostars are bright enough for X-ray spectroscopy, and we perform a variability analysis for these sources, covering a total of 154 ksec spread over more than two and a half years. Also in X-rays, IRS 5 shows the most pronounced variability, whilst the other two class I protostars IRS 1 and IRS 2 have more stable emission. X-ray data is also analyzed for the recently identified candidate class 0 source IRS 7E, which shows strong variability as well as for the Herbig Ae star R CrA for which we find extremely hot X-ray-emitting plasma. For IRS 1, 2 and 5, the hydrogen column densities derived from the X-ray spectra are at about half the values derived with near-infrared techniques, a situation similar to what has been observed towards some other YSOs.

Chapter 3 – Simultaneous X-ray, radio, near-infrared, and optical monitoring of Young Stellar Objects in the Coronet cluster

Subsequently, the *Coronet* cluster was studied in the first simultaneous X-ray, radio, near-infrared, and optical monitoring campaign of YSOs. In August 2005, we obtained five epochs of *Chandra* X-ray observations on nearly successive days accompanied by simultaneous radio observations at the NRAO Very Large Array during four epochs, as well as by simultaneous optical and near-infrared observations from ground-based telescopes in Chile and South Africa. Seven objects are detected simultaneously in the X-ray, radio, and optical/infrared bands; they constitute our core sample. While most of these sources exhibit clear variability in the X-ray regime and several display also optical/infrared variability, none of them shows significant radio variability on the timescales probed. We also do not find any case of clearly time-correlated optical/infrared and X-ray variability. Remarkable intra-band variability is found for the class I protostar IRS 5 which shows much lower radio fluxes than in previous observations, and the Herbig Ae star R CrA, which displays enhanced X-ray emission during the last two epochs, but no time-correlated variations are seen for these objects

in the other bands. The two components of S CrA vary nearly synchronously in the I band. The absence of time-correlated multi-wavelength variability suggests that there is no direct link between the X-ray and optical/infrared emission and supports the notion that accretion is *not* an important source for the X-ray emission of these YSOs. Only barely significant radio variability was found on timescales of days, in contrast to the variability previously found on timescales of weeks and months.

Chapter 4 – Corone in the Coronet: A very deep X-ray look into a stellar nursery Combining the *Chandra* X-ray data collected in the course of the multi-wavelength campaign with previous archival data, we obtain one of the deepest X-ray datasets ever obtained of a star-forming region. Its limiting luminosity is $L_{X,\min} \sim 5 \times 10^{26}$ erg/sec for lightly absorbed sources. The X-ray data are used to investigate the membership status of tentative members of the region, to derive plasma temperatures and X-ray luminosities of the YSOs, and to investigate variability on the timescale of several years. 48 of the 99 X-ray sources in the merged *Chandra* image can be identified with optical or near/mid-infrared counterparts. X-ray emission is detected from *all* of the previously known optically visible late-type (spectral types G to M) stellar cluster members, from five of the eight brown dwarf candidates, and from ten embedded objects (“protostars”) with class 0 or class I SEDs in the field of view. While the Herbig Ae/Be stars TY CrA and R CrA, a close companion of the B9e star HD 176386, and the F0e star T CrA are detected, no X-ray emission is found from any of the Herbig-Haro objects or the protostellar cores without infrared source. We tentatively find diffuse emission near R CrA / IRS 7. We argue that IRS 3 is most likely not a YSO, but rather a background star. We conclude that the X-ray emission of the *Coronet* YSOs is related to coronal activity, and find no indication of X-rays from accretion shocks. The X-ray emission of the AeBe stars TY CrA and HD 176386 originates probably from close companions. We find some evidence for significantly different X-ray properties of different YSO evolutionary stages. Finally, the X-ray data provide a complete census of YSOs in the *Coronet* region. Its IMF is consistent with the field-star IMF. Looking at its star-formation history, there is evidence for a highly variable star-formation rate in this region.

Chapter 5 – Searching for small-scale nonthermal radio emission from protostars by VLBI Looking for compact nonthermal centimetric radio emission, we performed VLBI observations of the four nearby protostars HL Tau, L 1551 IRS5, EC 95, and YLW 15. For maximum sensitivity, we used the High Sensitivity Array (HSA) where possible (all sources but YLW 15), yielding the currently most sensitive observations of this type of objects. While all four protostars were detected in VLA-only data, weak compact emission was only found in the VLBI data of YLW 15 VLA 2, constraining the size of its corona to $< 0.4 \times 0.1$ AU. Since this source is part of a binary system with observed orbital motion, further VLBI observations will allow to quickly determine the orbit very accurately.

Chapter 6 – A 1.3 cm radio flare from a deeply embedded source in the Orion Nebula Until now, only very few radio flares of YSOs have been observed in detail. Observing the Orion Nebula Cluster at a wavelength of 1.3 cm with the initial aim of probing circumstellar material of YSOs, a spectacular outburst was observed towards one source. Barely detectable at the beginning of the observation, this source quickly became the brightest object in the region with a peak flux density of ~ 45 mJy. It does not have an infrared counterpart even in deep VLT and HST data, but has been observed to flare in X-ray emission during the observations for the *Chandra* Orion Ultra-deep Project. A model fit to the X-ray spectrum allows to determine the absorbing column density towards the source. Also, fluorescent iron line emission was observed towards this source in X-rays. Curiously, an apparently variable *double* centimetric radio source was found at the position of the flare source. Presumably, it is a deeply embedded YSO. The

nearby YSO named GMR-A, observed to flare in previous radio observations, was found to be only slightly variable in our dataset.

Chapter 7 – Synchrotron radio emission from the T Tauri binary system V773 Tau A We present the observation of a millimeter radio flare of the pre-main sequence binary system V773 Tau A at about the moment of periastron passage. We examine different possible causes for the energy losses responsible for the e-folding time of 2.31 ± 0.19 hours of that flare. We exclude synchrotron, collisional, and inverse Compton losses because they are not consistent with observational constraints, and we propose that the fading of the emission is due to the leakage of electrons themselves at each reflection between the two mirror points of the magnetic structure partially trapping them. The magnetic structure compatible with both our leakage model and previous observations is that of a helmet streamer that, as in the solar case, can occur at the top of the X-ray-emitting, stellar-sized coronal loops of one of the stars. The streamer may extend up to $\sim 20 R_*$ and interact with the corona of the other star at periastron passage, causing recurring flares. The inferred magnetic field strength at the two mirror points of the helmet streamer is in the range 0.12 – 125 G, and the corresponding Lorentz factor, γ , of the partially trapped electrons is in the range $20 < \gamma < 632$. We therefore rule out that the emission could be of gyro-synchrotron nature: the derived high Lorentz factor proves that the nature of the emission at 90 GHz from this pre-main binary system is synchrotron radiation.

Chapter 8 – Searching for linearly polarized molecular line emission towards protostars The XPOL correlation polarimeter at the IRAM 30m telescope was used in a search for partly linearly polarized emission in several bright molecular transition lines towards prominent star-forming regions. For a better discussion of the results, the instrument response is simulated in order to quantitatively estimate the influence of the instrumental polarization and the role of extended emission. While in nearly all transitions towards all sources a polarized signal is found, its degree of polarization only rarely surpasses the polarization that can be expected due to instrumental effects, e.g. if extended emission is present. It is shown that extended emission in the surroundings of the target source indeed influences the resulting linear polarization. Towards G34.3+0.2, measured in the CS(2-1) line, the best evidence for astronomically polarized line emission was found.

Appendix A

Some constants and units

A.1 Astronomical constants

Astronomical Unit (AU)	$1.4959787066 \times 10^{11}$ m
parsec (pc)	3.0856776×10^{16} m = 206264.806 AU = 3.26 light years
solar mass (M_{\odot})	1.9891×10^{30} kg
solar luminosity (L_{\odot})	$3.845(8) \times 10^{26}$ W = $3.845(8) \times 10^{33}$ erg s ⁻¹

(from Cox 2000)

A.2 Units

radiation flux density	Jansky (Jy)	10^{-26} W Hz ⁻¹ m ⁻²
electric dipole moment	Debye (D)	3.33564×10^{-30} C m
magnetic field	Gauss (G)	10^{-4} T

Bibliography

- Acke B., van den Ancker M. E., 2004, *ISO spectroscopy of disks around Herbig Ae/Be stars*, A&A, 426, 151
- Akabane K., Nakajima H., Ohki K., Moriyama F., Miyaji T., 1973, *A Flare-Associated Thermal Burst in the mm-Wave Region*, Sol. Phys., 33, 431
- Allen L. E., Myers P. C., Di Francesco J., Mathieu R., Chen H., Young E., 2002, *Hubble Space Telescope/NICMOS Imaging Survey of the Ophiuchus (Lynds 1688) Cluster*, ApJ, 566, 993
- Anderson I. M., Harju J., Knee L. B. G., Haikala L. K., 1997, *A molecular disk and dense outflow in Corona Australis.*, A&A, 321, 575
- André P., 1987, *Radio Emission from Young Stellar Objects*. In: T. Montmerle and C. Bertout (eds.), p. 143
- André P., 1996, *Radio Emission as a Probe of Large-Scale Magnetic Structures Around Young Stellar Objects*. In: ASP Conf. Ser. 93, Radio Emission from the Stars and the Sun, ed. A. R. Taylor & J. M. Paredes, p. 273
- André P., Deeney B. D., Phillips R. B., Lestrade J., 1992, *VLBI survey of Rho Ophiuchi - A population of magnetized, diskless young stellar objects*, ApJ, 401, 667
- André P., Montmerle T., 1994, *From T Tauri stars to protostars: Circumstellar material and young stellar objects in the rho Ophiuchi cloud*, ApJ, 420, 837
- André P., Montmerle T., Feigelson E. D., Stine P. C., Klein K.-L., 1988, *A young radio-emitting magnetic B star in the Rho Ophiuchi cloud*, ApJ, 335, 940
- André P., Phillips R. B., Lestrade J.-F., Klein K.-L., 1991, *Direct VLBI detection of the magnetosphere surrounding the young star S1 in Rho Ophiuchi*, ApJ, 376, 630
- André P., Ward-Thompson D., Barsony M., 1993, *Submillimeter continuum observations of Rho Ophiuchi A - The candidate protostar VLA 1623 and prestellar clumps*, ApJ, 406, 122
- Ardila D. R., Basri G., Walter F. M., Valenti J. A., Johns-Krull C. M., 2002, *Observations of T Tauri Stars Using the Hubble Space Telescope GHRs. II. Optical and Near-Ultraviolet Lines*, ApJ, 567, 1013
- Asai A., Yokoyama T., Shimojo M., Shibata K., 2004, *Downflow Motions Associated with Impulsive Nonthermal Emissions Observed in the 2002 July 23 Solar Flare*, ApJ, 605, L77
- Aschwanden M. J., 2002, *Particle acceleration and kinematics in solar flares - A Synthesis of Recent Observations and Theoretical Concepts (Invited Review)*, Space Science Reviews, 101, 1
- Baars J. W. M., Genzel R., Pauliny-Toth I. I. K., Witzel A., 1977, *The absolute spectrum of CAS A - an accurate flux density scale and a set of secondary calibrators*, A&A, 61, 99
- Ballesteros-Paredes J., Klessen R. S., Mac Low M.-M., Vazquez-Semadeni E., 2006, *Molecular cloud turbulence and star formation*, in Protostars and Planets V, ed. B. Reipurth, D. Jewitt, & K. Keil
- Bally J., Feigelson E., Reipurth B., 2003, *X-Rays from the Vicinity of the Protostar L1551 IRS 5: Reflection or Fast Shocks?*, ApJ, 584, 843

- Bally J., Reipurth B., Davis J. D., 2006, *Observations of Jets and Outflows from Young Stars*, in Protostars and Planets V, ed. B. Reipurth, D. Jewitt, & K. Keil
- Barvainis R., Wootten A., 1987, *Upper limits on the polarization of ammonia emission in OMC 1*, AJ, 93, 168
- Basri G., Marcy G. W., Valenti J. A., 1992, *Limits on the magnetic flux of pre-main-sequence stars*, ApJ, 390, 622
- Bastian T. S., Benz A. O., Gary D. E., 1998, *Radio Emission from Solar Flares*, ARA&A, 36, 131
- Beasley A. J., Bastian T. S., 1998, *VLBA Imaging of UX Ari*. In: J. A. Zensus, G. B. Taylor, and J. M. Wrobel (eds.), p. 321
- Beckwith S. V. W., Birk C. C., 1995, *Vertical Disk Structure in HL Tauri*, ApJ, 449, L59
- Beckwith S. V. W., Sargent A. I., Chini R. S., Guesten R., 1990, *A survey for circumstellar disks around young stellar objects*, AJ, 99, 924
- Benz A. O., Güdel M., 1994, *X-ray/microwave ratio of flares and coronae*, A&A, 285, 621
- Berger E., Rutledge R. E., Reid I. N., Bildsten L., Gizis J. E., Liebert J., Martín E., Basri G., Jayawardhana R., Brandeker A., Fleming T. A., Johns-Krull C. M., Giampapa M. S., Hawley S. L., Schmitt J. H. M. M., 2005, *The Magnetic Properties of an L Dwarf Derived from Simultaneous Radio, X-Ray, and H α Observations*, ApJ, 627, 960
- Bibo E. A., The P. S., Dawanas D. N., 1992, *The evolutionary stage of the Herbig Ae/Be stars in the R Coronae Australis star-forming region*, A&A, 260, 293
- Birk G. T., Schwab D., Wiechen H., Lesch H., 2000, *X-ray activity in T-Tauri stellar magnetospheres*, A&A, 358, 1027
- Blumenthal G. R., Gould R. J., 1970, *Bremsstrahlung, Synchrotron Radiation, and Compton Scattering of High-Energy Electrons Traversing Dilute Gases*, Reviews of Modern Physics, 42, 237
- Boboltz D. A., Fey A. L., Johnston K. J., Claussen M. J., de Vegt C., Zacharias N., Gaume R. A., 2003, *Astrometric Positions and Proper Motions of 19 Radio Stars*, AJ, 126, 484
- Bontemps S., André P., Terebey S., Cabrit S., 1996, *Evolution of outflow activity around low-mass embedded young stellar objects*, A&A, 311, 858
- Bouvier J., Alencar S. H. P., Harries T. J., Johns-Krull C. M., Romanova M. M., 2006, *Magnetospheric Accretion in Classical T Tauri Stars*, in Protostars and Planets V, ed. B. Reipurth, D. Jewitt, & K. Keil
- Bower G. C., Plambeck R. L., Bolatto A., McCrady N., Graham J. R., de Pater I., Liu M. C., Baganoff F. K., 2003, *A Giant Outburst at Millimeter Wavelengths in the Orion Nebula*, ApJ, 598, 1140
- Broeg C., Fernández M., Neuhäuser R., 2005, *A new algorithm for differential photometry: computing an optimum artificial comparison star*, Astronomische Nachrichten, 326, 134
- Brown A., 1987, *Radio emission from pre-main-sequence stars in Corona Australis*, ApJ, 322, L31
- Cabrit S., Edwards S., Strom S. E., Strom K. M., 1990, *Forbidden-line emission and infrared excesses in T Tauri stars - Evidence for accretion-driven mass loss?*, ApJ, 354, 687
- Caillault J., Gagne M., Stauffer J. R., 1994, *ROSAT HRI observations of hot stars in the Orion Nebula*, ApJ, 432, 386
- Calvet N., Gullbring E., 1998, *The Structure and Emission of the Accretion Shock in T Tauri Stars*, ApJ, 509, 802
- Calvet N., Hartmann L., Kenyon S. J., Whitney B. A., 1994, *Flat spectrum T Tauri stars: The case for infall*, ApJ, 434, 330

- Campbell M. F., Niles D., Nawfel R., Hawrylycz M., Hoffmann W. F., Thronson, Jr. H. A., 1982, *Far-infrared sources in Cygnus X - an extended emission complex at DR 21 and unresolved sources at S106 and ON 2*, ApJ, 261, 550
- Casey B. W., Mathieu R. D., Suntzeff N. B., Walter F. M., 1995, *The Pre-Main-Sequence Triple TY CrA: Spectroscopic Detection of the Secondary and Tertiary Components*, AJ, 109, 2156
- Casey B. W., Mathieu R. D., Vaz L. P. R., Andersen J., Suntzeff N. B., 1998, *The Pre-Main-Sequence Eclipsing Binary TY Coronae Australis: Precise Stellar Dimensions and Tests of Evolutionary Models*, AJ, 115, 1617
- Cassinelli J. P., Cohen D. H., Macfarlane J. J., Sanders W. T., Welsh B. Y., 1994, *X-ray emission from near-main-sequence B stars*, ApJ, 421, 705
- Chandrasekhar S., Fermi E., 1953, *Problems of Gravitational Stability in the Presence of a Magnetic Field.*, ApJ, 118, 116
- Chauvin G., Lagrange A.-M., Beust H., Fusco T., Mouillet D., Lacombe F., Pujet P., Rousset G., Gendron E., Conan J.-M., Bauduin D., Rouan D., Brandner W., Lenzen R., Hubin N., Hartung M., 2003, *VLT/NACO adaptive optics imaging of the TY CrA system. A fourth stellar component candidate detected*, A&A, 406, L51
- Chen W. P., Graham J. A., 1993, *Ice grains in the Corona Australis molecular cloud*, ApJ, 409, 319
- Chini R., Kämpgen K., Reipurth B., Albrecht M., Kreysa E., Lemke R., Nielbock M., Reichertz L. A., Sievers A., Zylka R., 2003, *SIMBA observations of the R Corona Australis molecular cloud*, A&A, 409, 235
- Choi M., Tatematsu K., 2004, *High-Resolution Millimeter Imaging of the R Coronae Australis IRS 7 Region*, ApJ, 600, L55
- Ciolek G. E., Basu S., 2001, *The Razor's Edge: Magnetic Fields and Their Fundamental Role in Star Formation and Observations of Protostellar Cores*. In: T. Montmerle and P. André (eds.), p. 79
- Corporon P., Lagrange A. M., Beust H., 1996, *Further characteristics of the young triple system TY Coronae Austrinae.*, A&A, 310, 228
- Cortes P., Crutcher R. M., 2006, *Interferometric Mapping of Magnetic Fields: G30.79 FIR 10*, ApJ, 639, 965
- Cortes P. C., Crutcher R. M., Matthews B. C., 2006, *Interferometric Mapping of Magnetic fields: NGC2071IR*, ArXiv Astrophysics e-prints
- Cortes P. C., Crutcher R. M., Watson W. D., 2005, *Line Polarization of Molecular Lines at Radio Frequencies: The Case of DR 21(OH)*, ApJ, 628, 780
- Cox A. N., 2000, *Allen's astrophysical quantities*, 4th ed., New York: AIP Press; Springer
- Crutcher R., Heiles C., Troland T., 2003, *Observations of Interstellar Magnetic Fields*, LNP Vol. 614: Turbulence and Magnetic Fields in Astrophysics, 614, 155
- Curiel S., Girart J. M., Rodríguez L. F., Cantó J., 2003, *Very Large Array Observations of Proper Motions in YLW 15*, ApJ, 582, L109
- Damiani F., Micela G., Sciortino S., Harnden F. R., 1994, *Einstein X-ray observations of Herbig Ae/Be stars*, ApJ, 436, 807
- Deguchi S., Watson W. D., 1984, *Linear polarization of molecular lines at radio frequencies*, ApJ, 285, 126
- Dobashi K., Uehara H., Kandori R., Sakurai T., Kaiden M., Umemoto T., Sato F., 2005, *Atlas and Catalog of Dark Clouds Based on Digitized Sky Survey I*, PASJ, 57, 1

- Doppmann G. W., Greene T. P., Covey K. R., Lada C. J., 2005, *The Physical Natures of Class I and Flat-Spectrum Protostellar Photospheres: A Near-Infrared Spectroscopic Study*, AJ, 130, 1145
- Drake J. J., 2005, *Trouble on the Shock Front: TW Hydrae, X-rays and Accretion*. In: ESA SP-560, Proceedings of the 13th Cool Stars Workshop, ed. F. Favata & G.A.J. Hussain, p. 519
- Duchêne G., Ghez A. M., McCabe C., Weinberger A. J., 2003, *No Fossil Disk in the T Tauri Multiple System V773 Tauri*, ApJ, 592, 288
- Dulk G. A., 1985, *Radio emission from the sun and stars*, ARA&A, 23, 169
- Dutrey A., Guilloteau S., Ho P., 2006, *Interferometric Spectro-imaging of Molecular Gas in Proto-Planetary Disks*, in Protostars and Planets V, ed. B. Reipurth, D. Jewitt, & K. Keil
- Eiroa C., Oudmaijer R. D., Davies J. K., de Winter D., Garzón F., Palacios J., Alberdi A., Ferlet R., Grady C. A., Cameron A., Deeg H. J., Harris A. W., Horne K., Merín B., Miranda L. F., Montesinos B., Mora A., Penny A., Quirrenbach A., Rauer H., Schneider J., Solano E., Tsapras Y., Wesselius P. R., 2002, *On the simultaneous optical and near-infrared variability of pre-main sequence stars*, A&A, 384, 1038
- Eiroa C., Torrelles J. M., Curiel S., Djupvik A. A., 2005, *Very Large Array 3.5 cm Continuum Sources in the Serpens Cloud Core*, AJ, 130, 643
- Eisner J. A., Hillenbrand L. A., Carpenter J. M., Wolf S., 2005, *Constraining the Evolutionary Stage of Class I Protostars: Multiwavelength Observations and Modeling*, ApJ, 635, 396
- Endeve E., Holzer T. E., Leer E., 2004, *Helmet Streamers Gone Unstable: Two-Fluid Magnetohydrodynamic Models of the Solar Corona*, ApJ, 603, 307
- Favata F., Bonito R., Micela G., Fridlund M., Orlando S., Sciortino S., Peres G., 2006, *The discovery of an expanding X-ray source in the HH 154 protostellar jet*, A&A, 450, L17
- Favata F., Flaccomio E., Reale F., Micela G., Sciortino S., Shang H., Stassun K. G., Feigelson E. D., 2005, *Bright X-Ray Flares in Orion Young Stars from COUP: Evidence for Star-Disk Magnetic Fields?*, ApJS, 160, 469
- Favata F., Fridlund C. V. M., Micela G., Sciortino S., Kaas A. A., 2002, *Discovery of X-ray emission from the protostellar jet L1551 IRS5 (HH 154)*, A&A, 386, 204
- Favata F., Giardino G., Micela G., Sciortino S., Damiani F., 2003, *An XMM-Newton-based X-ray survey of pre-main sequence stellar emission in the L1551 star-forming complex*, A&A, 403, 187
- Favata F., Micela G., 2003, *Stellar Coronal Astronomy*, Space Science Reviews, 108, 577
- Feigelson E. D., 2005, *X-rays and Planet Formation*, Bulletin of the American Astronomical Society, 37, 1180
- Feigelson E. D., Broos P., Gaffney J. A., Garmire G., Hillenbrand L. A., Pravdo S. H., Townsley L., Tsuboi Y., 2002, *X-Ray-emitting Young Stars in the Orion Nebula*, ApJ, 574, 258
- Feigelson E. D., Carkner L., Wilking B. A., 1998, *Circularly Polarized Radio Emission from an X-Ray Protostar*, ApJ, 494, L215
- Feigelson E. D., Gaffney J. A., Garmire G., Hillenbrand L. A., Townsley L., 2003, *X-Rays in the Orion Nebula Cluster: Constraints on the Origins of Magnetic Activity in Pre-Main-Sequence Stars*, ApJ, 584, 911
- Feigelson E. D., Getman K., Townsley L., Garmire G., Preibisch Th., Grosso N., Montmerle T., Muench A., McCaughrean M., 2005, *Global X-Ray Properties of the Orion Nebula Region*, ApJS, 160, 379
- Feigelson E. D., Lawson W. A., 2004, *An X-Ray Census of Young Stars in the Chamaeleon I North Cloud*, ApJ, 614, 267

- Feigelson E. D., Montmerle T., 1999, *High-Energy Processes in Young Stellar Objects*, ARA&A, 37, 363
- Feigelson E. D., Townsley L., Güdel M., Stassun K., 2006, *X-ray Properties of Young Stars and Stellar Clusters*, Protostars & Planets V (ed. Bo Reipurth et al., Univ. Arizona Press), in press (astro-ph/0602603)
- Feigelson E. D., Welty A. D., Imhoff C., Hall J. C., Etzel P. B., Phillips R. B., Lonsdale C. J., 1994, *Multiwavelength study of the magnetically active T Tauri star HD 283447*, ApJ, 432, 373
- Felli M., Massi M., Churchwell E., 1989, *VLBI observations of Theta(1) Orionis A*, A&A, 217, 179
- Fernández M., Comerón F., 2001, *Intense accretion and mass loss of a very low mass young stellar object*, A&A, 380, 264
- Flaccomio E., Damiani F., Micela G., Sciortino S., Harnden F. R., Murray S. S., Wolk S. J., 2003, *Chandra X-Ray Observation of the Orion Nebula Cluster. I. Detection, Identification, and Determination of X-Ray Luminosities*, ApJ, 582, 382
- Flaccomio E., Micela G., Sciortino S., 2006, *ACIS-I observations of NGC2264. Membership and X-ray properties of PMS stars*, A&A, in press (astro-ph/0604243)
- Fleming T. A., Schmitt J. H. M. M., Giampapa M. S., 1995, *Correlations of Coronal X-Ray Emission with Activity, Mass, and Age of the Nearby K and M Dwarfs*, ApJ, 450, 401
- Forbrich J., Preibisch Th., 2007, *Coronae in the Coronet: A very deep X-ray look into a stellar nursery*, A&A, submitted
- Forbrich J., Preibisch Th., Menten K. M., 2006, *Radio and X-ray variability of young stellar objects in the Coronet cluster*, A&A, 446, 155
- Forbrich J., Preibisch Th., Menten K. M., Neuhäuser R., Walter F. M., Tamura M., Matsunaga N., Kusakabe N., Nakajima Y., Brandeker A., Fornasier S., Posselt B., Tachihara K., Broeg C., 2007, *Simultaneous X-ray, radio, near-infrared, and optical monitoring of Young Stellar Objects in the Coronet cluster*, A&A, in press
- Forbrich J., Schreyer K., Posselt B., Klein R., Henning Th., 2004, *An Extremely Young Massive Stellar Object near IRAS 07029-1215*, ApJ, 602, 843
- Freeman P. E., Kashyap V., Rosner R., Lamb D. Q., 2002, *A Wavelet-Based Algorithm for the Spatial Analysis of Poisson Data*, ApJS, 138, 185
- Furuya R. S., Shinnaga H., Nakanishi K., Momose M., Saito M., 2003, *A Giant Flare on a T Tauri Star Observed at Millimeter Wavelengths*, PASJ, 55, L83
- Gagné M., Skinner S. L., Daniel K. J., 2004, *Simultaneous Chandra and Very Large Array Observations of Young Stars and Protostars in ρ Ophiuchus Cloud Core A*, ApJ, 613, 393
- Garay G., Moran J. M., Reid M. J., 1987, *Compact continuum radio sources in the Orion Nebula*, ApJ, 314, 535
- Garmire G., Feigelson E. D., Broos P., Hillenbrand L. A., Pravdo S. H., Townsley L., Tsuboi Y., 2000, *Chandra X-Ray Observatory Study of the Orion Nebula Cluster and BN/KL Region*, AJ, 120, 1426
- Garmire G. P., Bautz M. W., Ford P. G., Nousek J. A., Ricker, Jr. G. R., 2003, *Advanced CCD imaging spectrometer (ACIS) instrument on the Chandra X-ray Observatory*. In: J. E. Truemper and H. D. Tananbaum (eds.), pp 28–44
- Garmire G. P., Garmire A. B., 2003, *X-ray emission from objects in the CrA dark cloud core*, Astronomische Nachrichten, 324, 153
- Getman K. V., Feigelson E. D., Grosso N., McCaughrean M. J., Micela G., Broos P., Garmire G., Townsley L., 2005a, *Membership of the Orion Nebula Population from the Chandra Orion Ultradeep Project*, ApJS, 160, 353

- Getman K. V., Flaccomio E., Broos P. S., Grosso N., Tsujimoto M., Townsley L., Garmire G. P., Kastner J., Li J., Harnden, Jr. F. R., Wolk S., Murray S. S., Lada C. J., Muench A. A., McCaughrean M. J., Meeus G., Damiani F., Micela G., Sciortino S., Bally J., Hillenbrand L. A., Herbst W., Preibisch Th., Feigelson E. D., 2005b, *Chandra Orion Ultradeep Project: Observations and Source Lists*, ApJS, 160, 319
- Ginzburg V. L., Syrovatskii S. I., 1965, *Cosmic Magnetobremstrahlung (synchrotron Radiation)*, ARA&A, 3, 297
- Girart J. M., Crutcher R. M., Rao R., 1999, *Detection of Polarized CO Emission from the Molecular Outflow in NGC 1333 IRAS 4A*, ApJ, 525, L109
- Girart J. M., Curiel S., Rodríguez L. F., Honda M., Cantó J., Okamoto Y. K., Sako S., 2004, *On the Evolutionary State of the Components of the YLW 15 Binary System*, AJ, 127, 2969
- Girart J. M., Rao R., Marrone D. P., 2006, *Magnetic Fields in the Formation of Sun-Like Stars*, Science, 313, 812
- Girart J. M., Rodríguez L. F., Curiel S., 2000, *A Subarcsecond Binary Radio Source Associated with the X-Ray-Emitting Young Stellar Object YLW 15*, ApJ, 544, L153
- Glassgold A. E., Feigelson E. D., Montmerle T., Wolk S., 2005, *X-Ray Flares of Sun-like Young Stellar Objects and Their Effects on Protoplanetary Disks*. In: A. N. Krot, E. R. D. Scott, and B. Reipurth (eds.), p. 165
- Glenn J., Walker C. K., Bieging J. H., Jewell P. R., 1997a, *Millimeter-Wave Spectropolarimetry of Evolved Stars: Evidence for Polarized Molecular Line Emission*, ApJ, 487, L89
- Glenn J., Walker C. K., Jewell P. R., 1997b, *HCO + Spectropolarimetry and Millimeter Continuum Polarimetry of the DR 21 Star-forming Region*, ApJ, 479, 325
- Goldreich P., Kylafis N. D., 1981, *On mapping the magnetic field direction in molecular clouds by polarization measurements*, ApJ, 243, L75
- Goldreich P., Kylafis N. D., 1982, *Linear polarization of radio frequency lines in molecular clouds and circumstellar envelopes*, ApJ, 253, 606
- Golub L., Pasachoff J. M., 1997, *The Solar Corona*, The Solar Corona, by Leon Golub and Jay M. Pasachoff, pp. 388. ISBN 0521480825. Cambridge, UK: Cambridge University Press, September 1997.
- Grady C. A., Perez M. R., The P. S., 1993, *The Accreting Circumstellar Gas Envelope of HD176386 a Young Star in the R-Coronae Star Formation Region*, A&A, 274, 847
- Graffagnino V. G., Wonnacott D., Schaeidt S., 1995, *HR 5110 superflare: an interbinary flare identified?*, MNRAS, 275, 129
- Greaves J. S., Holland W. S., Dent W. R. F., 2002, *Magnetic Fields in Gas Flows near the Galactic Center*, ApJ, 578, 224
- Greaves J. S., Holland W. S., Friberg P., Dent W. R. F., 1999, *Polarized CO Emission from Molecular Clouds*, ApJ, 512, L139
- Greaves J. S., Holland W. S., Ward-Thompson D., 2001, *Measurement of the Magnetic Field Direction in the NGC 2024 FIR 5 Protostellar Outflow*, ApJ, 546, L53
- Gregory S. G., Jardine M., Simpson I., Donati J.-F., 2006, *Mass accretion on to T Tauri stars*, MNRAS, 371, 999
- Groppi C. E., Kulesa C., Walker C., Martin C. L., 2004, *Millimeter and Submillimeter Survey of the R Coronae Australis Region*, ApJ, 612, 946
- Grosso N., Feigelson E. D., Getman K. V., Kastner J. H., Bally J., McCaughrean M. J., 2006, *X-rays from HH 210 in the Orion nebula*, A&A, 448, L29

- Grosso N., Montmerle T., Feigelson E. D., Andre P., Casanova S., Gregorio-Hetem J., 1997, *An X-ray superflare from an infrared protostar.*, *Nature*, 387, 56
- Güdel M., 2002a, *Multiwavelength Aspects of Stellar Coronae.* In: F. Favata and J. J. Drake (eds.), p. 367
- Güdel M., 2002b, *Stellar Radio Astronomy: Probing Stellar Atmospheres from Protostars to Giants,* *ARA&A*, 40, 217
- Güdel M., 2004, *X-ray astronomy of stellar coronae,* *A&A Rev.*, 12, 71
- Güdel M., Benz A. O., Schmitt J. H. M. M., Skinner S. L., 1996, *The Neupert Effect in Active Stellar Coronae: Chromospheric Evaporation and Coronal Heating in the dMe Flare Star Binary UV Ceti,* *ApJ*, 471, 1002
- Guedel M., Benz A. O., 1993, *X-ray/microwave relation of different types of active stars,* *ApJ*, 405, L63
- Guenther E. W., Lehmann H., Emerson J. P., Staude J., 1999, *Measurements of magnetic field strength on T Tauri stars,* *A&A*, 341, 768
- Guenther E. W., Stelzer B., Neuhäuser R., Hillwig T. C., Durisen R. H., Menten K. M., Greimel R., Barwig H., Englhauser J., Robb R. M., 2000, *A multi-wavelength study of pre-main sequence stars in the Taurus-Auriga star-forming region,* *A&A*, 357, 206
- Gullbring E., Barwig H., Schmitt J. H. M. M., 1997, *Simultaneous optical and ROSAT X-ray observations of the classical T Tauri star BP Tauri.,* *A&A*, 324, 155
- Hachisuka K., Brunthaler A., Menten K. M., Reid M. J., Imai H., Hagiwara Y., Miyoshi M., Horiuchi S., Sasao T., 2006, *Water Maser Motions in W3(OH) and a Determination of Its Distance,* *ApJ*, 645, 337
- Hamaguchi K., Corcoran M. F., Petre R., White N. E., Stelzer B., Nedachi K., Kobayashi N., Tokunaga A. T., 2005a, *Discovery of Extremely Embedded X-Ray Sources in the R Coronae Australis Star-forming Core,* *ApJ*, 623, 291
- Hamaguchi K., Corcoran M. F., White N. E., Neuhäuser R., Stelzer B., Balona L. A., 2004, *X-ray Variability during Optical Eclipses of a Young Binary System.* In: *Bulletin of the American Astronomical Society*, p. 742
- Hamaguchi K., Yamauchi S., Koyama K., 2005b, *X-Ray Study of Herbig Ae/Be Stars,* *ApJ*, 618, 360
- Harju J., Higdon J. L., Lehtinen K., Juvela M., 2001, *Imaging of Protostars in Corona Australis with the ATCA.* In: *ASP Conf. Ser. 235, Science with the Atacama Large Millimeter Array*, ed. A. Wootten, p. 125
- Hartmann L., 1998, *Accretion processes in star formation,* Cambridge: Cambridge University Press
- Hartmann L., Calvet N., 1995, *Observational constraints on FU Ori winds,* *AJ*, 109, 1846
- Hayashi M. R., Shibata K., Matsumoto R., 1996, *X-Ray Flares and Mass Outflows Driven by Magnetic Interaction between a Protostar and Its Surrounding Disk,* *ApJ*, 468, L37
- Henning Th., Launhardt R., Steinacker J., Thamm E., 1994, *Cold dust around southern Herbig Ae/Be stars,* *A&A*, 291, 546
- Heyvaerts J., Priest E., Rust D. M., 1977, *An emerging flux model for solar flares,* *Sol. Phys.*, 53, 255
- Hillenbrand L. A., 1997, *On the Stellar Population and Star-Forming History of the Orion Nebula Cluster,* *AJ*, 113, 1733
- Hodapp K., 1994, *A K' imaging survey of molecular outflow sources,* *ApJS*, 94, 615
- Imanishi K., Koyama K., Tsuboi Y., 2001a, *Chandra Observation of the ρ Ophiuchi Cloud,* *ApJ*, 557, 747

- Imanishi K., Tsujimoto M., Koyama K., 2001b, *X-Ray Detection from Bona Fide and Candidate Brown Dwarfs in the ρ Ophiuchi Cloud with Chandra*, ApJ, 563, 361
- Isobe H., Shibata K., Yokoyama T., Imanishi K., 2003, *Hydrodynamic Modeling of a Flare Loop Connecting the Accretion Disk and Central Core of Young Stellar Objects*, PASJ, 55, 967
- Jansen F., Lumb D., Altieri B., Clavel J., Ehle M., Erd C., Gabriel C., Guainazzi M., Gondoin P., Much R., Munoz R., Santos M., Schartel N., Texier D., Vacanti G., 2001, *XMM-Newton observatory. I. The spacecraft and operations*, A&A, 365, L1
- Jardine M., Cameron A. C., Donati J.-F., Gregory S. G., Wood K., 2006, *X-ray emission from T Tauri stars*, MNRAS, 367, 917
- Jeans J. H., 1928, *Astronomy and cosmogony*, Cambridge [Eng.] The University press, 1928
- Jeffers H. M., van Denbos W. H., Greeby F. M., 1963, *Index catalogue of visual double stars, 1961.0*, Publications of the Lick Observatory, Mount Hamilton: University of California, Lick Observatory
- Jørgensen J. K., Harvey P. M., Evans, II N. J., Huard T. L., Allen L. E., Porras A., Blake G. A., Bourke T. L., Chapman N., Cieza L., Koerner D. W., Lai S.-P., Mundy L. G., Myers P. C., Padgett D. L., Rebull L., Sargent A. I., Spiesman W., Stapelfeldt K. R., van Dishoeck E. F., Wahhaj Z., Young K. E., 2006, *The Spitzer c2d Survey of Large, Nearby, Interstellar Clouds. III. Perseus Observed with IRAC*, ApJ, 645, 1246
- Kant I., 1755, *Allgemeine Naturgeschichte und Theorie des Himmels oder Versuch von der Verfassung und dem mechanischen Ursprunge des ganzen Weltgebäudes nach Newtonischen Grundsätzen abgehandelt*, Königsberg und Leipzig: Johann Friedrich Petersen
- Kastner J. H., Huenemoerder D. P., Schulz N. S., Canizares C. R., Weintraub D. A., 2002, *Evidence for Accretion: High-Resolution X-Ray Spectroscopy of the Classical T Tauri Star TW Hydrae*, ApJ, 567, 434
- Kaufmann P., Correia E., Costa J. E. R., Zodi Vaz A. M., 1986, *A synchrotron/inverse Compton interpretation of a solar burst producing fast pulses at lambda less than 3-mm and hard X-rays*, A&A, 157, 11
- Kaufmann P., Raulin J.-P., de Castro C. G. G., Levato H., Gary D. E., Costa J. E. R., Marun A., Pereyra P., Silva A. V. R., Correia E., 2004, *A New Solar Burst Spectral Component Emitting Only in the Terahertz Range*, ApJ, 603, L121
- Koyama K., Hamaguchi K., Ueno S., Kobayashi N., Feigelson E. D., 1996, *Discovery of Hard X-Rays from a Cluster of Protostars*, PASJ, 48, L87
- Kraft R. P., Burrows D. N., Nousek J. A., 1991, *Determination of confidence limits for experiments with low numbers of counts*, ApJ, 374, 344
- Kroupa P., 2002, *The Initial Mass Function of Stars: Evidence for Uniformity in Variable Systems*, Science, 295, 82
- Kylafis N. D., 1983a, *Linear polarization of interstellar radio-frequency absorption lines and magnetic field direction*, ApJ, 275, 135
- Kylafis N. D., 1983b, *Polarization of interstellar radio-frequency lines and magnetic field direction*, ApJ, 267, 137
- Kylafis N. D., Shapiro P. R., 1983, *Polarization of interstellar molecular radiofrequency absorption lines*, ApJ, 272, L35
- Lada C. J., 1985, *Cold outflows, energetic winds, and enigmatic jets around young stellar objects*, ARA&A, 23, 267
- Lada C. J., 1987, *Star formation - From OB associations to protostars*. In: IAU Symp. 115, Star Forming Regions, ed. M. Peimbert & J. Jugaku, p. 1

- Lai S.-P., Girart J. M., Crutcher R. M., 2003, *Interferometric Mapping of Magnetic Fields in Star-forming Regions. III. Dust and CO Polarization in DR 21(OH)*, ApJ, 598, 392
- Laplace P. S., 1796, *Exposition du système du monde*, Paris: Imprimerie du Cercle-Social
- Lay O. P., Carlstrom J. E., Hills R. E., 1997, *Constraints on the HL Tauri Protostellar Disk from Millimeter- and Submillimeter-Wave Interferometry*, ApJ, 489, 917
- Lay O. P., Carlstrom J. E., Hills R. E., Phillips T. G., 1994, *Protostellar accretion disks resolved with the JCMT-CSO interferometer*, ApJ, 434, L75
- Lee C. W., Myers P. C., 1999, *A Catalog of Optically Selected Cores*, ApJS, 123, 233
- Lee J., Gary D. E., Qiu J., Gallagher P. T., 2002, *Electron Transport during the 1999 August 20 Flare Inferred from Microwave and Hard X-Ray Observations*, ApJ, 572, 609
- Lehtinen K., Harju J., Kontinen S., Higdon J. L., 2003, *Centimetre continuum emission from young stellar objects in Cederblad 110*, A&A, 401, 1017
- Lestrade J.-F., Preston R. A., Jones D. L., Phillips R. B., Rogers A. E. E., Titus M. A., Rioja M. J., Gabuzda D. C., 1999, *High-precision VLBI astrometry of radio-emitting stars*, A&A, 344, 1014
- Liebovitch L. S., 1974, *Discovery of a New Radiation Source Z-I in Taurus*, QJRAS, 15, 141
- Lim J., Takakuwa S., 2005, *Circumstellar/Protoplanetary Disks and Bipolar Jets at 5 AU Resolution*. In: C. Lidman and D. Alloin (eds.), p. 200
- Lis D. C., Goldsmith P. F., Dickman R. L., Predmore C. R., Omont A., Cernicharo J., 1988, *Linear polarization of millimeter-wave emission lines in clouds without large velocity gradients*, ApJ, 328, 304
- Loinard L., Mioduszewski A. J., Rodríguez L. F., González R. A., Rodríguez M. I., Torres R. M., 2005, *Multiepoch VLBA Observations of T Tauri South*, ApJ, 619, L179
- Looney L. W., Mundy L. G., Welch W. J., 2000, *Unveiling the Circumstellar Envelope and Disk: A Subarcsecond Survey of Circumstellar Structures*, ApJ, 529, 477
- López Martí B., Eislöffel J., Mundt R., 2005, *The very low-mass population of the Corona Australis and Chamaeleon II star forming regions*, A&A, 444, 175
- Lorenzetti D., Tommasi E., Giannini T., Nisini B., Benedettini M., Pezzuto S., Strafella F., Barlow M., Clegg P. E., Cohen M., di Giorgio A. M., Liseau R., Molinari S., Palla F., Saraceno P., Smith H. A., Spinoglio L., White G. J., 1999, *ISO-LWS observations of Herbig Ae/Be stars. I. Fine structure lines*, A&A, 346, 604
- Lucas P. W., Blundell K. M., Roche P. F., 2000, *A high-resolution radio survey of Class I protostars*, MNRAS, 318, 526
- Massi M., Chiuderi-Drago F., 1992, *Quiescent radio emission in UX ARIETIS*, A&A, 253, 403
- Massi M., Forbrich J., Menten K. M., Torricelli-Ciamponi G., Neidhöfer J., Leurini S., Bertoldi F., 2006, *Synchrotron emission from the T Tauri binary system V773 Tauri A*, A&A, 453, 959
- Massi M., Menten K., Neidhöfer J., 2002, *Periodic radio flaring on the T Tauri star V 773 Tauri*, A&A, 382, 152
- Massi M., Neidhöfer J., Carpentier Y., Ros E., 2005, *Discovery of Solar Rieger periodicities in another star*, A&A, 435, L1
- Matsumura S., Pudritz R. E., 2003, *The Origin of Jovian Planets in Protostellar Disks: The Role of Dead Zones*, ApJ, 598, 645
- McCabe C., Ghez A. M., Prato L., Duchêne G., Fisher R. S., Telesco C., 2006, *Investigating Disk Evolution: A High Spatial Resolution Mid-Infrared Survey of T Tauri Stars*, ApJ, 636, 932

- Megeath S. T., Allen L. E., Gutermuth R. A., Pipher J. L., Myers P. C., Calvet N., Hartmann L., Muzerolle J., Fazio G. G., 2004, *Initial Results from the Spitzer Young Stellar Cluster Survey*, ApJS, 154, 367
- Melrose D. B., Brown J. C., 1976, *Precipitation in trap models for solar hard X-ray bursts*, MNRAS, 176, 15
- Menten K. M., Reid M. J., 1995, *What is powering the Orion Kleinmann-low infrared nebula*, ApJ, 445, L157
- Mestel L., Spitzer L., 1956, *Star formation in magnetic dust clouds*, MNRAS, 116, 503
- Montmerle T., 2001, *X-ray Irradiation and Feedback Effects on Circumstellar and Interstellar Matter*. In: T. Montmerle and P. André (eds.), p. 731
- Montmerle T., 2003, *The role of accretion disks in the coronal activity of young stars*, Advances in Space Research, 32, 1067
- Montmerle T., Grosso N., Tsuboi Y., Koyama K., 2000, *Rotation and X-Ray Emission from Protostars*, ApJ, 532, 1097
- Moriarty-Schieven G. H., Snell R. L., 1988, *High-resolution images of the L1551 molecular outflow. II - Structure and kinematics*, ApJ, 332, 364
- Morris M., Lucas R., Omont A., 1985, *Molecular emission from expanding circumstellar envelopes Polarization and profile asymmetries*, A&A, 142, 107
- Mouschovias T. C., 1991, *Cosmic Magnetism and the Basic Physics of the Early Stages of Star Formation*. In: NATO ASIC Proc. 342: The Physics of Star Formation and Early Stellar Evolution, p. 61
- Mouschovias T. C., Ciolek G. E., 1999, *Magnetic Fields and Star Formation: A Theory Reaching Adulthood*. In: C. J. Lada and N. D. Kylafis (eds.), p. 305
- Mouschovias T. C., Spitzer L., 1976, *Note on the collapse of magnetic interstellar clouds*, ApJ, 210, 326
- Mouschovias T. C., Tassis K., Kunz M. W., 2006, *Observational Constraints on the Ages of Molecular Clouds and the Star Formation Timescale: Ambipolar-Diffusion-controlled or Turbulence-induced Star Formation?*, ApJ, 646, 1043
- Mukai K., 1993, *PIMMS and Viewing: proposal preparation tools*, Legacy, 3, 21
- Mundt R., Fried J. W., 1983, *Jets from young stars*, ApJ, 274, L83
- Mundy L. G., Looney L. W., Erickson W., Grossman A., Welch W. J., Forster J. R., Wright M. C. H., Plambeck R. L., Lugten J., Thornton D. D., 1996, *Imaging the HL Tauri Disk at $\lambda = 2.7$ Millimeters with the BIMA Array*, ApJ, 464, L169
- Mutel R. L., Lestrade J. F., Preston R. A., Phillips R. B., 1985, *Dual polarization VLBI observations of stellar binary systems at 5 GHz*, ApJ, 289, 262
- Myers P. C., Khersonsky V. K., 1995, *On magnetic turbulence in interstellar clouds*, ApJ, 442, 186
- Nagayama T., Nagashima C., Nakajima Y., Nagata T., Sato S., Nakaya H., Yamamuro T., Sugitani K., Tamura M., 2003, *SIRUS: a near infrared simultaneous three-band camera*. In: Instrument Design and Performance for Optical/Infrared Ground-based Telescopes. Edited by Iye, Masanori; Moorwood, Alan F. M. Proceedings of the SPIE, Volume 4841, pp. 459-464 (2003)., pp 459-464
- Neuhäuser R., Briceño C., Comerón F., Hearty T., Martín E. L., Schmitt J. H. M. M., Stelzer B., Supper R., Voges W., Zinnecker H., 1999, *Search for X-ray emission from bona-fide and candidate brown dwarfs*, A&A, 343, 883
- Neuhäuser R., Preibisch Th., 1997, *ROSAT detection of Class I protostars in the CrA Coronet.*, A&A, 322, L37

- Neuhäuser R., Walter F. M., Covino E., Alcalá J. M., Wolk S. J., Frink S., Guillout P., Sterzik M. F., Comerón F., 2000, *Search for young stars among ROSAT All-Sky Survey X-ray sources in and around the R CrA dark cloud*, A&AS, 146, 323
- Neuhäuser R., 1997, *Low-mass pre-main sequence stars and their X-ray emission.*, Science, 276, 1363
- Neuhäuser R., Comerón F., 1998, *ROSAT X-ray Detection of a Young Brown Dwarf in the Chamaeleon I Dark Cloud*, Science, 282, 83
- Nishio M., Yagi K., Kosugi T., 1996, *Loop Configuration of Solar Flares Revealed by Microwave and Hard X-ray Images*. In: A. R. Taylor and J. M. Paredes (eds.), p. 378
- Nisini B., Antonucci S., Giannini T., 2004, *Observations of the Brackett decrement in the Class I source HH100 IR*, A&A, 421, 187
- Nisini B., Antonucci S., Giannini T., Lorenzetti D., 2005, *Probing the embedded YSOs of the R CrA region through VLT-ISAAC spectroscopy*, A&A, 429, 543
- Nutter D. J., Ward-Thompson D., André P., 2005, *The pre-stellar and protostellar population of R Coronae Australis*, MNRAS, 357, 975
- Olofsson G., Hultgren M., Kaas A. A., Bontemps S., Nordh L., Abergel A., André P., Boulanger F., Burgdorf M., Casali M. M., Cesarsky C. J., Davies J., Falgarone E., Montmerle T., Perault M., Persi P., Prusti T., Puget J. L., Sibille F., 1999, *ISOCAM observations of the RCrA star formation region*, A&A, 350, 883
- Ozawa H., Grosso N., Montmerle T., 2005, *The X-ray emission from Young Stellar Objects in the ρ Ophiuchi cloud core as seen by XMM-Newton.*, A&A, 429, 963
- Palla F., Stahler S. W., 1999, *Star Formation in the Orion Nebula Cluster*, ApJ, 525, 772
- Pallavicini R., 1989, *X-ray emission from stellar coronae*, A&A Rev., 1, 177
- Parker E. N., 1955, *The Formation of Sunspots from the Solar Toroidal Field.*, ApJ, 121, 491
- Petrosian V., 1985, *Directivity of bremsstrahlung radiation from relativistic beams and the gamma rays from solar flares*, ApJ, 299, 987
- Phillips R. B., Lonsdale C. J., Feigelson E. D., 1991, *Milliarcsecond radio structure of weak-lined T Tauri stars*, ApJ, 382, 261
- Phillips R. B., Lonsdale C. J., Feigelson E. D., 1993, *Magnetic nonthermal activity in the T Tauri system*, ApJ, 403, L43
- Phillips R. B., Lonsdale C. J., Feigelson E. D., Deeney B. D., 1996, *Polarized Radio Emission From the Multiple T Tauri System HD 283447*, AJ, 111, 918
- Pontoppidan K. M., Fraser H. J., Dartois E., Thi W.-F., van Dishoeck E. F., Boogert A. C. A., d'Hendecourt L., Tielens A. G. G. M., Bisschop S. E., 2003, *A 3-5 μ m VLT spectroscopic survey of embedded young low mass stars I. Structure of the CO ice*, A&A, 408, 981
- Prato L., Greene T. P., Simon M., 2003, *Astrophysics of Young Star Binaries*, ApJ, 584, 853
- Prato L., Simon M., 1997, *Are Both Stars in a Classic T Tauri Binary Classic T Tauri Stars?*, ApJ, 474, 455
- Pravdo S. H., Feigelson E. D., Garmire G., Maeda Y., Tsuboi Y., Bally J., 2001, *Discovery of X-rays from the protostellar outflow object HH2*, Nature, 413, 708
- Pravdo S. H., Tsuboi Y., Maeda Y., 2004, *X-Rays from HH 80, HH 81, and the Central Region*, ApJ, 605, 259
- Preibisch Th., 1998, *Super-strong X-ray emission from a deeply embedded young stellar object in the Serpens cloud core*, A&A, 338, L25

- Preibisch Th., 2003a, *XMM-Newton study of the Serpens star-forming region*, A&A, 410, 951
- Preibisch Th., 2003b, *XMM-Newton study of the star forming region NGC 1333*, A&A, 401, 543
- Preibisch Th., 2004, *X-ray Activity and Accretion in Young Stellar Objects*, Ap&SS, 292, 631
- Preibisch Th., Kim Y.-C., Favata F., Feigelson E. D., Flaccomio E., Getman K., Micela G., Sciortino S., Stassun K., Stelzer B., Zinnecker H., 2005a, *The Origin of T Tauri X-Ray Emission: New Insights from the Chandra Orion Ultradeep Project*, ApJS, 160, 401
- Preibisch Th., McCaughrean M. J., Grosso N., Feigelson E. D., Flaccomio E., Getman K., Hillenbrand L. A., Meeus G., Micela G., Sciortino S., Stelzer B., 2005b, *X-Ray Emission from Young Brown Dwarfs in the Orion Nebula Cluster*, ApJS, 160, 582
- Preibisch Th., Zinnecker H., 1996, *Röntgenstrahlung from Herbig Ae/Be Stars*. In: MPE Report 263, Roentgenstrahlung from the Universe, ed. H.U. Zimmermann, J. Trümper, & H.W. Yorke, pp 17–20
- Preibisch Th., Zinnecker H., 2001, *Deep Chandra X-Ray Observatory Imaging Study of the Very Young Stellar Cluster IC 348*, AJ, 122, 866
- Preibisch Th., Zinnecker H., 2002, *X-Ray Properties of the Young Stellar and Substellar Objects in the IC 348 Cluster: The Chandra View*, AJ, 123, 1613
- Priest E. R., Forbes T. G., 2002, *The magnetic nature of solar flares*, A&A Rev., 10, 313
- Pudritz R. E., Ouyed R., Fendt C., Brandenburg A., 2006, *Disk winds, jets, and outflows: Theoretical and computational foundations*, in Protostars and Planets V, ed. B. Reipurth, D. Jewitt, & K. Keil
- Rebull L. M., Wolff S. C., Strom S. E., 2004, *Stellar Rotation in Young Clusters: The First 4 Million Years*, AJ, 127, 1029
- Reid M. J., Ho P. T. P., 1985, *G34.3 + 0.2 - A 'cometary' H II region*, ApJ, 288, L17
- Reid M. J., Menten K. M., 1990, *A subarcsecond H₂O maser shell surrounding a variable star*, ApJ, 360, L51
- Reid M. J., Menten K. M., 1997, *Radio Photospheres of Long-Period Variable Stars*, ApJ, 476, 327
- Rieke G. H., Lebofsky M. J., 1985, *The interstellar extinction law from 1 to 13 microns*, ApJ, 288, 618
- Robberto M., Beckwith S. V. W., Panagia N., Patel S. G., Herbst T. M., Ligorì S., Custò A., Boccacci P., Bertero M., 2005, *The Orion Nebula in the Mid-Infrared*, AJ, 129, 1534
- Rodríguez L. F., Anglada G., Curiel S., 1999, *The Nature of the Radio Continuum Sources Embedded in the HH 7-11 Region and Its Surroundings*, ApJS, 125, 427
- Rodríguez L. F., Canto J., Torrelles J. M., Gomez J. F., Anglada G., Ho P. T. P., 1994, *Subarcsecond VLA maps of the disk and the jet in HL Tauri*, ApJ, 427, L103
- Rodríguez L. F., Canto J., Torrelles J. M., Gomez J. F., Ho P. T. P., 1992, *VLA imaging of a possible circumstellar disk around HL Tauri*, ApJ, 393, L29
- Rodríguez L. F., Canto J., Torrelles J. M., Ho P. T. P., 1986, *The double radio source associated with L1551 IRS 5 - Binary system or ionized circumstellar torus?*, ApJ, 301, L25
- Rodríguez L. F., D'Alessio P., Wilner D. J., Ho P. T. P., Torrelles J. M., Curiel S., Gomez Y., Lizano S., Pedlar A., Canto J., Raga A. C., 1998, *Compact protoplanetary disks around the stars of a young binary system.*, Nature, 395, 355
- Roederer J. G., 1970, *Dynamics of geomagnetically trapped radiation*, Physics and Chemistry in Space, Berlin: Springer, 1970
- Rutledge R. E., Basri G., Martín E. L., Bildsten L., 2000, *Chandra Detection of an X-Ray Flare from the Brown Dwarf LP 944-20*, ApJ, 538, L141

- Ryter C. E., 1996, *Interstellar Extinction from Infrared to X-Rays: an Overview*, Ap&SS, 236, 285
- Scalo J., 1998, *The IMF Revisited: A Case for Variations*. In: G. Gilmore and D. Howell (eds.), p. 201
- Schmitt J. H. M. M., Liefke C., 2004, *NEXXUS: A comprehensive ROSAT survey of coronal X-ray emission among nearby solar-like stars*, A&A, 417, 651
- Schmitt J. H. M. M., Robrade J., Ness J.-U., Favata F., Stelzer B., 2005, *X-rays from accretion shocks in T Tauri stars: The case of BP Tau*, A&A, 432, L35
- Schmitt J. H. M. M., Zinnecker H., Cruddace R., Harnden F. R., 1993, *ROSAT detections of X-ray emission from young B-type stars*, ApJ, 402, L13
- Schwab F. R., Cotton W. D., 1983, *Global fringe search techniques for VLBI*, AJ, 88, 688
- Shang H., Li Z.-Y., Hirano N., 2006, *Jets and bipolar outflows from young stars: Theory and observational tests*, in Protostars and Planets V, ed. B. Reipurth, D. Jewitt, & K. Keil
- Shang H., Lizano S., Glassgold A., Shu F., 2004, *Free-free Radio Emission from Young Stellar Objects*, ApJ, 612, L69
- Shu F. H., Adams F. C., Lizano S., 1987, *Star formation in molecular clouds - Observation and theory*, ARA&A, 25, 23
- Shu F. H., Shang H., Glassgold A. E., Lee T., 1997, *X-rays and fluctuating X-winds from protostars.*, Science, 277, 1475
- Siess L., Dufour E., Forestini M., 2000, *An internet server for pre-main sequence tracks of low- and intermediate-mass stars*, A&A, 358, 593
- Simon M., Felli M., Massi M., Cassar L., Fischer J., 1983, *Infrared line and radio continuum emission of circumstellar ionized regions*, ApJ, 266, 623
- Skinner S. L., 1993, *Circularly polarized radio emission from the T Tauri star Hubble 4*, ApJ, 408, 660
- Skinner S. L., Briggs K. R., Güdel M., 2006, *The Unusual X-Ray Spectrum of FU Orionis*, ApJ, 643, 995
- Skinner S. L., Brown A., Stewart R. T., 1993, *A high-sensitivity survey of radio continuum emission from Herbig Ae/Be stars*, ApJS, 87, 217
- Skinner S. L., Güdel M., Audard M., Smith K., 2004, *New Perspectives on the X-Ray Emission of HD 104237 and Other Nearby Herbig Ae/Be Stars from XMM-Newton and Chandra*, ApJ, 614, 221
- Skinner S. L., Güdel M., Koyama K., Yamauchi S., 1997, *ASCA Observations of the Barnard 209 Dark Cloud and an Intense X-Ray Flare on V773 Tauri*, ApJ, 486, 886
- Smith K., Güdel M., Benz A. O., 1999, *Radio counterparts to extreme X-ray YSO's*, A&A, 349, 475
- Smith K., Pestalozzi M., Güdel M., Conway J., Benz A. O., 2003, *VLBI observations of T Tauri South*, A&A, 406, 957
- Snell R. L., Loren R. B., Plambeck R. L., 1980, *Observations of CO in L1551 - Evidence for stellar wind driven shocks*, ApJ, 239, L17
- Stapelfeldt K. R., Burrows C. J., Krist J. E., Trauger J. T., Hester J. J., Holtzman J. A., Ballester G. E., Casertano S., Clarke J. T., Crisp D., Evans R. W., Gallagher, III J. S., Griffiths R. E., Hoessel J. G., Mould J. R., Scowen P. A., Watson A. M., Westphal J. A., 1995, *WFPC2 Imaging of the Circumstellar Nebulosity of HL Tauri*, ApJ, 449, 888
- Stassun K. G., van den Berg M., Feigelson E., Flaccomio E., 2006, *A Simultaneous Optical and X-ray Variability Study of the Orion Nebula Cluster. I. Incidence of Time-Correlated X-ray/Optical Variations*, ArXiv Astrophysics e-prints

- Stäuber P., Doty S. D., van Dishoeck E. F., Benz A. O., 2005, *X-ray chemistry in the envelopes around young stellar objects*, A&A, 440, 949
- Stelzer B., 2004, *Quiescent X-Ray Emission from an Evolved Brown Dwarf?*, ApJ, 615, L153
- Stelzer B., Fernández M., Costa V. M., Gameiro J. F., Grankin K., Henden A., Guenther E., Mohanty S., Flaccomio E., Burwitz V., Jayawardhana R., Predehl P., Durisen R. H., 2003, *The weak-line T Tauri star V410 Tau. I. A multi-wavelength study of variability*, A&A, 411, 517
- Stelzer B., Flaccomio E., Montmerle T., Micela G., Sciortino S., Favata F., Preibisch Th., Feigelson E. D., 2005, *X-Ray Emission from Early-Type Stars in the Orion Nebula Cluster*, ApJS, 160, 557
- Suess S. T., Nerney S., 2004, *Flow in streamer boundaries, and streamer stability*, Advances in Space Research, 33, 668
- Suters M., Stewart R. T., Brown A., Zealey W., 1996, *Variable Radio Sources in the Corona Australis Cloud*, AJ, 111, 320
- Swartz D. A., Drake J. J., Elsner R. F., Ghosh K. K., Grady C. A., Wassell E., Woodgate B. E., Kimble R. A., 2005, *The Herbig Ae Star HD 163296 in X-Rays*, ApJ, 628, 811
- Takami M., Bailey J., Chrysostomou A., 2003, *A spectro-astrometric study of southern pre-main sequence stars. Binaries, outflows, and disc structure down to AU scales*, A&A, 397, 675
- Tanuma S., Shibata K., 2005, *Internal Shocks in the Magnetic Reconnection Jet in Solar Flares: Multiple Fast Shocks Created by the Secondary Tearing Instability*, ApJ, 628, L77
- Taylor K. N. R., Storey J. W. V., 1984, *The Coronet, an obscured cluster adjacent to R Corona Austrina*, MNRAS, 209, 5
- Teixeira R., Ducourant C., Sartori M. J., Camargo J. I. B., Périé J. P., Lépine J. R. D., Benevides-Soares P., 2000, *Proper motions of pre-main sequence stars in southern star-forming regions*, A&A, 361, 1143
- Thum C., Wiesemeyer H., Morris D., Navarro S., Torres M., 2003, *Versatile IF polarimeter at the IRAM 30m telescope*. In: S. Fineschi (ed.), pp 272–283
- Tout C. A., Pringle J. E., 1995, *X-ray coronae from dynamos in young Ae/Be stars*, MNRAS, 272, 528
- Tsuboi Y., Imanishi K., Koyama K., Grosso N., Montmerle T., 2000, *Quasi-periodic X-Ray Flares from the Protostar YLW 15*, ApJ, 532, 1089
- Tsuboi Y., Koyama K., Hamaguchi K., Tatematsu K., Sekimoto Y., Bally J., Reipurth B., 2001, *Discovery of X-Rays from Class 0 Protostar Candidates in OMC-3*, ApJ, 554, 734
- Tsuboi Y., Koyama K., Murakami H., Hayashi M., Skinner S., Ueno S., 1998, *ASCA Detection of a Superhot 100 Million K X-Ray Flare on the Weak-lined T Tauri Star V773 Tauri*, ApJ, 503, 894
- Tsuboi Y., Maeda Y., Feigelson E. D., Garmire G. P., Chartas G., Mori K., Pravdo S. H., 2003, *Coronal X-Ray Emission from an Intermediate-Age Brown Dwarf*, ApJ, 587, L51
- Tsujimoto M., Feigelson E. D., Grosso N., Micela G., Tsuboi Y., Favata F., Shang H., Kastner J. H., 2005, *Iron Fluorescent Line Emission from Young Stellar Objects in the Orion Nebula*, ApJS, 160, 503
- Tsujimoto M., Koyama K., Kobayashi N., Saito M., Tsuboi Y., Chandler C. J., 2004, *A High-Resolution Very Large Array Observation of a Protostar in OMC-3: Shock-Induced X-Ray Emission by a Protostellar Jet*, PASJ, 56, 341
- Turon C., Creze M., Egret D., Gomez A., Grenon M., Jahreiß H., Requiem Y., Argue A. N., Bec-Borsenberger A., Dommanget J., Mennessier M. O., Arenou F., Chareton M., Crifo F., Mermilliod J. C., Morin D., Nicolet B., Nys O., Prevot L., Rousseau M., Perryman M. A. C., et al., 1993, *Version 2 of the HIPPARCOS Input Catalogue*, Bulletin d'Information du Centre de Données Stellaires, 43, 5

- Uchida Y., Sakurai T., 1983, *Interacting magnetospheres in RS CVn binaries - Coronal heating and flares*. In: P. B. Byrne and M. Rodono (eds.), pp 629–632
- Vilas-Boas J. W. S., Myers P. C., Fuller G. A., 1994, *Dense cores in dark clouds. 9: Observations of (13)CO and C(18)O in Vela, Chamaeleon, Musca, and the Coalsack*, ApJ, 433, 96
- Vuong M. H., Montmerle T., Grosso N., Feigelson E. D., Verstraete L., Ozawa H., 2003, *Determination of the gas-to-dust ratio in nearby dense clouds using X-ray absorption measurements*, A&A, 408, 581
- Walter F. M., Stringfellow G. S., Sherry W. H., Field-Pollatou A., 2004, *V1647 Orionis (IRAS 05436-0007) in Outburst: The First Three Months*, AJ, 128, 1872
- Walter F. M., Vrba F. J., Wolk S. J., Mathieu R. D., Neuhäuser R., 1997, *X-Ray Sources in Regions of Star Formation. VI. The R CRA Association as Viewed by Einstein.*, AJ, 114, 1544
- Wang H., Mundt R., Henning Th., Apai D., 2004, *Optical Outflows in the R Coronae Australis Molecular Cloud*, ApJ, 617, 1191
- Wannier P. G., Scoville N. Z., Barvainis R., 1983, *The polarization of millimeter-wave emission lines in dense interstellar clouds*, ApJ, 267, 126
- Ward-Thompson D., Kirk J. M., Crutcher R. M., Greaves J. S., Holland W. S., André P., 2000, *First Observations of the Magnetic Field Geometry in Prestellar Cores*, ApJ, 537, L135
- Weigelt G., Beuther H., Hofmann K.-H., Meyer M. R., Preibisch T., Schertl D., Smith M. D., Young E. T., 2006, *Bispectrum speckle interferometry of the massive protostellar outflow source IRAS 23151+5912*, A&A, 447, 655
- Weintraub D. A., Kastner J. H., Whitney B. A., 1995, *In Search of HL Tauri*, ApJ, 452, L141
- Weisskopf M. C., Brinkman B., Canizares C., Garmire G., Murray S., Van Speybroeck L. P., 2002, *An Overview of the Performance and Scientific Results from the Chandra X-Ray Observatory*, PASP, 114, 1
- Welty A. D., 1995, *Discovery of a Pre-Main-Sequence Spectroscopic Binary: V773 Tauri*, AJ, 110, 776
- White G. J., Liseau R., Men'shchikov A. B., Justtanont K., Nisini B., Benedettini M., Caux E., Ceccarelli C., Correia J. C., Giannini T., Kaufman M., Lorenzetti D., Molinari S., Saraceno P., Smith H. A., Spinoglio L., Tommasi E., 2000, *An infrared study of the L1551 star formation region*, A&A, 364, 741
- White R. J., Hillenbrand L. A., 2004, *On the Evolutionary Status of Class I Stars and Herbig-Haro Energy Sources in Taurus-Auriga*, ApJ, 616, 998
- White S. M., Pallavicini R., Kundu M. R., 1992, *Radio flares and magnetic fields on weak-line T Tauri stars*, A&A, 259, 149
- Wilking B. A., Greene T. P., Lada C. J., Meyer M. R., Young E. T., 1992, *IRAS observations of young stellar objects in the Corona Australis dark cloud*, ApJ, 397, 520
- Wilking B. A., McCaughrean M. J., Burton M. G., Giblin T., Rayner J. T., Zinnecker H., 1997, *Deep Infrared Imaging of the R Coronae Australis Cloud Core*, AJ, 114, 2029
- Wilking B. A., Taylor K. N. R., Storey J. W. V., 1986, *The nature of the infrared cluster in the R Coronae Australis cloud core*, AJ, 92, 103
- Woitaj J., 2003, *A fourth component in the young multiple system V 773 Tauri*, A&A, 406, 685
- Zapata L. A., Rodríguez L. F., Kurtz S. E., O'Dell C. R., 2004, *Compact Radio Sources in Orion: New Detections, Time Variability, and Objects in OMC-1S*, AJ, 127, 2252
- Zinnecker H., Preibisch Th., 1994, *X-ray emission from Herbig Ae/Be stars: A ROSAT survey*, A&A, 292, 152
- Zirin H., Tanaka K., 1973, *The Flares of August 1972*, Sol. Phys., 32, 173

Acknowledgments

At this point, I would like to thank my supervisor Prof. Dr. Karl Menten for all his support and advice ranging from the big issues to details like ‘try dparm(7) 3’. Already from the start, I enjoyed the discussions with him which lead to the definition of the very different projects that I have worked on, all dealing with multi-wavelength variations of the same theme. Also the other members of my thesis committee, Prof. Dr. Pavel Kroupa and Dr. Arnaud Belloche have helped considerably not to loose track. I would like to thank Arnaud not only for this task, but also for all the help especially concerning the 30m and APEX telescopes. I am grateful to Prof. Dr. Ralph Neuhäuser in Jena for the hospitality granted throughout my PhD work as well as for his support.

I am indebted to several other people who have helped and supported me in the different projects this work consists of. In spite of its name, the MPIfR truly is a great environment for multi-wavelength work on star formation. Dr. Thomas Preibisch introduced me to the world of stellar X-ray astronomy while Dr. Maria Massi, Dr. Eduardo Ros, and Dr. Andreas Brunthaler helped me to find my way in Very-Long-Baseline Interferometry. Maria also let me join her long-term project on V773 Tau for which I analyzed the millimeter interferometry data. Dr. Friedrich Wyrowski answered many questions dealing with millimeter and centimeter radio astronomy while Dr. Endrik Krügel always astonished me when giving immediate in-depth explanations especially on problems dealing with interstellar dust. Dr. Thomas Stanke helped me with my first near-infrared observations from Calar Alto to the Very Large Telescope (and continues to be a collaborator on submillimeter projects as well).

Especially the simultaneous multi-wavelength project would not have been possible without many people. Next to already mentioned collaborators, I would like to thank Prof. Fred Walter (State University of New York) for providing access to the SMARTS 0.9m telescope as well as for help in data analysis, Prof. Dr. Motohide Tamura (National Astronomical Observatory of Japan) for providing access to the Infrared Survey Facility in South Africa, as well as to Drs. Noriyuki Matsunaga, Nobuhiko Kusakabe, Yasushi Nakajima, and Kengo Tachihara for carrying out the observations and help in organization and data analysis. Special thanks to Dr. Scott Wolk (Harvard-Smithsonian CfA) and *Chandra* Mission Planning for their scheduling efforts concerning *Chandra* and the VLA. After scheduling problems at the European Southern Observatory, I was happy that Alexis Brandeker (University of Toronto) and Sonia Fornasier (Università di Padova) agreed to join the project and share some of their observing time at the New-Technology Telescope during the *Chandra* observations. Thanks to Dr. Valentin Ivanov for technical help in preparing these Soff observations. Not only by serving as central contact point at times of travelling, including first data reduction and forwarding, Bettina Posselt (MPE/AIU) helped to make the observing plan happen. Thanks to Angeliki Field-Pollatou (SUNY) for swapping observing time at CTIO, to Dipankar Maitra (Yale University) for carrying out part of the optical observations in service mode and a great time at CTIO, as well as to Edgardo Cosgrove for nice observing support. Prof. Dr. Charles Bailyn (Yale University) on short notice kindly agreed to schedule additional simultaneous IR observations at CTIO which were then not carried out due to bad weather. Dr. Christopher Broeg introduced me to and let me use his differential-photometry code. Greatly contributing to the subsequent X-ray part of the project,

Dr. Lori Allen (CfA) provided me with her *Spitzer* IRAC images of the CrA star-forming region and the classification of the sources prior to publication.

For the VLBI observations as well as for the observing runs at the IRAM Plateau de Bure Interferometer, I would like to acknowledge the NRAO Data Analysts and the observatory staff at the VLA, the VLBA, Arecibo, the GBT, in Effelsberg, as well as at PdBI for carrying out the observations. Dr. Jan-Martin Winters (IRAM) was a great local contact for the V773 Tau project, I would like to thank him for his help during data reduction and analysis.

Collaborating with Dr. Helmut Wiesemeyer and Dr. Clemens Thum (both IRAM) on the XPOL project was and continues to be a pleasure. They have taught me a lot on millimeter polarimetry.

I am grateful also to Dr. Katharina Schreyer in Jena, for continued support and advice on millimeter radio astronomy. The projects I worked on in my diploma thesis have continued to grow, and I am happy to collaborate on these projects with her, as well as with Prof. Dr. Thomas Henning (MPIA), Dr. Randolph Klein (University of California at Berkeley), Bettina Posselt, and others.

Special thanks to my Kinderzimmer room mates in Bonn, Thushara, Jens, and Hauke (who graciously continues to provide the coffee machine) !

Nearly my entire studies were financed by Studienstiftung des deutschen Volkes, for which they of course deserve a special acknowledgment. In the last years, I also enjoyed their interdisciplinary PhD student meetings. Additional funding for attending conferences and for observing trips was provided not only by MPIfR, but also from DFG, IRAM, and the University of Hawaii. I also benefited from the International Max Planck Research School for Radio and Infrared Astronomy in Bonn.

During this work, I made extensive use of NASA's Astrophysics Data System Bibliographic Services (ADS), the SIMBAD database (CDS, Strasbourg, France), as well as Spiegel Online. The ADS also provides access to new motivation for studying Single-Event Events (SEEs, Liebovitch 1974). Thanks as well to the many people who put L^AT_EX advice on the web !

Lastly, I deeply appreciate all the support that I receive from my parents and especially from Bettina. Her name should be at the beginning of this list.

This work makes use of data products of the Two Micron All Sky Survey, which is a joint project of the University of Massachusetts and the Infrared Processing and Analysis Center/California Institute of Technology, funded by the National Aeronautics and Space Administration and the National Science Foundation. It is partly based on observations obtained with XMM-*Newton*, an ESA science mission with instruments and contributions directly funded by ESA Member States and NASA. IRAM is an international institute for research in millimeter astronomy funded by the Max-Planck-Gesellschaft, Germany, the Centre National de la Recherche Scientifique, France, and the Instituto Geografico Nacional, Spain.